THE DEVELOPMENT OF A STEERABLE NEEDLE ROBOT WITH BIOMATERIALS FOR THE APPLICATION OF 3D PRINTING *IN SITU* TOWARDS *IN VIVO* ARTIFICIAL MUSCLES

A thesis presented in partial fulfilment of the requirements
for the degree of
Doctor of Philosophy
in
Engineering
at Massey University, Palmerston North,
New Zealand.

Jean Henri Odendaal

2023

Contents

List of Tables

List of Figures

Abstract

Additive manufacturing is an emerging and continually growing field of research with exciting potential in the development of recent technologies through which to change the world as we know it. This thesis offers a look from a 3D printing perspective towards the diverse fields of artificial muscle fabrication, bioprinting, polymer chemistry which can affect shape change or other responses under stimuli, as well an in-detail investigation into steerable needle robotics and its potential as a mechanism for additive manufacturing. A limitation in the 3D printing of (bio)polymers involves a printed geometric construct requiring a separate print bed for this process which is independent from its intended location of use. As a response to this limitation, this thesis proposes an approach towards generating fibers or structures composed of individual fibers in the location of the structures use.

This thesis presents the research and development of a flexible steerable needle robot for the application of 3D printing (bio)polymers which could take the form of artificial muscles, bone, nerves, etc., *in vivo*. This is extremely challenging, however, and this thesis aims at building this capability towards achieving this goal in the future.

The chapters in this thesis explore the characteristics of an engineered steerable needle robot in application for 3D printing which include: its mechanisms, its control systems, its algorithms to accurately reach a target goal within a presented body, as well as its visualization system. Furthermore, this developed robot is then utilized to "3D print" a (bio)polymer inside of a prepared phantom body (e.g., gelatine) to fabricate a bio-fiber. While the bio-fibers presented by this thesis are simple and do not react under any stimulus to function as an artificial muscle, there is a further opportunity identified which could utilize advanced polymer chemistry to in fact achieve this result.

This thesis ultimately contributes towards the synthesis of multiple fields of research towards the goal of one day realizing the imagination of science fiction. Namely, the ability to quickly regenerate human tissue without the need for complex surgeries as well as the fabrication of fibers which could form part of artificial limbs or bodies.

Acknowledgements

I would like to begin by acknowledging that powerful force which can at a single moment capture the very essence of existence within the human spirit. That spirit which is, through this, ignited by a lightning bolt from the heavens to bring a light into the darkness of consciousness and expand through a burst of ethereal colour the very limits of the perception of human eyes. An ignition of a fundamental drive, a primal force which dictates that an individual should live in the present moment. In a phrase, that they should live supremely and to their best efforts. That, regardless of consequences and of failures, they should find courage and power in the act of life alone - for without the destruction of fire what could this universe filled with grandiose creation have ever hoped to generate. It is this impetus which drives humanity subconsciously, unknowingly, and sometimes dangerously forward. Forward we must all go towards this future, driven by this terrible yet beautiful energy, and by the spirits we discover within ourselves to unchain our minds and to take part in this eternal act of creation.

To my co-supervisors - Marie Joo Le Guen, Olaf Diegel, Nitin Bhatia, and Russell Wilson - thank you for your guidance and patience these past years. To my supervisor - Prof. Johan Potgieter - thank you for the opportunities you have given me and for your guidance. You have often told me that a person must sometimes be pulled from the fire. Saved, as it were, from potential destruction or even self-immolation. This would be the natural compulsion. As from mentor to disciple, the student strays at times into the depths of fire. You have pulled me from these flames, but I admit freely that I walked into these fires of my own will in search of the unknown and even unknowable. Humbly, I thank you for pulling me back when I had strayed too far.

I give my utmost thanks to my family. To my mother and father. To my brother. The depth of all individual power has its roots in the mystic space of this spiritual connection. I acknowledge that it is by and through my connection with my family that I have and will reach all the achievements in life.

I would also like to think the team at MAFDL, the SfTi National Science Challenge 3D / 4D printing spearhead, John Kennedy at GNS, and all others who are not mentioned by name who have contributed to the research that is presented in this thesis and to the ideas that it wishes to bring into existence in the future.

Thoughts give birth to a creative force that is neither elemental nor sidereal. Thoughts create a new heaven, a new firmament, a new source of energy, from which new arts flow. When a man undertakes to create something, he establishes a new heaven.

— *Paracelsus*

Chapter 1

Introduction

1.1 Research Approach

The 21st century marches towards a future that few individual minds can truly comprehend in isolation at present times. It is in the collective efforts, teamwork, and multibillion dollar investments from the most technologically advanced companies that the destiny of humanity achieves greater understanding, ultimate collective comprehension and hopeful good. In ancient history, humanity looked to the stars, to the natural world, and to themselves to find inspiration. The inspiration that drives forward all progress in human understanding. From the Greek minds of antiquity to the alchemical minds of the Middle Ages, and now to the modern and rational minds found at universities, research institutes, or simply technology start-ups, humanity has sought not only to understand the phenomena of the universe, but to perform an action of creation and sub-creation. Where does modern humanity find inspiration for grand and potentially revolutionary ideas and practical efforts?

Who can deny the formidable powers of media such as science fiction novels, television programs, films, and the growing mass of information of the internet on the human mind. Technology has dramatically simplified human means of communication, and as a tree diverges as it grows upwards, so has the branch of audio-visual media practically interconnected the whole of available human knowledge and subsequently inspired an almost infinite number of eager minds. Should one mind then draw inspiration from this collective imagination of countless other minds with their own knowledge and experience, so then can this one mind begin the journey towards individual discovery, the exploration of knowledge and subsequently meaningful contribution to this greater body of knowledge. What does this one individual gain from this effort which involves sacrifice and discipline?

One argument which considers this question involves the idea that an individual who begins this path begins to seek, to intend, to create. For such individuals, a single

action of creation may be the end of their personal journey, but for the resolute it is instead a series of journeys. An endless mission to drive forward the boundaries of self-discovery, knowledge and understanding, and human capabilities. This process is one of destruction and creation with the everlasting hope that the destruction will be for the better and that the action of new or sub-creation will present landscapes of fertile soil for even more branching trees. This thesis is such an action where the resulting research review plucks the fruits from the branches of previously developed trees, and from these seeds the advancement of technology through clear hypothesis and experiment plants a new tree. Research at its core states, thus, that the scientific method is the cultivation of innovative ideas and knowledge, i.e., the growth of a tree.

A discussion at the beginning of this PhD pointed the research towards 3D printing, due to personal interests of the author. Since this work must be related to engineering, and the realm of science fiction served to hold the initial spark of inspiration. A simple question was asked: "How can fibres which mimic natural muscle (through stimulus expand and contract) be 3D printed?" The applications of such a question, while still experimentally limited in research could have significant impact in the future. For example, prosthetic limbs are artificial in the sense that they hold no biological matter (e.g., cells) and aid the wearer in limited capacities — never perfectly replacing a lost limb.

These prosthetic devices are mechanical and sometimes even electronic, but there remains the question of a potential biological interface. What if the fundamental materials such as muscle fibre, nerves, bones, etc., could be 3D printed as part of a regenerative or additive process or device? What 3D printing process exists or could exist to achieve the manufacturing of such fibres or structures? There exists a concept of the future where technology and humanity have reached a type of synthesis.

Where technology may heal and enhance the individual powers of any one individual to affect greater works of creation and art within the infinity of the universe. This work seeks to explore the practical engineering and materials science aspects of this concept and contribute a step towards its ultimate realisation. These are the fundamental research questions of this thesis. The key question can thus be stated as: "Can a bio-fibre which reacts to stimulus (similar to natural muscle) be 3D printed?" These questions branch into offshoot questions, namely:

- What is a bio-fibre? How is it defined?
- Where and how should a bio-fibre be 3D printed?
- What stimuli exist to cause a reaction in a fibre – bio or otherwise?
- What function could such a reaction serve?

- How is 3D printing used to create this bio-fibre assuming a relevant implementation such as artificial muscles?

1.2 Research Aims

The first part of this research is purely investigative into previous works. It seeks the definitions and to establish the foundational background from which to propose a hypothesis and thereby deliverables. Chapter two of this thesis presents a literature review which enhances its scope to commercial outcomes at certain sections. It seeks to understand the nature of biological structures such as muscle and the current state-of-the-art in the replication of these structure, or even their enhancement. This took the form of an investigation into 3D printing technology and materials science, distinguishing between synthetic and bio-based polymers and their varying outcomes. the literature review further investigated and defined electroactive actuators, electroactive polymers as artificial muscles, shape memory polymers, and the field of 4D printing (defined as the changing of a 3D printed construct over time under specific stimulus which is fully reversible),. The main question in this investigation is: "How can artificial muscle of even a single fibre which mimics natural muscle be created? "Through these fundamental definitions, an investigation into 3D printing technology took place. The review further cross-referenced common additive manufacturing techniques such as Selective Laser Sintering, bio-printing through inkjet deposition, Stereolithography, etc., were cross-referenced with the definitions of artificial muscle fabrication. Since these definitions clearly exposed the fundamental structure as a bio-fibre, it was evident that the 3D printing process needed to create a single fibre or even networks of fibres. As a result, key opportunities are identified within current technology to satisfy the key research question.

Following this, the literature review surveyed the relevant polymer chemistry to understand and identify the materials (synthetic or bio-based in origin) which 3D printing technology could use to produce bio-fibres. It further identified significant limitations within the synthesis of polymer chemistry and 3D printing technology with only the most recent advancements in Additive Manufacturing enabling the usage of certain materials. As such, there exists opportunities for the further development of 3D printing to allow the usage of polymers with useful outcomes. The following challenges, hence, identify certain opportunities:

- The polymerisation strategy is a limiting factor (e.g., high heat may not be an effective means through which to produce bio-fibres).
- Low viscosity inks are most common for 3D printing.

- There remains a challenge in the production and placement of a bio-fibre since it must form part of a greater product or body (e.g., transplantable tissue, etc.).

These questions led this research to proof-of-concept experiments exploring 3D printing techniques with respect to the polymer chemistry. Essentially, to manufacture a bio-fibre of any description would require a suitable suspension matrix to function as its support. This removable / temporary matrix thus supports the extraction of the desired fibre or network of fibres. The capability to enter this matrix and effectively polymerise a material is the core assumption involved, which further expands to the understanding that such a matrix must be, by definition, self-healing. As a result, directly producing a fibre in the exact location and desirable orientation in a greater structure, as opposed to producing a fibre separately and then seeking to meld this fibre with a greater product, is a promising avenue of further research. This eliminates the assumption that the matrix inside of which the fibre is 3D printed must be self-healing. Due to the unique challenges this assertion presents, there exists little research associated with directly addressing them. The original research question thus evolved into: "How could a bio-fibre be 3D printed internally and already in a desired location within a body (natural or synthetic)?". Answering this question could partially solve the original question of 3D printing muscle fibres, with the key research problem primarily involving materials science rather than 3D printing technology.

This research then identified steerable needles as an opportunity for the application of 3D printing. Originally used as a surgical technique known as percutaneous intervention, steerable needles offer a minimally invasive technique through which to penetrate a body (e.g., human body, gelatine block, etc.). The key question then revealed itself: "How can steerable needles be used with which to 3D print polymers?" In more direct terms: "How can a technique which does not immediately serve itself towards the deposition of polymers and the subsequent embedding of fibres through a polymerisation process be advanced through engineering?" This question forms the basis of the hypothesis, stated as:

> ***The generation or embedding of simple bio-fibres is possible using steerable needle technology and bio-based polymers.***

This simple hypothesis focuses the thesis into the primary deliverable of effectively producing fibres within pre-existing bodies. From this single deliverable, the research focus splinters into the following areas: steerable needles in terms of an electro-mechanical device controlled through software, polymerisation strategies using steerable needles, the details (mechanical properties, etc.) associated with the bodies that the steerable needles steer through, the polymer chemistry to produce bio-fibres, and the characteristics of the resultant bio-fibres.

1.3 Objectives

1. To demonstrate a custom steerable needle robot applied as a 3D printing technique – key variables: stage, tank, injection system, attachment system, rotation for steerability precision, steerability algorithm and accuracy.

2. To determine the optimal settings and setup required for steerable needle 3D printing – key variables: insertion speed, draw speed, flow rate, polymerisation rate, curvature, insertion depth, length, gauge, custom needle geometry (bevel tipped).

3. To investigate and characterise the fibres drawn using the steerable needle technique proposed within a characterised suspension medium such as gelatine – key variables: fibre morphology, repeatability, precision, rigidity, melting point, polymerisation type.

1.4 Thesis Outcomes

Chapter 3 investigated steerable needles and attempts to model the optimal conditions for steering proprietary injection needles within a suspension medium (or similar) to fabricate fibres at specific positions *in situ* towards future experiments *in vivo*. The action of fibre polymerisation (using ionic or photo-initiated cross-linking mechanisms) occurred at the end position through a reversal process which draws a fibre as the steerable needle reverses along the insertion path for a specified length. The chapter includes a novel experimentation setup where the state of the art in needle steering directs development towards incorporating a polymer injection or fibre embedding system. Since gelatine has mechanical properties that allow for the straightforward analysis of the movement of bodies or projectiles within it, a gelatine mould was prepared as the suspension medium for the fibres to print. This investigation further investigated a range of gelatine concentrations with different mechanical characteristics using two distinct mechanical testing approaches (rheometry, quasistatic analysis).

This chapter also explored an interesting detail involved with the setup associated with using steerable needles — depending on the body in which a steerable needle travels to reach a certain target location, different material characteristics (mechanical, etc.) would affect the behaviour of the needle. In short, stiffer materials would allow for greater maximum deflections as the needle travels through the body. A question then arises, “How can the material properties of the body be identified and quantified accurately?”. Certain steerable needle setups exist which allow for the constant sampling of the strain caused on the needle because of the surrounding material using sensors. This chapter explored using hyperspectral imaging (HSI) to analyse a body which with

certain mathematical inferences could accurately estimate the material properties of the body in question. This is a passive technique as opposed to an active sensing / sampling process, however, there remains an opportunity to create a database of material types (associated with certain material characteristics) using hyperspectral imaging specifically for the use of this steerable needle 3D printer.

Utilising the latest research in steerable needle motion planning algorithms for resolving end-positions within a medium, this research attempted to inject and polymerise fibres at this end-position and for whatever length and in whatever orientation is arbitrarily desired. Since there are limitations in the curvature of needles, chapter three highlights a needle steering model that determines the maximum radius of curvature and the conditions where an end-position cannot feasibly be resolved using the proposed needle 3D printing system.

Furthermore, these fibre fabrication experiments made use of stereo cameras and ultrasound detection systems to validate the deflection curvatures (Chapter 3) as well as the "trueness" of any end-position sought for resolution (Chapter 3). By extension, biomaterials were sought for application within this system to demonstrate its potential capacity in revolutionary future technologies, namely sodium alginate and calcium chloride which on reaction gel into calcium alginate fibres. The real-time embedding or fabrication of such solid fibres through polymer chemistry (Chapter 4 and 5) is the key point of difference between this research and other research that investigates percutaneous intervention. Literature has extensively investigated most other research applications such as drug delivery or catheter installation. Additionally, there currently exist a variety of steerable needle devices / robots, but which lack adequate injection systems nor a suitable framework within which to apply the 3D printing principles as proposed by the hypothesis.

Current research defines the aspects of needle steerability and polymer chemistry are particularly well, however, researchers have not yet synthesised these aspects within the context that this thesis proposes. As such, this thesis is concerned with reaching specific points within a body to fabricate specific lengths or networks of fibres (gels), this demonstrates that this synthesis is novel and that the resulting experiments are of interest.

Furthermore, there is the question of whether the definition of this research as "3D printing" is appropriate since the deposition of materials internal to a body through the mode of injection does not necessarily construct a 3D geometry. However, since this technique can form networks of "fibres" or "filaments" which lend themselves towards constructing the internal structures of a body, "3D printing" serves as the most effective definition currently available to describe these processes. Chapter 5 specifically explores the characteristics of the fibres in terms of their mechanical properties.

Chapter 5 is the culmination of the research and development of a 3D printing steerable needle robot and demonstrated the application of steerable needles within a 3D printing context. Overall, this chapter attempted to understand the effectiveness of the 3D printing process using steerable needles as well as certain polymer chemistry (namely, sodium alginate and calcium chloride reaction to form calcium alginate fibres). A potential future phase of research which stems from this chapter involves the usage of more complex polymer chemistry for certain applications. In the case of artificial muscle fibres, future research could investigate and / or develop conductive polymers, specifically designed to operate under the constraints of the steerable needle 3D printing system proposed by this thesis.

Chapter 6 acts a discussion surrounding the previous chapters. The impact of the results of these chapters were reflected upon as a completed body of work in retrospect. Finally, this chapter weighs steerable needle 3D printing as a concept in terms of suitability with respect to materials, effectiveness, limitations, and advantages.

Chapter 7 concludes the thesis with respect to the highlighted research questions as presented in chapter one. The hypothesis is referred to and analysed with respect to the objectives presented in this chapter. As a result, this chapter finalises the significance, impact, and the limitations of the research as a whole as well as pointing next steps for this research as well as future areas of interest.

Chapter 2

Literature Review

The process of history is combustion. — Novalis

2.1 Introduction

Additive Manufacturing (AM), as a field, has far reaching potential into the design and fabrication of complex geometries with a variety of polymer chemistry. It is in this fusion that fields such as tissue engineering and the development of soft robotics, among others, continue to grow. Exoskeletons, multi-functional devices, wearable devices, textiles, and prostheses are among the most notable end results of the development of versatile polymer chemistry, advances in control engineering, and intelligent sensing electronics. There remains, however, a deep reliance on metal assemblies, electromagnetic actuators, and combustion engines (or similar). However, the advancements in fields such as additive manufacturing and similarly biopolymer chemistry are leaders in the development of new materials based on nature and mechanisms found therein as well as paradigms through which to process these materials in meaningful and decisive ways. Notably, natural muscle remains the single-most impressive actuator in that it offers a level of endurance, dexterity, agility, and regeneration simply not possible within the current state of robotics.

This review discusses the latest developments in artificial muscles with a specific focus on electroactive actuators, and certain limitations and drawbacks are highlighted within the field. Furthermore, the polymer chemistry to investigate the development of bio-based artificial muscles is elucidated as well as the additive manufacturing techniques used to produce them. These techniques provide the ability to control the shape, size, density and inter-connectivity of the material being printed to define a suitable architecture for an application which is a discerning factor in the usage of

artificial muscles in real-world applications. The most exciting works lately are the efforts towards bioprinting skin grafts on burn victims as well as the 3D bioprinting of organs [132, 145].

There are three main components which are particularly interesting to query: (1) What actuator technology approach is currently most suitable to achieve not only electroactive actuators, but which possess a certain level of biocompatibility? (2) What 3D printing approach is the most promising towards fabricating such actuators? Which polymers are most suitable to either approach? Is there a way to pivot 3D printing technology in a novel fashion to achieve this development (3) What engineering sophistication is required to facilitate the synthesis between a biomaterial and a conductive polymer or the embedding of a conductive biopolymer in order to achieve a bio-fibre that when stimulated with electricity deforms suitably (contraction, etc.) and yet maintains structural integrity? By determining the optimal printing configuration and orientation for single or multiple fibres printed, as well as a means to achieve electroactivity, it is envisioned that these questions may be answered and that a future scope for research within these fields summarily described.

According to the aforementioned challenges, it is conceivable that such research may result in development of novel processing techniques and materials towards fabricating bio-fibres which are effective artificial actuators or as the building blocks towards this concept. This is due to the critical aspects of the research and the key gaps in technology that can be inferred. Namely, the literature identifies several challenges within current bioprinting techniques - viscosity, environmental control factors, adhesion, etc. There is minimal literature that attempts to synthesise biomaterials and conductive polymers into singular fibres or 3D constructs due to these challenges, however, the opportunity is well identified. This is mainly due to a lack of viable methods through which to, necessarily, hybridise biopolymers such as collagen with conductive materials. This opportunity stems from the advancement of 3D printing and materials processing technology, as well as the sophistication of materials science. Such a theoretical 4D bio-fibre may contribute towards the development of bio-based artificial muscles as a prosthetic replacement or other applications within fields yet unnamed.

2.2 Artificial Muscles

A broad field of research across disciplines of engineering and materials science, artificial muscles or actuators can be defined as a group of materials and devices that demonstrate shape changing behaviour — contraction, expansion, and rotation — using external stimulus (light, electricity, temperature, pressure) and motion mechanisms (torsion, bending, etc.) [130]. While artificial muscles are intended to mimic natural muscle mechanisms and much research has been dedicated to achieving an equivalent, there is

a distinction between engineered artificial muscles and artificially developed biological muscles for *in vivo* use. Muscle acts as a linear actuator which is suited to sporadic displacements and adaptable stiffness on stimulus ranging from micron to meter lengths. Fundamentally, there are ten general metrics with which to characterise and measure the performance of artificial muscles [130]:

- Stress (σ) — Force experienced over a cross-sectional area under which the actuator. is tested at rest or at excitation
- Strain (ϵ) — Displacement of the actuator material length at rest to excitation.
- Work (Energy) Density (W) — The output work released by a muscle during excitation with normalised to actuator mass and volume.
- Power Density (P) — The work density normalised to the actuation state.
- Catch-State (Lock-Up State) — The holding position of either an excited or at rest state that consumes no energy.
- Actuation Direction — The quality of an actuator to actively change length and or direction on stimulus.
- Cycle Life — The number of cycles an actuator survives before failure.
- Efficiency — The ratio of output work over input energy (e.g., electricity, heat, etc.).
- Bandwidth — The range of frequency over which an actuator can be excited
- Stimulus Magnitude — The energy providing power and control to the actuator material (e.g., Voltage, Current, Heat, etc.).

Muscles are highly optimised structures that are essentially the same for all animals and the differences between various species are negligible. Natural muscles, which can lift relatively heavy loads with rapid response times, are powered by a complex chemo-electro-mechanical mechanism. Their operation depends on a chemically reversible hydrogen bonding reaction between two polymers — actin and myosin. Having a cylindrical shape, muscle cells range in diameter between 10 and 100 μm with a length of a few centimeters. Muscle performance varies greatly between individuals as well as between species with stresses of 150-300kPa at 25% strain which amounts to roughly an average of 50W/kg and an energy density of 20–70 J/kg [38]. Energy density is inversely proportional to the speed at which the muscle attempts to actuate. This energy is provided by an adenose triphosphate hydrolysis reaction with Ca^{2+} ions being the impulse to switch the conformational changes of muscle striction [117, 38]. It is

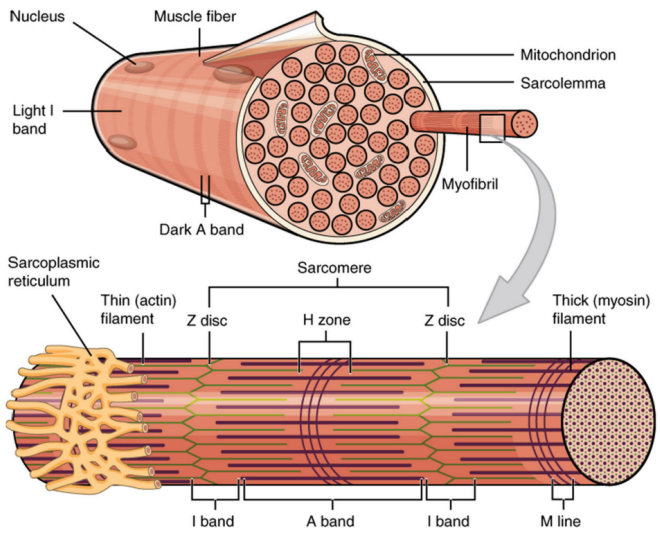

Figure 2.1: Structure of a myofibril. "Reproduced from [149] under the Creative Commons Attribution License"

important to note that while muscles produce the linear forces necessary to lift loads and cause displacements, it is rather the mechanical advantage associated with the rotary actions of joints that affects the overall strength of an organism.

The functional unit of natural muscle contraction is the myofibril which is comprised of several hundred protein filaments. When placed in parallel these myofibrils make up the muscle fibre, and hence multiple muscle fibres form muscle. The myofibrillar sarcomere comprises three types of polymeric filaments.

- 1. The central filament — being thick and composed of the protein myosin — which when arranged in parallel forms the A-band.
- 2. On either end of the central filament is a connecting filament (found in the I-band) which in turn connects to the Z line — composed of the protein titin.
- 3. The thin filament is polymeric and along with various proteins, it is composed of multiple actin proteins. These filaments originate in the Z-line and partially overlap the central filaments in the A-band.

These filaments align perfectly in parallel within the myofibril where the alignment is continued through the cross-linking of the sarcomere in the A- and I-bands, see Figure 2.1. The thick A-band filament proteins are formed through extensive cross-linking which firstly, align the filaments which results in lattice structure forming distinct A- and I-band junctions. Importantly, the polymers involved in this structure are particularly hydrophilic — capable of absorbing water thousands of times their own volume. As such, the muscle-filament lattice, is a highly cross-linked and hydrophilic polymer gel.

In 1959, Garamvolgyi [201] demonstrated that an electrical current is capable of triggering a contraction on an isolated myofibril. From this, it is determined that on the formation and suspension of an actin-myosin gel, which remain stable until critical conditions are reached, the gel can contract — both folding the internal gel matrix and releasing water. This was demonstrated by Szent-Györgyi in 1951 [201]. As such, this behaviour implies that natural muscle polymers consist of polymer-gel state transitions [164]. With respect to artificial muscles these polymer gels within natural muscle are well organised into a complex framework while artificial muscles are in contrast dispersed randomly. All three filament types are believed to shorten or contract under a phase transition which also shortens the sarcomere. Experiments on isolated molecules of titin have revealed the behaviour of connecting filament. It was found that titin molecules had sawtooth-like tension changes that imply a one-by-one unfolding of the filament's tandem immunoglobulin-like domains. The length change occurs as the compact "beta-barrel" domain structure of the immunoglobulin domain gives way to an extended random structure (reference). This connecting filament is lengthened by such unfolding. If thick filaments shorten during contraction, it is likely that shortening would occur one molecule at a time in each half-filament and as such would shorten in a step-down procedure [16].

The sarcomere may also shorten in steps if the thin filament is bound to the cross-bridges during the filament-shortening steps; myosin phase-transition contributes to the shortening of the sarcomere [16]. The thin filament may bring about stepwise length changes as well. Unlike the thick and connecting filaments, whose shortening can directly shorten the sarcomere, thin filaments are differently situated. Because of their arrangement they would need to facilitate contraction in a different way. An example mechanism within artificial muscles is an inchworm-like process – like that reported in PAMPS gels [150]. The long narrow gel repeatedly cycles between curling and straightening. Repeating cycles advances the gel by an appreciable magnitude because the ends of the gel are hooked to a ratchet in such a way that each cycle results in a step advance [16]. Similarly, electroactive polymers may be used to produce fibres or filaments which can cycle through step phases (extension on contraction) depending on the voltage-current signal provided. These types of artificial muscles are categorised as electric and ionic-based actuators depending on the exact mechanism of actuation. This is not dissimilar to the mechanisms of natural muscle; however, the polymer chemistry and manufacturing techniques are yet to successfully produce an effective equivalent.

2.2.1 Electric

Electric field actuation mechanisms are achieved through electrostatic interactions between electrodes or molecular reorganisation within the actuator material structure

and is commonly known as electronic artificial muscles and are one type of electroactive polymers (EAPs) [33, 17]. Low elastic modulus polymers (dielectrics elastomers (DEAs) and electrostrictive polymers) actuate or suffer displacement because an electric field can easily rearrange the electric dipoles. DEA actuators are thin, elastomeric films coated on both sides with electrodes, see Figure 2.2. When an electric field is applied across the electrodes, the electrostatic attraction between the opposite charges on opposing electrode and the repulsion of the like charges on each electrode generate stress on the film causing it to contract in thickness and expand in area [130, 17].

Any decrease in thickness results in concomitant increase across the film because most elastomers used are essentially in-compressible. Typically, DEs within a 1–10mm thickness range possess operating voltages from 500V to 10 kVs [28]. The area expansion can be readily measured if the films are subjected to tensile pre-strain: the non-active areas in tension surrounding the active area pulls the expanded active area and keeps it flat. It is likely that power will only be consumed during an active area expansion and no power will be consumed to maintain the DE at a stable actuated state because the driving currents are low and the device is electrostatic in nature [33].

Although some energy may be recovered after the actuation cycle there is usually some leakage of current through the dielectric which is affected by the material and its thickness. As a result, the dielectric only consumes a little power to maintain its current actuation state. It has been found that DEAs are able to produce large strains between 10% to 100% and can even reach up to 380% with high enough electric fields. Silicone based actuators can yield stress up to 7.7 MPa while acrylic based actuators can yield up to 3.2 MPa. It is due to electrostatic attraction between the two surfaces of the elastomer films that cause compressive strains. Contraction in one direction will cause expansion in the other two because the elastomer maintains constant volume. Most mechanisms use expansion perpendicular to the applied field because it will result in large displacements [99, 17].

The **electrostrictive relaxor ferroelectric polymer actuators** have high work density of 1 MJ/m3 and strain up to 7–10%. These actuators generate high stress, around 45 MPa and frequency up to 100 Hz [17]. In electrostrictive relaxor ferroelectric actuators, the application of an electric field aligns polarised domains within the material. When the applied field is removed, the permanent polarisation remains. Ferroelectrics are characterised by a curie point, a temperature above which thermal energy disrupts the permanent polarisation. Reversible conformational changes for actuation are primarily driven by the alignment of the polar groups within the ferroelectrics. Contraction is induced within these actuators by the application of an electric field perpendicular to the chains which induces the aforementioned polarisation. The result is a contraction in the direction of polarisation and an expansion perpendicular to it [99].

a)

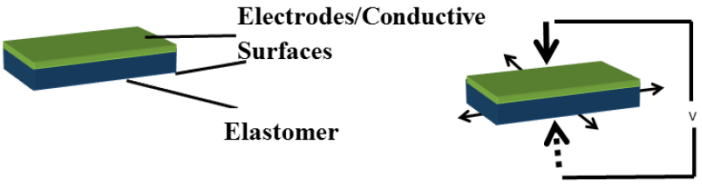

b)

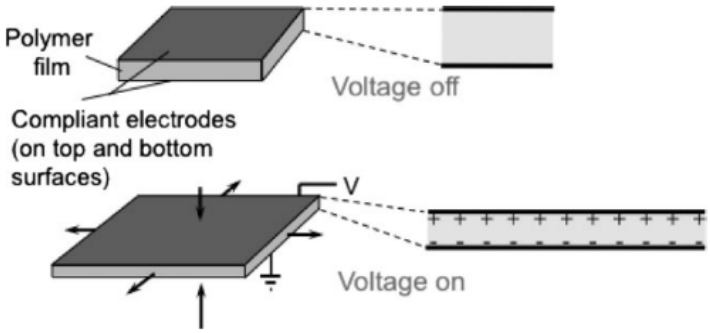

Figure 2.2: a) Structure of a Dielectric Elastomer. "Reproduced from [99] under the Creative Commons Attribution License" b) Two electrode dielectric elastomer — field attraction / repulsion causes squeezing deformation. "Reprinted, with permission, from [28] "

All relaxor-based ferroelectric polymers are based on the P(VDF–TrFE) copolymer. These polymers behave as relaxor ferroelectrics, which are characterised by a peak in dielectric constant and strong frequency dispersion. P(VDF)-based ferroelectric actuators have two major limitations [99]:

- Actuation utilising the polarisation contraction process only occurs at temperatures above the Curie temperature (e.g., room temperature).
- Hysteresis, which is the state memory associated with transitions, causes actuation to need more energy.

Certain studies suggest that in order to deal with the Curie temperature of certain polymers (e.g., P(VDF–TrFE)), defects can be introduced into the material which effectively reduces the size of the crystallites within the copolymer. As a result, this lowers the energy barrier required for the transition between paraelectric and ferroelectric states. This lower energy barrier may result in lower hysteresis [99, 17]. However, the persistent usage of energy and high strains will eventually break down the elastomer and electrodes resulting in diminished electrical properties and mechanical fatigue [137].

2.2.2 Hydraulically Amplified Self-Healing Electrostatic Artificial Muscles

The latest advancement in dielectric elastomer design have recently developed into what are known as hydraulically amplified self-healing electrostatic artificial muscles (HASEL) [83]. HASEL is described as:

> "...an electrohydraulic system to activate all-soft matter hydraulic architectures.".

It is in the utilisation of fluids within soft structures which when electrostatic forces act upon them a hydraulic pressure is distributed within a structure, thus resulting in shape change or displacement. In simple terms, fluids produce pressure in certain distributions depending on the electrostatic forces which act upon them, thereby driving a desired shape change. This behaviour is achieved through the use of liquid dielectrics that are essentially self-healing and can instantly recover from dielectric breakdown [5]. There are several types of HASEL actuators (donut, planar, etc.) as reported by Rothemund et al. in 2021 with an in-depth analysis of each type's characteristics. Reportedly, HASEL actuators reach actuation strain of ¿100 % and high specific power outputs (614 W/kg peak) at 22.5 kV. This is much more powerful than conventional DEAs at similar voltages [180]. However, while conventional DEAs are effective in actuation and sensing capabilities. There are several constraints which include a stretchable material system, dielectric layers, and electrodes that often result in scalability problems that reduce their overall effectiveness.

Silicone based elastomeric materials were the first materials utilised in the development of HASEL actuators. There are two key designs using elastomeric materials (donut and planar actuators). The donut actuator works on the principle of a spherical shell filled with a liquid dielectric and concentrically placed electrodes which when a voltage is applied the electrostatic forces displace the liquid to the furthest edge of the shell. This increase in thickness under high voltage has displayed fairly large actuation strains (¿50% at a voltage of 20kV) [180]. Another type is planar actuators which consist of a plane where the electrodes cover the near entirety of the liquid dielectric region [5]. Once a voltage is applied, the thickness decreases and the surface area increases. This is similar to conventional DEAs; however, the dielectric component is liquid in contrast. As such, planar actuators reach greater actuation strains at the same voltage. Planar actuators in series are capable of lifting substantial weights — such as a gallon of water [5], see 2.3.

HASEL actuators can also be fabricated, utilising thermoplastics, using arbitrarily designed 2D geometries and heat sealing / bonding layers of a dielectric material (e.g., biaxially oriented polypropylene — BOPP) to form a shell. These shells are subsequently

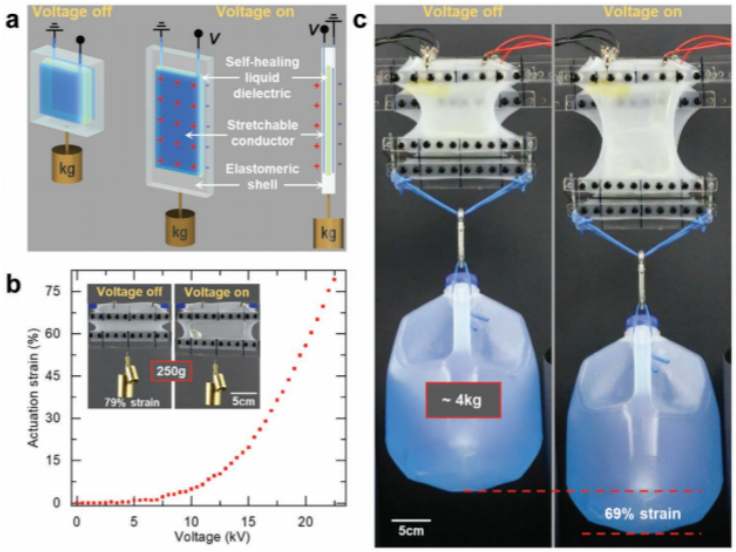

Figure 2.3: Planar HASEL actuators a) Elastomeric shell which elongates under voltage b) HASEL linear actuator. c) Six planar HASEL actuators lifting 4kg. "Reprinted, with permission, from [5]"

filled with liquid dielectrics and coated ionic electrodes [180], see Figure 2.3. While this technique is effective in rapidly producing single HASEL actuators, it is ineffective in mass production due to the complexity and cost of the fabrication process. There are several types of thermoplastic-based HASEL actuators that are capable of inhabiting complex geometries and designs.

Within these two categories of HASEL actuators (elastomeric and thermoplastic), elastomeric actuators are the "strongest" of the two in practice especially since more than one elastomeric actuator can act in tandem [137]. This poses the question how thermoplastic type designs could be designed to behave similarly. Also, since these actuators make use of thermoplastic, often completely synthetic and non-biodegradable, they cannot truly be compared to natural muscle. A bio-based HASEL-like actuator could be a step towards achieving not merely a mimic of nature but nature itself. It, thus, becomes a question about which materials are most suitable to fabricate similar artificial muscles.

2.2.3 Ionic

In ionic artificial muscles (usually ionic polymer gels), actuation is caused by the ion transport within the polymer material and exchange of ions between the actuator and an electrolyte solution. First discussed in the early 1950s by Kathalsky, et al. when such a gel shrinks or swells, it is in response to a change in the environmental pH levels resulting from the displacement or redistribution of water. This principle forms part

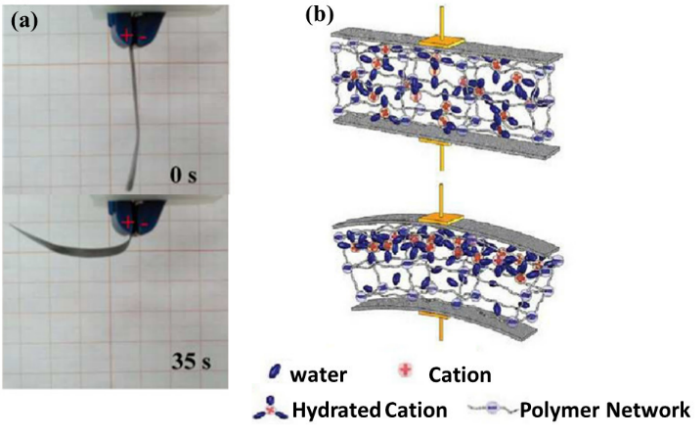

Figure 2.4: The actuation of IPMC (b) the applied force causes the cation migration. "Reproduced from [99] under the Creative Commons Attribution License"

of a field of study named mechanochemistry [103, 95]. In order for ions to balance across the polymer phase and displace the entrained solvent, an electrical current needs to induce a potential change across the polarity of the polymer gel. Ionic EAPs need low voltage to induce actuation (1–7 V). Regardless, high energy requirements are associated with these actuators due to the amount of charge that needs to be transferred. Ion based actuators are fabricated using conducting polymers (otherwise known as conjugated polymers or CPs), carbon nanotubes (CNTs) and ionic polymer-metal composites (IPMC). IPMCs consist of an ion-exchange polymer film usually coated with electrodes made up of metals (gold, silver, etc. or other even polymers such as graphene. Metal-based electrodes are comprised of platinum / gold / silver nanoparticles, see Figure 2.4. When a voltage is applied between two electrodes, ions are attracted and or repulsed towards the oppositely charged electrode. This results in deformation between the two electrodes. These actuators were reported with maximum actuation strains of 3.3%, a stress of 30 MPa, using frequencies of up to 100 Hz [126, 17].

Baughman et al. in 1990 [19] first proposed actuators based on CPs. They were developed consequently to actuate due to the uptake of counterions during electrochemical redox cycling. Deformation utilising this mechanism occurs perpendicular to the polymer chains which indicated that ions and solvents are merged into these chains. CPs are a class of electroactive polymers which are activated by the transport of ions through the polymer chains. Electrochemical or chemical stimulation through electrolytes is usually required for actuation to occur. As such, these conducting materials must be doped with ions [151]. The principle of CPs operate under a dimensional change mechanism triggered by the addition or removal of charge from the polymer structure when ions travel across it, see Figure 2.5. Three major factors impact the properties of CPs and their performance in terms of their shape changing behaviour (be it bending

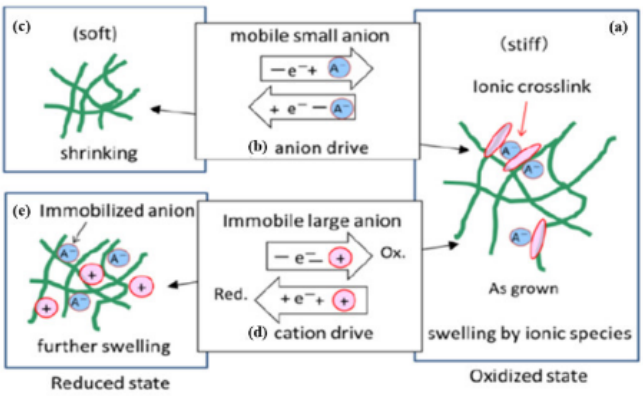

Figure 2.5: The mechanism of actuation in conducting polymers (A) oxidised state, (B) anion drive, (C) cation drive, (D) and (E) reduced state. "Reproduced from [99] under the Creative Commons Attribution License"

or stretching), namely, the solvent and salt used during fabrication and the electrolyte during actuation [168].

CPs, reportedly, have relatively high tensile strengths of up to 100 MPa and can withstand a stress of up to 34 MPa as well as a strain of up to 20 % [168]. Compared to DEs and other ionic polymer-based actuators, CPs possess a fairly diminutive strain rate, which is due to the characteristics of the polymer, the effectiveness of the electrolyte, and due to the diffusion of ions through the polymers. Evaporation of the solvent plays a significant role in the performance lifetime of CPs, and encapsulation methodologies have been investigated to prolong the use of these actuators. Notably, certain types of CPs are in development with internal ion conduction that bypass the problem of the external solvent evaporating or being subject to environmental conditions [168, 36].

Alternatively, carbon nanotubes, which are single graphite layers oriented in a cylinder shape within the nanometer scale, can be used as an actuator. CNTs possess impressive mechanical properties and boast a tensile modulus equivalent to that of diamond (640 GPa). While CNTs behave more similarly to DEAs, utilising electrostatic reactions, their displacement across the nanotubes is caused by a voltage applied to internal nanotube electrodes within an ionic solution. CNT films or yarns are used most often to achieve actuation of this nature. Due to the porosity of the fibres, ionic transport occurs quickly (10ms) with impressive strain and power rates [109].

2.2.4 Opportunities for Artificial Muscles

While artificial muscles have advanced dramatically within the last quarter century, the majority of research has focused on developing actuation mechanisms, metric models, and material science with a minimal focus on their fabrication method. It is a matter of

simply producing artificial muscles for data collection and scientific research with little concern for the development of potentially useful applications which poses the question: "How can the current state of the art in artificial muscles be utilised in an impactful, real-world environment?" This leads to the dilemma of how they are fabricated. The fabrication techniques, as have been discussed, are often limited in scope and production. Furthermore, the opportunity of additive manufacturing is widely overlooked, especially when concerned with the flexibility that it offers [180].

Electroactive-type artificial muscles are improving yearly and are able to produce excellent performances, both compared to natural muscle as well as electromagnetic motors, see Table 2.1. Especially since these muscles can potentially be designed as a network to maximise mechanical advantage, which reduces the need for transmission systems that do have certain efficiencies and losses. It is, however, the lifetime of these actuators which need greater improvement since natural muscle still outperforms the best electroactive actuators by 10^3. The field of artificial muscles has exciting potential in the future of robotics (e.g., soft) and in other fields where the particular multi-functionality of artificial muscles may be suitable.

Table 2.1: A comparison on artificial muscle types — "Adapted from [16, 28, 99, 168, 126]"

Actuator Mechanism	**Actuator Type**	**Strain**	**Stress (MPa)**	**Work Capacity (kJ/m3)**	**Advantages**	**Disadvantages**	**Life Cycle**
Natural Muscle	Mammalian Skeletal	20-40%	0.1-0.35	8	High energy density fuel, Regeneration	Low work density / capacity	10^9
Electric Field Actuation	Dielectric elastomeric actuators Electrostrictive polymer-based actuators	10-380%	7.7	150	Simple mechanism, Large strains, Low current	High voltages, Cost	10^6 - 10^8
Ion-Based Actuation	Conductive polymer-based actuators	12%	34	100	Low voltage, High stress, High work density	Need encapsulation, Low efficiencies	106
	Ionic polymer metal composite-based actuators	3.30%	30	5.5			

It is, however, interesting to note that there is a distinction between the development of artificial muscles and the development of natural muscle tissue from bio-based polymers and cells. The two are invariably linked however there is minimal literature concerning artificial muscles from the perspective of using muscle cells or bio-based polymers such as collagen or elastin. This is an area of research worth exploring especially when concerned with the development of bio-based robots, e.g., a robot capable of actuation and sensing.

2.3 Polymers for Artificial Muscles

Polymers are (macro)molecules comprised of repeating sub-units — monomers. With a diverse range of properties, natural biopolymers (e.g., proteins, polysaccharides, etc.) and synthetic polymers (e.g., polystyrene, polyethylene, carbon-based, etc.) are used in many applications such as in the development of biological structures and the mimicry of biological functions. Polymers are uniquely suitable for development due to their flexibility in terms of properties which are highly customisable, such as their rheological properties, mechanical properties, and sensitivities [71]. Considering the architectures of electroactive actuators, it is necessary to understand the state-of-the-art polymers to achieve a certain level of conductivity and potentially function as capacitors for energy storage or otherwise achieve deformation. Furthermore, while this type of electroactive polymers can be achieved summarily utilising purely synthetic or non-bio based materials, it is necessary to investigate the potential for bio-based materials for usage as artificial muscles.

2.3.1 Synthetic Materials

Distinct types of conductive materials present different properties. Conductive polymers are organic polymers that conduct electricity and are easily conjugated to other polymers to form a conductive scaffold. However, most of the conductive polymers are not water soluble and cannot be degraded *in vivo* [50]. Carbon nanomaterials are commonly used as conductive polymers due to their high conductivity. Such polymers include carbon nanotubes, graphene, etc. One key challenge associated with these materials are that they are not soluble in water, but they possess good biocompatible characteristics. Metal-based conductive materials, often used as electrodes in actuators, such as gold and silver have suitable conductivity but are generally toxic to cells and cannot be used to great effect within biological system [50, 229]. Depending on the application and absolute necessity of bio compatibility conductive polymers have advantages and disadvantages.

Conductive carbon-based polymers, with electrical, magnetic, and optical properties

were first proposed in 1970s [50]. These polymers are synthesised more easily and demonstrate improved processability (the ability of a material to be processed into a shape or form) in comparison with traditional conductive materials in the context of biofabrication. Conductive materials such as polypyrrole (PPy) and polyaniline (PANI) have proved popular in multiple studies as conductive, biocompatible materials and are often blended with other suitable biopolymers [173, 71].

As a result of this blending of conductive polymers with other biopolymers, a hybrid conductive polymer can be produced with suitable mechanical, electrical and chemical properties. It is usually non-conductive polymers with more desirable mechanical or biological characteristics that is selected for blending. So far hydrogels present the most promising option for producing hybrids which can be utilised in specific applications [69, 184]. Electroactive hydrogel composites made up of PPy and others have been produced in the past which have been blended proteins and polysaccharides have been produced. The key to conductive materials is the doping process that introduces charge carriers (polarons and bipolarons) into the polymer matrix [15]. This process changes a semi-conducting polymer into a conductive polymer

2.3.2 Biomaterials

Hydrogels

Hydrogels (also known as aqua gels) are a 3D network of hydrophobic polymer chains that are crosslinked through physical or chemical bonding procedures with water as the distribution medium. These cross-linked chains are the result of covalent, hydrogen bonding, Van der Waals forces, and physical entanglements [105]. In simpler terms, hydrogels are solid gel that encapsulate liquid within a large 3D matrix. Hydrogels are natural or synthetic polymers and experience highly water absorbent properties, see Figure 2.6 for a classification. As a result, hydrogels can well up to 400 times their original weights. They are classified as either natural or synthetic, but composites may arise as previously mentioned depending on the requirements of the application. Furthermore, hydrogels may demonstrate environmental responses (pH, light, electricity, magnetic fields.

Conductive polymers can also be synthesised as hydrogels allowing the production of electroactive hydrogels. These hydrogels are usually composites, and oligomers formed hydrogels demonstrate good biocompatibility and good electroconductivity. PANI, PPy, and polythiophene (PT) among others, have been widely used as conductive polymers whose conductivity is mainly because of their alternated single and double bond. They can be physically blended into polymer systems and conjugated onto polymer chains [30, 134]. Due to the critical impact that conductive polymers can make within the biomedical field (e.g., tissue-engineered grafts, wound dressings, soft

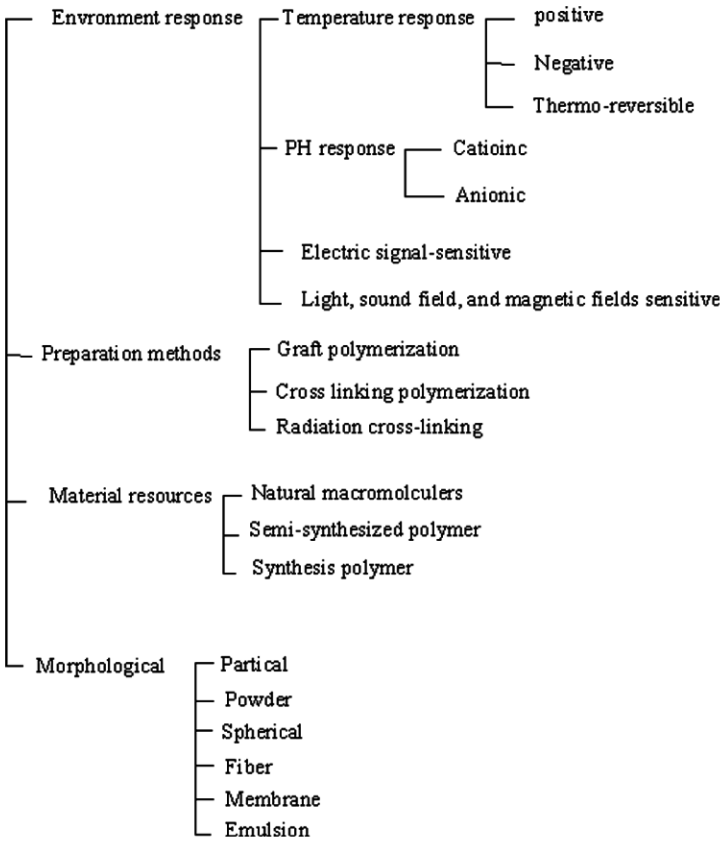

Figure 2.6: Classification of hydrogel materials. "Reprinted, with permission, from [105]"

actuators), publications that combine 3D printing and electrically conductive hydrogels are increasing in popularity [48].

Conductive polymer hydrogels operate similarly to most electronic semiconductors. They possess conjugated π (p) systems which consist of overlapping p-orbitals forming π bonds. Charge transfer is induced, resulting in its conductivity, within a polymer and its internal chain network when the electrons internal to the π bonds are redistributed through the stacking of aromatic rings and perfectly conjugated π systems (p-p stacks) [48].

Doping

An important parameter in conductive polymers is the dopant. Dopant is necessary for conductive polymers and impact the overall conductivity, material morphology and cell behaviour. It is the dopant that increases the efficiency at which electrons are shuffled throughout the conductive polymer chains. More specifically, dopant refers to charge entities such as ions or charge side groups which participate in the

oxidation reaction internal to a polymer. The network chains internal to conductive polymers are provoked towards charge transfer through the polymer by the deterioration of electronic conformation within these networks. Note, p-type charge transfer is considered an oxidation reaction and n-type transfer is considered a reduction reaction. Conductive polymer as hydrogels operate symbiotically in the sense that since hydrogels are particularly absorbent of liquids, it is possible for the ionic contribution (i.e., dopant) to scale upwards and significantly impact the overall conductivity of the final hydrogel [147, 48]. Other than the most common examples of conductive polymer hydrogels already mentioned, conductive particles such as graphene and CNTs can be introduced to hydrogels to provide some conductivity.

Doping is the primary process to improve the electrical properties of conductive polymer hydrogels (CPHs) to those of a metal and occurs during and/or after the synthesis of conductive polymers. The doping process can be accomplished through several methods: chemical doping, photo-doping, charge injection doping, electrochemical doping, non-redox doping and secondary doping. The most widely used techniques are chemical and electro-chemical methods [72, 198].

Synthesis conditions (such as temperature, solvent and water content, oxidation and pH environment) have a strong effect on the conductivity and mechanical properties and surface morphology of polymers. Reliable and reproducible chemical synthesis are negatively influenced by variations in these effects. The conductivity of a polymer is strictly dependent on the quantity of dopant used [69]. The type of dopant required to be incorporated in the polymer can drive the choice toward the more appropriate synthesis method. Conducting polymers can be reversibly doped and undoped due to their electronic structure and this offers relevant benefits in drug delivery applications[72, 198].

The semiconducting characteristic of the extended conjugated system can be enhanced by the doping process, in analogy with what occurs for semiconductors. Conducting polymers are not usually conductive in the basic form and doping of the conjugated backbone results in a highly conducting state of the polymer. Doping of conjugated polymers increases the electrical conductivity of the material and in some cases by several orders of magnitude [15].

Cells are a core component of bioprinting, and it is in the selection of the types, number, and combination of cells that provide bioprinted tissue its functional aspects. Cell sources that can be implement in bioprinting are usually donor human tissue, animal tissue and stem cells (derivations as well). Cell types, however, are limited in their applications and compatibilities to both the hardware that aims to print them and in their interactions with other cells. Cell lines are cell populations derived from primary cells that are self-replicating and retain certain functionalities from their original cells [195]. Cell lines are useful for early testing and development of bioprinting. Additionally,

primary cells are harvested from living tissue (except for stem cells). Primary cells have specific functionalities are terminally differentiated cells which means that they cannot proliferate. The development of tissue constructs, and organs have made use of primary cells along with biomaterials to remarkable success due to their ability to metabolise drugs [21].

Biomaterials perform a key role in interfacing hardware and biology (cells, environments, etc.). They are highly dependent on the printing technique employed and integrate all the biological components usually found *in vivo* environments. Biomaterials range from hydrogels and extracellular matrices (ECMs) to cermet implants in applications for drug delivery, pacemakers, artificial organs / tissue, etc. [195, 21]. Certain biomaterials are used as bioinks in bioprinting and are usually in one of two categories — melt curable polymers and soft biomaterials such as hydrogels with a high-water content. Melt curable polymers are commonly used as scaffolds due to the extreme temperatures and solvents necessary to process them and are seeded with cells in post-processing. Hydrogels and similar biomaterials are distinguished into two further classifications, namely, natural and synthetic polymers of which a large variety of composites and combinations can be prepared. These polymers cannot achieve the same plateau of mechanical properties (stiffness, tensile strength, elasticity, etc.) as melt curable polymers. Hence, biomaterials, in order to function within a biological environment, must be:

- Non-toxic and non-carcinogenic.
- Chemically stable, non-corrosive, and survive biological stresses.
- Malleable into specific geometries [110].

Biomaterials are bound to certain requirements which dictate their effectiveness for certain applications and printing methodology. The requirements are described as the following:

- Formability
  - Bioprinting techniques require a material to be in a certain form and phase for successful processing.
  - When it comes to selecting a material, it must be ensured that it can be produced in the desired form using a particular technique.
- Water content
  - Water content determines the absorption rate and diffusion through a hydrogel.

  - If the content is too high, cell proliferation may deteriorate.
  - Water is bound in the gel by hydration of the polar hydrophilic groups.
  - Water content is determined by the light absorbance through the gel or the percentage change between the gel and dry phase of the hydrogel.

- Biocompatibility
  - "The quality of not having toxic or injurious effects on biological system" [40]
  - "The ability of a material to perform with an appropriate host response in a specific application" [40]
  - Biocompatibility consists of interactions that occur between tissue and the material. No material is definitively biocompatible in all the applications and environments that they are used.
  - A material implanted into the human body must perform a specific purpose. As such, it must continuously perform a function without fail.
  - A biocompatible material must be to both react and not react to the *in vivo* environment of the host depending on the conditions.

- Mechanical Properties
  - Flexural, tensile, fatigue, creep strengths, wear resistance and elasticity are a few of the properties to consider in a biomaterial.

- Biodegradability
  - The ability for a material to degrade into simpler substances under exposure to certain environmental conditions (e.g., bacteria, fungi, etc.).
  - A desirable feature for a biomaterial is that the degradation rate is synchronised with the tissue in-growth rate (the rate at which new tissue grows into a material placed in the body in the context of medical implants).

- Bioactivity
  - Bioactivity implies that a material induces positive and desirable responses from the biology in which it is surrounded.
  - The term was first proposed by Larry Hench in 1971 [76] and has evolved mean that any material can bond to soft tissue and release biological stimulants.
  - Current strategies which are used to control the chemical signalling of molecules to drive cell behaviour include adhesive patterning or the incorporation of releasable biomolecules such as hormones, enzymes and other regulators.

2.3.3 Biomaterials for Electroactive Artificial Muscles

There are four approaches to producing conductive and potentially electroactive hydrogel structures [48].

- Ionic Conductivity
- Addition of Conductive Particles
- Postpolymerisation / coating
- In Situ Polymerisation Conductivity

Ionic conductivity in hydrogels is usually produced by the formation of hydrogels within electrolyte solutions. This method does not usually require the addition of other conductive polymers such as PPy or graphene. The hydrogels would intrinsically consist of ions which causes an increase in conductivity across the hydrogel, but the stability of this conductivity is heavily dependent on how well the hydrogel can retain these intrinsic ions. This approach is often used in stretchable electronics [48, 229, 206].

Conductivity by the addition of particles which result in composite hydrogels are formed by the introduction of conductive particles (such as graphene) into polymerised hydrogels. This approach results in high conductivities as opposed to the other approaches (>20 S/cm) [48, 192]. Toxicity is a major concern with this approach in the biomedical fields due to the non-biodegradability and chemical structures of nanoparticles of conductive particles. As a successful example of this approach, cardiac fibroblasts were seeded on bioplotted conductive hydrogel patterns and resulted in decent cell maturation when a conductive hydrogel ink was applied. This points to an application in tissue engineering and biosensors [192].

Postpolymerisation is concerned with the immersion of hydrogels in monomer or oxidant solutions of a desired conductive polymer. The conductive hydrogel is formed by soaking a hydrogel in oxidant and subsequently in monomer solution, or vice versa. Alternatively, this process could be used to coat hydrogels or formed constructs to achieve a certain conductivity. This approach allows the conductivity functionalisation to occur in a subsequent step to the formation of a hydrogel. The challenge then becomes the ability for a formed hydrogel to allow the diffusion and penetration through the bulk material [74, 222]. Previous research has demonstrated this approach towards the development of biocompatible as well as conductive constructs or scaffolds in the field of bioelectronics and biosensors [227, 222]

In situ polymerisation describes the formation of conductive polymers within a hydrogel matrix (e.g., proteins or polysaccharides) by the addition of monomers of the intended conductive polymer. This is a process which forms the conductive matrix simultaneously to the hydrogel matrix. This process can result in homogenous formation

of the conductive polymer networks throughout the hydrogel. Previous work has demonstrated that in situ polymerisation of conductive polymers along with dopants can result in a conductive hydrogel network with applications in bioelectronics [48, 155].

Yow et al. demonstrated the fabrication of collagen-polypyrrole fibres using interfacial polyelectrolyte complexation (IPEC / PEC), which is a common technique to form fibres [228]. This technique occurs at the interface between two solutions containing oppositely charge polyelectrolytes. When the charge is neutralized at the interface between two polyelectrolytes, it leads to the creation of an insoluble complex. This complex can adopt a fibrous shape if it is stretched and pulled from the interface between the two polyelectrolytes. This occurs at room temperature and being water-based is well suited to the requirements of biology. By entrapping pyrrole monomers into its hydrophobic cavity using 2-hydroxypropyl-β-cyclodextrin, PPy can be incorporated into a collagen-based fibres that are drawn using the PEC technique. This process results in a biofunctional, electroactive fibre system which can be used in tissue engineering.

2.3.4 Hybrid or Composite Materials

There exists the desire to fabricate 3D structures with sufficient strength, size, shape, biocompatibility, as well as the capability to function as an electroactive actuator. In response to the inadequate properties of bio-based polymers in isolation, much work is being done to develop hybrid systems that can produce synthetic biopolymers (with relevant properties) with cell-laden hydrogels to produce successful tissue constructs. The synthetic biopolymers provide the physical support of a geometry, or any other property insufficiently handled by bio-based hydrogels, and the hydrogels stimulate biological actions and reactions (cell proliferation, regeneration, etc.). Early indicators point towards this hybrid methodology of producing tissue constructs as improving the structural capabilities a fibre [10, 47]. See Table 2.2 for the most commonly used electroactive polymers (EAPs) and their properties. The greatest challenge remains in that the crosslinking methodology (e.g., UV light, temperature, chemical reactions, etc.) has a negative impact on the biologically active component of a polymer hybrid or gel. In turn, mechanical weakness and a lack of structural integrity may result as is indicated by this inverse relationship between mechanical strength and biocompatible processing. This requires an approach for material design for processing in that a polymer of purely synthetic or biological origin may be used as the matrix within which cells may proliferate, however, this “scaffold” must be developed with biocompatibility in mind. As such, the future in developing materials for artificial muscles (specifically of electroactive function) may require a combination of mechanically strong but not biocompatible “inner shells” which are surround by biocompatible “outer shells” which can aid the proliferation of cells and achieve a function of deformation or reaction to

stimulus. With reference to natural muscle, this idea is not completely far-fetched, however challenging in a processing and materials science space.

Table 2.2: Summary of EAP materials. "Reproduced from [71] under the Creative Commons Attribution License"

Polymers	Key Properties	Limitations	Main Biomedical Applications
Polypyrrole (PP)	High Conductivity High stability in air Electroactivity pH Biocompatibility Low Solubility	Insolubility in organic solvents Poor Processability No Biodegradability	Neural Probes Drug Delivery Coatings Tissue Engineering Biosensing Bioactuators
Polyaniline (PANI)	High Conductivity Environmental Stability Suitable Redox Properties Biocompatibility	Low solubility in organic solvents Electroactive pH < 4 Poor Processability No Biodegradability Instability in Air	Drug Delivery Coatings Tissue Engineering
Polythiophene (PTh)	Biocompatibility High Doping Levels	Low solubility in organic solvents Poor Processability No Biodegradability	Biosensing Coatings
Poly(3,4-ethylenedioxythi- ophene) (PEDOT)	High Transparency High Stability in its oxidation state vs. biological reducing agent Low Oxidation Potential High Compatibility with aqueous electrolytes	Low solubility in organic solvents Poor Processability No Biodegradability	Biosensing Neural Probes Drug Delivery

2.4 The Methods of 3D Printing for "Synthetic" and Bio-Based Polymers

2.4.1 3D / 4D Printing

Brief Definition

4D printing was first coined in 2013 by a research group from the Massachusetts's Institute of Technology (MIT) at a TED talk given by Tibbits [207]. It was defined as static 3D printed objects which shift their shape over time. Immediately after, the first research paper on 4D printing was published by same group using the concept of printed active components (PAC) where a printed sheet transforms into a complex geometric configuration using the shape memory effect (SME). The definition of 4D printing as the sum of time and 3D printing has morphed into the concept that the shape, properties, and overall functionalities of a 3D structure could evolve over time when stimulated by factors such as temperature, water, light, acidity, electricity, etc. [66, 133].

Since 4D printing is inherently derived from 3D printing and the polymers associated with this technology, AM technologies are cross compatible with 4D printing with the full range of techniques available. There are seven categories of AM, namely, binder jetting and material jetting (which fall under inkjet technology), material extrusion, photopolymerisation, powder bed fusion, energy deposition (usually with lasers like selective laser sintering (SLS), and sheet lamination. 4D printing offers a few advantages over 3D printing which are: (i) it fabricates intelligent devices using smart material which change shape over time; (ii) it can fabricate self-folding or assembling structures which will allow thin walled structures to be printed faster and more easily; (iii) a 4D printed structure is usually the combination of several materials into an appropriate configuration that is a single printed object. As a result of the differences in materials, it is possible for this final structure to retain certain materials properties (e.g., expansion, flexibility, swelling, etc.) [171]; (iv) the object is triggered by external stimulus, which is determined by the type of response required and hence affects the materials used for printing.

There are at minimum two states at which a 4D printed structure can exist — the original state (shape, etc.) and the shape under stimulus [233]. Consequently, a 4D structure is categorised into three areas of functionality: (i) self-assembly which is concerned with materials that can minimised in shape and when placed in a specific location can assemble itself according to the programmed stimulus. Several research groups have attempted to achieve this self-assembly functionality. For example, the transfer of equipment through small spaces in the human which self-assemble at a desired location for medical purposes is one application; (ii) multi-functionality is concerned

with integrating sense and actuation functions within a material. Multi-functional and adaptive 4D printed tissues are one example of the application of this area of 4D printing [96]; (iii) self-repair is concerned with the utility of self-disassembly, error correction, recyclability, etc. Self-healing hydrogels are one potential application [205].

2.4.2 Bioprinting

A Brief History

3D bioprinting originates from the initial work done by Tom Boland in 2003 based on inkjet printing technology [221]. This technique of using inkjet printheads to print molecules which bind to each other (with varying degrees of success) was based on earlier work using techniques such as photolithography [197, 65] (for the synthesis of oligo DNA chips) and pin arrayers which deposit cells or proteins [189]. Hence, the key motivation to investigate ink jet-based printing was due to cells drying out using pin arrayers and is one of the first key works to demonstrate a working AM technique to deposit cells. The impact of this work is significant because at the time it was published in 2003, tissue engineering had relied solely upon moulding techniques to develop scaffolds which would be coated with cells to manufacture organs (e.g., human bladders, etc.) [13].

In the same year, Garbor Forgacs at the University of Missouri created multi-cellular spheroids which was the first step towards 3D printing scaffold free cells [26]. Immediately after in the following year, Doug Chisey at the Naval Research Laboratory, applied laser-based techniques towards printing bioinks into 3D structures [18]. From this point, the first international bioprinting workshop was organised leading to key discussions between Doug Chrisey, Brian Derby and Vladimir Mironov [127]. They defined bioprinting as "the use of material transfer processes for patterning and assembling biologically relevant materials — molecules, cells, tissues, and biodegradable biomaterials — with a prescribed organisation to accomplish one or more biological functions" [127]. See Figure 2.7 for the timeline of development in bioprinting.

The first commercial printer, developed in 2009 [13], attempted the production of nearly full functional replacement skin constructs. As a result, more recent work has extended into bioprinting functional ear-shaped constructs, heart valve models, liver tissue models, bone tissue, and muscle fibre tissue [119, 51]. The techniques utilised in bioprinting varies substantially with a wide variety of AM technologies being used for the construction of complex multi-cellular geometries. Because of the requirements inherent in certain biological tissues, certain AM methods matched with specific materials and cross-linking approaches are best suited to constructing tissue (scaffolds, fibres, etc.) with certain properties, biological components, matrix architectures, etc. [161]. A key aspect of any technique associated with bioprinting is biomaterial formulations and their associated rheological properties, chemistry and printability — cell compatibility

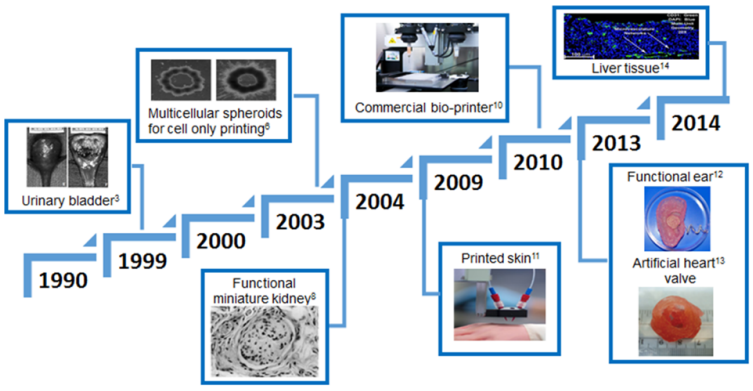

Figure 2.7: A Historical Timeline of the Advances in Bioprinting Technology. "Reprinted (adapted) with permission from [90]. Copyright [2022] American Chemical Society"

and survivability [161].

The original bioprinters were modified inkjet printers based on depositing cell-aggregates or tissue-spheroids onto hydrogel biomaterial substrates [221], where the chemical interactions between the cells would cause controllable fusion into definable constructs, see Figure 2.7 [194]. These cell-aggregates are now more commonly known as bioinks, and the substrates were coined biopaper. However, "biopaper" has become obsolete as new innovations with bioinks have absorbed its original functionality, hence bioink encompasses all the materials and combinations of bioprinting. The approaches associated with bioprinting have since evolved into two independent areas: (i) cell aggregate bioprinting, or scaffold-free bioprinting which does not rely on environmentally supportive environments; (ii) the biopaper materials have developed into bioinks of themselves which pertain to cell-encapsulation (usually within a hydrogel) — this evolved into extrusion bioprinting [51].

Furthermore, several other techniques have been developed, modified or improved from traditional 3D printing technology. Namely, laser-assisted bioprinting (LAB), stereolithography(SLA), extrusion-based bioprinting, inkjet based (material jetting) and robotic dispensing have been developed due to the micro-scale resolutions at which these techniques are able to print and pattern materials in complex geometries. Therefore, the 3D printing of biological structures encompasses two types of constructs: (i) acellular functional scaffolds which are coated with cells, generally; (ii) cell-laden constructs which recapitulate *in vivo* processes. Each type of construct bespeaks specific requirements for bioprinters and applications in which they could be useful [161]. Potential bioprinting applications have developed to include the printing of nanoparticles to form fibres, the printing of single cells within a particular configuration, reconstructive bone / organ scaffolds (e.g., corneas, etc.), printable medicine, or bioactive coatings [161]. The technology has not yet advanced to the stage where complete organs and / or tissue

certifiably suitable for transplantation into the human body can be fabricated.

Key Parameters

Printing dynamics are important when consistent patterning and functionality in the final product are required. Resolution, orifice size, matrix composition, viscosity, and as such the resulting droplet size, cell aggregation, cell patterning, cell viability and cell placement all contribute to the quality and functionality of a printed construct. **Resolution** in 3D printing is defined as the quality of a printed part, or, in other words, it can be described as the minimum distance or length that material can be accurately deposited. In inkjet printers, patterns are made on a drop-by-drop basis (e.g., drop-on-demand and CIJ) which merge to form lines and hence patterns and geometries in layers. The resolution of an inkjet printer is fully dependent on the printhead used during printing. Additionally, the minimum droplet size is also dependent on the type of printhead. For clarification, the actual resolution at which a part is printed is different to the resolution at which a printhead deposits droplets. This is due to the dispersion and spread of droplets on the substrate or surface on which they fall, see Figure 2.8 for the common process through which 3D tissue or geometry may be constructed using bioinks and hydrogels. Subsequently, the actual resolution of an inkjet printer is usually lower than the minimum droplet size since the printed pattern also enlarges when the drop merge and dry [79, 34].

The **delivery matrix** (e.g., hydrogels) used to develop biological constructs determine the ultimate properties of a printed structure. It is through cross-linking (chemical or with UV) usually when the delivery matrix is in the liquid phase that subsequently hardens. The delivery matrix provides structural stability and safety for cells so that a relatively rigid structure can be printed. Cell proliferation is also affected by the selection of the hydrogel depending on the application of the structure. Furthermore, a matrix must facilitate and sustain all interactions between the environment and the structure, and as mentioned previously this also impacts the final characteristics of a construct. It is not uncommon for multiple types of delivery matrices which encapsulate a variety of different cell types to be required in the printing of complex tissue. Collagen I and alginate are most the commonly used biomaterials used for this purpose [88, 106].

Viscosity is arguably the most important factor when printing any type of material using inkjet technology, particularly for bioprinting and tissue engineering. Clogging is the major problem with inkjet bioprinting as only lower viscosity materials can successfully be printed [80]. This inability to process high-viscosity biomaterials significantly reduces the number of potential biomaterials in developing tissue constructs. In simple terms, the higher the viscosity of the material to be ejected through a nozzle, the higher the applied forces become to induce ejection. One solution to this problem is to

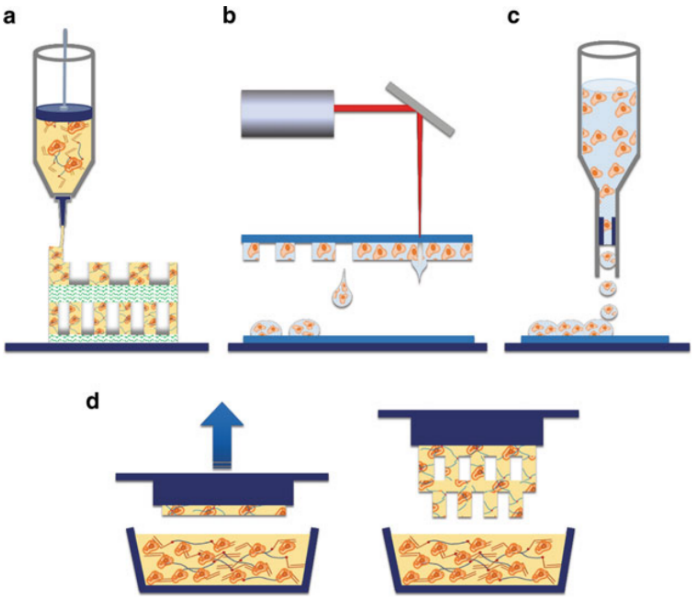

Figure 2.8: Fabrication of 3D tissue constructs by layer-by-layer deposition of bio ink followed by different printing and cross-linking strategies. (A) Extrusion based printing where pressure produces continuous "fibres" (B) Laser-assisted bioprinting which uses laser diodes to print material at specific points. (C) Inkjet based bioprinting strategy. (D) Stereolithography based bioprinting. "Reprinted, with permission, from [12]"

modulate the viscosity of a material by mixing other materials with it or alternatively using cross-linkers at different ratios at specific times during the printing process [162]. Various studies have shown that modulating formulation concentrations of materials like GelMA make it possible to decrease viscosity and improve printability [86, 140].

Techniques

Through a synthesis of computer aided design (CAD), high resolution electronics (e.g., stepper motors, micro-controllers), computer aided modelling (CAM) and the use of G programming language (creating machine instructions) — usually found in the "slicing" software, it is possible to precisely control the geometry, mechanical properties, inter-connectivity, porosity, and the structure of biochemicals as they are laid down or deposited during an AM process. Typically, the equipment consists of an x-y-z gantry system which when programmed using G-code compiled from a CAD model using "slicing" software, proceeds to create the 3D structure using the materials setup in the cartridges, tubes, vats, nozzles, etc. which are usually pumped using the principles of peristaltic motion (when fluid) or fed using mechanical drive systems or robotics. This general description of most AM techniques varies hugely across them, and in terms of bioprinting applications, they have vastly different results. Certain techniques are

more suited to printing certain materials (poly(3,4-ethylenedioxythiophene) polystyrene sulfonate-PEDOT:PSS) in specific configurations (e.g., bone, cartilage, cardiac muscles, etc.) than others, due to the physical principles applied in them, which affect the viscosity, cell viability, printability, and mechanical properties [34]. Furthermore, based on these aspects, printing techniques are classified into contact and non-contact techniques: (1) Contact — "the printing technique requires contact between the delivery apparatus and the receiving substrate" (e.g., Extrusion) [40]. (2) Non-contact — "the material is delivered (ejected) to the substrate located very close to the delivery mechanism (almost touching)." (e.g., Inkjet and Laser based printing) [40].

Bioprinting Approaches

There are three approaches to bioprinting: (1) **biomimicry**, (2) **autonomous self-assembly**, (3) and **micro-tissue based methodologies**, see Figure 2.9 [23]. These approaches can be undertaken separately or together depending on the complexity and type of tissue. A biomimicry approach attempts to engineer each component of the target tissue and it is difficult to replicate the complexity of a tissue even though the approach is fairly straight forward. There are several key aspects to biomimicry, firstly, the selection of a scaffold geometry and material is essential. Secondly, the scaffold must approximate the structural and mechanical properties, and the interactions between cells with the ECM of the target tissue. Thirdly, a set of bioreactors should be used to regulate the environmental parameters which mimic the chemical, mechanical, and electrical variables specific to a tissue type. Hence, the key component to successful biomimicry is the ability for the environment to adjust itself as the cells proliferate throughout a scaffold and the printed tissue matures over time. This is usually done once a tissue is printed.

Autonomous self-assembly is an approach to replicate an embryonic environment with the intended goal of producing the correct anatomy. The approach involves printing or producing separate parts or units that when placed in the correct environment and in contact with each other will self-organise and recapitulate accordingly. While biomimicry attempts to externally influence the maturation of tissue, this approach simply develops the separate units and uses the natural understanding that cells and other structures organise to develop tissue. This is a scaffold-free methodology and has been proven to result in high cell densities, good cellular interactions and growth, and longer overall function. This approach has successfully been used to develop a variety of tissue types — e.g., the first blood vessel using smooth muscle cells, cardiac muscle tissue, etc. [191, 112].

The microtissue approach in bioprinting refers to the development of the smallest structural and functional units to form a target tissue type. It is based on the biological

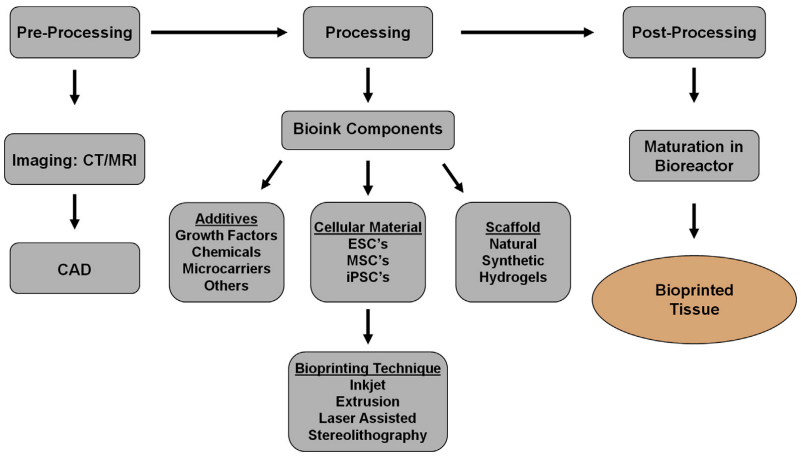

Figure 2.9: Bioprinting Structure. "Reproduced from [23] under the Creative Commons Attribution License"

fact that simpler units are combined *in vivo* and contribute function to the whole of the surrounding tissue. Microtissues are often integrated into bioinks, which can enhance the speed of the bioprinting process. — reducing the frequency of nozzle clogging. Tissue maturation is reportedly much faster using a microtissue approach and combining this approach with biomimicry or the autonomous self-assembly approach, microtissues can be bioprinted without scaffolds, which relatedly reduces the rate of production [191, 128].

Furthermore, there are three phases associated with bioprinting. **Pre-processing** involves determining the anatomical structure of the target tissue through imaging, etc. and developing a CAD model for bioprinting. The **processing** phase is next and is the stage at which the tissue is manufactured. Secondly, a specific printing method and formulating the necessary printing materials (bioinks, scaffolds, bioreactors, etc.) must be selected. Each of these selections have impact on the final product — its properties and effectiveness. Lastly, the **post-processing** phase occurs immediately after the processing phase and is concerned with maturing bioprinted tissue and preparing it for *in vivo* usage. For most applications this occurs within a bioreactor which recreate the required environments with variable success. Tissue and cell viability are often reduced and weakened during the maturation stage [23, 129].

Inkjet

Originally patented by William Kelvin in the 19th century, inkjet technology was not realised until the 1950s due to the inability to generate the direction and size of droplets. There are two methods of delivery associated with inkjet printing — drop-on-demand and continuous inkjet printing (CIJ). Continuous inkjet printing involves a stream of ink which is consistently being interrupted by pressure when it flows through a nozzle. This

forms a stream of individual droplets that are selected using conductive that is charged via induction as the drop forms — this holds the stream at particular potential and charges each drop at a different voltage. As the drops fall through an electric field the size, amount and direction of the droplet is controlled depending on the charge. Droplets that do not get charged are recycled into the nozzle for re-use. This phenomenon is often called the Rayleigh breakup, which is used as the basis for CIJ, first employed by Sweet at Stanford University in the 1960s [107].

In drop-on-demand a short jet which condenses into a single droplet. This droplet which forms the head and is followed by the "tail-end" of the liquid eventually detaches from the nozzle and is pulled towards the head droplet forming satellite droplets. Ideally, the jet would form a single spherical drop, but usually results in a main drop followed by a series of satellite droplets. Unlike CIJ, the droplets are not directed using electrostatic principles, but by a series of nozzles arranged in an array within a printhead. By controlling the relative motion of the drop to the substrate as well as the timing of its ejection from an appropriate nozzle in the array, the drop can be positioned precisely where needed.

There are two different approaches to generate the ejection pressure required for a drop - (1) piezoelectric and (2) thermal [107], see Figure 2.10. The basic process of inkjet printing stays consistent over the three different approaches with a methodology comprising filling a cartridge with ink that is forced somehow through a nozzle or orifice. Piezoelectric inkjet printers use acoustic waves, or dynamic physical parts which change shape causing pressure and thus squeezing an ink through the output orifice. By using acoustic waves, it is possible to precisely manipulate wave parameters (duration, amplitude, and frequency). This results in highly controllable printing parameters and excellent printing precision due to the ability of piezoelectric printing to control droplet sizes [85]. Thermal inkjet printing (or bubble jet) utilises a heat generating element (usually with electricity) which increases the temperature within the ink reservoir attached to the nozzle. As the ink increases in temperature a vapor bubble is formed and as it expands causes the ejection of a droplet [85]. Drop diameters, drop volumes, and drop speeds in inkjet printing range between 10 to 100 μm, 0.5 to 500 pL, and 5 to 8 $m.s^{-1}$ for drop-on-demand and 10 to 30 $m.s^{-1}$ for CIJ, respectively. Inkjet printing biomaterials is generally restricted to a viscosity below 20 cP (centi-Poise) and inflict significant shear forces in order to form droplets which reduces cell viability and in the case of thermal inkjet printing high temperatures can cause cell death in the nozzle.

Material jetting is a common "inkjet printhead" style AM process in which droplets of build material (such as photopolymer or thermoplastic materials) and support material are selectively deposited [190]. The material is jetted onto a build platform by using either a Continuous or Drop-on-Demand (DOD) approach, where it solidifies permitting

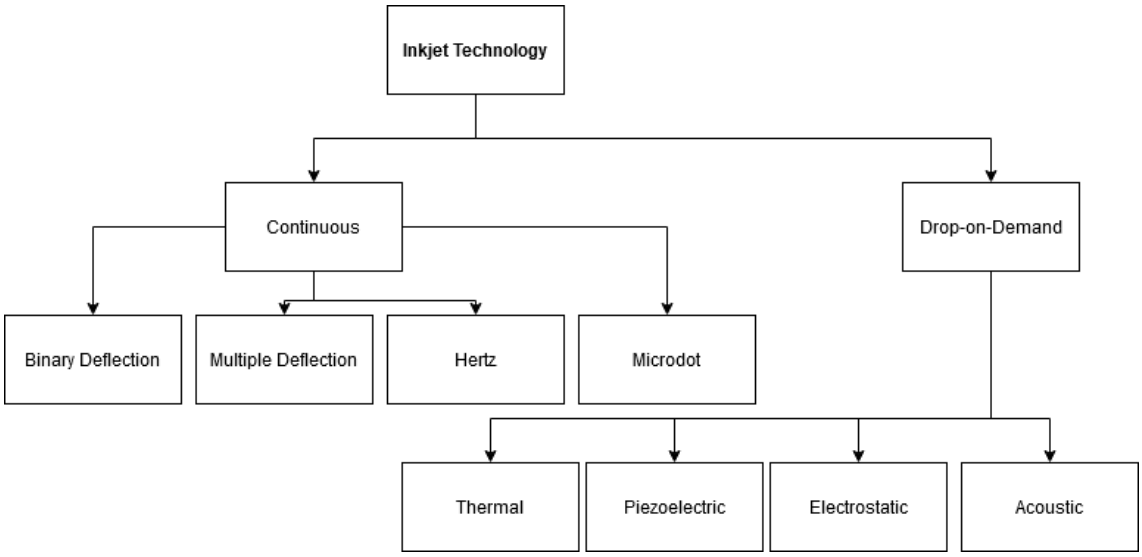

Figure 2.10: Inkjet Printing. "Developed from [79]"

to build the model layer-by-layer. The material is deposited from a nozzle which moves horizontally across the platform. In the last step of this method, the layers are cured using UV light. Limitations of this method are due to the narrow window process of the inkjet actuator, which refers to the fact that the actuator can only deposit ink in very small, precise locations. In contrast, multi-actuator jetting systems are novel methods which allow the printing of materials with various levels of viscosity and electrical properties [90]. There are key challenges, as previously discussed, in using this technique to fabricate biomaterials that are structurally rigid and biologically alive.

Reactive inkjet printing (RIJ) is an emerging multi-head material jetting sub-technique which combines the deposition and chemical reactions of materials in a single action. This allows for the fabrication of structures which can be synthesised *in situ* simultaneous to the construction of their 3D geometries [98]. RIJ is considered to be a chemical synthesis tool using inkjet printing where one reactant can be added to another to form a sum product which has properties unique to itself. There are two definitions of RIJ — 'Single RIJ' and 'Full RIJ'. Single RIJ is involved in the dispensing of droplets which react to a previously deposited material onto a substrate. Full RIJ deposits two reactant materials subsequent to each other using independent printheads which when they meet react to form the intended structure and resulting properties. The challenge with this latter definition is the drying of the first deposited reactant [70]. Since the viscosity of fluids is the main limiting factor in material jetting, recent research has investigated applying RIJ to printing highly viscous materials.

Extrusion

The most widely known form of 3D printing, extrusion 3D printing (e.g., fused deposition modelling — FDM) makes use of thermoset materials that are brought to near melting point through a nozzle (the action of extrusion) and lays the material in a certain geometry, using a continuous bead of thermoplastic, which solidifies as it cools on the printing bed (e.g., steel, glass, etc.). This technique builds a series of layers and the speed at which it does this is fully programmable and dependent on the motor electronics of the machine being used. This technique is compatible with a broad range of ink viscosities (> 6 x 10^7 mPa/s). Furthermore, multiple material parts can easily be printed using the extrusion methodology allowing multi-functional parts with tailored mechanical properties. FDM printers, traditionally, print plastics at 250 ℃but thermoplastics which cross-link under heat at near body temperatures are more useful in terms of biofabrication.

Any hydrogel to be used in extrusion must be printable at around 37℃to enable cell propagation without the addition of chemical cross-linking mechanisms. Extrusion-based printing is capable of much higher cell densities in comparison to inkjet strategies (which is preferable in printing tissues and more analogous to real physiology and cytology). However, cell viability is reduced (86% to 40%) [37] as a result — this is often due to the high shear forces and pressures experienced during printing. Nozzle clogging often occurs as a result of reducing dispensing pressure — the material does not experience enough shear forces to escape the nozzle [6]. One common approach (to bypass this problem) is to seed cells at a later time once the structural polymers have cured.

Scaffold-free bioprinting makes use of cell aggregates and / or cell-based filaments that are printed in architectures which fuse over time into larger, more intelligent constructs. Multiple layers of different aggregates, etc. care printed into physiologically relevant structures and positions, which after a curing and maturation period, fuse into a single 3D form. This approach has successfully built vascular systems. The company Organovo has made use of this technique extensively.

Laser-Based

LAB and / or LIFT is a 3D printing methodology which was originally develop for patterning metals in applications for fabricating computer chips. Laser pulses burst through a ribbon supported by precious metal (e.g., Gold, Titanium) layers containing bioinks which are vaporised causing a high-pressure bubble that squeezes individual droplets onto a printing substrate past the ribbon. A 3D structure is developed to a high resolution which enable bioprinting micro-tissues — DNA, cell aggregates, etc. This method has achieved single cell deposition resolutions as well as maintaining the cell density. Due to being a nozzle-less technique a wider range of potential materials

can be used. Unfortunately, this technique is particularly expensive to prepare and operate in comparison to other techniques [34, 188, 27].

Stereolithography (SLA) utilises the principle of photo-curing or photo-polymerisation in which an ultra-violet (UV) light or laser is directed in a specific path over a layer of photo-sensitive liquid polymer resin. This method of cross-linking hardens layers of resin until a full 3D geometry is completed. Particularly useful for curable acrylics, it is generally unsuitable for biofabrication purposes due to the need for intense UV radiation to induce the cross-linking, along with lengthy post-processing times and limited material selection [23, 34]. Designing biomaterials for SLA is particularly challenging in that photo-crosslinkable polymers are required, which limits the overall material selection. Additionally, this technique may expose cells to harmful levels of UV radiation and requires the careful selection of photoinitiators [12].

2.4.3 3D Printing in Suspension Baths — Embedded 3D Printing

Thus far, the 3D printing techniques discussed face several key challenges in printing biomaterials or other soft and sensitive materials, such as elastomers, gels, and hydrogels which are often used in fabricating constructs in tissue engineering or regenerative medicine. More specifically, hydrogels (polysaccharides or proteins) which are often collagen or fibrin-based in practice require sensitive processing operations and environments in order to not collapse, deform, or other support itself after an attempt to fabricate them into sensible constructs. These thermo-mechanical and chemical requirements (elastic modulus <100 kPa) often cannot be avoided and as such the materials are damaged and the integrated cells die, which is not a desirable outcome for 3D bioprinting [142, 77].

More recently (between 2014 and 2020), 3D printing in suspension media has emerged as an approach to fabricate materials with high shape fidelity and self-supporting properties as well as complex structures with cellular and extracellular relevance. More commonly known as freeform reversible embedding of suspended hydrogels (FRESH), this technique is a step away from conventional 3D printing techniques in that it deposits material directly into a supported area that prevents collapse and settling. This directly addresses the manufacturability and biological challenges of bioprinting.

Gel suspension or embedded 3D printing operates under two key principles. Firstly, the suspension media can hold and encapsulate a printed material without mixing or diminishing the material in any capacity. This means that at an applied stress overcoming the yield stress of the media, the media will relax from its solid, gel-like state to a more a fluidic state allowing the displacement of the media by the penetrating material. Secondly, the media recovers its original position in a process called self-healing, which is defined as the spontaneous recovery of the microstructure and bulk

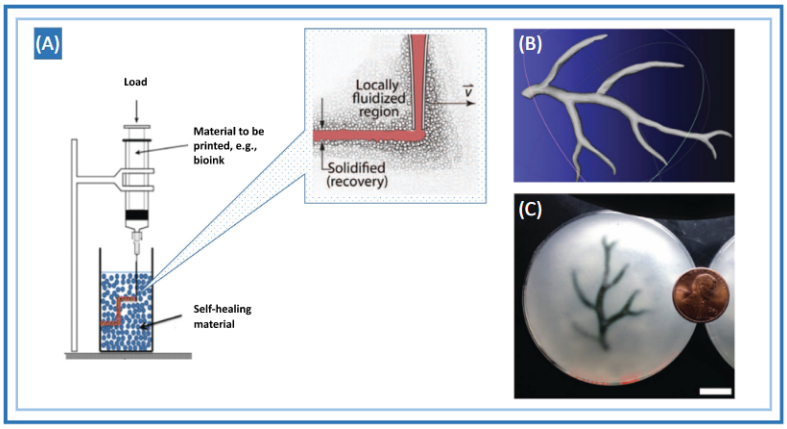

Figure 2.11: (A) Writing of bioink in a suspension medium, (B) CAD of arterial tree, (C) Example of printed arterial tree in a suspension medium. "Reproduced from [122] under the Creative Commons Attribution License"

rheological properties of a fluid after it has flowed. As such, it is clear to note that the suspension media offers reversible state transitions to accommodate the deposition of a material within its body and furthermore support or aid the printed material. One key challenge in this technique is the extraction of the printed structure from the suspension. However, in some cases the suspension medium is retained after printing. Key advantages of the technique include [77, 122, 22]:

- Prevented Collapse
- Continuous Extrusion or Deposition
- Prevented Dehydration of Printed Materials
- Omnidirectional Printing
- Suspension Medium doubling as an Extracellular Matrix
- Cells are kept alive using tightly controlled environments

This technique especially supports the printing of a wide variety of materials, regardless of viscosity, although the high pressures and shear stresses involved in high viscosity material deposition may hamper cell survival. There are no scaffolding materials required however to fabricate well-defined shapes. A study of printing tissue analogs with decellularised ECM bioinks with relatively low viscosity (10 cP) demonstrated, that while these bioinks could not be printed singularly without support frameworks using conventional techniques, they could be successfully printed within the suspension medium. Collagen, fibrin, and even pure cells without biomaterial support have been printed [122]. For example, the Angelini group used a polyacrylic acid particle-based

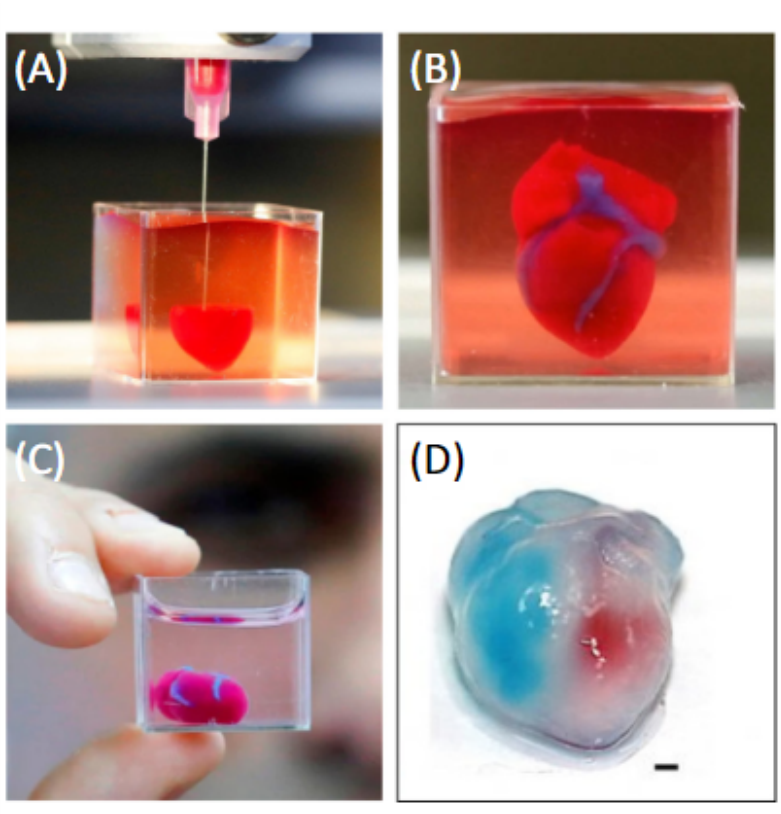

Figure 2.12: (A–C) Miniaturised heart, (D) The heart extracted from the suspension medium and dyed to demonstrate the hollow internal chambers. "Reproduced from [122] under the Creative Commons Attribution License"

suspension medium to print biological constructs within close proximity. Hinton et al. printed a human brain using a gelatine slurry suspension medium. Dvir et al. used this technique to print a miniaturised human heart using stem cell derived cardiomyocytes and endothelial cells within a bath of alginate microparticles surrounded by xanthan gum, see Figures 2.11 and 2.12. As such the FRESH technique demonstrates its usefulness in successfully printing mechanically weak materials into mechanically rigid and anatomically correct structures [146]. See heading 3.3.1 for further analysis into the embedded 3D printing techniques.

2.4.4 Strategies & Preparations

Inkjet Approach

From a practical perspective, the inkjet 3D printing approach would require the processing of higher viscosity materials in order to achieve suitable results in printing artificial muscle fibres as has been extensively discussed. Due to the precise nature in which artificial muscles fibres must be printed, especially when using biomaterials, the

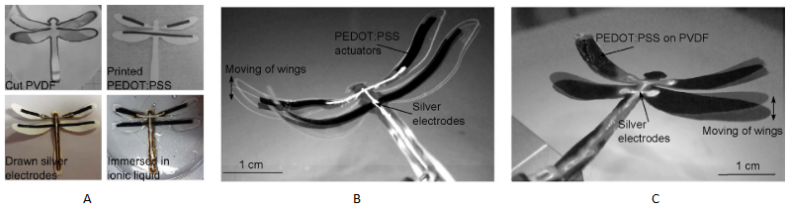

Figure 2.13: (A) Fabrication steps — (1) PVDF membrane is cut to shape, (2) PEDOT:PSS actuators printed where actuation is desired, (3) Silver electrodes connecting actuators, (4) Shape is doped with ionic liquid . (B) Printed Actuators. (C) Actuators produced by drop casting and cutting. "Reprinted, with permission, from [193]"

environmental conditions must be tightly controlled with temperature, pH, and humidity regulated throughout the fabrication process. Furthermore, the technology associated in depositing the biomaterials or conductive polymers must be keenly selected or modified to allow for higher viscosity materials and materials that are semi-conductive. Hence, technology must either be innovated or sourced in order to broaden the selection of biomaterials to allow for more viscous materials to be processed, specifically for the purpose of printing materials with viscosity greater than 25 cP, which is particularly uncommon in research due to these inherent challenges in the technique. In this vein, state-of-the-art inkjet printheads developed by Xaar propose to solve these challenges, at least partially, through their fluid re-circulation technology which keeps an ink in constant motion and has proven to prevent clogging hence allowing more viscous materials to be processed, see the Figure above. The 501 GS8 has a droplet volume range of 8–40 pL, particularly good drop placement accuracy, and is among less than a handful of inkjet printheads capable of processing high viscosity materials [1].

The principal process of inkjet printing an electroactive polymer solution has been reported by Bar-Cohen who demonstrated the inkjet printing of piezoelectric polymer actuators on polycarbonate substrates. The process incorporates steps where EAP layers are annealed thermally at 130 ℃and the top electrodes are sintered using Ar plasma. By following this method, all the processing steps are compatible with low-cost polymer substrates. It was found that the actuators fabricated yield free deflections of approximately 20 m, blocking forces of 3 mN and resonance frequencies of 230 Hz [154].

Table 2.3: Additive Manufacturing — Bioprinting. Adapted from [123, 40, 145, 138, 232, 87, 153, 94, 113, 101]
.

Manufacturing Process	Applications	Technology	Benefits	Limitations	Common Materials
Inkjet-based bio-printing non-contact	Musculo-skeletal Neural Skin	Acoustic Ejection Droplet Piezoelectric Ejection Droplet Thermal Ejection Droplet	2D Resolution Low Cost Fast High Throughput High Precision	Z-resolution limited Low Viscosities Required (e.g., <25cP)	Hyaluronic Acid Gelatine Alginate Fibrin Collagen Agarose
Extrusion-based bioprinting contact	Musculo-skeletal Vascular	FDM FFF	High-Accuracy Well-Established Technology Material Variety User-Friendly	Thermoplastics Only	Hyaluronic Acid Alginate Agarose
Laser-based bioprinting non-contact	Vascular	Laser Guidance Direct Write Laser Induced Forward Transfer SLA SLS Electrohydrodnamic Jetting	3D Resolution	Limited Material Selection Difficulty in achieving thickness Photo-Sensitive Polymers may damage cell viability	Stem-Cells, etc.

Simaite et al. demonstrated in 2016 that inkjet printing conducting polymers (PEDOT:PSS) towards fabricating ionic-based artificial muscles is achievable but requires complex pre-processing and post-processing procedures. This study reported the difficulty in successfully processing PEDOT:PSS solution due to its rheological properties which limits its printability (i.e., satellite droplets, adhesion problems) and hence limited strain curves when doped. Using silver electrodes and PEDOT:PSS actuators, the study achieved a significant level of strain across the PVDF membrane., see Figure 2.13. While certain conductive polymers (e.g., PEDOT:PSS) are biocompatible, there remains the challenge of integrating these polymers with biopolymers (e.g., collagen) during the inkjet printing process [193].

Multiple studies report that, while a variety of sensible biomaterials can be printed, particle aggregation and clogging of the dispensing nozzles remain challenging. This difficulty combined with the sensitivity of biomaterials to its environment and the speed it must be cross-linked using ultraviolet, chemical, or pH means, can negatively affect the cytotoxicity of the printed materials in the final 3D structure [141]. Furthermore, the act of dispensing droplets through the inkjet nozzles exposes any biomaterial in any form to particularly high shear stresses which may causes further damage to the encapsulated cells or living components of the materials. As such, combining the printing of conductive polymers with biomaterials that remain "living" after processing using inkjet technology is relatively unexplored territory within research with very few studies reporting success in this effort [34].

Embedded Approach

The FRESH approach utilises thermoreversible suspension mediums within a bath which enables the deposition of hydrogels or other materials into complex 3D constructs. Based on the research, FRESH innovated the deposition and embedding of one hydrogel into a second hydrogel which supports and maintains the fidelity of the first, cross-linked hydrogel. Generally, these support baths are comprised of gelatine microparticles that change state depending on the input stress. This property of behaving like a solid at low shear stresses and high shear stresses along with the self-healing nature of the gel makes this technique highly attractive to printing materials that would otherwise collapse if printed in air. As part of the FRESH technique, once the 3D construct is printed, the gel can be melted in a non-destructive manner by raising the temperature of the support medium to 37 ℃. Due to this behaviour, a nozzle can move through the bath unobstructed and deposit a material that remains in place as it is deposited without damaging the gel's structural integrity [175, 78].

Hinton et al. modified a MakerBot Replicator with a custom syringe extruder with a 150 μm diameter needle. The support bath was a gelatine microparticle slurry to

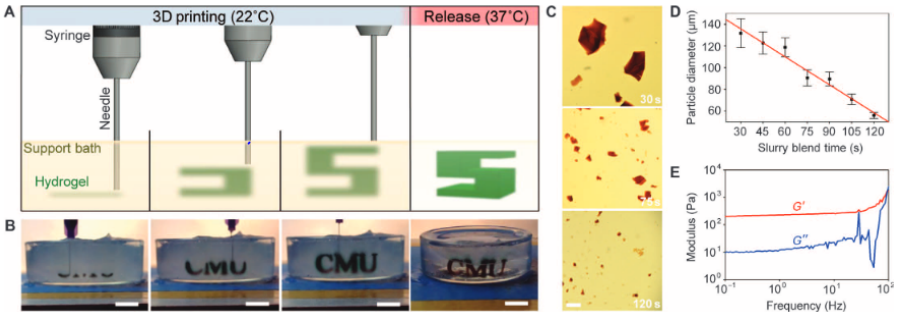

Figure 2.14: (A) FRESH process schematic, (B) The letters "CMU" released by melting the gelatin. (C) Gelatine microparticles after blending. (D) The mean Feret diameter of gelatine particles as a function of time. (E) Rheological analysis of storage and loss modulus for gelatine support demonstrating Bingham plastic behaviour. "Reprinted with permission from AAAS [77] under the Creative Commons Attribution License'

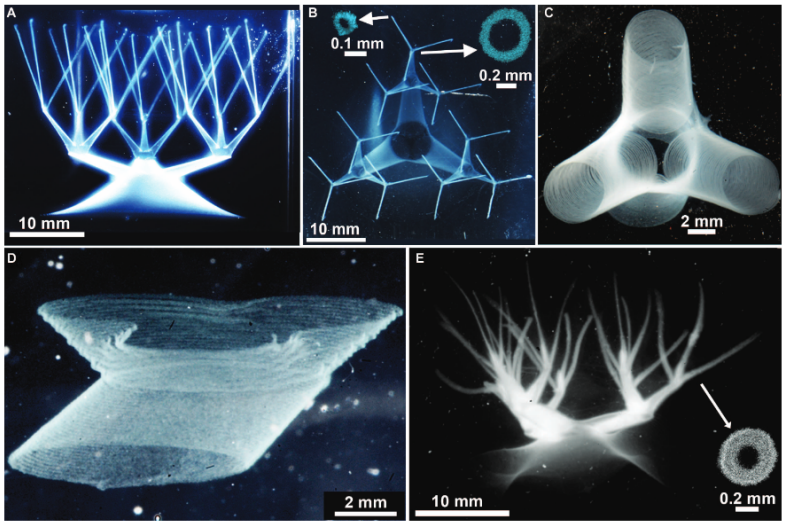

Figure 2.15: (A – B) Hollow Vessel Network. (C) High Resolution image of truncated vessels about 100 μm in diameter (D) Junctions with curvatures. (E) Crosslinked network removed from the granular gel bath. "Reprinted with permission from AAAS [22] under the Creative Commons Attribution License"

have Bingham plastic rheology. A solid block of gelatine hydrogel was blended into a microparticle state and centrifuged to remove supernatant and produce the slurry. Notably, gelatine is biocompatible and may bind to the polysaccharides or proteins that are printed within it. Through integrin binding, the gelatine may enhance the adhesion [77], see the Figure 2.15.

Skylar et al. reported a biomanufacturing method called sacrificial writing into functional tissue (SWIFT). This technique generates organ specific tissues with high cell density, maturation, and the desired functionality by patterning sacrificial inks within

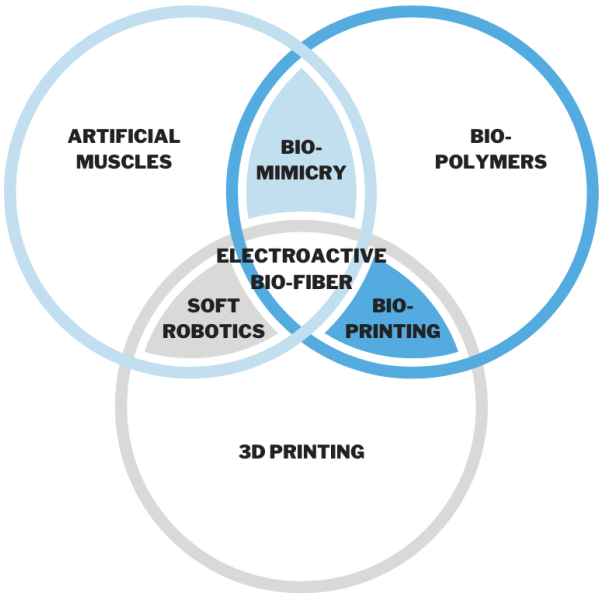

Figure 2.16: Venn Diagram of the relationship between artificial muscles and the potential results which can be achieved through their synthesis in engineering and materials science

a matrix which upon removal yields perfusable channels in the form of conduits. By using organ building blocks (OBBs) and ECMs, this group demonstrated that functional cardiac tissue could be fabricated successfully using embedded 3D printing within slurry or gel suspensions [196].

Rocca et al. demonstrated multimaterial bioprinting by modifying a Lulzbot TAZ 5 and depositing alginate bioink within a Pluronic F127 gel bath. An alternative support medium is Carbopol granular medium, investigated by Bhattacharjee, et al. [22] Embedded 3D printing is an emerging technology which has the potential to vastly improve the sophistication of tissue engineering and bioprinting. While this technique has been used in the past for a variety of desired output, it still has room for development, especially in the 4D printing research space. It is, hence, evident that through embedded 3D printing complex, biologically alive 3D constructs and tissue can be fabricated and potentially fabricate fully programmable tissue or near-tissue constructs.

2.5 Discussion

There exists a desire to fabricate a single or series of fibre(s) which display certain desired characteristics (electroactivity, biofunctionality, mechanical strength, structural integrity, inter-connectivity etc.).The literature reports that the principles of gel-suspension 3D printing are mainly responsible for achieving this result. This method overcomes the numerous challenges associated with conventional 3D printing of fibres. These difficulties

include: a restriction to the 2D printing plane; exposure to unintended environmental factors (temperature, humidity, etc.); a lack of sufficient support during printing which results in failure; multiple steps utilising different machinery and / or experimental rigs to achieve certain characteristics (e.g., the doping process, cell culturing, etc.). Fundamentally, each fibre should present certain mechanical and electrical characteristics which may be compared to existing data concerning EAPs. This corresponds to the characterisation of the fibres which may include the following methods: Mechanical property testing; Fibre surface morphology; Electrical stimulation properties (e.g., deformation percentage, conductivity, etc.); Cell proliferation assay.

Since the state of the art 3D printing techniques are primarily concerned with producing structure in a top-down layer by layer fashion (i.e., in the case of the FRESH technique, a self-healing gel is required to effectively print material but what if this was not the case), which has certain drawbacks as have been identified in the literature, especially when concerned with the fabrication of artificial muscles, a new technique may or approach may be developed where a print-in-place (*in situ* system may be devised, see 2.16. There are already practical developments realising the potential of in situ printing such as the implementation of skin bioprinters [145]. Furthermore, this may be advanced to a stage where in vivo 3D printing may be performed for the applications of regenerative medicine or other non-medical research areas.

By embedding prepared structural elements (i.e., conductive plates or electrodes) within a gel suspension matrix to function as the electrodes as well as providing support after the printing process is completed (much like bones or joints), fibres may be inter-weaved between these elements to construct bands mimicking those of natural muscle. These bands, consisting of individual fibres, will each be composed of a conductive internal biopolymer (e.g., polypyrrole) and an external cellular biomaterial (e.g., collagen). If this is achieved, logically, by attaching a function generator or simply inducing a charge between the two poles between the fibres, the fibres should contract, expand, or otherwise exhibit shape-changing behaviour in response. This research avenue requires, however, a significant amount of materials design as well as a potentially novel fabrication technique.

In principle, if a 3D printing technique could deposit biomaterial(s) or otherwise within a geometry such as a gel bath without causing considerable damage to its surroundings, it is possible to fabricate fibres at pre-determined locations within complex geometries that when fabricated may not have been possible during its production process. For example, in the production of thermoplastic HASEL actuators, a syringe needle is used during the post-process to inject a liquid dielectric into the prepared cavity to allow for future actuation. This begs the question: “What if it is possible to inject or deposit bio-based material(s) at a location where it may be useful for actuation

or other purposes?" Furthermore, this idea may be particularly useful, especially when attempting to deposit material in otherwise and formerly unreachable locations. For example, the connective tissue between joints or the singular muscle fibres within the bicep. One potential solution could be utilizing an in situ printing approach such as a skin bioprinter, but instead of printing outside the body, it would have the capability to print within the body. This concept, if possible, from an engineering perspective, would enable future advancements in several fields of research and potentially provide a building block technique through which complex geometric structures may be achieved such as the intricate network of the animal nervous system.

2.6 Experimentation & Observations

As a result of the investigation into the FRESH technique, a simple experiment was designed which tested the concept of using needles within a gel. According to the FRESH or embedded 3D printing principles, a self-healing gel is an absolute requirement. In essence, the gel simply acts a suspension matrix into which certain (bio)polymers are deposited and subsequently polymerised through a chemical reactant or stimulus. Many suspension matrix-based materials are developed for this purpose to remarkable success. However, for the purposes of this proof-of-concept test, simple food gelatine was used in ratio to water. The purpose of this experiment was to observe the relationship between gelatine and a needle syringe — seeking the concept of 3D printing polymers within any gel, self-healing or not. See the below methods and materials for the details on this experiment.

2.6.1 Materials

- Generic gelatine powder
- Syringe with needle
- Food colouring — red
- Tank

2.6.2 Method

1. Mix 250g of gelatine powder into 5L of water — a 7.5% ratio.
2. Cool the gelatine mixture overnight at 2deg C.
3. Prepare the food colouring and the syringe.

Figure 2.17: Proof-of-concept using a non-self-healing gel and dye to indicate the needle tracks.

4. Insert the needle into the solidified gelatine at certain points and at different depths.

5. Drag the needle to simulate the concepts discussed in literature while simultaneously depositing the food colouring.

6. Observe the gelatine and food colouring.

2.6.3 Results

As seen in Figure 2.18 above there are noticeably clear needle tracks in the gelatine. As the needle was dragged across the gelatine from the top, it effectively destroyed and marred the surface to the depth of the needle tip. This leaves the food colouring essentially exposed and unsupported in terms of the concept of a suspension matrix. Since the suspension matrix has been defined previously as an enclosing body which supports the integrity of materials which are delicate on deposition and polymerisation, a gel which does not "heal" or enclose the printed material to keep the material in place

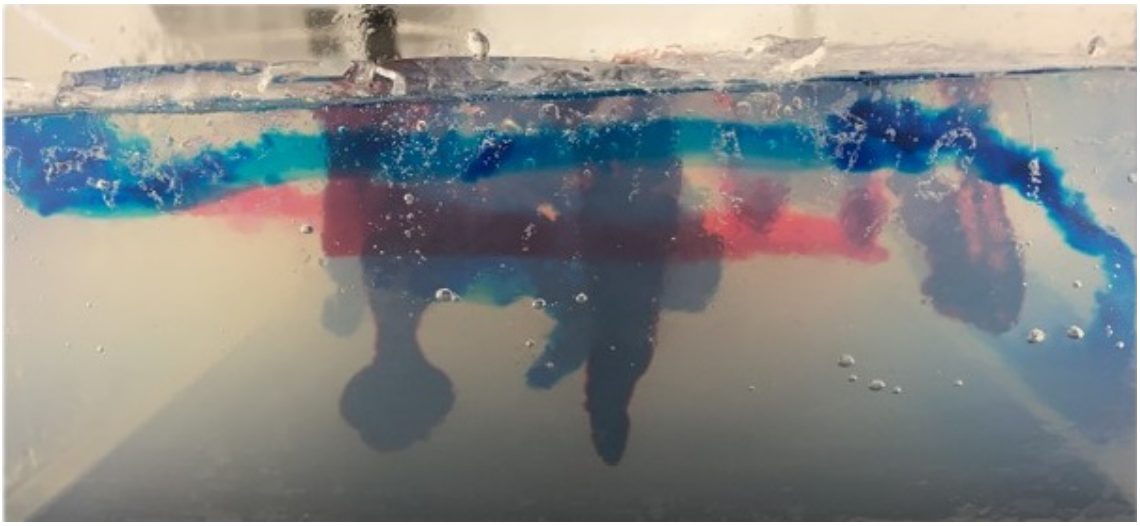

Figure 2.18: Proof-of-concept using a non-self healing gel and dye to indicate the needle tracks.

is effectively useless. This is the simple and expected observation, but the consequence of this observation leads to an interesting question, "How can the damage caused by the needle to the gelatine be minimised while maintaining the effectiveness of depositing a material into the gelatine similar to embedded 3D printing techniques?".

2.7 Steerable Needles

Steerable needles are used, broadly, in minimally invasive therapies to treat certain parts of the human body which are preferable or more effective than traditional surgical treatments. For example, lung cancer, can be biopsied effectively by deploying a steerable needle through a bronchoscope [62]. Other clinical operations include thermal ablation therapy, drug therapy and delivery, radioactive seed implantation and many other procedures which effect organs such as the prostate, heart, or liver, etc [3, 14]. Currently, the needles which are used in these procedures are restricted by multiple challenges, namely:

- Needle Rigidity
  - This has an effect on the path that the needle can travel where — the less flexible or more rigid a needle is: the straighter the path it will travel on penetration
- Tissue Deformation
- Needle Bending under force

- Movement Error

These challenges are the primary conditions which cause the needle to deviate along the intended path to reach a particular target accurately. At present, these operations are primarily manual with minimal automation which result in several circumstances where, for example, in order to correct a deviated needle, it is removed and subsequently reinserted at a different position in order to reach the target goal. This results in major discomfort as well as pressure on the tissue of the human body. This, ultimately, may cause a degree of damage to the tissues and organs of the body. A key consideration to make, however, despite the already enormous challenges in accurately reaching a target goal within the human body is the existence of simply termed "obstacles" such as bone, other organs, veins and arteries, and other sensitive tissues which must not be penetrated [219]. As such, the concept of the obstacle avoidance becomes necessary. This, however, is once again constrained by the ultimate flexibility of the needle to be used in an operation. It is, thus, logical to state that since thinner or smaller needle diameters are more flexible due to their mechanical properties, the ability to deposit drugs or other substances within the body at the target location becomes a challenge — this becomes a major point of this thesis.

This thesis is confined to flexible steerable needles with the major constraint of depositing materials while simultaneously maintaining the ability to deposit relatively large quantities of materials in order to "3D Print". In the first consideration a flexible, this thesis defines the constituent characteristics of flexible, steerable needles, and secondly the constraints associated with a needle and its capability to effectively deposit a (bio)polymer as the hypothesis proposes. The key variable to consider in terms of this flexibility is the maximum curvature this needle can achieve within a body of a certain stiffness. This curvature is defined in terms of its flexibility (in terms of its elastic modulus). Furthermore, the needle design must be considered to enable the ability to deposit materials at an adequate flow rate which suits the aims of the research question of this work — this may be defined in the amount of polymer which is deposited per milliliter (mL).

2.7.1 Needle Properties and Kinematics

The properties of a flexible, steerable needle depend entirely on its design in terms of materials (generally 304 stainless steel) and the mechanics of its tip. Generally speaking, the most common type of steerable needle utilises the principle of the bevel-tipped needle [231]. When the needle is inserted into the body of a certain stiffness, the needle tip or bevel is subjected to lateral forces of a certain related degree. These forces cause the needle to bend or deflect in the direction that the forces direct the tip. This results in an arc. This can be taken one step further by defining a total path from entry point

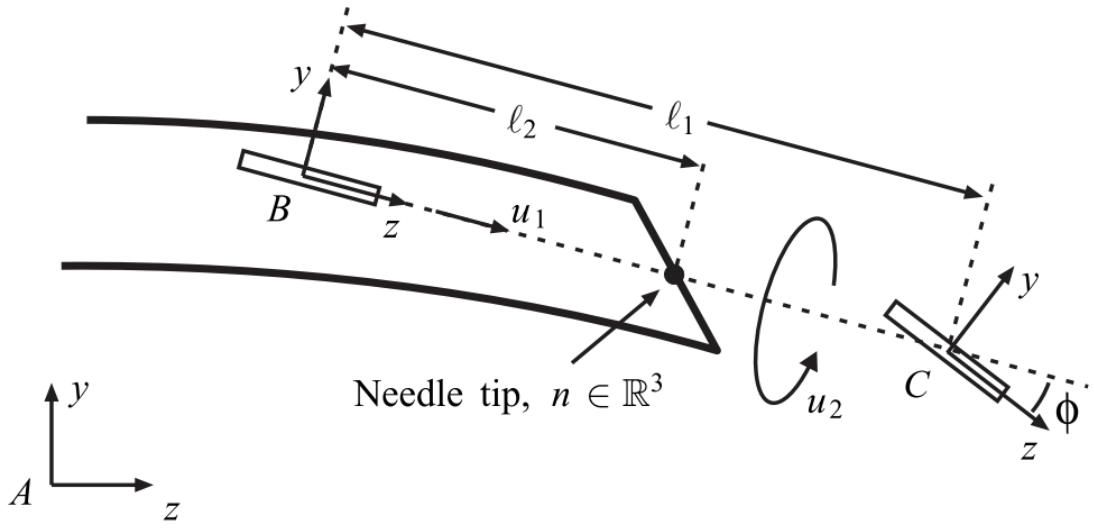

Figure 2.19: The Webster model of a bevel tip needle steering robot with an x-y-z configuration. "Reprinted from [218] with permission"

to goal point in terms of minuscule "arcs" subject to the time it takes to reach this path — this is dependent on the insertion speed as well as material properties of the penetrated body.

The question then arises: "How can the needle direction be controlled in a fashion to avoid obstacles as well as reach a goal point satisfactorily?" This can be defined in robotics or mechatronics terms — the needle must have *two degrees* or more of freedom. Generally, the systems used in literature are two-degree-of-freedom robots consisting of an insertion motion (or translation) as well as a rotation motion along the axis of the needle body. According to the seminal paper from Webster, et al. in 2006, the robot may be defined in terms of a modified unicycle model. In simple terms, when the needle is turned along its axis as the needle travels forward then the needle body will follow the path of this rotation — this model is non-holonomic [218]. Through a series of axial and translational re-orientations, a desired path may be achieved to reach a distant and not easily accessible goal point.

In Figure 2.19, basic kinematic model of steerable needles can be seen. This model can be understood by drawing an arc of length between the needle tip position at "B" towards the direct next position at "C". The position at "B" has a specific x-y-z orientation in the frame space which differs from the orientation at position "C". This consists of a length (l_1) between these two positions. Thus, several variables are required in order to effectively move from point "B" to point "C". The insertion velocity (u_1)

and an angular velocity (u_2) define the control inputs associated with this motion. Furthermore, there may be an angular difference between position "B" and "C" which is defined as φ. This angular distance is significant towards the kinematic calculations. Hence, it follows as:

$$g_{ab}(t) = g_{ab}(0)\epsilon^{(u_1\hat{V}_1+u_2\hat{V}_2)t} \tag{2.1}$$

$$n(t) = R_{ab}(t)l_2e_3 + p_{ab}(t), \tag{2.2}$$

where $R_{ab}(t)$ and $p_{ab}(t)$ are the rotational and translational 3D matrices of the transformation matrix g_{ab} in world space and $n(t)$ represents the needle tip coordinates at a specific time. These equations only consider the simple x-y-z coordinates irrespective of their orientation with respect to the world frame.The twist vectors detailing the coordinate unit x-y-z (e_1, e_2, and e_3) vectors are described as:

$$V_1 = \begin{bmatrix} e_3 \\ \kappa e_1 \end{bmatrix} and\ V_2 = \begin{bmatrix} 0_{3x1} \\ \kappa e_3 \end{bmatrix} \tag{2.3}$$

The curvature of the arc between these points, as previously mentioned, is defined as follows:

$$\kappa = \frac{tan(\phi)}{l_1} \tag{2.4}$$

As a result, These equations of V_1 and V_2 provide a method through which the next coordinate "C" from "B" can be calculated over time knowing the input insertion and rotational velocities. This may further be developed using a duty cycling control scheme [125]. There is another equation from this model which is more discrete and independent of time and simplifies to a step operation between "B" and "C". As follows:

$$g_{ab}(k+1) = g_k\epsilon^{(u_1(k)\hat{V}_1+u_2(k)\hat{V}_2)t} \tag{2.5}$$

$$n(k) = R_{ab}(k)l_2e_3 + p_{ab}(k), \tag{2.6}$$

The equation includes two control velocity inputs, $u_1(k)$ and $u_2(k)$, which correspond to changes in the distance between two coordinate points and their difference in angles at a specific step, k. By using these inputs, it's possible to compute a single arc that represents the trajectory between an arbitrary starting coordinate and an arbitrary destination coordinate in world space.

However, in order to plan a complete path between a start coordinate and a goal coordinate, we need to define the goal point first. This process is known as path planning and requires iterative development of a path that connects the two points. Therefore, given a start and goal coordinate, we can use the equation and path planning techniques to create a path that guides an agent or robot from the start point to the goal point.

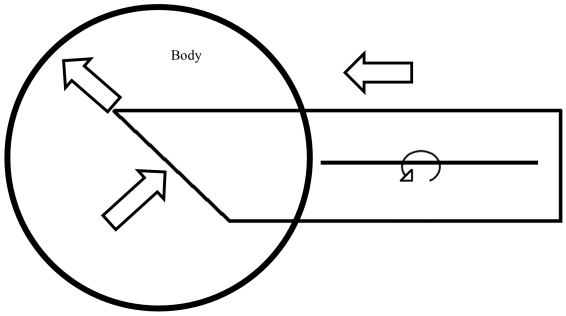

Figure 2.20: The behaviour of a bevel-tipped needle in all directions as it travels through a body. It cuts tissue in the direction of the pressure which the surrounding body places on the bevel.

2.7.2 Path Planning

By utilising the previously explored kinematics, the path as a whole that a needle travels when inserted into a body can be generated utilising a variety of techniques. These techniques are classified as 2D or 3D path planning, based on the imaging techniques which offer a feedback loop to the system as either 2D (cameras, ultrasound, CT, etc.) or 3D (MRI, etc.). In other words, the needle tip position is constantly assessed using either 2D or 3D techniques. It is then further categorised into numerical based approaches and search-based approaches. Numerical approaches to path planning involve generating an optimal path utilising the maxima or minima value from the input kinematic function. While search-based approaches use algorithms to calculate all the possible trajectory paths through artificial intelligence, sorting algorithms, sampling algorithms, etc.

One 2D numerical approach use a finite element model of a steerable needle which designs a non-linear optimisation function which attempts to achieve the shortest, feasible path at the best accuracy while avoiding obstacles [8]. Similar to the previous example, a probabilistic method known as the 'Markov Decision Process' was utilised to handle obstacle avoidance which calculated the maximum probability that a needle could reach a target point successfully. An innovation on this method [204] attempts to consider the direct effect of the deformation of tissue on the planning of the trajectory as well as the real-time movement of the needle tip in terms of its angle. The effects of the forces, see Figure 2.20 of the body on the needle tip causes a certain amount of uncertainty which this method considers which results in a more stable path generation algorithm.

A different approach to 2D path planning involves the Lyapunov energy optimization algorithm [183]. This algorithm uses optimization function equations and neural networks to calculate a trajectory for a needle moving through an unknown environment. However, this method has a drawback of having long computation times and

non-trivial performance in terms of feedback. Another optimization algorithm [84] uses a multi-objective approach and employs optimization, dynamic weighting, particle swarm algorithms to plan a trajectory that optimizes the intended goal point while considering the risks posed by surrounding obstacles. This algorithm takes into account the length of the trajectory and the obstacles' impact on it. This algorithm based on particle swarm algorithms (PSO) optimises the accuracy, risk, and path length by using a multi-objective, dynamic weighting optimisation function. While this algorithm states that it can reach multiple target goals accurately while avoiding all obstacles, it is another highly inefficient path planning algorithm and is both time-consuming and resource intensive. It provides high precision and excellent computational performance while minimizing trauma to the penetrated tissue. However, during its operation, various errors may occur, which can significantly limit its usability.

One example of a 3D numerical approach involves the introduction of Gaussian white noise at the input to establish a probability density function as a kinematic model. This generated a path by estimating a cloud of reachable space in the target area of the needle tip. This allows a relative margin of error for the needle tip to reach a target point in 3D space [157] and results in unreliable calculations within complex environments. A fuzzy logic model [108] was further developed to probabilistically and continuously generate accurate and smooth paths by analysing previously generate discrete paths, which as individual candidates do not accurately achieve the end-goal. This algorithm allows a generated path for complex path planning problems but has the key disadvantage of having high calculation costs and long runtimes.

A further 3D numerical example [53], again uses an optimisation-based function based on the unicycle model which compiles the input variables such as: duty cycle speed, path length, deviation, etc., in order to simplify the number of calculations and improve the processing time to generate the path. Interestingly, this specific work compared two distinct approaches to needle steering: stop-turn motion, continuous or spiral motion. This is significant since these approaches result in relatively different outcomes and are handled vastly differently from a control perspective.

Another algorithm [24] utilises a multi-objective optimisation approach which attempts to generate a path to multiple end-goals from a single-entry point. It relates the construction loss cost in terms of tissue damage to the total penetration depth. As such, this algorithm can reach multiple target points through a combination of (re-)insertion, retraction in full or in part and axial rotation. This method however can have poor outcomes in terms of accuracy.

Among the more interesting of the numerical 3D path planning algorithms is known as the observable Markov decision algorithm [220] which combines the movement of the needle tip with an external observation system (e.g., MRI). It aims to find the optimal

trajectory by considering the uncertainty of the needle tip position. This tends towards an integration between the control schemes and attempts an effectively real-time path planning algorithm which updates the path depending on the position of the needle tip. This, however, is resource intensive and can fail without reaching the intended end-goal and take excessively long times to calculate a solution.

Search-based path planning algorithms, in contrast to numerical-based path planning, attempt to calculate all the feasible trajectory paths using computative searching and sorting algorithms. It has considerably faster and more resource efficient computation times, however, the generated output path may not be the optimal path. Some common search methods include rapid exploration random tree method (RRT), artificial intelligence methods using neural networks, random road marking method (PRM), etc. Fundamental to the search-based approach is the usage of local and world reference frames and coordinate spaces to generate trajectory paths. Significantly, the RRT algorithm has been used most successfully in the planning a path in a world reference frame [226]. The key effect of this approach is the ability to select and optimise a path. This technique like many others of this type cannot be used to plan in real-time and within effective control feedback loops.

Key researchers in 2011, Alterovitz et al., [9] and Patil et al., [158] furthered this relatively basic RRT algorithm by proposing in the former case a fast search roadmap method and in the latter case introducing target-biasing and navigation algorithms within a 3D reference frame. The result of these works was to shorten the processing time required to generate a solution (according to the paper by 2-3 orders of magnitude). This was furthered by the proposal of a real-time path planning algorithm which reaches 3D targets in an environment while considering obstacles and uncertainties [159].

Alterovitz, et al., continued this work into RRT and PRM by attempting to weigh the efficiency of the method with respect the accuracy of the end-goal as rapidly-exploring roadmap (RRM), see Figure 2.22. It, thus, makes a decision to continue a search-based on user parameters which define the path cost, risk, and allowable uncertainty. Fu et al. [62, 63] proposed a method to extract a cost-map from CT scanned images and then utilise these images to efficiently plan a safe trajectory through the target body. It suggests an "any-time" approach to solving a motion plan computation. It also includes other search-based algorithms within its procedure to select the most optimal cost algorithm to select a suitable if not optimal trajectory.

Alternatively, path risk assessment functions [29] have been developed where a safe distance is maintained between the trajectory path and any defined obstacles. By combining this approach with well-defined PRM techniques, paths can be optimized by selecting the shortest paths generated while also controlling the number of curves or bends required to reach the end-goal, see Figure 2.23 .

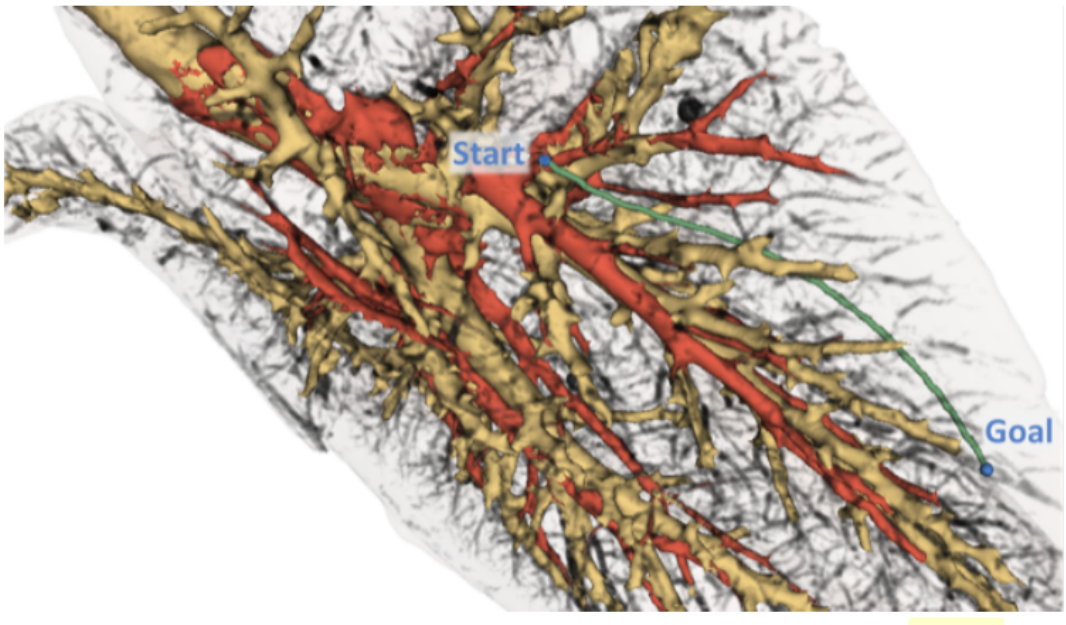

Figure 2.21: A steerable needle path inside of a CT scan of a lung using a minimised cost motion planning approach utilising the RRT search algorithm. A clear start point and end point are indicated. "Reprinted, with permission, from [62]"

Other search-based approaches which include medical imaging technology (MRIs, ultrasound, etc.) in a closed-loop feedback controller include a fuzzy logic controller [183] or motion re-planning algorithms based on input sampling which calibrates to account for uncertainty and accuracy. For example, ultrasound images may estimate a curvature within a feedback loop controller, which while running an RRT algorithm may update the controller in real-time when there are deviations in the needle tip along the prescribed initial path [136, 212].

In the period from 2015 - 2022 many advances have been made in terms of improving the previously fundamental search-based algorithms. This improvement has primarily been achieved by: re-optimisation strategies (specifically of the needle entry point to reach the goal point); evaluation and re-evaluation function of needle paths to find an optimally short and risk-free needle path [223]; the usage of advanced finite element methods (vector intrinsic, etc.) to calculate the deformation of both needle and body (see 2.24 as the needle travels to develop an interaction model and thus use RRT to plan the final trajectory [82]; more detailed input parameters which consider the body characteristics such as the location and orientation of obstacles, the material properties of different sections of the body, etc., through which optimally safe paths can be generated [223]; and the advancement of the RRT algorithm itself to integrate with control methods to continually plan a path before and while the needle tip travels through a body [56].

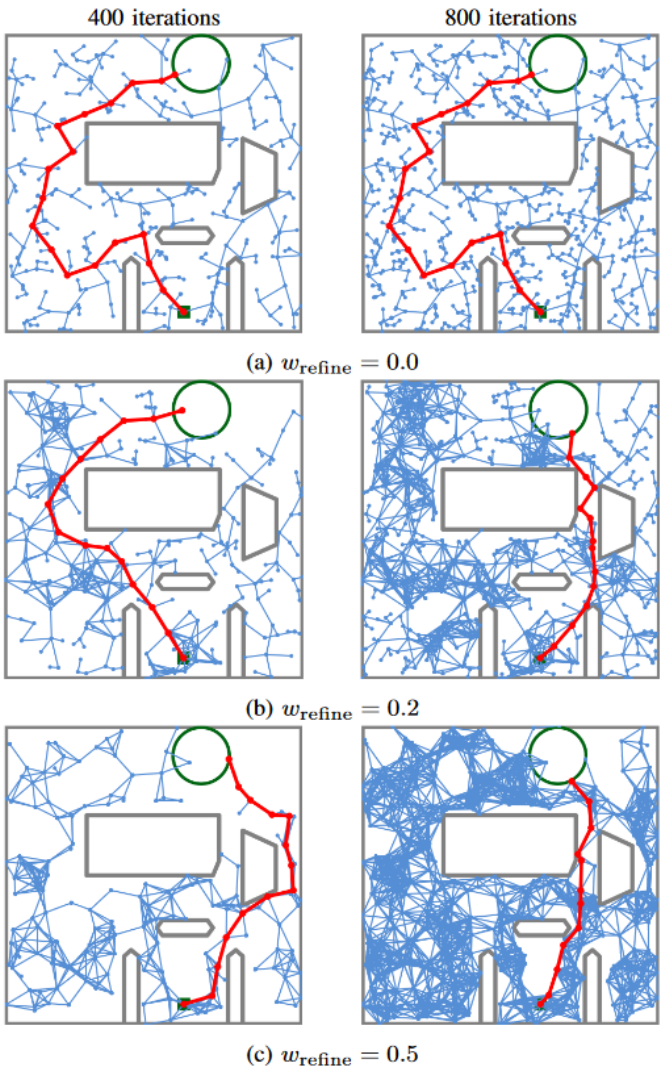

Figure 2.22: The increasing RRM weight which explores the space to finally reach an end-goal target. From more sub-optimal paths seen in (a) to increasingly refined and converged path from (b)-(c) which is dependent on the refinement parameter. "Reprinted, with permission, from [9]"

Thus far, only the most common of path planning algorithms have been discussed which are recognised to be well-accepted and effective in practice. There are, however, different strategies to path planning such as inverse solution planning, geometric graphic planning, etc. In terms of inverse solution planning, this method works under the concept that the needle trajectory from a 3D frame can simplify into two vertical planes intersected by a line to join the points to form a curve [53]. The advantage of this approach is its suitability for environments in which its properties must be considered. A follow-up to this research developed a dynamic 3D path planning algorithm utilising the conversion procedure of a 3D path into 2D components to form a trajectory [97].

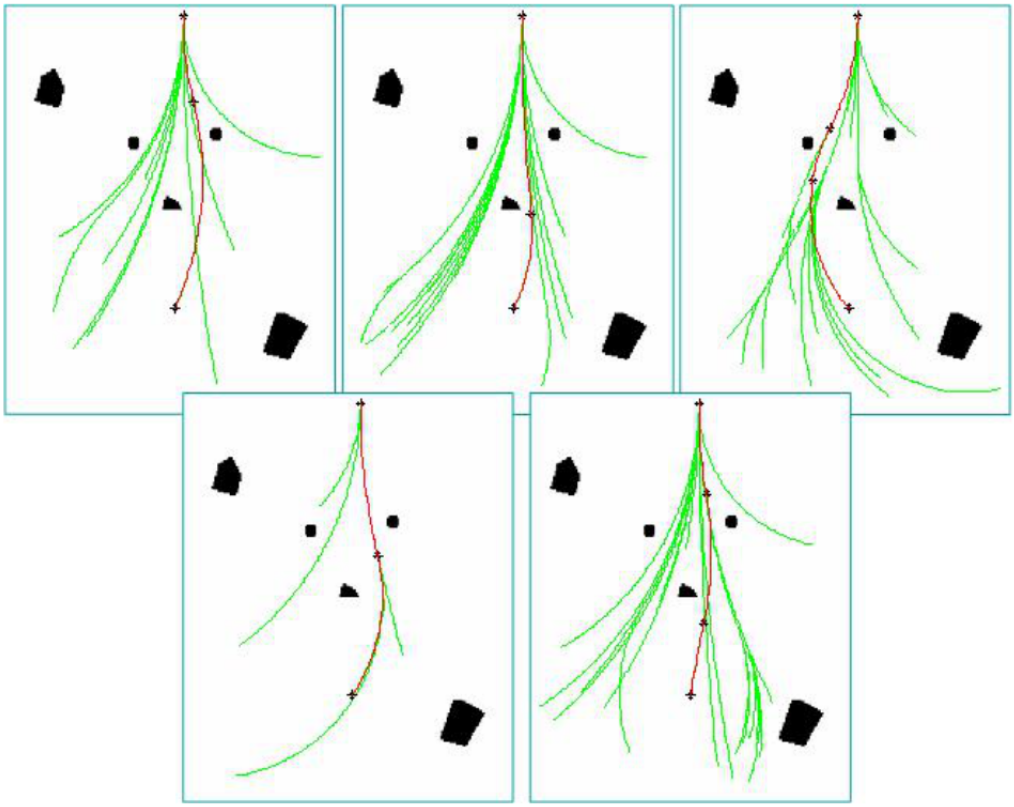

Figure 2.23: RRT output trials with an output tree of possible paths to the end goal and the red line depicting the final path. “Reprinted, with permission, from [29]”

An approach known as the “N+1 point” is particularly interesting since it simplifies the path planning computations by segmenting a path into discrete parts (N). It categorises a needle trajectory as the entry point, a point near an obstacle, and the goal point A separate technique known as geometric graphic method uses an S-shaped double-arc path planning algorithm similar to the Markov decision algorithm to avoid obstacles. By using a polygonal tangent method to limit the area of the plane where the entry point, obstacles, and goal point are positioned and thus continually modify the planning path depending on the arc that the needle travels [97]. A particularly useful approach known as the Haystack (HST) algorithm simulates the tissue and the needle deformation leading towards highly accurate iterative optimisation of needle paths. It even suggests a methodology to handle the deformation caused by external factors such as breathing [73].

It is clear from these literature sources that there are multiple approaches in order to generate a needle path. These approaches may further be classified, as is common in literature, as “online” or “offline”. “Online” approaches form part of the control methods

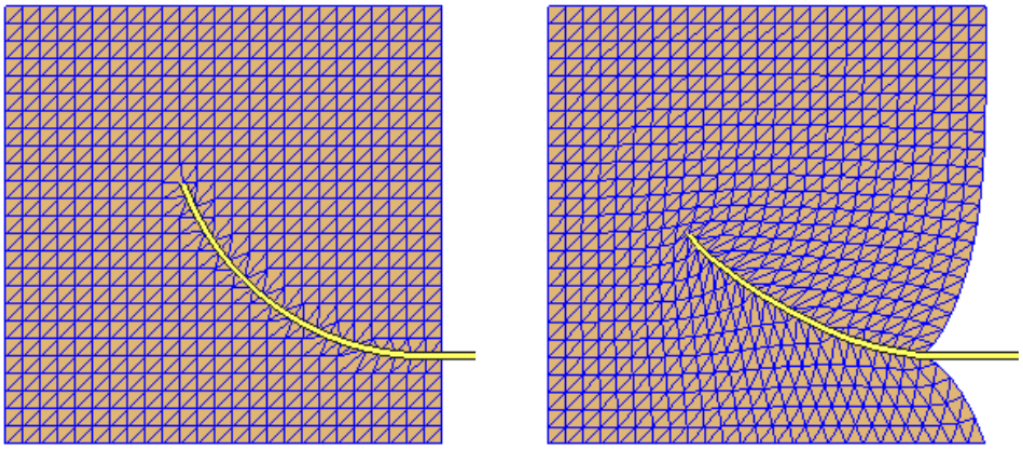

(a) Rigid Tissue (b) Deformable Tissue

Figure 2.24: A simulation of the interaction between the needle and body on insertion. A stiffer body results in less friction for the needle and a clear and constant curvature results. In contrast in (b) a reduced curvature is observed, and the deformation of the tissue causes a deviation in the final point a needle tip can reach "Reprinted, with permission, from [8]"

utilising x-rays, CT scans, or ultrasound, which allows the algorithm to continually update the needle path to attain as a high an accuracy to the end-goal as possible. "Offline" approaches similarly utilise CT scans, x-rays, or vision systems to function as a setup procedure for a needle path - to identify obstacles, needle behaviour, tissue behaviour, etc. - without necessarily being connected to the control methods of the steerable needle system or continually updating the path of the needle as it travels through a body.

2.7.3 Needle Imaging Processes

The field of study that involves steerable needles can be classified into three main categories: motion planning, needle tip navigation and position control methods, and electro-mechanical systems as steerable needle robots. When it comes to literature, the most exciting research is focused on improving motion planning capabilities. Every year, more advanced algorithms are being developed for surgical applications. However, there is growing recognition of the importance of control methods, and a closer connection between path planning algorithms and control schemes that implement these paths is emerging.

Firstly, needle tip imaging is the first problem that must be solve for either "offline" or "online" path planning approaches. This is done for two main reasons: 1. the

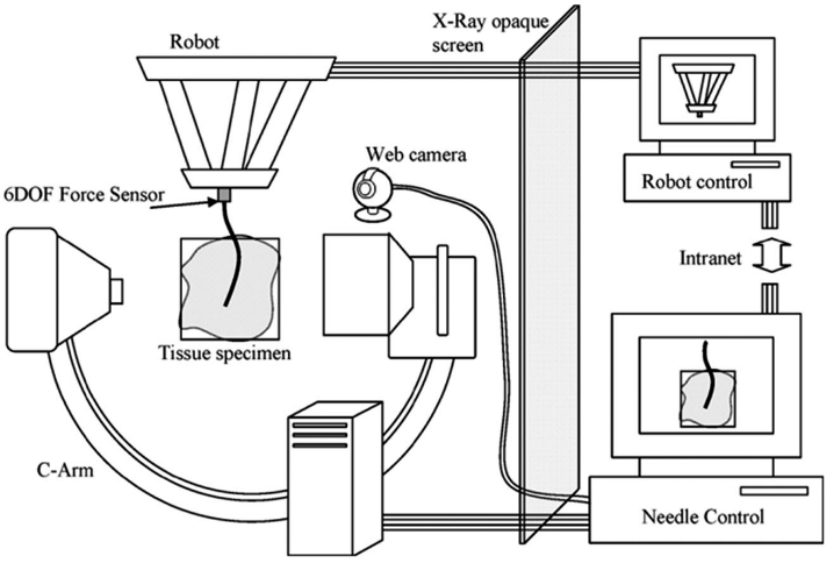

Figure 2.25: An experimental setup with x-ray equipment for the testing of a flexible steerable needle "Reprinted, with permission, from [67]"

environment of the body must be defined in terms of obstacles (bones, nerves, veins, etc.); 2. the needle tip must be tracked, triangulated, or noted in order to effectively run the path planning algorithm and generate suitable and / or optimal paths.

There are different strategies to perform the imaging of the body in question as well as the needle tip. Magnetic resonance imaging (MRI), computed tomography (CT) scans, electromagnetic scanning systems (see Figure 2.27) [159], x-ray scanning (see Figure 2.25), Brightness or B-mode ultrasound, stereoscopic cameras (see Figure 2.28), etc. An example of electromagnetic tracking system which approached path planning using a procedure of rapid re-planning. By updating the tracked coordinate position of the needle tip, the path could be updated with a new trajectory from its current position to account for any inconsistencies or variabilities as it travelled along its original paths. Similarly, x-ray imaging equipment setup in a certain configuration. The key challenge with any single tracking mechanism (x-ray, electromagnetism, CT scanning, etc.) is inaccuracy in measurement. This leads to relatively complex robotic control systems such as a 6-DOF parallel robot control system [67] whereby correction algorithms are proposed to compensate for mechanical error and imaging error, see Figure 2.25. These imaging techniques are often coupled with force-torque sensors to handle any differences in the body characteristics as it the needle is inserted.

Electromagnetic or ultrasound transducers are relatively effective imaging equipment which may be used within steerable needle systems with x-rays being more accurate than these and CT scanning being the most advanced imaging technology. An example

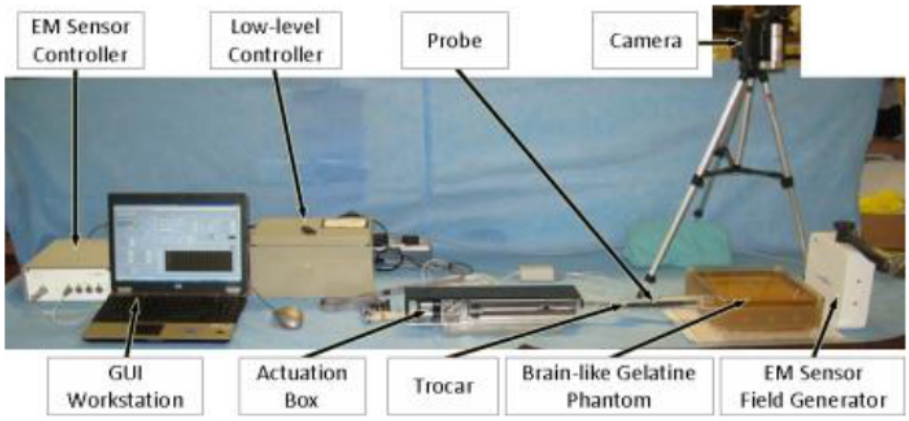

Figure 2.26: An experimental setup with electromagnetic equipment for the testing of a flexible steerable needle. "Reprinted, with permission from [29]"

of an electromagnetic system is a case where four electromagnetic sensors were attached within segments of the steerable needle itself and detected using a transducer placed above the area where the needle is inserted. This provides a continuous reading of the different parts of the needle, see Figure 2.26. This is often coupled with a duty-cycling approach (mentioned in the previous section) to the control scheme of the robot and allows an effective and accurate closed-loop system with an error of less than 3mm [159, 118, 163].

Ultrasound offers a safer and more cost-effective approach than CT scanning or MRIs but with lesser final accuracy in needle tip control. Other challenges, however, such as image noise, echo, and other non-uniformity of tissue in bodies exist causing difficulties in attaining a highly accurate image. Certain research has investigated techniques to reduce the noise in ultrasound imaging and smooth the image using techniques such as interpolation to maintain needle tip position, see Figure 2.27. The most advanced research using ultrasound showed high accuracy using image processing techniques (colour thresholding, etc.) [144, 143, 176, 235, 4].

CT scanning has been used with steerable needles to offer highly accurate feedback to the needle insertion process. One such proposed device [59] used a mounted CT scanner display and a mounter mirror display through which to track the needle in a body while accurately estimating the output 2D needle tip position. The key intention is to guide the needle accurately through the insertion process of the needle. Similarly, MRIs have been used in similar applications, however MRI has the disadvantage of having a delayed imaging speed in comparison to the former imaging strategies.

There are multiple advancements in using MRIs, specifically, in the registration and segmentation of scanned images into 3D space objects which can be manipulated using

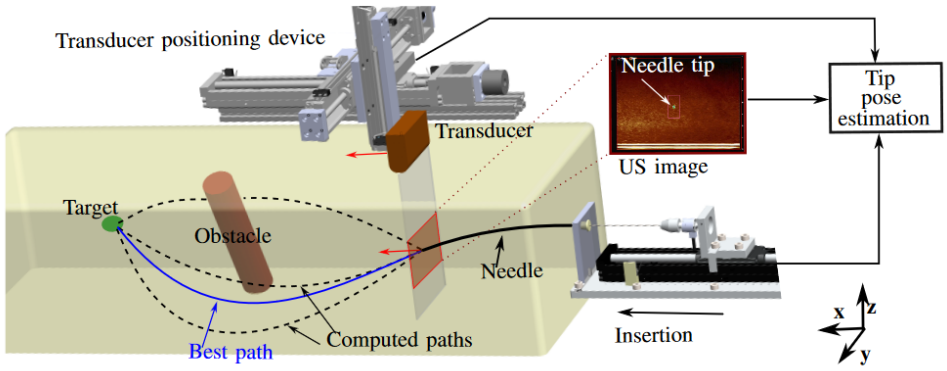

Figure 2.27: An experimental setup with ultrasound equipment for the testing of a flexible steerable needle. "Reprinted, with permission, from [136]"

software in order to obtain a holistic view of the area and obstacle in which the needle must steer [100, 203]. Optical fibre grating sensors embedded in the steerable needle are often used in synthesis with the MRI approach. This is due to their ability to measure the strain of the needle tip as it is inserted and through a feed-back loop estimate the current coordinate position of the needle tip. In conjunction with an MRI, this dual approach allows the needle tip to accurately track its own position while simultaneously detecting any obstacles as well as the desired end-position [182, 49].

2.7.4 Needle Control Processes

Thus far, this review of steerable needles has explored the vision technologies available to identify all obstacles, the target points, and even in some cases the needle tip itself as it is inserted into a monitored body. By utilising these vision technologies, the next step in effectively controlling the steerable needle is in terms of the mechanical processes through insertion and rotation are completed. The earlier explored concept of 'arcs' between successive points from the entry point and the goal point is therefore an effective approach towards describing steerable needle motion. There exist an insertion length and a rotational angle associated to reach a subsequent point from the current position point. In literature, there are two primary modes which attempt to solve this problem: tele-operation (or manual / partial-manual control), and fully autonomous control.

Manual operation of steerable needle devices or robots consists of an operator manually driving the insertion and rotation controls of the needle tip. This is often referred to as a master-slave manipulator [148, 177, 186]. Generally, PI or PID controllers are used in conjunction with these manual controls to enable the operator the ability

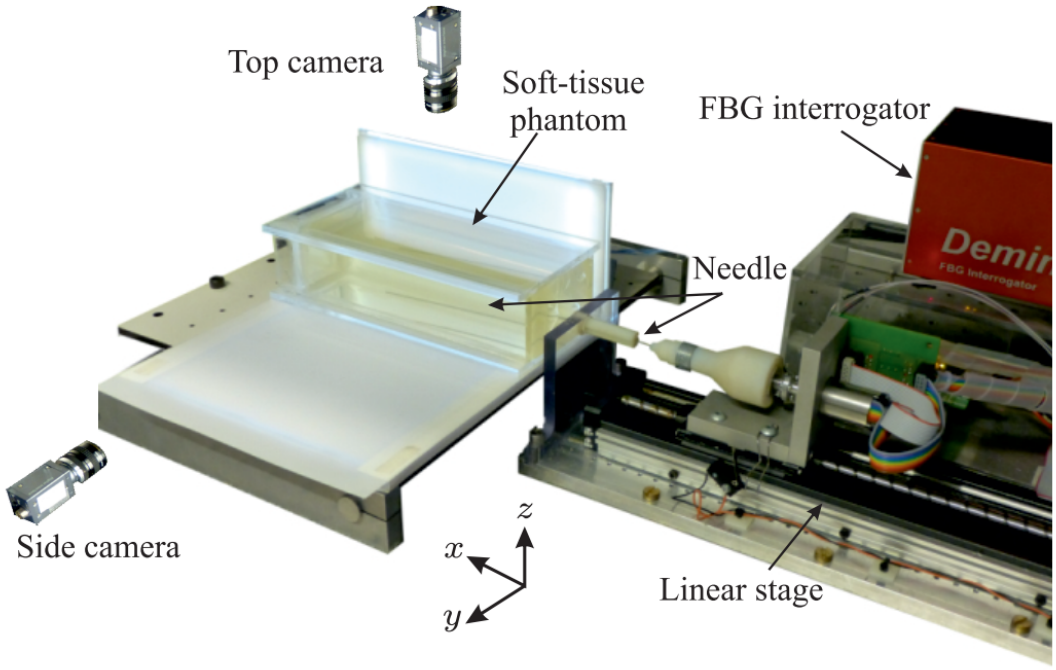

Figure 2.28: An experimental setup with a needle integrated with FBG sensors coupled with two device cameras for reference validation. "Reprinted, with permission, from [2]"

to enable finer motions of the steerable needle as well as automate certain steps of the entire process. Such an automation step may involve the initial pose of the needle at the entry point to ensure that on insertion the needle will travel in the correct orientation. These controllers are often integrated with force-torque sensors or optical fibres which provide key sensor data within the feedback loop to optimise the total accuracy of the system [67, 52], see Figure 2.29.

An alternative control strategy involves extracting the 2D plane related to the state space system of the steerable needle kinematics model [92]. This approach maintains the plane and applies feedback linearization to the kinematic model. An observation and controller are designed and applied to the system as shown in Figure 2.30. A key detail of this strategy is that the radius of curvature of the inserted needle with respect to the material properties of the body that is penetrated must be acquired in order to effectively run the controller. An advancement of this work suggested a simulated model to function as an estimation model for the parameters associated with the steerable needle [139]. There is however a drawback that must be considered: since path planning algorithms have already explored been explored, a key consideration involves the physical interaction between the needle and the body it penetrates where there will be deformation of both entities, primarily depending on the rigidity of the body when penetrated.

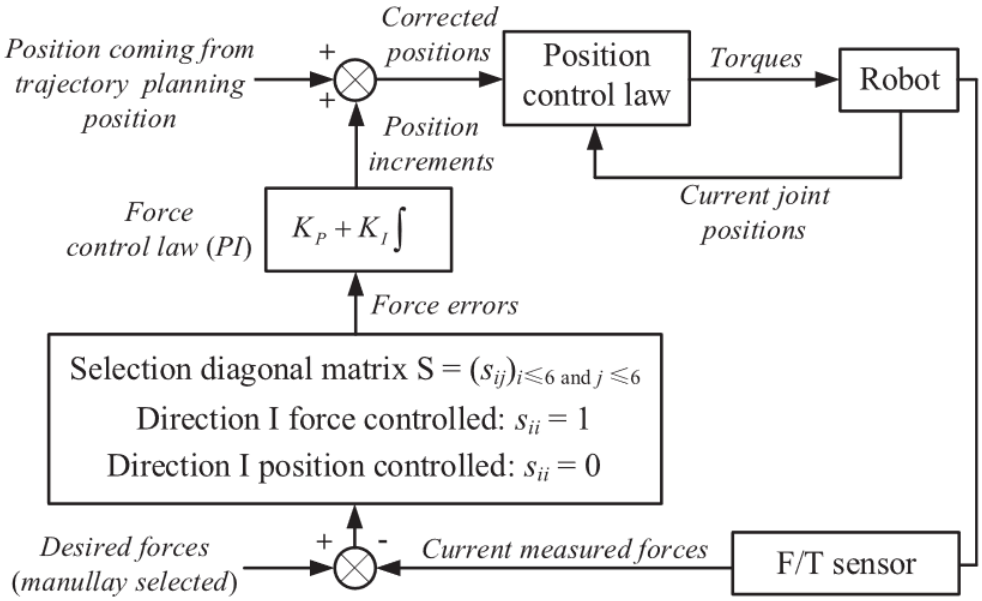

Figure 2.29: Force and position control feedback loop "Reprinted, with permission, from [52]"

One paper in literature considers this in terms of the controller where a rotational feedback control system was implemented to compensate for any torsional deformation in the needle because of the rotational stresses of the body it punctures [172, 75]. There are several tactics to account for these deformations such as: predictive control algorithms to estimate the amount of rotation required to move the needle in a continuous spiral; sliding mode controller which use motion characteristics to minimise the amount of control inputs [181]; optical fibre sensors constructed into the needle body to enable strain sensing to estimate the current coordinate position (this method is reported to be accurate to within 1.3mm of a target goal) [2, 209], see Figure 2.31; LQG controllers making use of Kalmann filters for state estimation and LQR as control policy to effectively guide the needle tip through any observable noise in the imaging system [210].

All the previous examples are partially autonomous control procedures which require an operator to perform certain tasks in order to effectively use the steerable needle device but is not limited to manually driving the needle with controls. Based on the available literature, there are strides being made towards fully autonomous steerable needle devices which can complete all the necessary steps independently. This involves effectively generating accurate paths in a full feedback loop. For example, ultrasound images can be used to determine the coordinates and the pitch-roll angles of the needle tip based on the needle rotation speed [54]. Another method to emerge involves the robot guidance of steerable needles specifically by ultrasound imaging which makes use

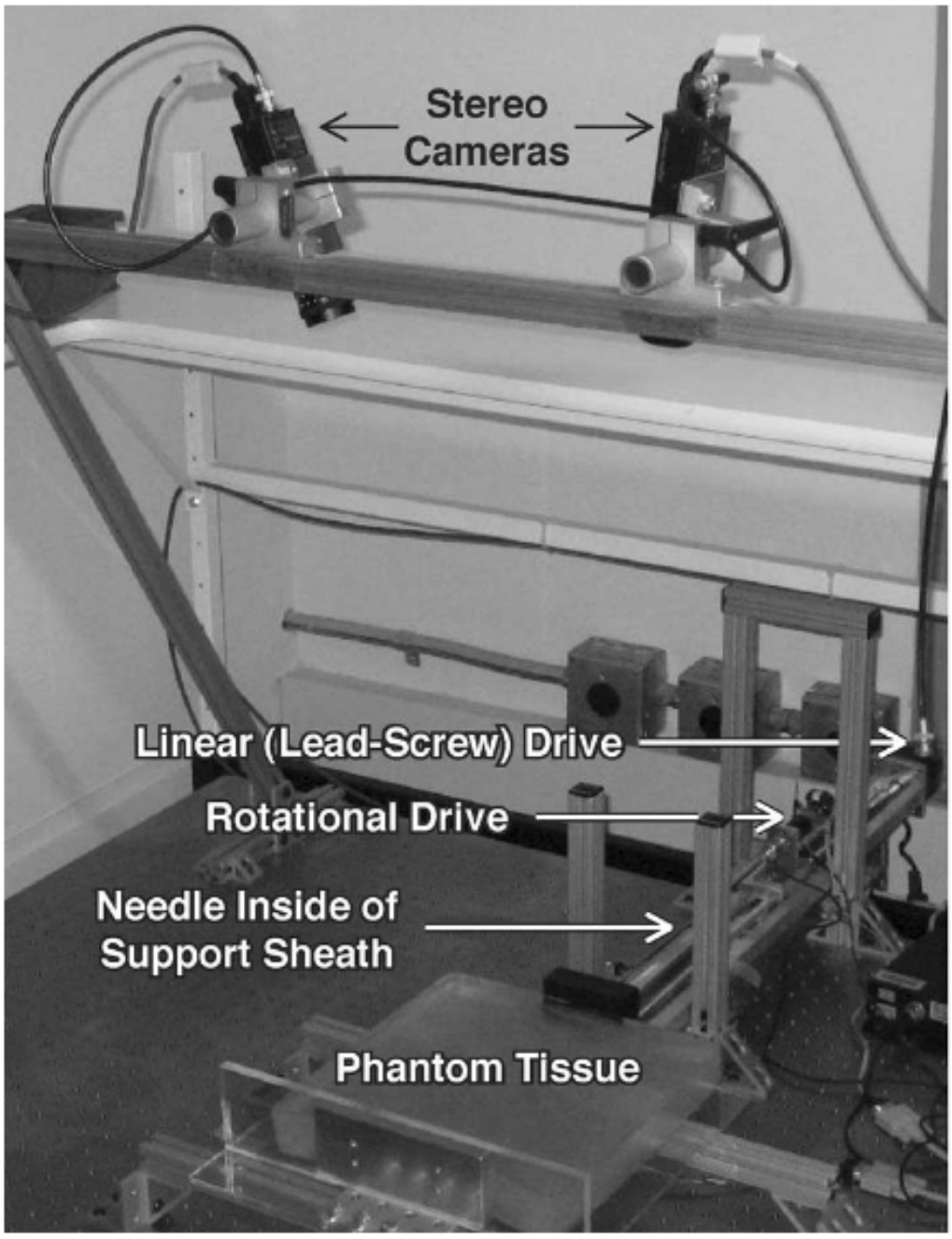

Figure 2.30: Needle steering robot with two stereoscopic cameras as observers and needle controller. "Reprinted, with permission, [92]"

of a sampling consensus algorithm (RANSAC) and dynamic region of interest algorithm to track the path of the needle. This method also innovated in terms of needle design whereby the needle body was modified to have a hollow section which echoes in response to the ultrasound scanning — this led to a disadvantage whereby the integrity of the

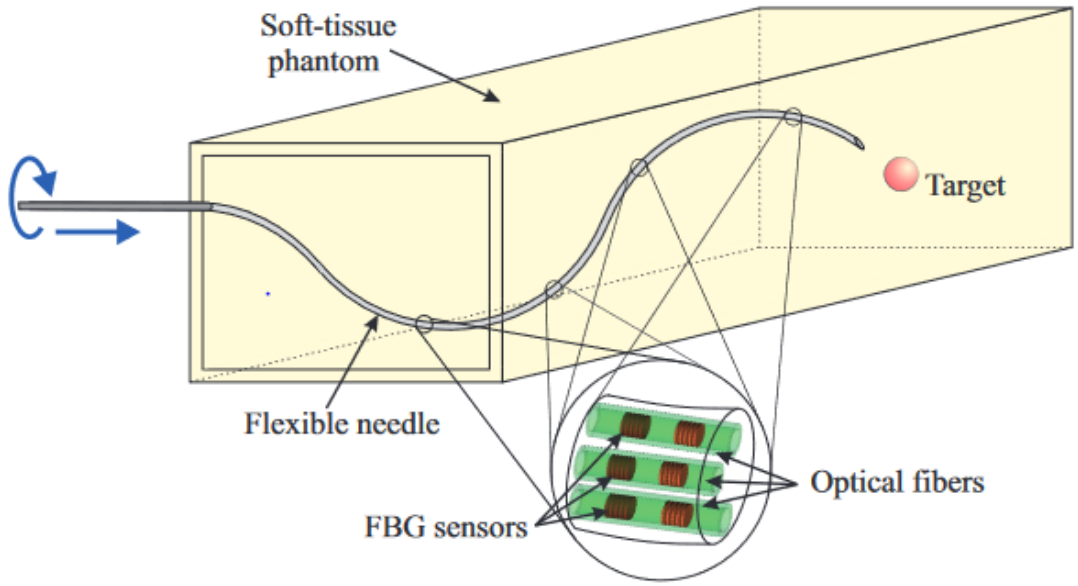

Figure 2.31: Twelve Fibre Grating sensors located on the needle shaft during insertion into a phantom body. "Reprinted, with permission, from [2]"

needle was particularly weaker and could be damaged during insertion [124]. Another strategy combines inverse kinematics, collision detection, RRT, and the theory of node addition to effectively plan an insertion procedure whereby certain high priority needle zones are identified and characterised through effective 3D scanning of the interested area [20]. This technique optimises the path of the needle using its vision system which streamlines the process tremendously. the development, however, of interfaces whereby the guidance systems can compensate for deformations, etc., with manual control are a crucial point to note and the most promising area of research for the immediate future. An operator may immediately intervene and offer 3rd party guidance to the controller to maximise the final accuracy, reliability and effectiveness of the insertion procedure into the body [215].

2.7.5 Flexible Steerable Needle Designs for Control

Until this point only the most common, traditional form of flexible steerable needles — bevel tipped — have been discussed. This is generally known as a *passive* type of steerable needles. Much research has invested into the development of more active needles where the needle tip itself is controlled as opposed to only the needle shaft in the case of the bevel tipped needle. This active control allows more refined control over the needle trajectory, but the complexity in the design and controller of these needles

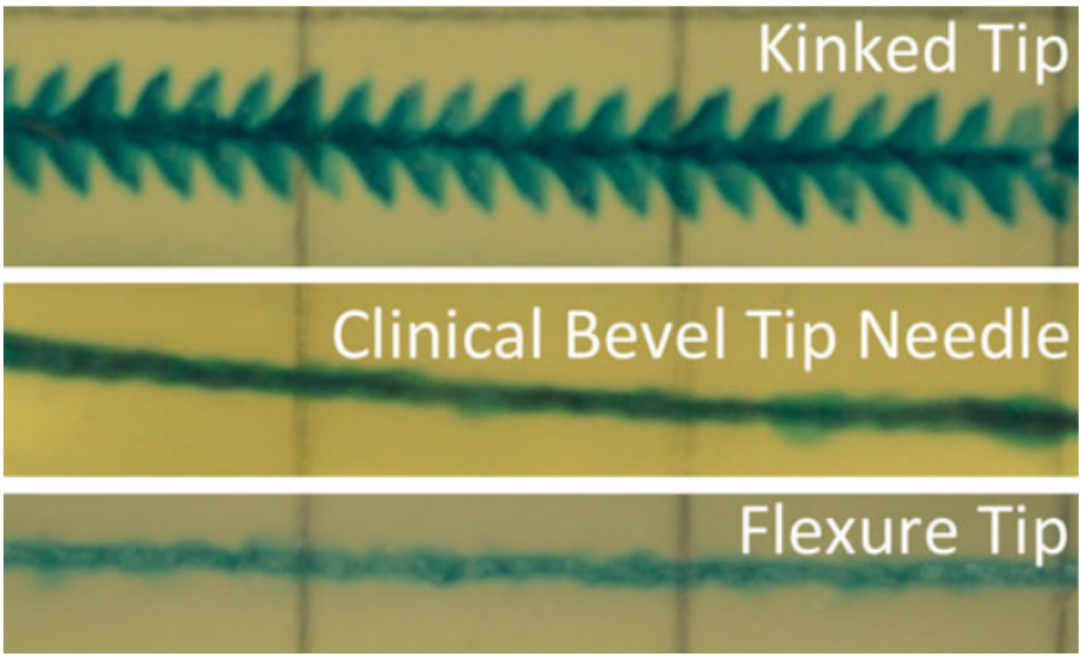

Figure 2.32: A comparison of needle types and their effects on the penetrated body. "Reprinted, with permission, from [199]"

are increased. A few examples of such *active* needles are: flexure needles, programmable bevel tip needles, pre-curved coaxial tube needles which may consist of nitinol wires, and continuum robot based needles [185, 39, 45, 58, 217, 200], see Figures 2.32, 2.33 and 2.34. There are some situations where these specifically designed needles are more advantageous than the traditional bevel tipped needle. These needles may provide more stable insertion paradigms, greater achievable curvatures and flexibility, the ability to reach more difficult targets in obscure areas, etc.

It is important to note, however, the difficulty in manufacturing more active style needles. In many cases, these needles are prone to being weak and may fail during usage. Additionally, their designs are often very complex, and they do not offer an obvious way to perform one of the most fundamental functions of a needle: extracting or depositing fluids from a body. Nonetheless, research in this area is promising, and future steerable needle devices may utilize complex needle designs to achieve this simple requirement.

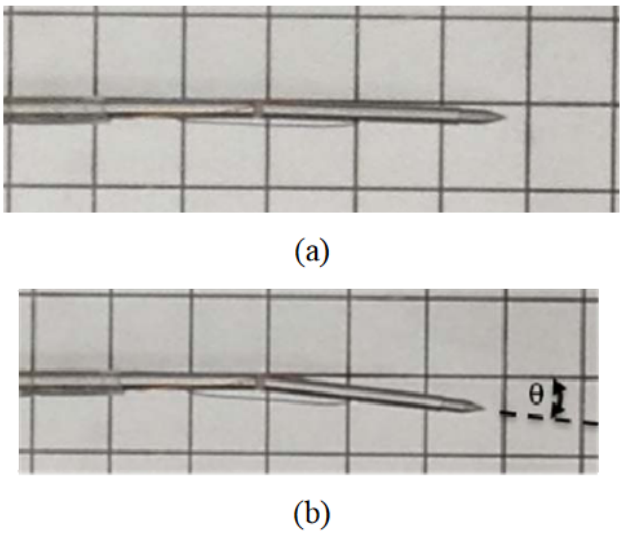

Figure 2.33: A flexure-based needle tip before and after actuation. The needle tip bends by an angle (θ). "Reprinted, with permission, from [45]"

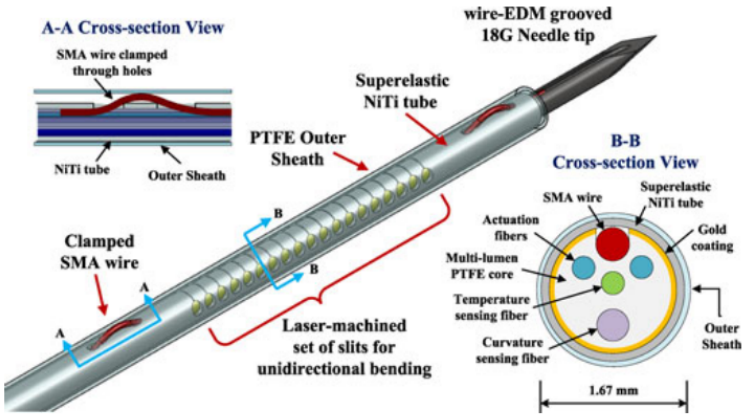

Figure 2.34: A cross sectional view of the design of an active coaxial needle. "Reprinted, with permission, from [182]"

2.8 Chapter Conclusion

This review identified the key factors associated with 3D / 4D printing fibres using bio-based polymers. It was, furthermore, investigated what processes and materials are involved in providing a "4D behaviour" to these bio-fibres through electroactivity. The elucidation of the relationship between the diverse scientific fields of study (which include Biotechnology, Additive Manufacturing, and Artificial Muscle Actuators) was the overall outcome of this investigation. While these fields are concerned with vastly different physics and chemistry details, there is significant overlap between them especially

when attempting to achieve the production of bio-based constructs. The identification of ionic and electric type EAPs, embedded 3D printing or FRESH, along with an investigation into the potential polymers suitable to effectively fabricate a bio-fibre, thus, provides a concise foundation from which further research can develop into their practical implementation.

Artificial muscles are highly versatile actuators with tremendous potential within multiple industries. Their fabrication and effective materials thus far have been limited to purely synthetic based or non-biocompatible polymers. There is wide potential within materials science research and the development of additive manufacturing techniques to fabricate more sophisticated artificial muscles in more complex fashions that can match or exceed the properties of natural muscle. Bio-inspired robotics with wearable devices and prostheses are becoming more common within day-to-day life and it is due to the rapid advancements within engineering, materials science, and robotics design.

It further identified an opportunity for the development of artificial muscles (electric or otherwise) utilising 3D printing techniques such as FRESH. Similarly, it produced an experiment whereby the basic principles and problems were tested and observed. These observations, namely the requirement of self-healing gel matrices to function as incubators for biomaterials, led towards the need for a minimally invasive process through which a biomaterial could be deposited, polymerised, and subsequently embedded internal to a pre-existing body (human, etc.). Steerable needles were, thusly, identified and investigated in terms of its primary fields of research. Motion planning, steerable needle control methodologies, and flexible needle design types were thoroughly defined in this chapter.

To review in summary, these fields remain highly theoretical in implementation and a high degree of research is required to make it feasible within medical environments. However, steerable needles have exciting potential as a minimally invasive technique through to enter a body causing the minimum amount of trauma possible to the body. Furthermore, steerable needles may effectively avoid obstacles and reach difficult targets using state-of-the-art path planning algorithms. Furthermore, in terms of the aims of this thesis, which is to 3D print bio-fibres which have responsivity, it becomes clear that steerable needles offer an interesting solution to this problem since, unlike other techniques such as FRESH which can produce organs in a petri dish, steerable needles could directly deposit biomaterials exactly where they are needed and even go a step further and provide a mode through which these materials could be polymerised into a fibre.

There are, however, enormous challenges in achieving these goals. The development of effective steerable needles using the current available technology notwithstanding these challenges. The primary problem of this thesis becomes one where a steerable

needle device or robot must be developed which could allow the inclusion of a means through which materials could be deposited as well as polymerised. This problem which has multiple sub-problems which include the development or implementation of a path planning algorithm and / or a custom control mechanism to include the deposition of non-trivial amount of biomaterial. Therefore, in order to achieve the greater aim of 3D printing artificial muscle fibres in vivo, this problem must be simplified into its constituent components. These components consist of designing and developing a steerable needle robot with 3D printing capabilities, implementing a path planning algorithm of any kind into this robot, as well as developing a means through which the aforementioned materials could be polymerised in place inside of a body. As a result of these multi-disciplinary challenges, this thesis presents a step towards these ultimate goals. Therefore, the hypothesis of this thesis is offered as:

> ***The generation or embedding of simple bio-fibres is possible using steerable needle technology and bio-based polymers.***

Chapter 3

The development of a steerable needle robot for 3D printing

3.1 Introduction

Time and times are but cogwheels, unmatched,
grinding on oblivious to one another.
Occasionally - oh, very rarely! - the cogs fit; the
pieces of the plot snap together momentarily
and give men faint glimpses beyond the veil of
this everyday blindness we call reality. —
Robert E. Howard

This chapter consists of investigating the design of a flexible steerable needle device or robot (bevel tipped or otherwise) for the application of 3D printing. It attempts to define the conditions for proprietary long injection needles (e.g., spinal tap needles) to be robotically steered within a body or medium to fabricate or "3D print" fibres at specific positions *inside of* a body. In other words, liquid polymers are injected in this body at an end position while the needle is reversing. This assumes that the body consists of a sufficient stiffness to keep the needle in place during its reversal.

The work in this thesis makes this assumption towards the development of an open-loop steerable needle system. Therefore, polymers or materials will then be polymerised and essentially drawn in the reverse of insertion for a specified length using ionic, photo-initiated, or any feasible alternative cross-linking mechanisms to form internally embedded fibres of certain characteristics and behaviours. An experimentation setup is presented here where the state-of-the-art in needle steering motion planning is used and pointed towards incorporating a liquid polymer injection procedure to enable polymerisation processes.

In order, therefore, to validate the hypothesis suggested in this thesis, it is necessary to define the contributions of the following chapters including this chapter. Since path planning algorithms are relatively well-established in computing workable trajectories and due to the fact that the primary concern is in the evaluation of the potential of steerable needles using polymerisable biomaterials, an open-loop feedback controller using a selected path generating algorithm is developed to integrate with a custom-built steerable needle robot with 3D printing capabilities. 3D printing capabilities in this respect is defined as: the ability to deposit a polymer (in any state — liquid, gel, etc.) and subsequently undergo polymerisation through any means possible.

This may result in a polymerisation process where a secondary, reactant polymer is added to the initially deposited polymer through ionic polymerisation. Other polymerisation strategies may include temperature, light, etc. Therefore, the robot that is designed henceforth is designed considering a liquid or gel injection system. This relates to Objective 1 as defined in the Introduction as is relevant to the proposed hypothesis.

For the phantom body in which polymers are tested using this "3D printing" technique, gelatine has been selected due to it being among the most common phantom bodies used in literature and due to its equivalent mechanical properties to human tissue and muscle. Furthermore, since gelatine has mechanical properties that allow for the straightforward analysis of the movement of bodies or projectiles within it, gelatine is prepared as the suspension medium for the fibres which it is attempted to print. Since it is already established in literature that the characteristics of the body which is punctured by a needle may cause certain deformations in both needle and body, it becomes necessary to evaluate this interaction in fundamental ways. A range of gelatine concentrations with different mechanical characteristics and their response to the steerable needle printing system is, therefore, also investigated.

Some key questions to consider in this development of a steerable needle 3D printer:

- How does needle length affect curvature when insertion speed is controlled?
- How do fibre characteristics vary when insertion speed and material type is controlled across various needle lengths and insertion depths, if at all?
- Can fibres be fabricated repeatably using predetermined chemistry and what are the optimum conditions?
- Does insertion speed and injection flow rate influence fibre characteristics
- How does needle type (bevel, etc.), length, and or gauge affect the potential for steerability and printability?

3.2 Background

To begin this chapter, a definition of steerable needles is proposed as a 3D printing technique, as outlined in table 3.1. The integration of steerable needle technology is explored with with additive manufacturing, which necessitates a clear understanding of the concept of steerable needle 3D printing. When attempting to reach a target within a penetrable or puncturable body, it is crucial to consider the process of polymerizing a material into a fibre and whether it can be deposited at the desired location and orientation.

Table 3.1: An application case for steerable needles utilised within 3D printing technology

Definition of Steerable Needles for 3D Printing		
Case 1	**Case 2**	**Case 3**
If a self-healing medium cannot be prepared (e.g., Foam), then it is necessary to minimize the damage to the surrounding medium as printing takes place	**If the path towards an end goal within a medium is obstructed and constrained**, then it is necessary to create a path of curves to reach that goal	**If a fiber of an arbitrary length and orientation is required in a specific location within a medium for any reason**, then it is necessary to create a path and draw the fiber in the orientation and length desired
A mechanism based around needle insertion is required to minimize this damage	A planner and controller is required to plot a path avoiding obstacles with feedback to reach a desired goal point	A relationship between the retraction rate of the needle and the pumping or drawing rate of the fiber in the "cavity" left behind
Steerable needles from the well-described percutaneous intervention technique suits this definition	Path planning is done through search-based algorithms, RRT, RCS, etc., while the machine controller interprets this path and implements the necessary motions to achieve it	**Option 1**: A liquid (or resin) injection system whereby polymerization occurs in the path to a goal point **Option 2**: A premade fiber (or wire) is inserted through the inner diameter of the needle and simply drawn and separated from the needle on retraction

3.3 Motion Planning for Steerable Needle 3D Printing

This section contributed towards a publication and presentation in The 2022 28th IEEE International Conference on Mechatronics and Machine Vision in Practice (M2VIP2022), see Appendix C.

3.3.1 Steerable Needle Setup

Previous research into steerable needles has revealed a wide selection of needle types with varying tips (bevel angle, etc.) and thicknesses which affect the manner in which

its steering mechanisms operate. Bevel-tipped needles are well known to curve along the direction of its bevel when it experiences a resistant force when penetrating a body of a certain stiffness and are the most commonly used needle in the medical percutaneous intervention procedure. Ultimately, it is the stiffness of a body which influences the maximum curvature over insertion length a needle of certain characteristics can achieve.

Alternatives to the bevel-tip [185, 199, 41] are consistently investigated and proposed to allow for greater curvatures over lesser insertion lengths in terms of tip design, material selection, etc. This work is primarily concerned with developing an approach to allow for any steering mechanism within the motion planning, control scheme, and 3D printer "setup". The only condition remaining is the requirement of an inner diameter of the needle to allow for the deposition of material once a trajectory is achieved.

Utilising the most critical research [218, 63] in steerable-needle-motion-planning techniques for resolving start to end-position trajectories within a medium, this work attempts to inject and polymerise a bio-material from end-position and along the path and for whatever length and in whatever orientation is arbitrarily desired by a user. Since there are limitations in the maximum curvature of long needles [148, 159], a model is developed to determine the maximum curvature and the conditions where an end-position cannot feasibly be resolved [63] using the proposed needle 3D printing system.

The needle path operates similarly to how a bicycle is ridden. Inserting the needle moves the bicycle forward. Rotating the needle reorients the front wheel of the bicycle. This causes the bicycle (or needle) to travel along the path that this reorientation radius specifies according to constraints. A reference transformation matrix between three frames is defined in terms of:

- The world to the needle tip
- The needle tip to the next point on the curvature path
- This consists of a rotational matrix and a translation vector

Controlling the motion of the needle tip in real space:

- Knowing the next position and orientation of the following point, the rotational angle and arc distance between positions can be deduced

Another key consideration of this work lies in the orientation in which a material is desired to be polymerised (a bio-fibre) along its trajectory from the end position. In other words, if the desired orientation of the fibre is a straight line from the end point to an arbitrary point along its trajectory, the trajectory must be tailored algorithmically to enable the reaching of the end position in a desired orientation.

3.3.2 Kinematics for 3D Printing

Fundamentally, steerable needle approaches are defined as non-holonomic systems (e.g., a bicycle) [218]. Inserting the needle forward moves the "bicycle" forward and when it is rotated the front wheel of the bicycle "reorients" and the path of the needle changes according to the expected radius of travel induced by this reorientation. The key variable in controlling steerable needles within a body is its maximum curvature(κ_{max}) which is dependent on the properties of the needle design and the body within which it is inserted. From a functional perspective of bevel-tipped needles, the direction of the trajectory changes as the direction the bevel is facing changes when axially rotated.

There are three main categories to any steerable needle kinematic problem: 1. The configuration space and the respective poses of both needle and body; 2. The control variables of the needle tip pose with respect to its desired motion trajectory; 3. The constraints associated with controlling the needle tip pose and motion within an electro-mechanical system for automation.

Configuration Space: Two spaces worthy of consideration in the path planning approach are defined. First, the pose of the tip of the needle at each iterative point within its trajectory ($\chi \subset S\varepsilon(3)$). Second, the regions in which the needle tip will travel or the 3D workspace ($W\epsilon\mathbb{R}$) which is sub-defined into goal regions (W_{goal}) and obstacles(W_{obs}).

Control Variables: Following the approach from [63], the control variables are further defined as: the starting pose or configuration (χ_{start}); the end goal pose (p_{goal}); the allowable tolerance ($\tau > 0$); the maximum insertion length(l_{max}); and the maximum curvature (κ_{max}).

Constraints: For simplicity, a sub-definition is presented below, of the behaviour of bevel-tipped needles with respect to the Pfaffian constraints (the constratins expressed in Pfaffian forms which involve the skew-symmetric matrix that encodes the non-holonomic constraints) associated with the non-holonomic model approach [218] for the purposes of 3D printing:

- Constraint 1: Straight lines are achievable when the axial velocity (rotation) > insertion velocity (insertion) — this is defined as continuous-motion.
  - Normally, a bicycle moves in straight lines when the front wheel is re-oriented and is kept stable but in this case the wheel must continually rotate at a velocity greater to that of the insertion velocity.
- Constraint 2: Curves are constrained through step-wise (start-stop) movements between orientation turns and insertion arc lengths — defined as position / step-based discrete motion, where other works have explored time-based discrete motion (e.g., duty cycling to achieve certain trajectories and end-positions [125]).

– In order to achieve a certain turn radius required by the motion planner, the front wheel of the bicycle has to turn a certain angle from its current position before moving forward (being inserted further).

Now, having defined a 3D workspace (i.e., the penetrable soft body) in terms of its dimensions and inner obstacles using CT scans, 3D scans, etc., it is then proceeded to define the behaviour of the needle within this workspace in terms of its κ_{max}. This is done to enable the motion planning algorithm to resolve a trajectory from χ_{start} and p_{goal}. It is suggested here that there are multiple approaches in order to solve this problem. 1. Experimentally measure the maximum curvature over insertion length using any measurement tools available (e.g., computer vision, high-spec. cameras). 2. Define a relationship between the rheological properties of the soft body and the properties of the needle to approximate κ_{max}.

Once this is achieved and a motion plan generated in terms of positional vector coordinates (the first coordinate is the start and the last is the goal coordinate) within the 3D workspace, the work can proceed to the overall control scheme which interprets these vector coordinates and calculates the machine code necessary to achieve each individual or discrete pose along the path of the motion plan.

3.3.3 Path Planning Approach

Motion planning for steerable needles is an area of intense study especially with regard to its primary applications within the medical field, since targets must be reached while avoiding critical anatomical structures within the body. Various methods [125, 210, 187, 57] in literature have been proposed recently to develop an optimal motion planning approach in order to avoid these internal obstacles while still feasibly reaching a target as quickly as possible along the shortest achievable path. These methods, however, are not necessarily able to guarantee a motion plan in finite time or at optimal cost.

A recent paper by [63] presents a run-time efficient motion planner based on RRT, AO-RRT, and Resolution Complete Search (RCS) that returns a motion plan (trajectory) within finite time while avoiding any internal obstacles. The algorithms proposed by this paper, for the generation of motion plans to enable the 3D printing of polymers internal to the trajectory achieved when a needle is experimentally steered within a body, is utilised to enable the motion planning of this work. The given algorithm takes a series of inputs such as the maximum curvature of a needle, a 3D representation of the environment with goal regions and obstacles, and implements a planner that utilizes point clouds and 3D visualization software to represent the coordinate data of a trajectory within the world reference frame.

This algorithm can be used to plan the motion of a steerable needle in a 3D environment, taking into account the maximum curvature of the needle and the presence

of obstacles. The planner uses the 3D representation of the environment to divide it into goal regions and obstacles, and then generates a trajectory that avoids the obstacles and reaches the desired goal regions while respecting the maximum curvature of the needle.

To represent the trajectory in the world reference frame, the algorithm utilizes point clouds and 3D visualization software. The point clouds represent the trajectory data, while the 3D visualization software provides a visual representation of the trajectory within the context of the environment. This allows for easy visualization and analysis of the trajectory, and can aid in verifying that the planned motion of the needle is safe and feasible within the given environment.

Generally, the world frame is recorded using MRIs, CT scans, or ultrasound to produce 3D coordinate data which represents the body that is to be punctured with a steerable needle. These techniques may also identify any obstacles of note within the areas that it scans. This is critically important to the path planning process. Once this body data is recorded, consisting of goal regions and obstacle regions, then set registration is performed which converts the body data into usable coordinate space. This coordinate space known as the world frame inhabits the allowable regions that the needle tip is allowed to travel. If the needle tip coordinates violate the area, then the path planner fails to generate a trajectory. The experiments presented in this thesis employ the approach proposed by Fu et al. to prepare and represent the body space. This approach is implemented using a combination of proprietary software such as SolidWorks, CloudCompare, and MeshLab.

The strategy developed by Fu et al. provides a systematic method to prepare and represent the body space for experiments. By utilizing proprietary software such as SolidWorks, CloudCompare, and MeshLab, this strategy can be effectively implemented. SolidWorks allows for the creation of 3D models of the objects of interest, while CloudCompare and MeshLab enable the processing and manipulation of point cloud data for further analysis.

By utilizing this approach and software tools, the body space can be accurately and efficiently represented for experimental purposes. This allows for the investigation of various characteristics and properties of the body space, providing insight into the behavior of objects within the space and aiding in the development of novel techniques for manipulation and control.

Before an output trajectory is generated there are two key control inputs that need consideration:

- The maximum radius of curvature or deflection over length that is available to the needle on insertion — units (mm/mm).
- The start and goal position coordinates with orientation (x-y-z, pitch, yaw, and roll).

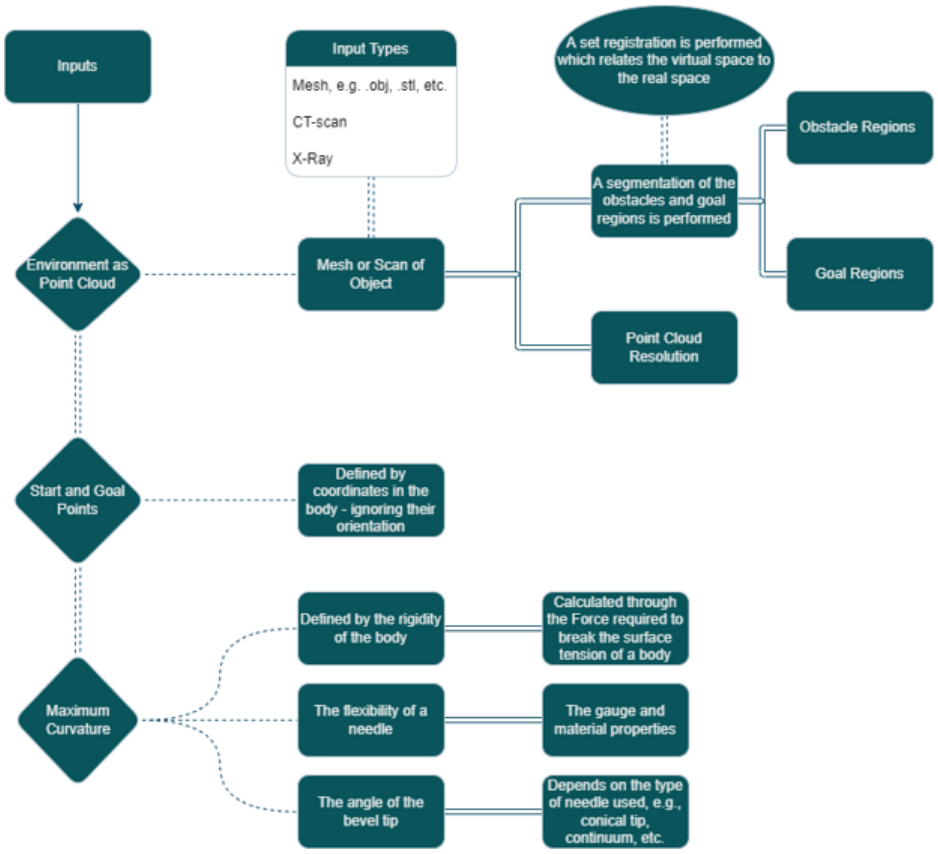

Figure 3.1: Input diagram detailing the input process towards steerable needle 3D printing

- The diameter of the needle.

From these inputs, the path planning algorithm uses one of its searching algorithms to generate a trajectory from the entry to the goal point while avoiding all obstacles between the two. This trajectory is generated into a series of points with specific position coordinates and orientations. Depending on the length of the trajectory path, many coordinate positions are produced as output. In order to utilise these coordinate position in the control mechanism of the steerable needle robot, they must be re-registered with the world frame after which they may be used in several calculations to determine the exact motions required by the robot to complete the path.

3.4 Control Scheme for 3D Printing

In order to effectively observe, continually track, and control a steerable needle as it punctures a body reference transformation matrix between two frames is defined: the current needle pose frame and the immediate next needle pose frame. This consists of a

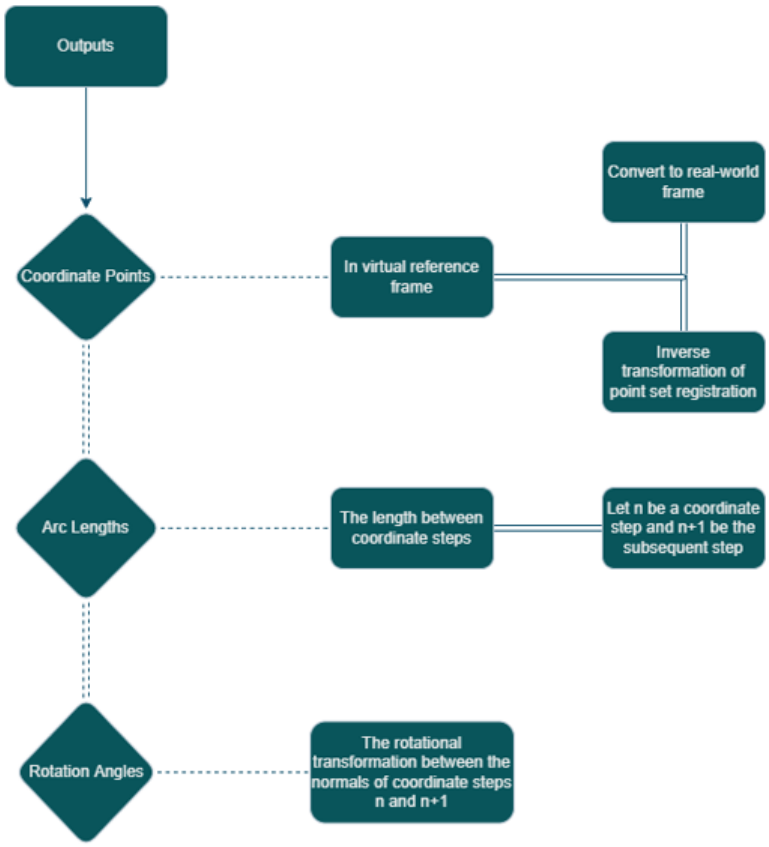

Figure 3.2: Output diagram detailing the outputs towards steerable needle 3D printing

rotational matrix and translation vector of these two frames on the motion path until the end position. By knowing these individual orientations, the rotational angle and arc distance between the current pose and the next pose can, thus, mathematically be calculated. This is done using unit-vector mathematics and trigonometric calculations. Hence, the motion is subdivided into individual paths from the current position to the next position (n -> n+1). The length between these paths can be considered to be 'arcs' and the angle between them can be calculated using the vector angle at which the next pose differs to the current pose. Referring to constraint 2, defined earlier, the needle tip must be at a certain angle in order to curve towards the position of the next pose. These arcs, therefore, have a certain radius of curvature if the next pose is at a different rotational position to the current.

Instituting this into our control scheme, the following may further be defined:

- Control Law 1: When there is no rotation between poses (angle = 0), then the arc between them is straight.
- Control Law 2: When there is rotation between poses (angle > 0), then the arc has a curvature as described by the highest possible κ_{max} possible over the arc

length.

- Control Law 3: Straight lines are achievable the rotation velocity (w) is equal to or greater than the insertion velocity (u) as a ratio (u/w) of pitch — linear distance traveled per radian of rotation. The curvature (κ) -> 0 across the insertion length at speed.

- Control Law 4: Curves are possible when the rotation velocity (w) is less than the insertion velocity (u), then the curvature (κ) tends towards κ_{max} across the insertion length at set speed according to the ratio.

In order to exemplify Control Law 3 and 4, we first attempt to calculate the linear velocity of the rotational drive by relating it to the radius of curvature we are interested in travelling by the rotational speed (times the pitch) + insertion speed of the needle base. In this case, however, since we want the radius to be 0 it would result in no rotational velocity at all. But there is a difference we must recognize, the rotational velocity of the base of the needle and the rotational velocity of the needle in the direction of its radius. We can only effectively control the base of the needle. But we know that the forces acting on the bevel tip will force the tip to travel in the direction of its angle if it does not rotate. The simplest way to understand this behaviour is to understand the behaviour of a screw. When a screw is inserted into an object, it is simultaneously rotated. This is represented by the linear distance traveled by the screw per radian of rotation known as pitch. Since forces will act on the bevel tip of the needle it will continually create "rotations" as it is inserted like the pitch of a screw.

Another analogy to this problem could be defined as follows: straight lines behave similarly to drills wherein the constant rotation results in a straight path, i.e., the needle tip is not given enough time to curve since the angle of the bevel tip is continually changed. Curves behave similarly to a bicycle in the sense that when the needle is inserted into the body, it only curves for as long as the "wheel" or bevel direction is in the direction that causes that turn, i.e., the rotational velocity is 0.

Therefore, the path planner generates a coordinate trajectory path that is then analyzed through mathematical manipulations to determine the precise motions required to transition from position n to $n+1$. For example, a trajectory with 44 discrete points must be converted into specific motion actions from position n to $n+1$. Since the controller proposed by this thesis is developed to act independently of time, a process is used where an arc is estimated between each discrete point. A Python script, see Figure 3.3 was written in order to handle the coordinate frame matrix transformation of these coordinate position as well as mathematically calculate the motor motions required to fulfil a path from the n to n+1 position — this path section is described as an arc where the entire trajectory is merely a sequence of arcs. This arc consists of a length and a

```
############ CALCULATE ANGLES - ANGULAR POSITION OF NEEDLE TIP
    ############
teeth = 30 #pulley teeth
pitch = 2 #mm
ratio = 5
motorangle = 1.8
micro = 16
step_distance = (teeth * pitch * ratio)/(360/motorangle * micro) #
    steps/mm or 40 steps per mm
#print(step_distance)
x_coords = np.empty(((len(pre_g)),1), dtype=float)
s_angle = 0
np.seterr(divide='ignore', invalid='ignore')
for x in range(len(pre_g)-1):
    unit_vector_start = traj_trans.normals[x] /
        np.linalg.norm(traj_trans.normals[x])
    #print(unit_vector_start)

    unit_vector_1 = traj_trans.normals[x+1] /
        np.linalg.norm(traj_trans.normals[x+1])
    #print(unit_vector_1)
    dot_angle = np.clip(np.dot(unit_vector_start, unit_vector_1),-1.0,1.0)
    angle = np.arccos(dot_angle)

    if (np.isnan(unit_vector_start[-1])) :
        angle = 0
    s_angle = angle+s_angle
    #print(step_distance)
    print(angle*180/3.14159265)
    print(s_angle*180/3.14159265)
    travel_distance = (s_angle*180/3.14159265)/motorangle * step_distance
    print(travel_distance)
    x_coords[x] = '{:.5f}'.format(travel_distance)
    #x_coords[x] = '{}{:.5f}'.format('X',travel_distance)
    #print(x_coords[x])
```

Figure 3.3: The python code which calculates the angle between two coordinate positions and performs a conversion into machine interpretable distance

rotational angle (or twist / bend) from the first position to the second position.

Since position n+1 is offset from position n in terms of its rotational orientation in 3D-space as well as a certain x-y-z distance, linear algebra is used to calculate the angle between the vectors of n and n+1. This angle equates to the dot product of the unit-vectors of these two positions. This angle which is calculated in radians is then further converted into degrees and finally into a number of the rotational steps of a drive shaft attached to a pulley, this is covered in more detail in the upcoming section.

Following the calculation of the total motor steps required to rotate the needle shaft an x number of degrees relative to the orientation of position n+1 to n, the total arc length is calculated that the needle tip must travel to reach n+1 which equates to the insertion length and hence motor revolutions. This distance is essentially equal to

the hypotenuse of a right triangle. Logically, if the number of position coordinates is increased, then the resolution with which this hypotenuse angle can be calculated will be more accurate in the final result. The arc lengths and angle changes associated with each coordinate position are recorded, and the resulting data is automatically converted into machine code (gcode). This code can be effectively interpreted by the controller board of the steerable needle robot, enabling it to precisely execute the motions required to follow the original trajectory path.

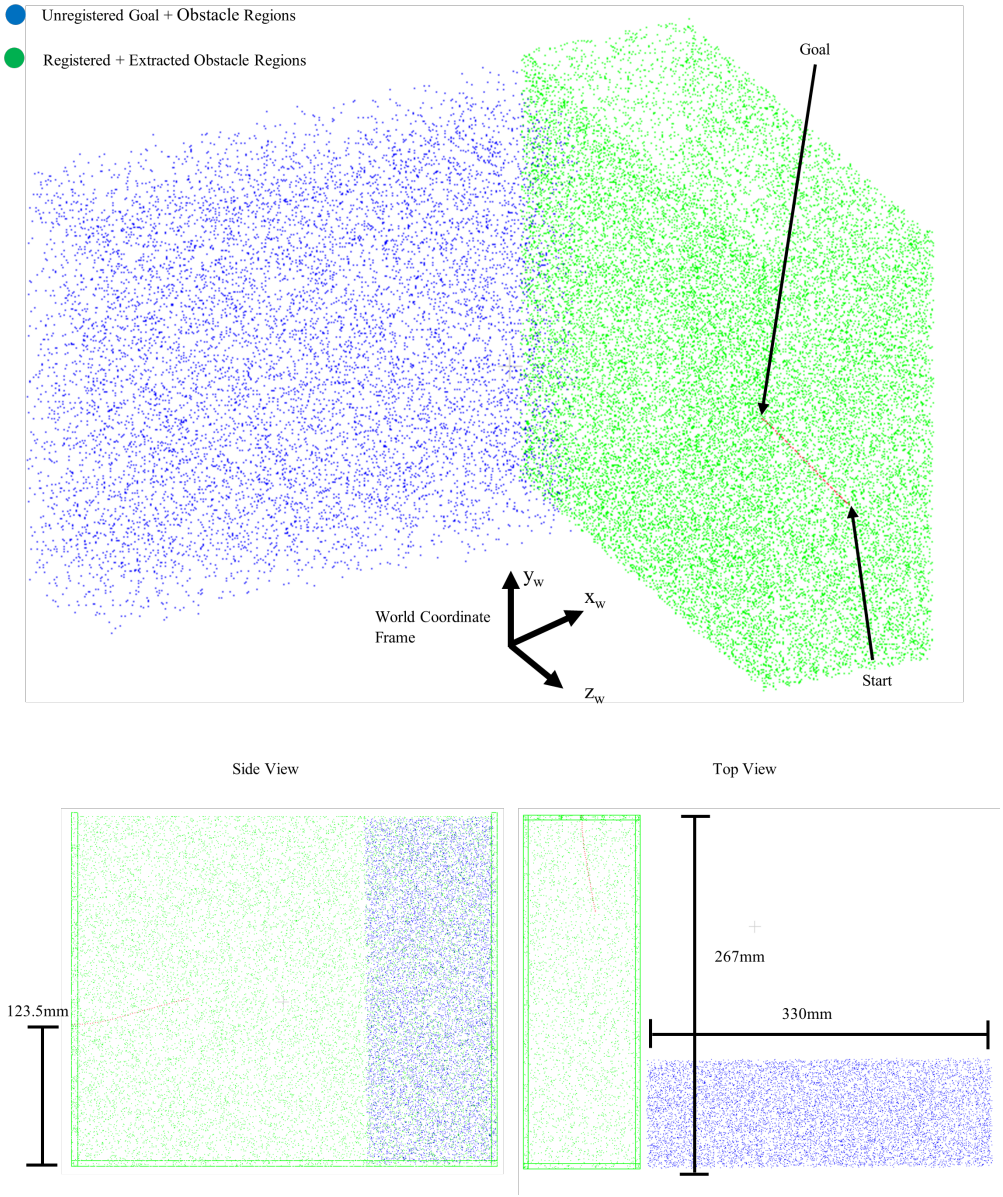

Figure 3.4: A visualisation of the gelatine phantom body with planned trajectory. The **Blue** points represent the entire (obstacles and goal regions) target body in the Real Space where it is not necessarily aligned with the steerable needle coordinate frame. The **Green** points represent the extracted obstacles of the body, that must be avoided by the needle. This body of points is now registered (or aligned) with the steerable needle coordinate frame. The **Red** points represent an example generated trajectory based on an entry coordinate position and a goal coordinate position, taking into account the needle parameters.

Table 3.2: Output trajectory coordinates from the RCM motion planner with input, where the Cartesian coordinates are x-y-z, and the vector coodinates Nx-Ny-Nz which represent the coordinates three-dimensional space. The Scalar value represents a colour-coding for recognisability when computed graphically.

x	y	z	Nx	Ny	Nz	Scalar
-115.871	139.202	-613.251	-0.603443	-0.716415	-0.0984383	-0.33603
-114.685	138.66	-614.767	-0.606876	-0.715867	-0.0894014	-0.333531
-113.527	138.095	-616.297	-0.610249	-0.715247	-0.0803556	-0.330999
-112.399	137.504	-617.839	-0.613561	-0.714556	-0.0713017	-0.328434
-111.3	136.89	-619.393	-0.616811	-0.713793	-0.0622407	-0.325836
-110.231	136.252	-620.958	-0.62	-0.712959	-0.0531735	-0.323205
-109.193	135.59	-622.534	-0.623127	-0.712054	-0.044101	-0.320542
-108.186	134.905	-624.12	-0.626192	-0.711077	-0.0350241	-0.317847
-107.209	134.197	-625.716	-0.629194	-0.710029	-0.0259436	-0.31512
-106.26	133.471	-627.319	-0.630403	-0.709773	-0.022584	-0.313537
-105.312	132.747	-628.925	-0.630339	-0.710128	-0.0233902	-0.312801
-104.365	132.027	-630.532	-0.630274	-0.710482	-0.0241964	-0.312064
-103.417	131.311	-632.141	-0.630208	-0.710836	-0.0250026	-0.311328
-102.468	130.599	-633.752	-0.630142	-0.711188	-0.0258087	-0.310591
-101.519	129.892	-635.364	-0.630075	-0.71154	-0.0266148	-0.309853
-100.57	129.189	-636.978	-0.630006	-0.71189	-0.0274209	-0.309115
-99.6208	128.49	-638.594	-0.629937	-0.71224	-0.0282269	-0.308377
-98.671	127.796	-640.211	-0.629868	-0.712589	-0.0290329	-0.307638
-97.7208	127.106	-641.83	-0.629797	-0.712936	-0.0298388	-0.306899
-96.7703	126.42	-643.45	-0.629725	-0.713283	-0.0306447	-0.30616
-95.8194	125.738	-645.072	-0.629653	-0.713629	-0.0314506	-0.30542
-94.8687	125.061	-646.696	-0.629988	-0.714158	-0.0315534	-0.303477
-93.9331	124.39	-648.332	-0.6317	-0.715293	-0.0292506	-0.297415
-93.0191	123.725	-649.982	-0.633383	-0.716395	-0.0269465	-0.291338
-92.1269	123.068	-651.647	-0.635037	-0.717464	-0.0246412	-0.285249
-91.2567	122.418	-653.326	-0.636661	-0.7185	-0.0223347	-0.279146
-90.4086	121.774	-655.019	-0.638256	-0.719502	-0.0200271	-0.27303
-89.5829	121.139	-656.726	-0.639821	-0.720471	-0.0177187	-0.266901
-88.7796	120.51	-658.447	-0.641356	-0.721407	-0.0154094	-0.26076
-87.999	119.89	-660.18	-0.642862	-0.72231	-0.0130994	-0.254608
-87.2411	119.277	-661.927	-0.644331	-0.723156	-0.0107556	-0.248532
-86.5057	118.671	-663.685	-0.645754	-0.723921	-0.0083412	-0.242632
-85.7928	118.072	-665.455	-0.64715	-0.724655	-0.00592641	-0.236721
-85.1027	117.48	-667.236	-0.648518	-0.725357	-0.00351136	-0.230801
-84.4354	116.895	-669.029	-0.649858	-0.726028	-0.00109616	-0.22487
-83.7909	116.317	-670.832	-0.651169	-0.726668	0.00131909	-0.21893
-83.1696	115.747	-672.645	-0.652453	-0.727276	0.00373428	-0.21298
-82.5713	115.184	-674.468	-0.653708	-0.727853	0.00614931	-0.207021
-81.9963	114.628	-676.302	-0.654935	-0.728398	0.00856407	-0.201053
-81.4446	114.08	-678.144	-0.656134	-0.728912	0.0109785	-0.195076
-80.9164	113.54	-679.996	-0.657304	-0.729394	0.0133924	-0.189091
-80.4117	113.008	-681.857	-0.658446	-0.729845	0.0158057	-0.183098
-79.9306	112.483	-683.726	-0.65956	-0.730264	0.0182184	-0.177097
-79.7987	112.336	-684.257	-0.65987	-0.730377	0.0189015	-0.175396

3.5 Steerable Needle 3D Printer

3.5.1 Definition

An electro-mechanical system (see Figure 3.5) is presented where three main modules are used to achieve the defined control scheme for the motion planning approach: **1. An insertion and rotation mechanism** whereby a long, flexible needle may be steered.

2. A computer vision camera system whereby the experimental results may be collected and the needle internal to the body monitored if it is not opaque. Furthermore, alternatives are being investigated within the current setup, such as ultrasound imaging, magnetic resonance, strain sensing, etc., to track the needle inside of an opaque body where cameras are unsuitable, for future experiments. This system is intended for use as a 3D printer whereas a material is "extruded" or deposited in place, it is polymerised in place. As such, 3D printable material would need to be identified and / or designed to conform to the constraints and intentions of this system, where, for example, photo-polymerisation is not effective when it needs to penetrate or diffract through a body.

3. An injection system and procedure which enables the deposition and polymerisation of a material *inside of* a body. It is this addition to the steerable needle system that defines the 3D printer capability, where the steerable needle is means through which to penetrate a body to deposit a 3D printable material.

3.5.2 Vision System

Thus far, multiple methodologies (which have previously been explored and defined) through which to track and quantify the motion of the needle within a body have been explored. To succinctly recap, these methods include: stereoscopic vision in the case of non-opaque bodies; Ultrasound or magnetic resonance; strain sensors and magnetism where the deflection of the needle has an electro-magnetic output in terms of strain.

The initial experiment approach involves the use of stereoscopic cameras to monitor the x-z (side view) and x-y (top view) planes, thereby allowing us to triangulate through measurement (computer vision, etc.,) the exact coordinate positions of the needle tip as it is inserted. The Intel RealSense^{TM} depth camera allows for effective tracking of the needle tip through its in-built calibration software, wide field of view, and associated real-time viewer which enables the recording and measuring of the needle tip. These cameras have proved, thus far, able to effectively track the needle tip and allow for relatively precise measurements along the x-z and x-y planes to validate the accuracy of the insertion mechanisms compared to the coordinates generated by the motion planning algorithms.

The accuracy of these cameras' coordinates is verified through their built-in distance

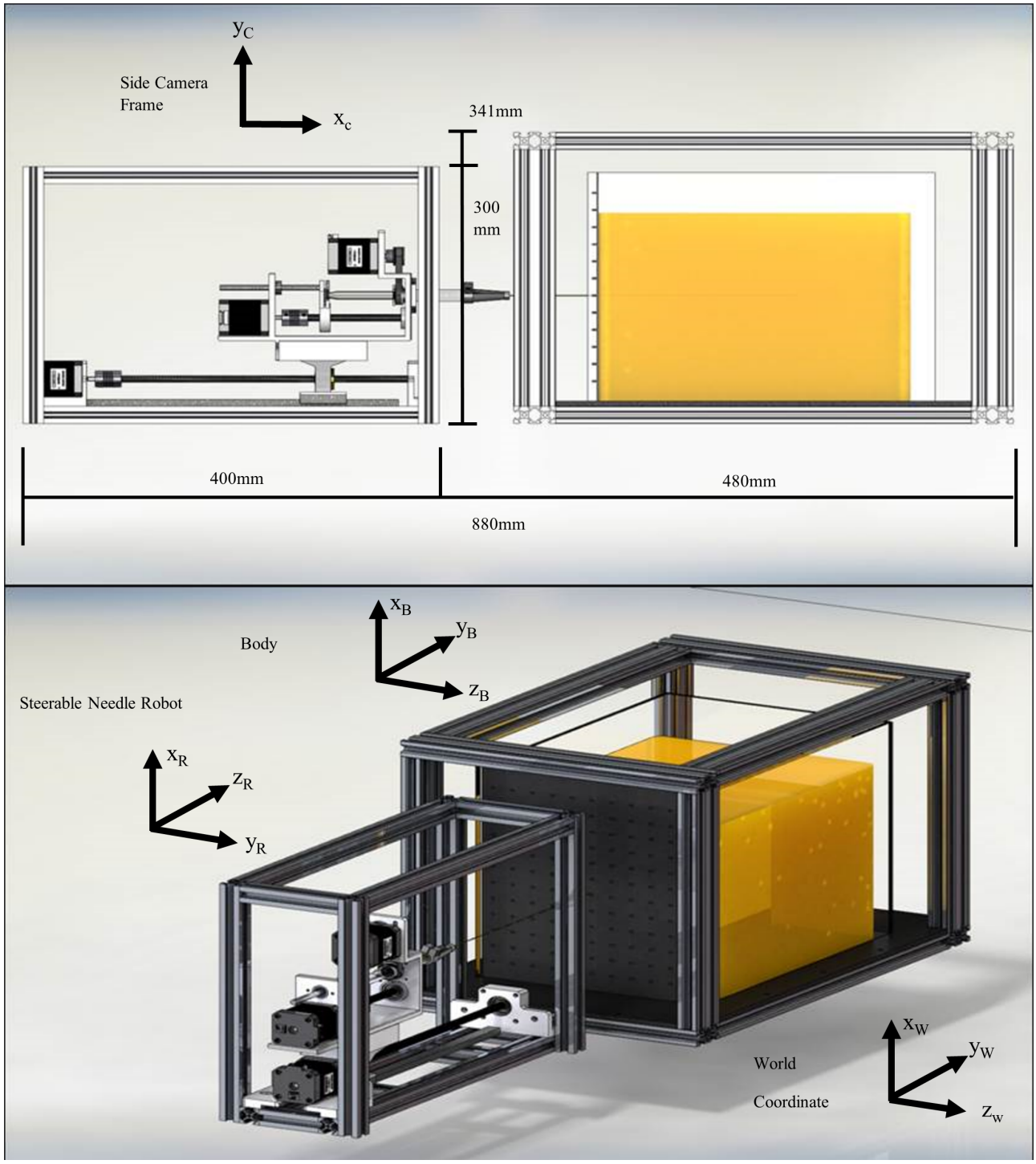

Figure 3.5: Steerable Needle 3D Printer with dimensions and the robotic coordinate frames

measuring capabilities, which are demonstrated by measuring the distance between the rear supporting frames of the body platform. This measurement, which is confirmed by

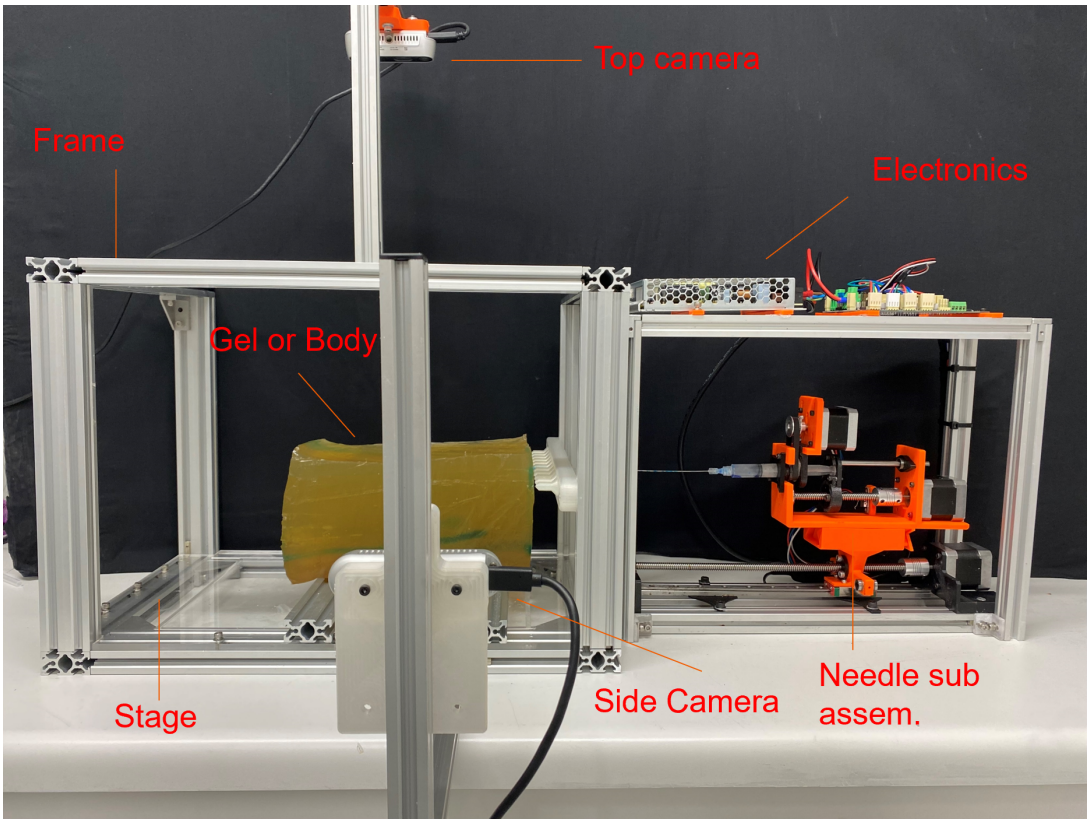

Figure 3.6: A view of the steerable needle 3D printer with all its respective components

a stainless-steel ruler, is 48.3cm. Consequently, this system is utilized to triangulate the needle's position within the gelatine body by measuring the distance between the needle tip and its entry point, which is a known coordinate location within the system.

Subsequent chapters will delve into two pivotal experiments that necessitate the utilization of the vision setup described in this paper. The first experiment entails measuring the maximum curvature of a 19G bevel-tipped needle, which is inserted to a maximum depth of 150mm inside a gelatine body that has been prepared beforehand. By analyzing the needle's maximum deflection curvature, a feedback loop is established into the path planning algorithms, which enables the creation of more intricate needle trajectories that can be simulated in 3D space. Consequently, a second experiment is proposed, which involves measuring, cross-referencing, and statistically analyzing the real coordinates from more complex motion plans, where the needle must navigate through intricate curves and twists to reach its intended endpoint.

3.5.3 Phantom Body

Since steerable needles involve penetrating a body to reach a distant position, it is necessary for experimentation purposes to prepare a suitable body that enables the

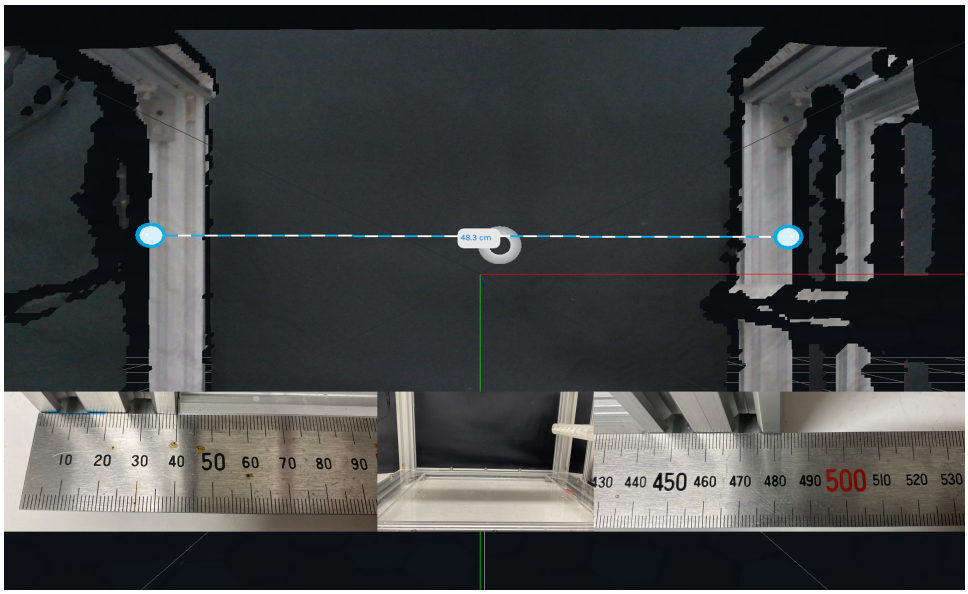

Figure 3.7: The calibration truth using the side-view Intel RealSense^{TM} camera

characterisation of our 3D printing system. Historically, gelatine is used for steerable needle testing, thus, moulds of 250 bloom type A gelatine are prepared for these experiments. The rheological characteristics (yield modulus, stiffness, etc.) of the body or suspension medium (in this case gelatine) have a direct relationship with the maximum curvature which a needle can reach at any given time during its insertion, see 3.6.

Therefore, it is speculated that such a relationship can be generalised depending on these rheological characteristics and thus the maximum curvature can be approximated without experimental testing to a satisfactory degree. For example, if the needle must travel through a body without the in-built capability to sense the stiffness or forces which will act on its bevel (thus affecting the maximum curvature) then at least knowing the rheological characteristics of the body through other means will allow the system to approximate as accurately as possible the necessary motions to incur and update the motion plan accordingly. This enables, potentially, the simplification of needle designs to allow for better 3D printing capability. In the case of the phantom body, the experimental setup specifically prepares the following: A stage area in which a body may be "locked into space" with definable and known entry points; a modular sheathing guidance frame translatable in the x-z axes to allow for a number of different entry points to the body, see Figure 3.8. A sheath is essential towards ensuring that the needle tip passes as close as possible to the needle entry point. For reference, entry holes of the sheath are 1mm in diameter, therefore an allowance of 1mm error at the entry must be considered. The phantom body, which is prepared as a solution of gelatine, is moulded into a custom-built transparent box (330mm x 110mm x 270mm) which allows

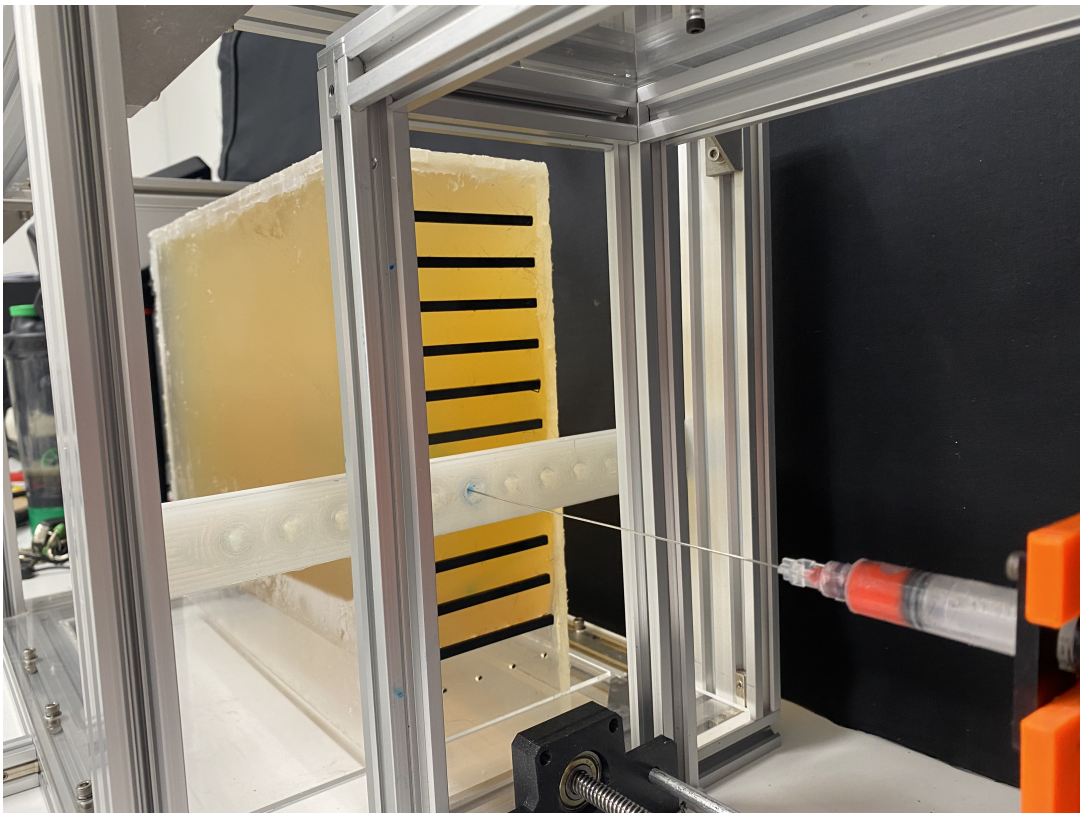

Figure 3.8: The phantom body stage, gelatine housing which is used the phantom body with resealable entry holes, and needle guidance sheath.

for the entry of the needle through a repeatably sealing system. The procedure through which this phantom is prepared will be discussed in more detail in Chapter 4.

3.5.4 Injection System and Procedure

The core of our research involves proposing a procedure through which a material may be polymerised using steerable needles. After reaching the end-goal position, the polymer is slowly deposited while the needle retracts, and since backwards motion has a mostly negligible effect on the needle (depending on the body characteristics), the needle will conform to the path it has already created. Through these means fibres can be effectively fabricated with certain characteristics and behaviours *inside of* a body, see Figure 3.9. The injection module consists of three essential axes: 1. the insertion axis or "z-axis of motion"; 2. The "y-axis" which pumps the attached syringe loaded with polymers; 3. the "x-axis" which controls the rotation of the needle shaft using a pulley mechanism which drives the trajectory that the needle takes. It is in the open-loop control of these axes that the trajectory generated by the motion can be fulfilled. These axes are assembled with NEMA17 motors and trinamic stepper drivers controlled by

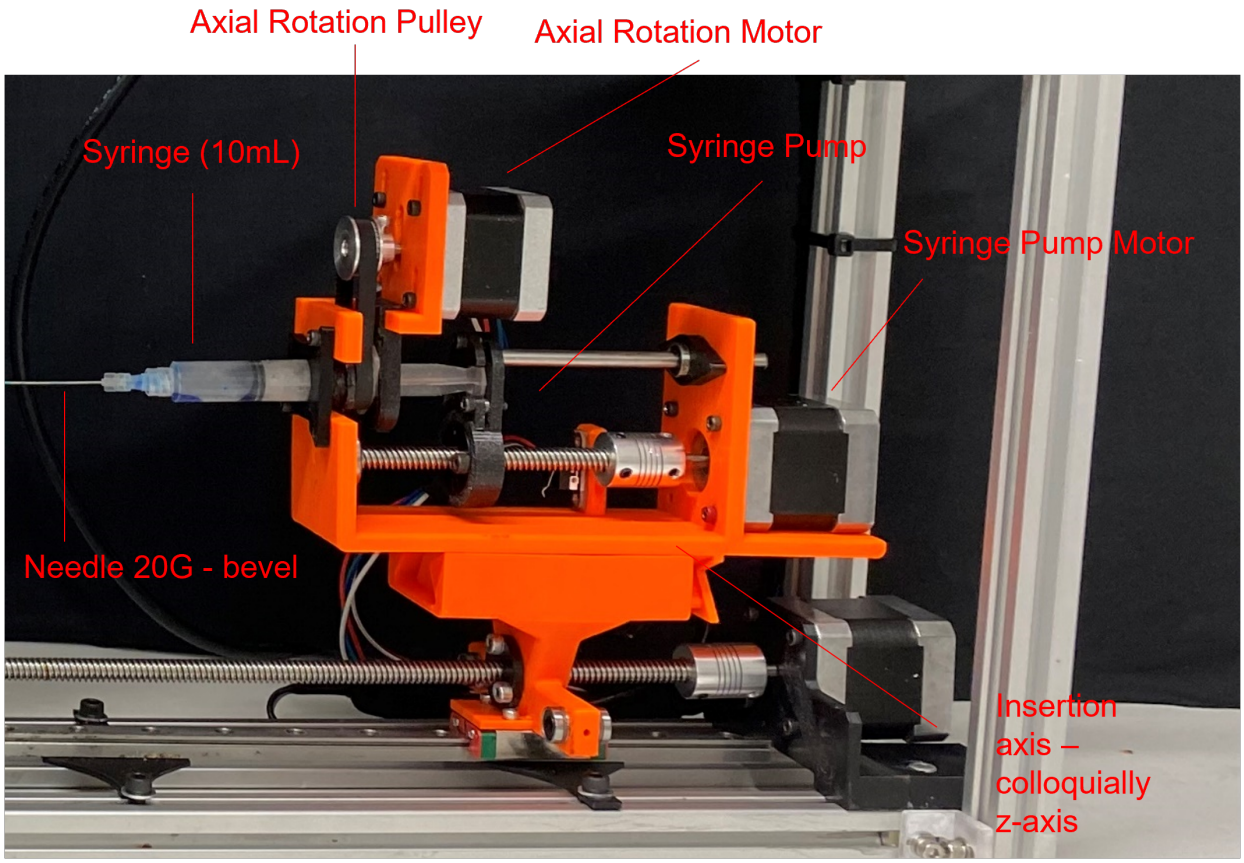

Figure 3.9: Designed Injection System for 3D printing polymers in the Steerable Needle 3D Printer

a DUET3D motherboard. For the purposes of injection, a general-purpose luer lock 10mL syringe is used which is fixed into an interchangeable locking mechanism for a syringe pump — the "y-axis". This axis has an actuation distance of 150mm through which the plunger of the syringe can travel at maximum 100mL.

Before the syringe is assembled into the system, a calibration procedure is initiated to align the axis. Upon completion of the homing process and storage of the current position, the axis automatically moves to a loading position. The syringe can now be securely fastened to the system with the plunger in an extended position, and filled with the desired liquid polymer for injection. Once the syringe is loaded, the needle is attached to the syringe's locking mechanism in a safe and secure manner. Due to the mechanical layout of the rectangular-shaped needle locking mechanism, a detection process is employed to ensure that the bevel-tip faces downwards. With the completion of this calibration step, the y-axis is now ready for needle steering, followed by the subsequent deposition and polymerization of the desired polymer.

3.6 Needle-Body interactions and strategies to account for body and needle characteristics

Numerous models have been proposed in the literature that aim to identify the deformation of body structures (such as skin, tissue, and muscle) as a needle punctures these areas. The ultimate goal of these models is to develop a feedback loop control system that enables the needle to adjust its movements based on its surroundings. [52, 14, 183, 124]. Such a system precludes the usage of sensor integrated needle designs such optical fibres, force-torque sensors, etc. For the purposes of the proposed robotic system in this thesis, such modifications to the needle presents several challenges towards depositing the less than perfectly liquid (bio)polymers — in other words viscous materials. These two key challenges include: Needle inner diameter w.r.t polymer viscosity; A closed-loop feedback controller which can continually update needle tip position such as those proposed in literature. Since, this thesis is concerned with proposing a flexible needle steering system with 3D printing capabilities, these challenges must be further defined and developed towards resolving them. Firstly, since no needle type could be identified in literature which suits the purpose of the proposed system, general spinal tap and other clinical needles have been selected which at least could deposit a polymer satisfactorily.

However, future work could investigate the design and development of a flexible steerable needle with sensing capabilities incorporated. Secondly, an open-loop system which has been presented in the previous chapters was developed to enable the testing and evaluation of the core research questions and hypothesis. While this system cannot at the time of writing continually update its position and account for different material properties along its, it can, however, through "pre-procedure or printing" prepare for such circumstances if the material properties could be accurately estimated. There are several challenges associated with this since, when a steerable needle is driven through the body the mechanical properties can differ vastly and is rarely perfectly homogeneous. This is another area which requires significant research and development.

Having defined these challenges, an opportunity is presented of a unique solution to the problem of material or body identification. Hyperspectral imaging is often used in overhead agricultural surveying technology to detect and offer insights into a wide range of information regarding the quality and yield of crops. This technique has in recent years pushed further ahead and is reported to even be able to classify samples at the molecular level. Often this is only used as a quality control measure, but this technique has been identified by this thesis as potentially capable of offering insights into the material type and properties of the phantom body or tissue that is to undergo steerable needle 3D printing [44, 170]. As a non-destructive, cost effective, time effective

analysis technique, it is, therefore, a promising avenue of research to further enable the goals of this thesis and account for the challenges previously discussed. By integrating machine/deep learning, this technique could be utilized to estimate the mechanical properties of bodily materials [156, 213].

Coincidentally and promisingly, hyperspectral imaging has reported use in several medical applications such as the diagnosis of diseases as well as image-guided surgeries, which according to literature is done collaboratively with other techniques such as ultrasound, etc. [116]. As an overview, hyperspectral imaging is defined as an analysis technique which uses a light emitting and receiving feedback system which can quantify the diffuse reflectance of samples [44]. It detects the reflectance quantified against the wavelength of light emitted ranging from ultraviolet to infrared. This multi-spectral data goes through further processing which can provide 3D spatial data from these 2D detections, known as a hypercube, of the sample that was scanned. These light interactions allow this technique to detect spectral differences, see Figure 3.10. This analysis technique is, therefore, suitably promising to enable steerable needle 3D printing as a control step during the total feedback loop. In other words, if hyperspectral imaging processes can accurately identify a certain material (gels, tissue, food, etc.) then it may through a database as well as certain further processing be able to estimate the material stiffness and therefore its interaction with a flexible steerable needle as it punctures this material.

Table 3.3: The spectral ranges of hyperspectral imaging

Name	Spectral Range (mm)
Ultraviolet (UV)	200–400
Visible	400–780
Near Infrared	780–2500
Mid Infrared	2500–25000

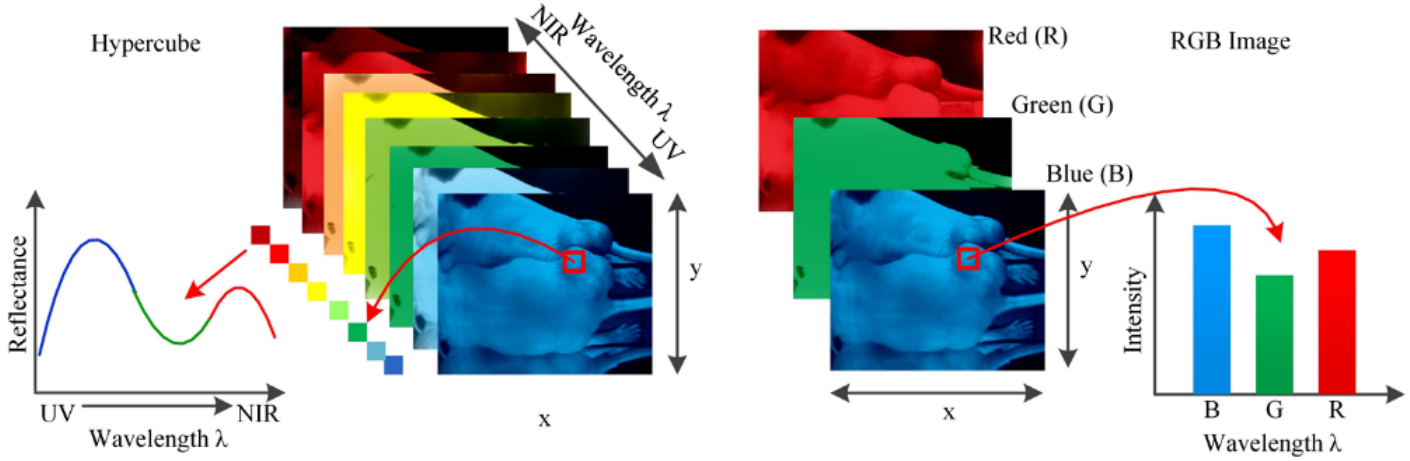

Figure 3.10: A comparison between the hyperspectral hypercube and simple RGB. "Reprinted, with permission, from [116]"

3.7 Using machine learning and hyperspectral imaging to identify and predict the mechanical properties of gelatine

To streamline steerable needle research by enabling the estimation of the maximum curvature of deflection of the needle, hyperspectral imaging as a technique is investigated through which to identify a material (such as gelatine) type and characteristics. Furthermore, the mechanical properties of gelatine is investigated through which to build a relationship between the hyperspectral results which is through machine learning able to identify specific concentrations of hydrogels (such as a simple example like gelatine) and their related mechanical properties in terms of yield strength, elastic modulus, etc. This section contributed towards a publication and presentation in The 2022 28th IEEE International Conference on Mechatronics and Machine Vision in Practice (M2VIP2022), see Appendix C.

3.7.1 Introduction

Hydrogels are three-dimensional network structures able to contain large amounts of water. They exist naturally in the form of polymer networks sourced from natural or synthetic polymers such as collagen or gelatine [35]. [160]. Environmentally sensitive hydrogels can serve a wide variety of applications because of their ability to respond to environmental changes typically by exhibiting changes in volume and texture [35, 121]. Analytes and biomarkers including glucose, proteins, and DNA also elicit hydrogel responses [224, 31]. Furthermore, these networks may be used as composites with other polymers to result in improved mechanical properties or other desirable characteristics which are not inherent to them, such as the capability to be 3D printed [160]. Because of such a wide variety of response triggers, hydrogels can be incorporated into sensors or actuators, or can be utilised in controlled drug delivery systems, biosensors, tissue engineering scaffolds, artificial organs, wound healing bandages, physiological membranes, contact lenses, and microfluidic valves. Further, natural polymers have received attention for agricultural applications for their excellent biodegradability, biocompatibility, bioactivity, and hydrophilic character [91].

However, one of the most challenging issues during functional manufacturing of hydrogels is to ensure that the active components can maintain their structural stability during storage using it for various aforementioned applications. The mechanical properties described by its stiffness or otherwise (non-)elastic behaviour quantify the deformation of hydrogels at compression and shear, being correlated with their consistency and density.

Mechanical testing involves physically subjecting a hydrogel to tension, compression,

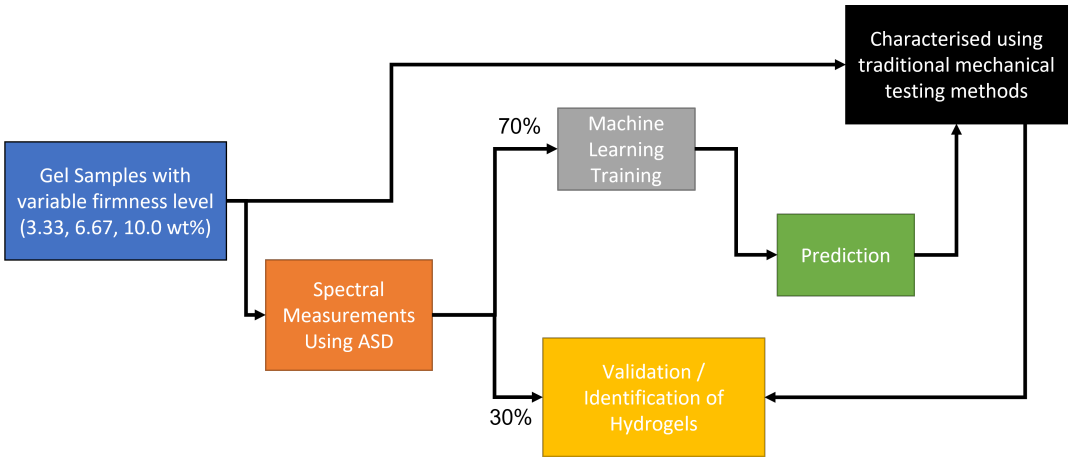

Figure 3.11: A diagram describing the HSI identification processes.

indentation, shear rheometry, etc., which may destroy the sample. Alternatively, non-destructive techniques such as direct permeability which measures a flowing fluid through a gel at a known rate measuring the pressure or chromatography or light-scattering which are used to indirectly relating using mechanical estimate from certain characteristics such as a sample's relationship between its molecular weight and concentration. The primary goal of these destructive techniques is to build a response profile of a hydrogel (or otherwise) in terms of its mechanical characteristics to certain stimuli. For example, shear rheometry or frequency-based testing can describe a sample in terms of its viscoelastic response (e.g., storage and loss modulus). While non-destructive techniques offer deeper insight to molecular and chemical properties such as performed by the light-scattering technique [152]. There is, however, a desire for non-destructive mechanical characterisation of hydrogels with good accuracy and precision that could be used to build a deeper understanding of the direct relationship between molecular and mechanical properties, see Figure 3.11.

In general, spectroscopy is the study of electromagnetic radiation and its production from or its interaction with, matter [111]. More specifically, HyperSpectral Imaging (HSI) records the so-called spectral profile of an underlying object in hundreds of narrow contiguous spectral bands, which is used to characterise objects provided the objects are spectrally distinct [120]. A spectral profile that includes all spectral bands is highly accurate because it takes advantage of the physical relationship between an object and the electromagnetic radiation it absorbs, scatters, or emits. This relationship is based on the fundamental principle that objects interact with electromagnetic radiation in a specific way, which is determined by their material properties and surface characteristics. By analyzing the complete spectral profile, researchers can gain valuable insights into the composition and structure of objects, which can aid in a wide range of applications, such as remote sensing, medical imaging, and material analysis. The

accuracy of the spectral profile is further enhanced by advancements in technology, such as hyperspectral imaging, which provides even higher resolution and more detailed spectral information. [166]. However, the accuracy tends to fall for complex scenarios, for instance, characterising similar types of samples for texture analyses. It is because each such sample comprises similar spectral characteristics, the performance of spectral characterising is fundamentally challenging due to the curse of dimensionality [174]. In recent years, advances in machine vision increased our understanding of underlying patterns from complex features [225].

Thus, in this chapter, a novel approach is proposed which attempts to combine the physical principles of HSI with machine learning by utilising the physical spectral characteristics of the underlying surface. This work aimed at developing a fast and reproducible method using spectroscopy and machine vision to provide deeper insight into the mechanical properties of hydrogels. In contrast to destructive sampling, spectroscopy offers a rapid and non-destructive alternative to accurately determine the properties of hydrogels.

3.7.2 Materials and Method

Generating Training Set

Three samples of 250 bloom 20 mesh gelatine (GELITA Australia Pty Ltd) of the following concentrations — 3.33%, 6.67%, and 10% were prepared. These 150 mL samples were produced by mixing the respective concentrations of gelatine powder in cold water which were left to 'bloom' for 15 minutes. After which, the gelatine is heated to 60°C and immediately poured into containers. The samples are then cooled at 2°C for 24 hours at which point they are ready for analysis.

Spectral measurements

The spectral measurements were collected using an ASD FieldSpecPro (Analytical Spectra Devices, Inc., Boulder, CO, USA) using an ASD FieldSpec 4 Hi-Res (Malvern Panalytical Ltd., Malvern, United Kingdom) measuring spectra in the 350 to 2500 nm range. In the VNIR region (<1000 nm), the instruments comprise a 512-element silicon photodiode array to provide the spectral resolution of 3 nm and a sampling interval of 1.4 nm, see Figure 3.12. In the SWIR region (>1000 nm), the instruments comprise two sets of thermoelectric (TE)-cooled indium gallium arsenide (InGaAs) photodiode arrays and provide the spectral resolution of 10–12 nm and 8 nm for ASD FieldSpecPro and FieldSpec 4 Hi-Res, respectively with the sampling interval of 1 nm. To limit the sampling uncertainty, a total of 30 spectral measurements were captured by randomly changing the location of the probe within the sampling area, see Figure 3.13.

Figure 3.12: The ASD FieldSpecPro

Figure 3.13: The measuring of the gelatine spectra using the ASD

Spectral pre-processing

Spectral pre-processing is an essential step to remove noise from the data which might affect the model performance. Further, low signal to noise ratio regions (350–400 nm and 2450–2500 nm) were excluded from the analyses. As derivative transformation helps to determine the location of the spectral absorption features and to reduce the finer scale noise [208], first derivative transformation was applied on the reflectance data using a Savitzky–Golay filter with a smoothing window width of 13, polynomial order of 3 and derivative order of 1.

Model development

Gaussian distribution is the basic building block of Gaussian processes [169]. With Gaussian Process Regression (GPR), which evolves from a family of Bayesian framework, the multivariate case of Gaussian distribution (defined by a mean vector and a covariance

matrix) at discrete points can be derived. The discrete points are called test points. The objective of GPR is to learn the underlying distribution of test points together with training data as a multivariate distribution. In order to perform regression on the training data, Bayesian inference is used to condition the probability distribution with test and training dataset, which is also distributed normally.

Regression via supervised learning

With the above basic framework of GPR, the important question is to define the mean and the covariance matrix. The covariance matrix is determined by its covariance function, which is often also called the kernel of the Gaussian process. Thus, GP is also known as kernel-based machine learning algorithm, where the kernel parameters are determined by the choice of covariance/kernel function, as well as the data used to make predictions.

A GP assigns probability distribution over a set of possible functions that fit the input data and converts them into posterior probabilistic estimates [169]. GPR also facilitates prediction uncertainty with a simple relation between covariance of train-test data and test-test data to estimate mean of the predictions. Using that the standard deviation and confidence intervals around the predictions could be estimated to reflect the complex distribution of nonlinear relationships in the data.

A non-parametric Gaussian process model is specified as:

$$p(f(x)\theta) \sim gp(0, k(x, x^{'}) + I \cdot \sigma_y^2 \tag{3.1}$$

where x is the input training spectra, $k(x, x^{'})$ is a kernel matrix to approximate covariance function, which can be implemented with variety of functions and σ_y is Gaussian noise. It was found that the automatic relevance determination (ARD) squared exponential function as a useful kernel to extract gel firmness from spectra. The model hyperparameters were optimised using a gradient based optimisation algorithm that maximises the marginal likelihood in the training data [165, 11, 169].

A GP assigns probability distribution over a set of possible functions that fit the input data and converts them into posterior probabilistic estimates [169]. GP also facilitates prediction uncertainty with a simple relation between covariance of train-test data and test-test data to estimate the mean of the predictions. Using that the standard deviation and confidence intervals around the predictions could be estimated to reflect the complex distribution of nonlinear relationships in the data.

Feature selection

Hyperspectral spectra comprise of hundreds of spectral features, however, not all of them are informative. In this section, important absorption features were observed as predominantly located in the visible-near infrared region (VNIR) (400–1000 nm). Further, a few weak features are present in the short wave-infrared (SWIR) region (1000–2500 nm), representing higher overtones of SWIR absorption. Thus, full spectra were used to develop the model. These knowledge-based spectral features emphasise the expert knowledge and sensitivity of each spectral band to sample texture characteristics as a tool for representing beliefs held by an expert.

Implementation

A GP learning model was developed using Python (v3.6.2; Python Software Foundation, 2019). The spectral dataset from each sample was combined and divided randomly into training and test in a ratio of 70% and 30%, respectively. Further, since the statistical performance of a model developed on empirical data to another dataset is challenging [61, 68], the generalisation performance of the model was further validated on an independent dataset. The independent dataset was collected on three different samples and not used to train the model.

Accuracy evaluation

The confusion matrix, also known as the error matrix, was used to evaluate the performance of the GPR classification model on the set of test data.

3.7.3 Results and Discussion

As the database contains three types of hydrogel samples (Fig. 3.14), it was noticed that a large variation in spectra within the 350-–1100 nm spectral region, whilst a low variation was observed in the 1100-–2500 nm region. Thus, a 350-–1100 nm spectral region was used to develop the model. In total 90 samples were measured for each firmness level. Further, using the statistical resampling technique 100 more samples were created.

From the confusion matrix results shown in Fig. 3.15, it is clear that in terms of accuracy, the GPR achieved >90% accuracy, which can provide relatively good performance compared to other traditional methods of measuring the gel firmness. For the efficiency side, it is apparent that once the prediction model was developed, the speed of prediction was good and not necessarily proportional to the amount of data. For example, when the number of test samples was increased by a factor of three through statistical sampling, the fraction of time taken to predict the extra samples

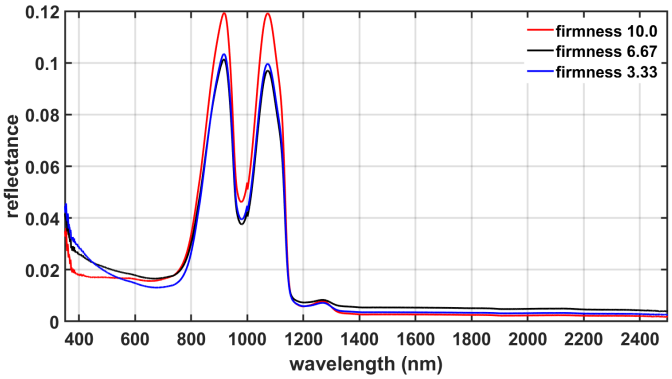

Figure 3.14: Mean reflectance spectra of the three types of firmness are shown

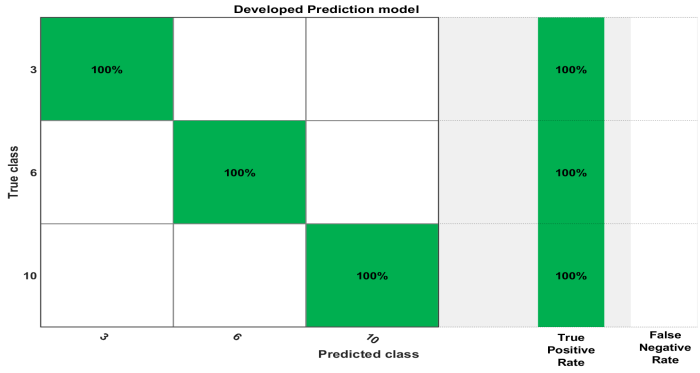

Figure 3.15: The confusion matrix of the GPR classification model on the test samples

is indifferent. Thus, repeatability of the prediction is easy to achieve. Finally, based on the above experimental results, hyperspectral data with machine vision can achieve better performance on this targeted problem.

Like any other material, hydrogels absorb, reflect, and emit the radiant flux received per unit area (irradiance). These physical principles are used to differentiate firmness of hydrogels to offer a cost-effective and non-destructive tool to gauge hydrogels' firmness. An estimation of hydrogels' firmness using hyperspectral data is reliable and extremely accurate because it utilises a physical relationship between hydrogels surface and its spectral absorption features i.e., a set of narrow and contiguous bands with low noise that are sensitive to hydrogels characteristics. When considering the widely used spectral range of 400–2500 nm, hydrogels related absorption features predominantly located in the visible-near infrared region (VNIR) (400–1000 nm). Further, a few weak features are present in the short wave-infrared (SWIR) region (1000–2500 nm), representing higher overtones of SWIR absorptions.

Recently, machine-learning algorithms (e.g., random forest regression (RFR), support vector regression (SVR) and Gaussian Process Regression (GPR)) extended their usefulness to estimate firmness of organic materials. However, their performance depends on the quality of the spectral data, which is influenced by the pre-processing techniques and the number of samples. Higher accuracy compared to the studies over other organic materials was observed [32, 165, 234]. This might be because fruit firmness was influenced by multiple complex physical factors (e.g., cell structure, skin thickness, turgor pressure) and chemical (e.g., pectin concentration, water content) whereas variability in the distribution of firmness within a sample of hydrogels is small which does not impact the relationships between firmness and near-surface spectral characteristics. In addition, the measurement of firmness used as training dataset is not prone to higher error values, making it less challenging to obtain accurate firmness readings of a sample.

Further, model uncertainty describes how well a model fits the data under given variable conditions and this can be apportioned into different sources i.e., perturbation in the spectral and reference sampling, instrument noise and statistical model parameters [165]. Water content and ageing of the sample is one of the major factors that obscures the chemical absorption across the full range spectrum. Sensor spectral quality and viewing angles is another predominant factor that influences the hydrogel spectral characterisation. However, it is observed that the model could predict well under these variations i.e., could differentiate in the firmness level due to the aging of the sample, which shows the robustness of the model. This information is critical in machine learning based modelling studies to evaluate model reliability.

Ultimately, this model could be used in the context of the 3D printing steerable

needle robot as an identification mechanism through which an unknown body could be identified through its measured reflectance. This estimate can be mathematically related to the expected mechanical properties of the body and, hence, to the expected behaviour of the needle as it travels inside of that body. The next section explores the mechanical properties of gelatine for an investigation into this potential.

3.8 The mechanical properties of gelatine utilising various testing techniques

3.8.1 Introduction

This section presents a step towards specifically exploring the mechanical characteristics of gelatine through which to relate the HSI machine learning that was previously proposed. It explores a range of gelatine concentrations, each with a distinct spectral response, as well as mechanical characteristics. Therefore, to serve as a database from which to test the HSI processes as well as the future results of the proposed steerable needle robot.

Furthermore, two separate analysis techniques were completed, namely: a quasistatic examination of gelatine under compression using a dynamic mechanical analyser (DMA); and the characterisation of gelatine using rheometry to investigate the linear viscoelastic region to acquire thereby the shear modulus through which to calculate the Young's modulus. These analyses were completed (similar to the experiment in the previous section) using a range of gelatine concentration — 3.33%wt, 6.67%wt, 10%wt, and 15%wt. The key variable of interest to note in these experiments is the resulting Young's modulus which can further inform the behaviour of the flexible steerable needle as the robot inserts it into the phantom body (gelatine or otherwise). It is in the effort to develop a system where hyperspectral analysis may be used concurrent with a steerable needle robot in order to accurately estimate the curvature of the needle as it travels through a body that the following work is presented.

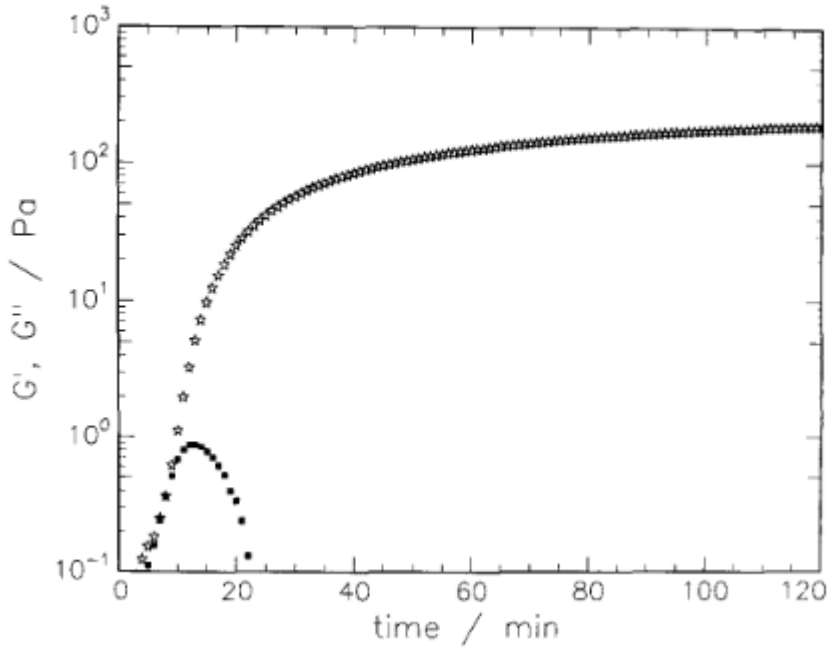

Figure 3.16: A curing curve noting the Storage and Loss Moduli for a 3.8%wt gelatine sample. "Reprinted, with permission, from [179]"

3.8.2 Background

There are numerous studies which investigate the mechanical behaviour of gelatine gels due to the wide variety of applications in which they can be used — primarily in the food and medical industries. To establish a benchmark for the experiments and to provide a basis for comparison with prior studies in similar domains, several papers examining gelatine will be referenced. Specifically, previous research has investigated gelatine using rheometry, a method that is replicated in this section using the specific type of gelatine employed in the steerable needle experiments [211, 179]. Furthermore, research has been done into characterising gelatine using static or quasistatic compression to analyse gelatine blocks or cubes for the stress-strain curve to determine the mechanical properties [60], see Figure 3.17. Further research investigates the rheological properties which include viscosity, etc., but for the purposes of this thesis, the focus will be constrained to rheometry and mechanical testing to allow for the further development and integration into the proposed steerable needle robot.

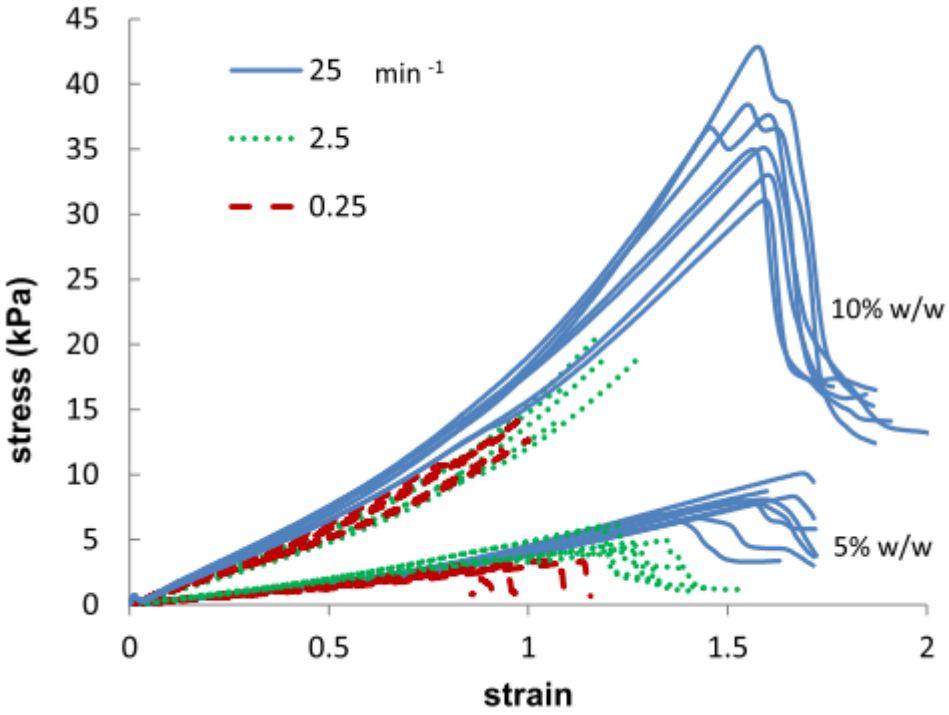

Figure 3.17: The compression stress-strain curve for 5%wt and 10%wt at different strain rates. "Reproduced from [60] under the Creative Commons Attribution License"

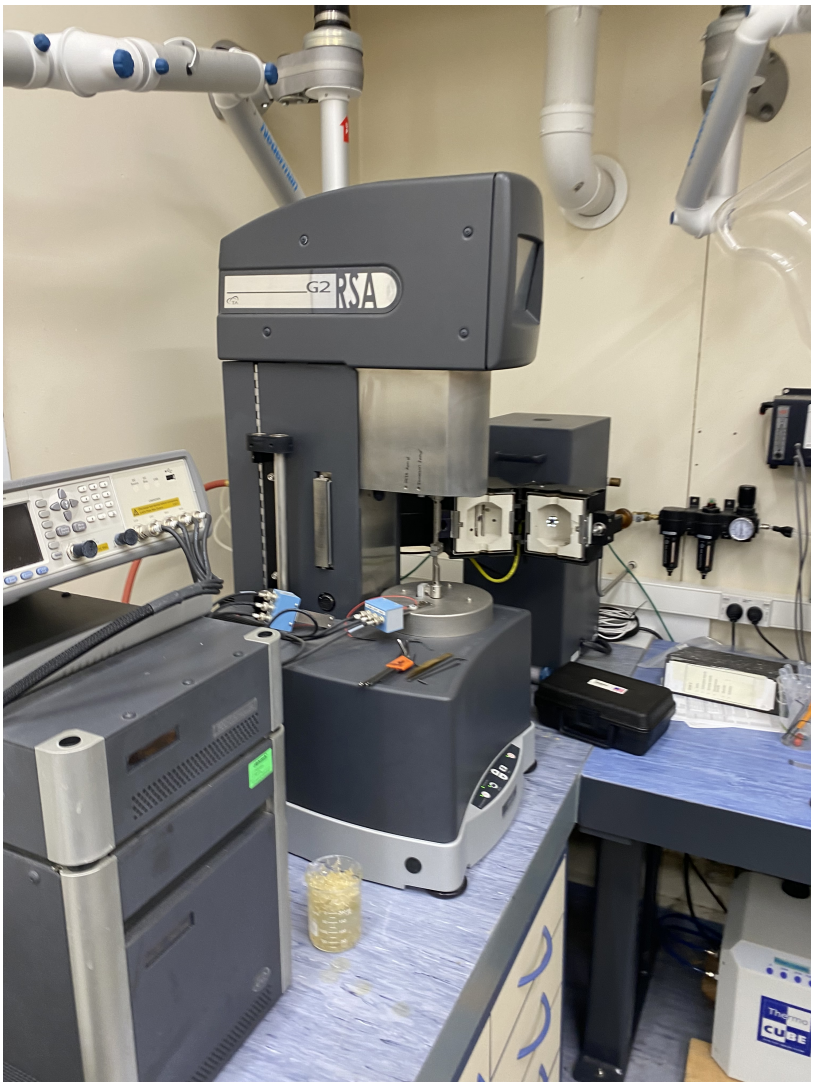

Figure 3.18: Gelatine cube compression testing machine — Dynamic Mechanical Analysis RSAG2

3.8.3 Dynamic Mechanical Analysis — Materials and Method

Firstly, large gelatine blocks (300mL) were prepared in order to perform the quasistatic examination of four different concentrations of gelatine (3.33%wt, 6.67%wt, 10%wt, and 15%wt). The process for this preparation, repeated four times in total, is as follows:

1. 250 bloom 20 mesh gelatine powder (GELITA Australia Pty Ltd) is poured into room temperature or below, preferably distilled, water at the specified weight — 3.33%wt at 300mL of water equates to 9.99g of gelatine powder, 20g at 6.67%wt, 30g at 10%wt, and 45g at 15%wt.

2. These mixtures are lightly stirred for approximately 5 minutes and left to rest for

another 10 minutes — this is known as the blooming process.

3. Once bloomed the gelatine mixture is raised in temperature to approximately 75° C and left at this temperature for another 5 minutes.

4. The hot mixture is then poured into a 500mL container.

5. This liquid gelatine is then left at 2° C for 24 hours.

6. The gelatine blocks were then removed from their containers and subsequently cut into 10x10x10mm cubes in preparation for insertion into the compression testing apparatus.

To conduct the compression tests, a dynamic mechanical analyzer, specifically the RSA-G2 Solids Analyzer from TA Instruments, was utilized. The compression fixture geometry used in this study was circular with a diameter of 25mm, and a 30N capacity load cell was employed to record force data from each specimen. The related data was collected using TRIOS software, also from TA Instruments, as depicted in Figure 3.18. The following procedure was followed to load 80 gelatine specimens into the compression fixture geometry for data collection:

1. The cube was extracted from refrigeration at 2° C measured with vernier callipers across its length, width, and height which is recorded in TRIOS, see Figure 3.19.

2. The cube is then placed on the bottom half of the fixture.

3. The top half of the compression fixture geometry is then lowered through machine controls to make contact with the top surface of the gelatine cube.

4. The loading gap is then updated, and the sampling rate is set to 2.0 pts/s with a linear strain rate of 0.025 mm/s.

5. The compression is then initiated through TRIOS and the force data is recorded.

6. Once the sample has been satisfactorily compressed, see Figure 3.20, as evidenced by the output data on the TRIOS software, the top half of the fixture geometry is raised through machine controls to a 20mm loading gap.

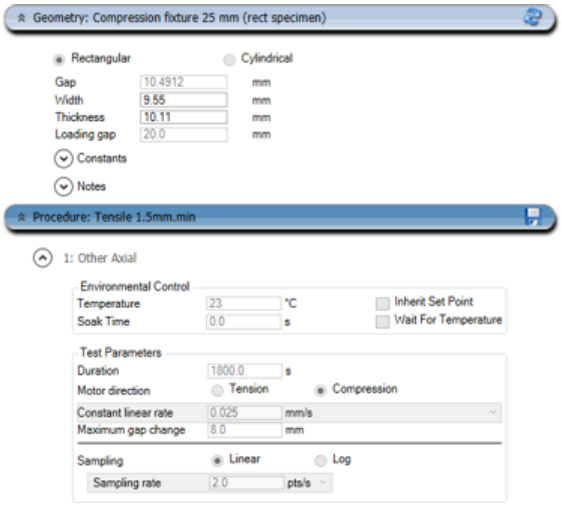

Figure 3.19: Gelatine cube compression test TRIOS settings

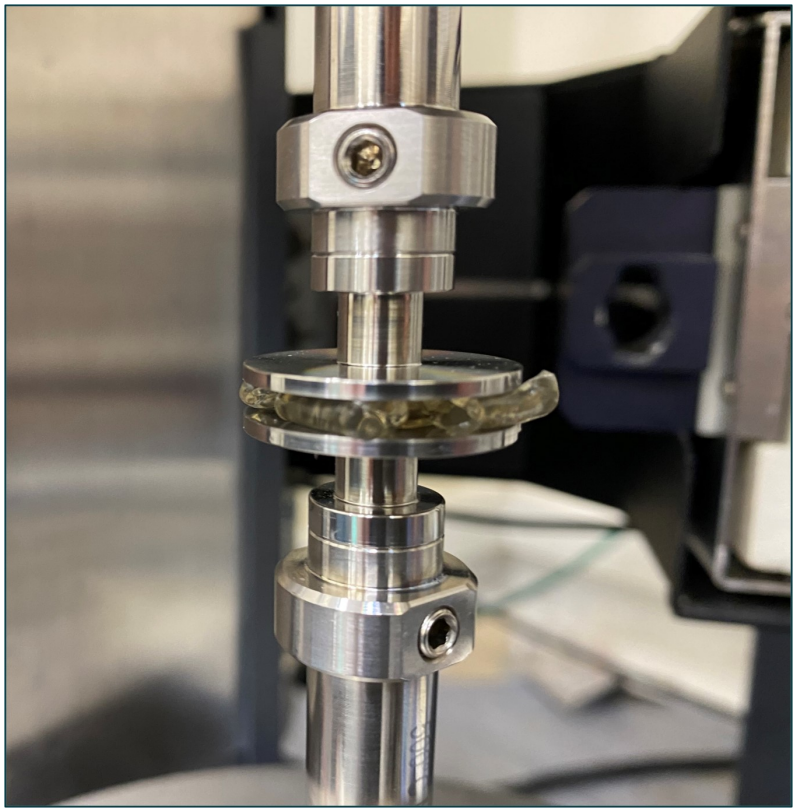

Figure 3.20: Gelatine cube compression test

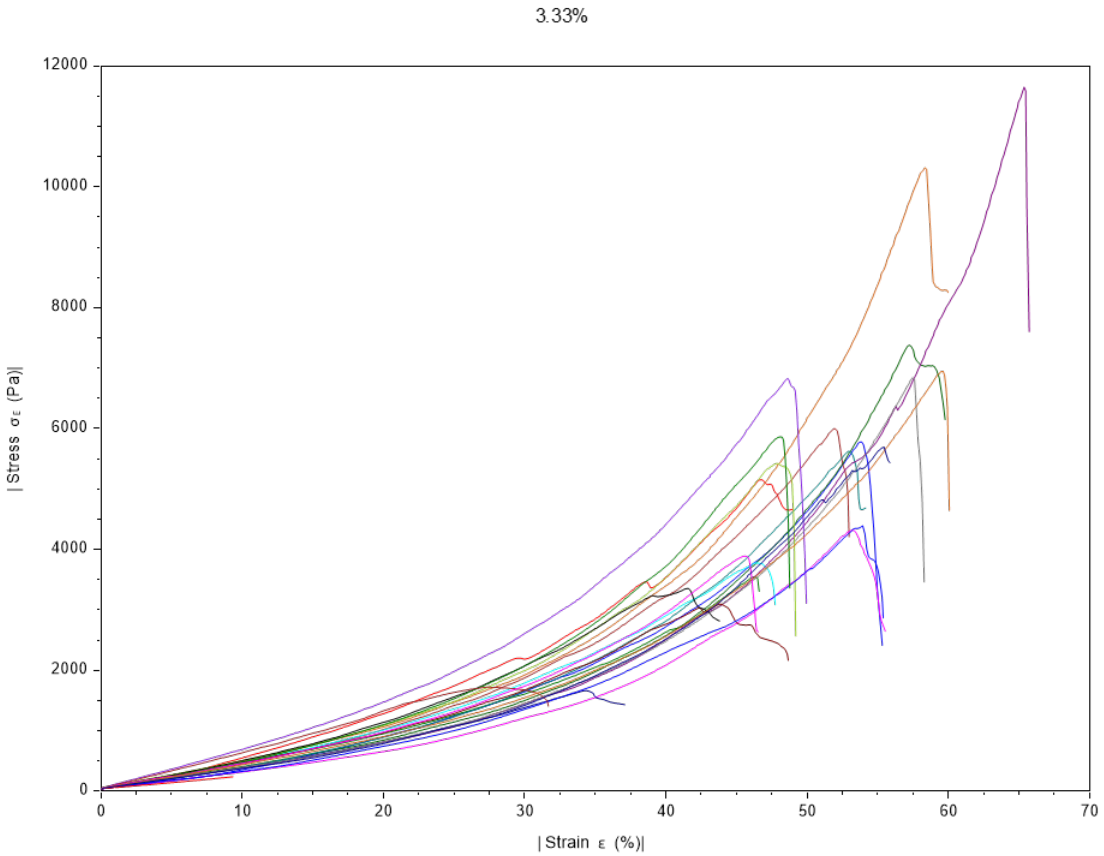

Figure 3.21: 3.33% gelatine compression test results

3.8.4 Dynamic Mechanical Analysis — Results and Discussion

This section reports the results from a total of 80 samples which were processed using the procedure outline in the previous methods section. This section will continue as follows: the output graphs for each concentration of gelatine is presented and discussed; statistical analysis of the relationships between these concentrations of gelatine is presented in the form of boxplots with reference linear and polynomial curvature fits; finally, the statistical characteristics of these concentrations are presented in a table which estimates the yield modulus (or stiffness) within a certain confidence interval.

To begin, the first group of samples which underwent compression testing were the 3.33%wt cube specimens. The stress-strain curve presented in Figure 3.21 follows a similar pattern to the stress-strain curves of similar type in literature. Noticeably, there appear to be one or two outliers with fracture points at higher rates of strain. This could be due to the way that the gelatine buckles under force. In other words, these cubes were structured such that as the compressive force begins to splinter the gelatine, these breakages would align themselves in such a way that more force would be required to cause the cube to fail (fully crumple and relax the stress of the load cell).

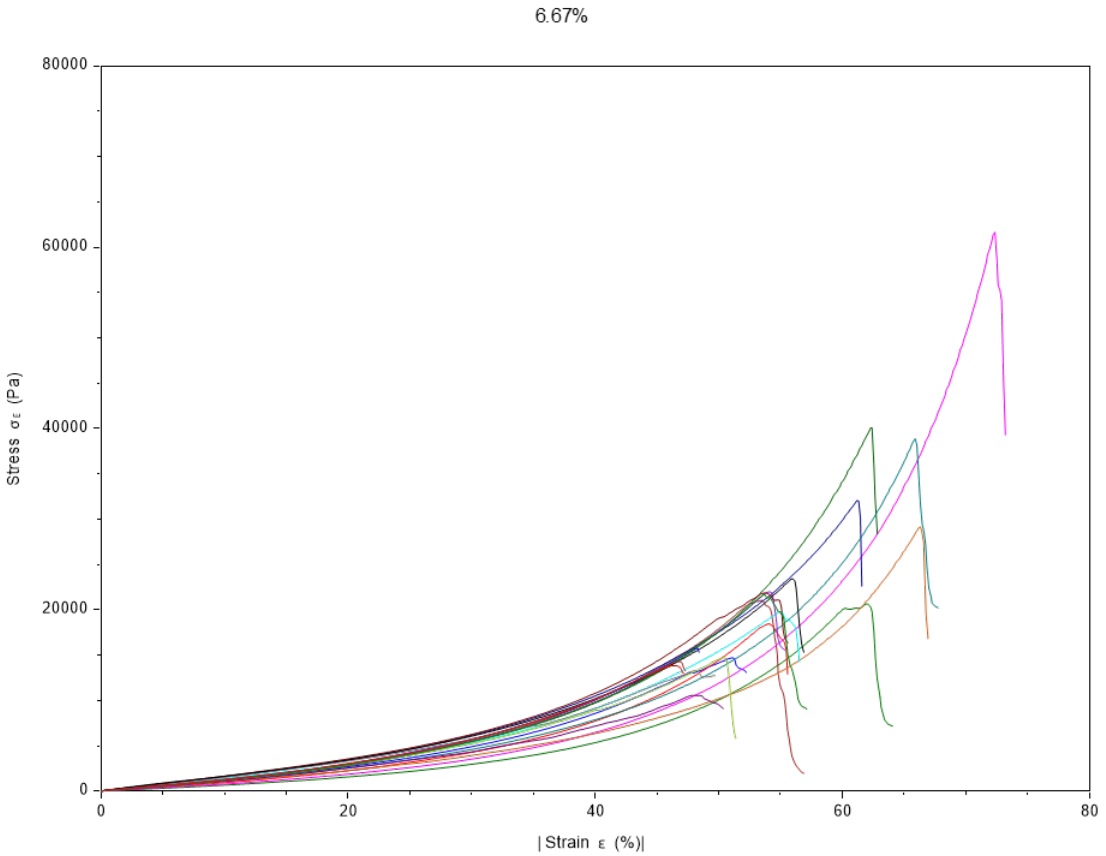

Figure 3.22: 6.67% gelatine compression test results

Next, the 6.67% gelatine specimens are present in Figure 3.22 with a similar grouping structure to that of the 3.33%wt specimens but at a relatively higher fracture force at similar strain.

The 10%wt specimens graphically present a relatively dramatic jump in the stress required to cause the cubes to fail, but again fail at a similar strain rate.

Finally, the 15%wt, see Figure 3.24 again increases significantly in fracture stress, but at a relatively larger strain as compared to the previous specimens. This larger strain could largely have to do with these specimens being of a much stiffer quality than the previous which were relatively "softer" and more delicate to handle. These specimens retain their current shape remarkably well.

In Figure 3.25, a complete visual comparison of all the specimens is presented. This plot invariably demonstrates that at 15%wt and at an increasing rate, gelatine becomes "stiffer" as the concentration increases. This result is expected. Noticeably, however, this graph report interesting behaviour when the specimens are compared. The lower concentration specimens possess particularly linear stress-strain curves. This effect is dramatically accentuated when the two lower concentrations are compared with higher

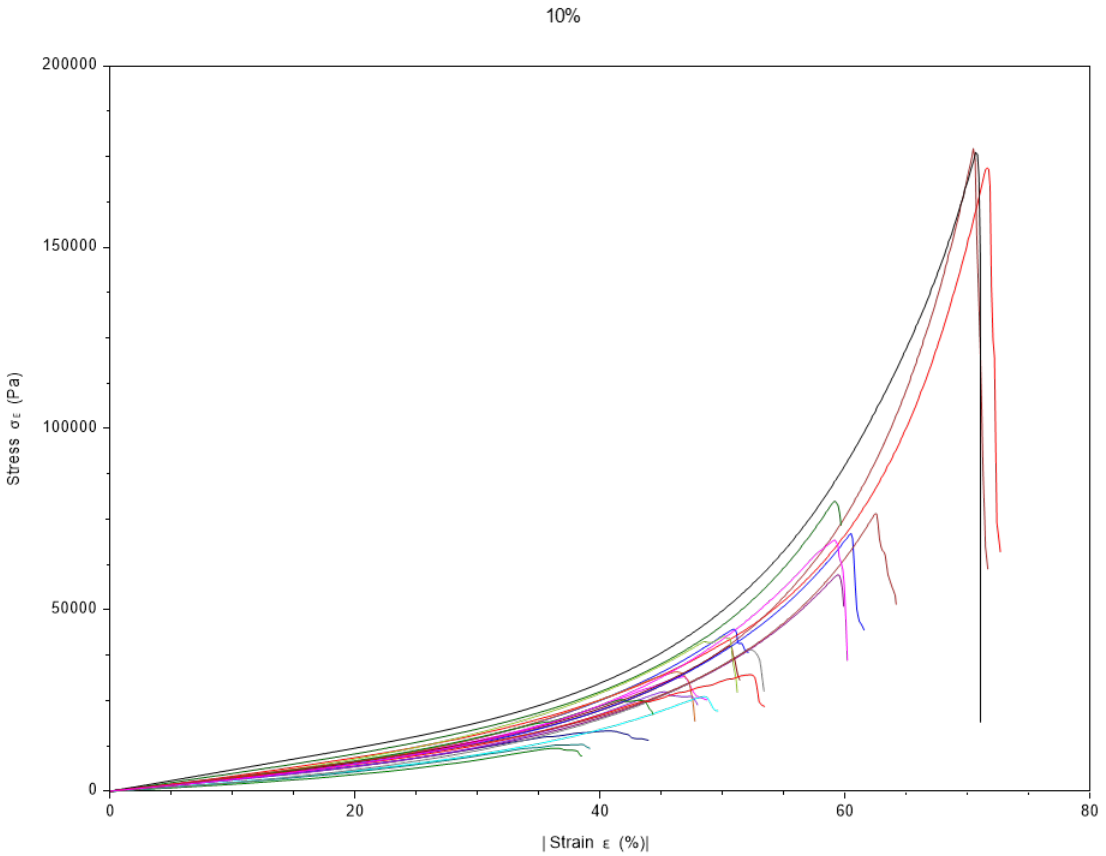

Figure 3.23: 10% gelatine compression test results

concentrations which tend to curve. Interestingly, the 15%wt stress-strain plot curves even more dramatically than the 10%wt plot. This is especially true as the plot tends towards the fracture point of the specimens. A plausible explanation for the observed visual behavior could be that the upper specimens exhibit greater stiffness and molecular orientation compared to the weaker specimens, hence requiring more force at a faster rate to fracture. Interestingly, the strain rates from these graphs seem to be similar, with only slight deviations.

In order to better understand the relationship between these concentrations, an attempt is made to graphically demonstrate these sample blocks into boxplots which describe this data in terms of its quartiles. This is done to ascertain visually any variation between the samples, and any skewness or spread. Furthermore, linear regression and polynomial regression is applied to analyse the relationship between the samples. The fracture points, yield moduli, Young's moduli, and strains are visually represented henceforth.

In Figure 3.26, the fracture points of the different gelatine concentrations are presented with both a linear and polynomial regression or fit. It is visually clear that

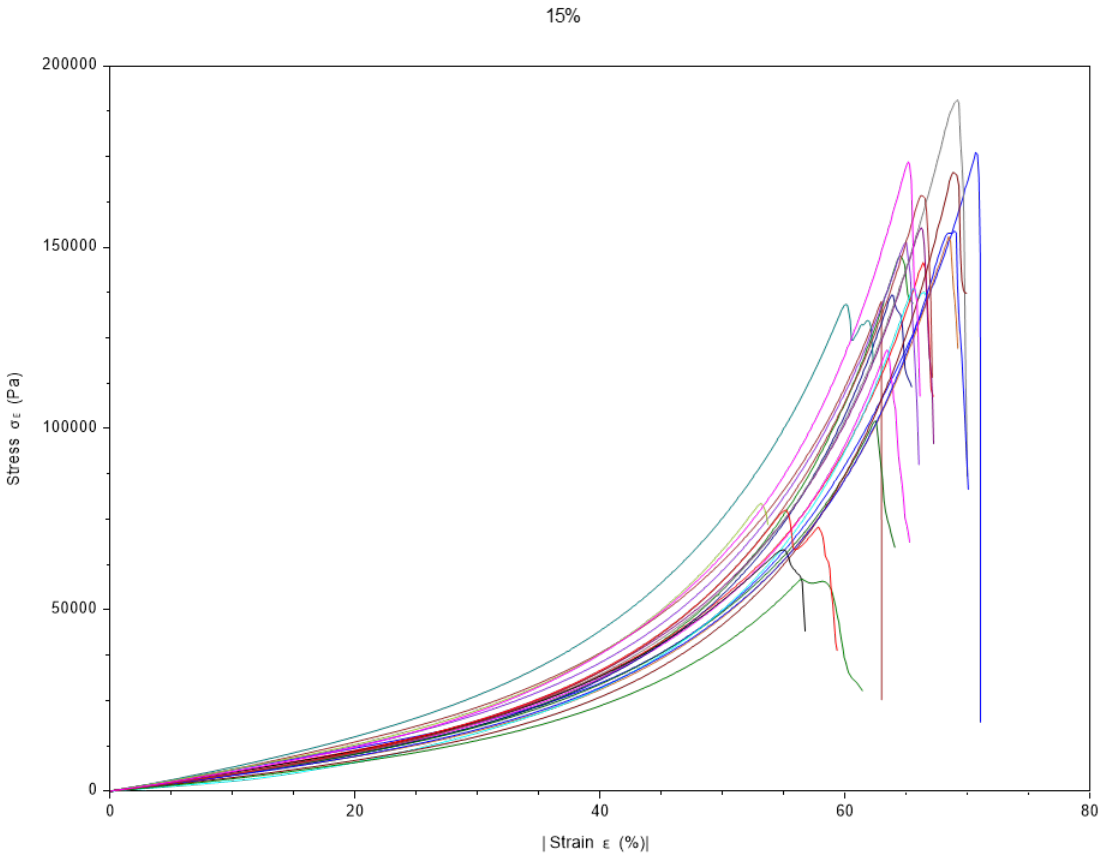

Figure 3.24: 15% gelatine compression test results

there appears to be a strong linear relationship between the specimens. However, the 6.67%wt appears to tend weaker than the fit suggests.

Similarly, the Young's modulus (refer to Figure 3.27, which is equivalent to the slope of the stress-strain curve, between the four different specimens follows a linear relationship of increase as the concentration increases.

Again, the boxplot of the Yield modulus (which is approximated at roughly 30% strain) presents a similar and even stronger linear fit than the rest, intersecting the medians of each concentration block. It is, therefore, clear that the mechanical properties of concern to this thesis are dependent on the concentration of the gelatine during its production. A boxplot comparing the strains of the four concentrations, however, shows minor variation between the 3.33%wt, 6.67%wt, and 10%wt specimens with the 15%wt specimen boxplot having a clearly higher reported strain than is initially expected. As previously explained, this is potentially due to the way that the cubes yielded and fractured under stress. Since the 15%wt is clearly stiffer, its fracturing may not have occurred immediately as it did in the other specimens.

Finally, a table presenting the expected mechanical properties is presented, see Table

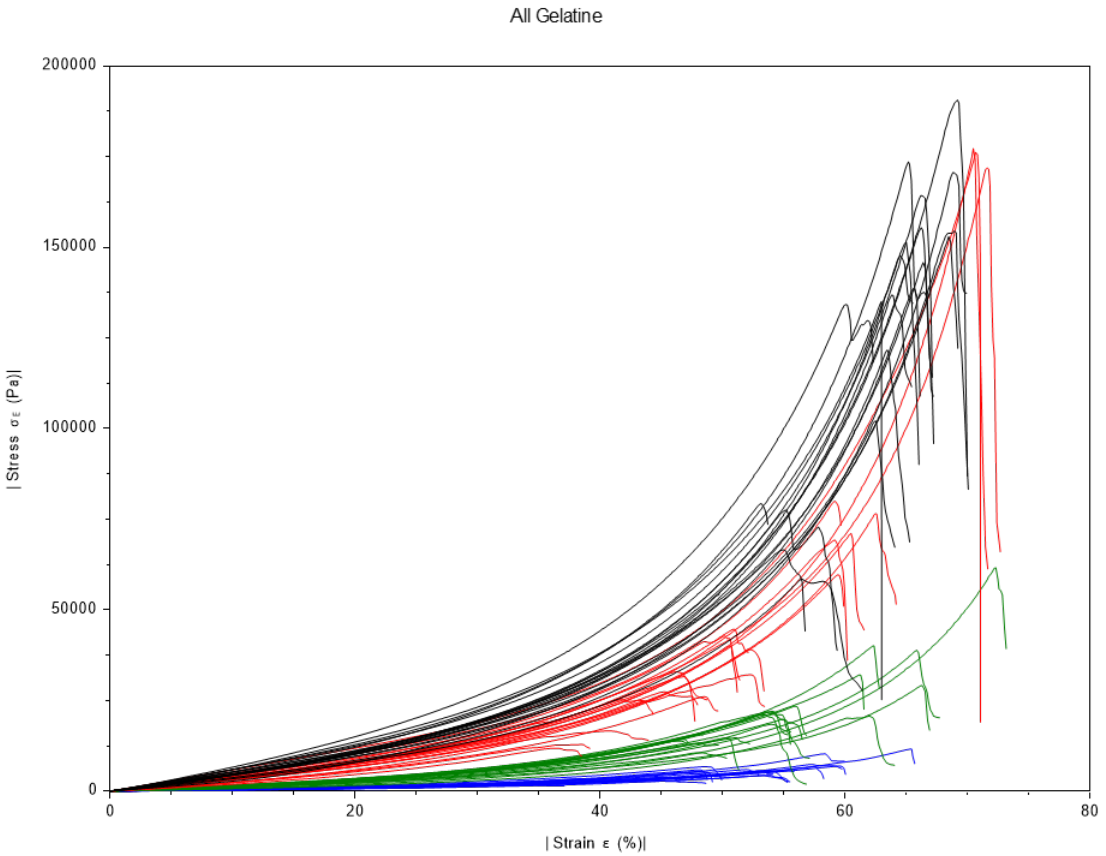

Figure 3.25: All gelatine compression test results for visual comparison

3.4. According to the table, the average Young's modulus for the gelatine concentrations are 4.5 kPa, 14 kPa, 38 kPa, and 55 kPa, respectively, falling well within the expected range for each concentration as compared to 3.17.

Table 3.4: Mechanical properties of each concentration

wt%	Stiffness (Pa)	Stiffness Standard Deviation	Avg. 30% Yield Modulus	Avg. Fracture Point	Avg. Strain
3.33	4536.98	950.61	1729.07	5584.01	50.39%
6.67	13676.54	2514.27	5192.29	23382.46	55.43%
10.00	37668.62	8411.33	13402.31	59021.86	53.05%
15.00	54817.38	9872.19	19047.21	132806.41	63.64%

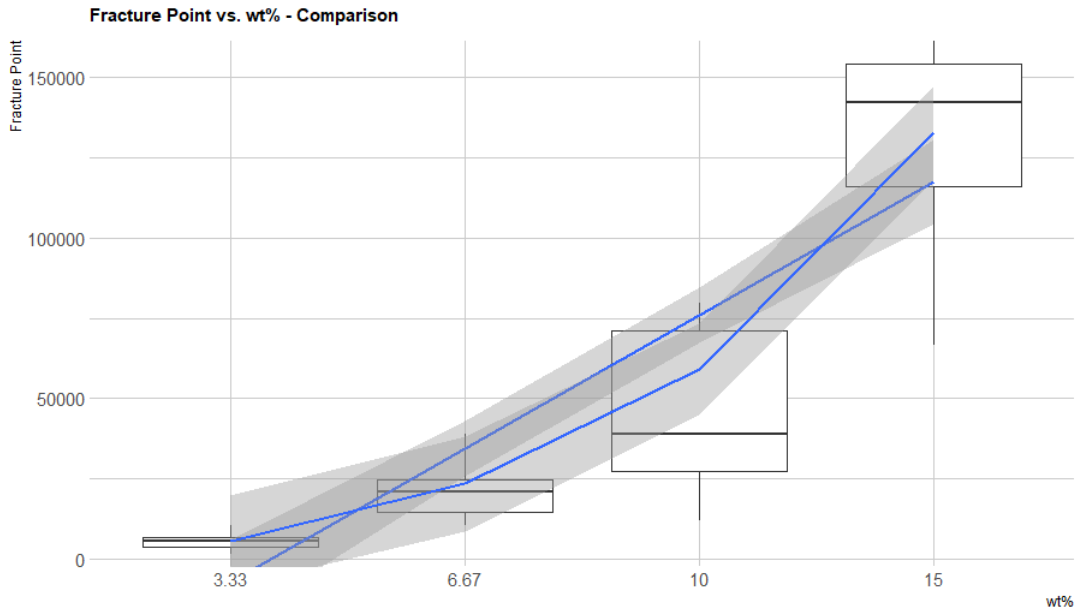

Figure 3.26: Fracture point (Pa) box plot comparing polynomial and linear fits

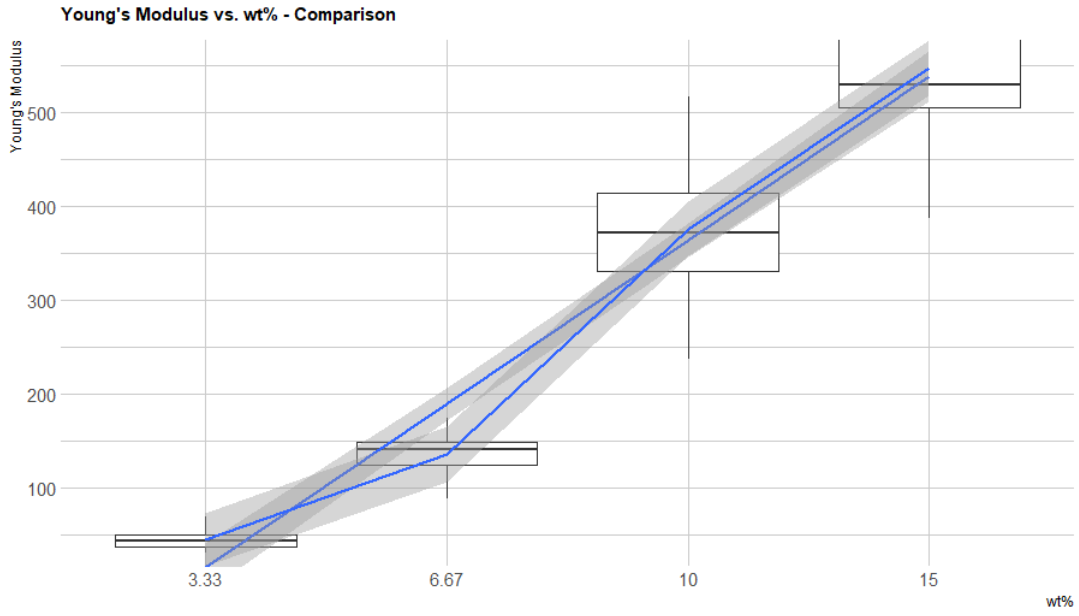

Figure 3.27: Young's Modulus (Pa) box plot comparing polynomial and linear fits

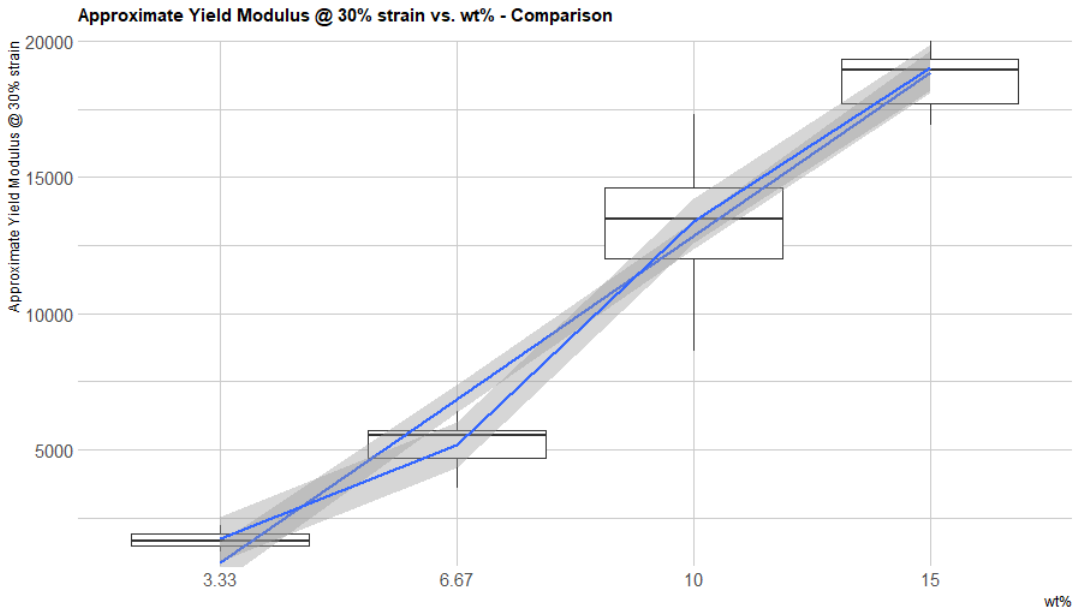

Figure 3.28: Approximate Yield Modulus (Pa) of different concentrations of gelatine

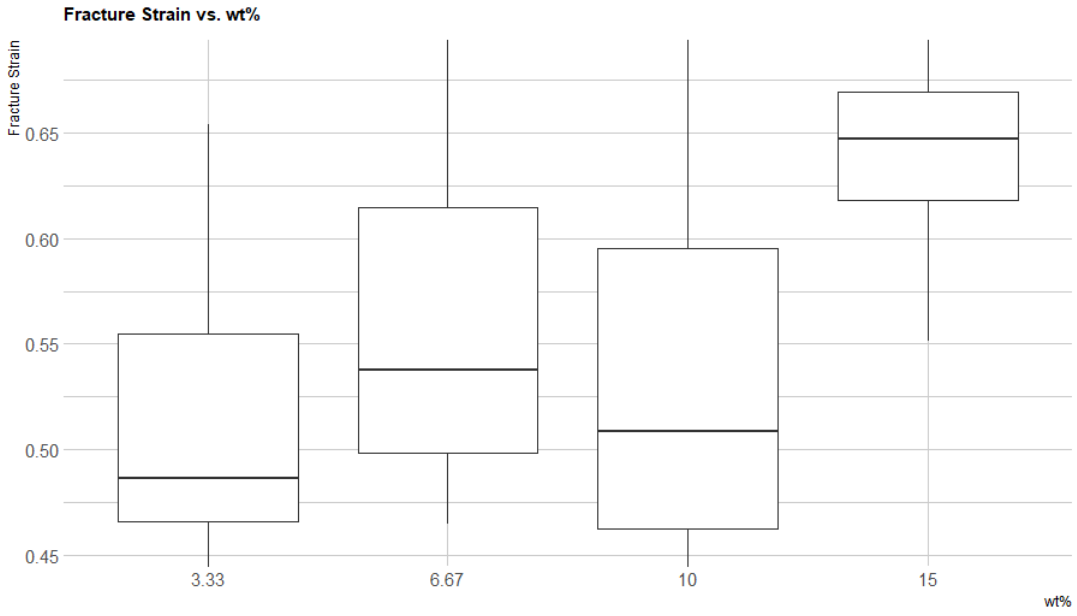

Figure 3.29: Fracture strain (%) box plot comparison by concentration wt%

3.8.5 Rheometery for viscoelastic testing — Materials and Method

In this section, we present an alternative method to compressively test gelatine and characterize its stiffness. The first step involves rheological analysis, followed by an indentation test to gain a better understanding of the surface behavior of gelatine when subjected to a force load.

The Young's modulus is determined by two crucial variables that are measured using the rheological analysis method presented in this chapter: the storage modulus and loss modulus. The storage modulus (G') measures the material's ability to store elastic energy when deformed. It represents the ratio of stress to strain when a material is subjected to a sinusoidal deformation at a given frequency. The stiffer the material, the higher its storage modulus, and the more elastic energy it can store.

On the other hand, the loss modulus (G") measures the material's ability to dissipate energy when deformed. It represents the ratio of the viscous stress to strain when a material is subjected to a sinusoidal deformation at a given frequency. The more viscous the material, the higher its loss modulus, and the more energy it dissipates as heat. [185, 211].

Given this background, the following methodology is presented:

1. Prepare three pots filled with 300mL of room temperature water (may be distilled, but this is not significant for the experiments).
2. Mix 3.33%wt, 6.67%wt, 10%wt of gelatine 250 bloom powder in each pot, stirring gently to prevent clumping.
3. Let the mixture bloom at room temperature for roughly 10-15 minutes until thickened.
4. Warm each pot to roughly 60° C and simmer for approximately 10 minutes or until the solution is liquid and has reached temperature.
5. Extract the hot gelatine liquid with a syringe and deposit into 20mL test tubes for each concentration of liquid gelatine.
6. Pour the remaining gelatine into 400mL containers.
7. Store the containers of gelatine at 2° C for 24 hours.

There are two parts of this examination of gelatine: 1. Rheology using a parallel-disc geometry (Anton Paar Physica rheometer (MCR301)); 2. Texture analysis (Texture analyser TAXT plus) with a 12mm circular probe as the "bloom" or stiffness indentation test.

The rheology was completed using the following method:

1. Rheometer with a parallel disc-geometry – Anton Paar Physica rheometer (MCR301) [185]

2. Determine the response of the gelatine to a strain change at a constant velocity (e.g., 10 rad/s) to determine the linear viscoelastic region

3. Response of the gelatine to a frequency change between 100Hz and 0.1Hz at 0.5% strain (within the linear viscoelastic region).

4. The dynamic shear modulus, and consequently the Young's modulus (measured in kPa), was determined by analyzing the storage modulus and loss modulus at various frequencies.

5. Taking the average of the storage modulus ($G^{'}$) and the loss modulus ($G^{''}$), the dynamic shear modulus (G^{*}) can be calculated.

$$G^{*} = G^{'} + G^{''} \tag{3.2}$$

$$E = 2G^{*}(1 + v) \tag{3.3}$$

6. This calculation for the Young's modulus (E) uses a dynamic shear modulus equation, see below, where literature defines the Poisson's ratio as (v) = 0.5 [211], see the equations 3.2 and 3.3.

An indentation test as texture analysis of the gelatine samples were completed using the following procedure:

1. The containers holding the samples were stored at 2 °C before each indentation test. It is important that the specimens are kept at temperature to maintain the integrity of the surface of the gelatine.

2. The texture analyser with a 12mm circular indentation fixture probe is raised to a 10mm loading gap.

3. The container is then placed on the specimen stage.

4. The probe is lowered until making contact with the upper surface of the gelatine

5. The indentation procedure which consists of lowering the probe a distance of 4mm is then initiated across different portions of the surface area a total of ten repetitions.

6. A force by distance value (N/mm) is then determined, which elucidates the compressive stiffness of a material.

7. In order to calculate the material behaviour in terms of Young's modulus, the equation 3.5 was used, based on 3.4 where E is the elastic modulus, P is the force at maximum indentation depth, R is the contact radius of the probe, h is the depth of indentation considering potential "sink-in", and v is the assumed Poisson's ratio at 0.5 (an incompressible solid) [43], and where p_m is the mean contact pressure ($p_m = \frac{P}{\pi * R^2}$).

$$P = \frac{2 \cdot E \cdot R \cdot h}{1 - v^2} \tag{3.4}$$

$$p_m = \frac{2 \cdot E \cdot h}{\pi \cdot R \cdot (1 - v^2)} \tag{3.5}$$

Using these methodologies, it is attempted to offer another methodology through which to characterise the mechanical (elastic) properties of the gelatine samples, as an effort towards generalising the viscoelastic properties of a range of gelatine types which the hyperspectral machine learning model may be used as a prediction model. It is in this prediction of the viscoelastic properties that the control mechanisms of the proposed steerable needle robot may be further informed. Please refer to the background subsection, which presents some previous work into similar gelatine samples for reference.

3.8.6 Rheometery for viscoelastic testing — Results and Discussion

In Figure 3.30, a curve can be observed that is consistent with previous research [179]. As the temperature of the gelatine sample is lowered from room temperature (21° C) to 2 ° C, the "curing" process begins, and the curve begins to flatten out. This indicates that the gelatine is undergoing a curing process, after which both the shear and loss modulus tend to increase over time due to the compressive "packing" of the gelatine. This results in a slight upward skewing of the results. For the 3.33%wt gelatine concentration, a storage modulus of 1420 Pa and a loss modulus of 12.70 Pa were obtained using rheological analysis.

When these values are applied to the equations 3.2 and 3.3 with an assumed Poisson's ration of 0.5, the Young's modulus is thence calculated as 3054.30 Pa.

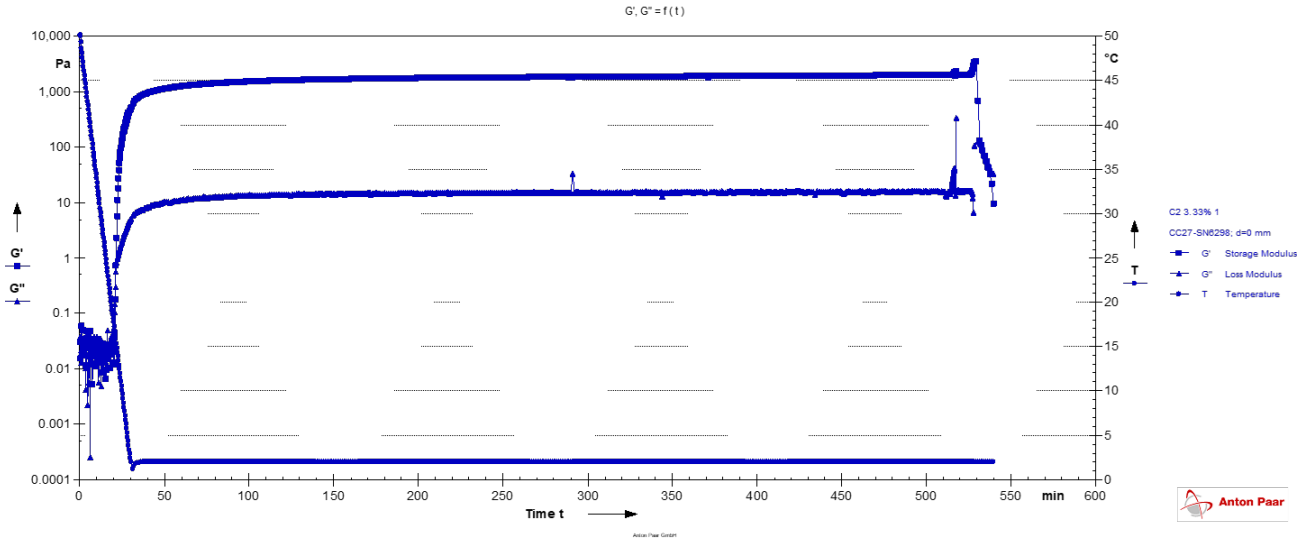

Figure 3.30: The Storage and Loss Moduli related to a decrease in temperature graph of a 3.33%wt as recorded over time

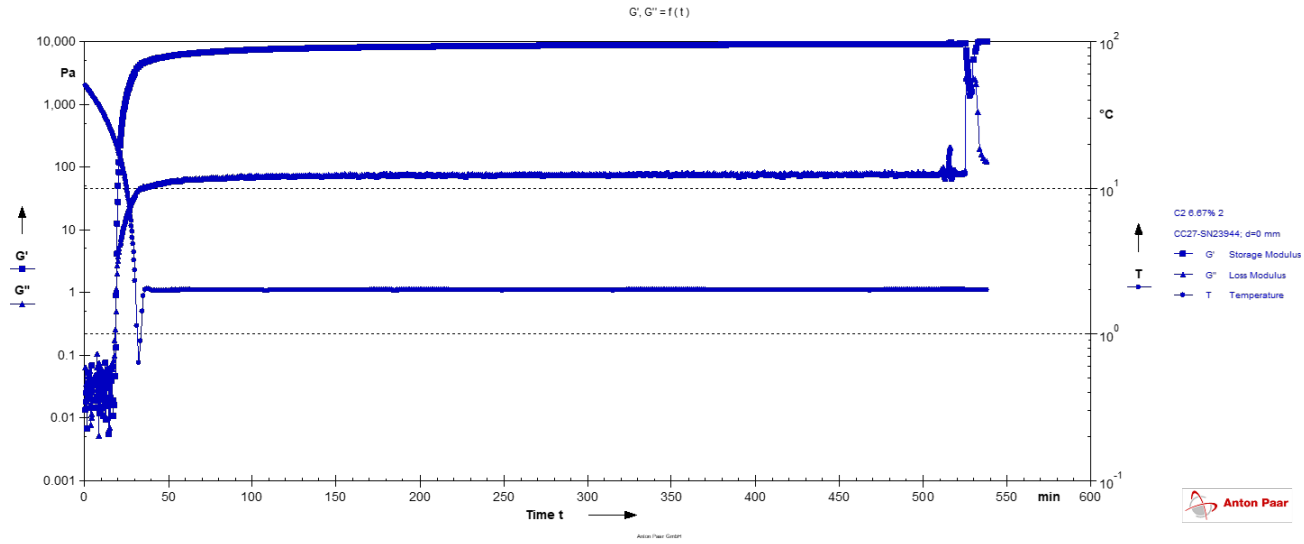

Figure 3.31: The Storage and Loss Moduli related to a decrease in temperature graph of a 6.67%wt as recorded over time

In Figure 3.31, a similar curve to the previous gelatine concentration is seen, but with a much greater storage modulus (tending towards 4000–4500 Pa). It is interesting to note that the loss modulus is less than the storage modulus by a factor of 10. Repeating the process using the equations 3.2 and 3.3, the Young's Modulus (E) can be calculated at 6.67%wt gelatine at 15270.77 Pa.

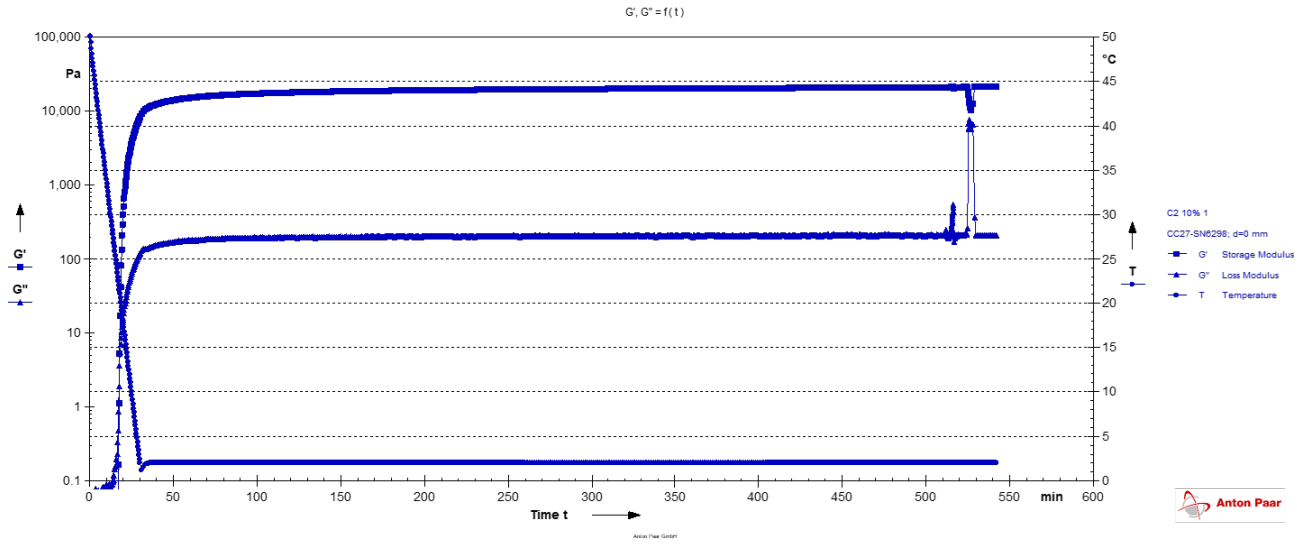

Figure 3.32: The Storage and Loss Moduli related to a decrease in temperature graph of a 10%wt as recorded over time

In Figure 3.32, the storage and loss modulus increase substantially in comparison to the lesser concentrations. The storage and loss modulus tends towards greater figures than in the 6.67%wt gelatine specimen (15000 Pa). Again, using the calculations as presented by this methodology, the Young's modulus is estimated at 37502.81 Pa. Please refer to table 3.5 for a comparison of the values using rheometry.

Table 3.5: The mean averages of the storage modulus and loss modulus of the viscoelastic response rheometry along with the calculated Young's modulus for 3.33%wt, 6.67%wt, and 10%wt gelatine

Concentration	Storage Modulus (Pa) — Mean	Loss Modulus (Pa) — Mean	Calculated Young's Modulus (Pa), where v = 0.5
3.33%	1420.00	12.70	4260.17
6.67%	4260.17	51.00	15270.77
10%	15270.77	153.00	37502.81

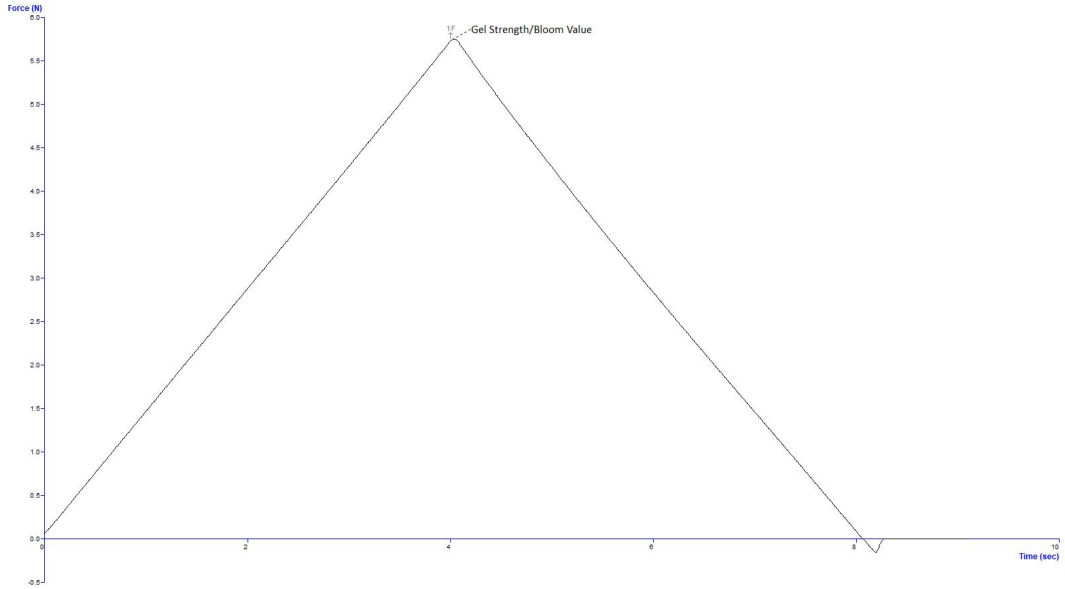

Figure 3.33: A graphic representation of the indentation test, specifically for the 10%wt specimen

Next, the results from the indentations testing using a texture analyser are presented. In order to understand the output,the following terms are defined which will be used accordingly: Bloom strength is a measure of the strength of a gelatin or agar gel. It is the force required to depress a standard probe of a certain size into the surface of a gel to a specified depth.

Bloom strength as reported in the thesis has the unit of N/mm. We compare the bloom strengths in this unit across different concentrations of gelatine. In industry, bloom strength is defined as "Bloom grams" or "Bloom units". This is where 0.098 N/mm = 1 Bloom unit. For the purposes of comparison, this thesis does not make this conversion since it is an unnecessary step in understanding how gelatine strengths when its concentration increases.

Figure 3.33 shows graphically the response of the gelatine to the 4mm indentation by the 12mm diameter probe. In this graph, the peak point indicates the gel strength of bloom value of the gelatine samples. This specific graph refers to the 10%wt specimen with the other specimens having identical peaks at lower values. This "gel strength" is an indication of the stiffness of the gelatine in terms of N/mm. Extrapolating the values, as is presented in Table 3.6, the stiffness of the gelatine concentration 3.33%wt, 6.67%wt, and 10%wt are 0.68 N/4mm (0.17 N/mm), 2.75 N/4mm (0.69 N/mm), and 5.63 N/4mm (1.41 N/mm), respectively.

These equate to bloom strengths of approximately 70, 275, and 560 depending on the concentration of gelatine. Bloom strength indicates that the cohesive molecular strength (by the average molecular weight of its constituent parts) of gelatine and thereby its

strength or stiffness [89]. Technically, this bloom strength only strictly accounts for the 6.67%wt as per the rigours of the bloom strength test [43], however, it is used here for the other specimens in order to gain insight into the behavioural changes of gelatine as its concentration decreases or increases from this midpoint.

There appears, however, to appear to be a minor discrepancy between the reported bloom strength by the manufacturer of the gelatine and the test. This could be due to other additives to the used water in which the gelatine powder "bloomed". It varies by a minor degree, and for the purposes of this thesis, adequately serves to demonstrate the strength of the gelatine that is used in the flexible steerable needle experiments and for further feedback control using HSI and machine learning.

In order to calculate the estimate Young's Modulus, follow the equation 3.5 was followed and through fitting the output data of the indentation test in terms of its maximum force at the indentation depth, the Young's modulus was calculated, see Table 3.7.

Table 3.6: A table which presents the raw results from the indentation tests and the stiffness of the three gelatine specimens

Start Batch conc 3.33%_	conc 3.33%_		Start Batch conc 6.67%_	conc 6.67%_		Start Batch conc 10%_	conc 10%_	
conc 3.33%_01	conc 3.33%_	0.688	conc 6.67%_01	conc 6.67%_	2.800	conc 10%_01	conc 10%_	5.769
conc 3.33%_02	conc 3.33%_	0.671	conc 6.67%_02	conc 6.67%_	2.718	conc 10%_02	conc 10%_	5.607
conc 3.33%_03	conc 3.33%_	0.672	conc 6.67%_03	conc 6.67%_	2.707	conc 10%_03	conc 10%_	5.544
conc 3.33%_04	conc 3.33%_	0.676	conc 6.67%_04	conc 6.67%_	2.789	conc 10%_04	conc 10%_	5.560
conc 3.33%_05	conc 3.33%_	0.693	conc 6.67%_05	conc 6.67%_	2.826	conc 10%_05	conc 10%_	5.808
conc 3.33%_06	conc 3.33%_	0.681	conc 6.67%_06	conc 6.67%_	2.748	conc 10%_06	conc 10%_	5.665
conc 3.33%_07	conc 3.33%_	0.671	conc 6.67%_07	conc 6.67%_	2.684	conc 10%_07	conc 10%_	5.482
conc 3.33%_08	conc 3.33%_	0.669	conc 6.67%_08	conc 6.67%_	2.704	conc 10%_08	conc 10%_	5.531
conc 3.33%_09	conc 3.33%_	0.669	conc 6.67%_09	conc 6.67%_	2.762	conc 10%_09	conc 10%_	5.633
conc 3.33%_10	conc 3.33%_	0.675	conc 6.67%_10	conc 6.67%_	2.763	conc 10%_10	conc 10%_	5.732
End Batch conc 3.33%_	conc 3.33%_		End Batch conc 6.67%_	conc 6.67%_		End Batch conc 10%_	conc 10%_	
Average:	conc 3.33%_ (F)	0.677	Average:	conc 6.67%_ (F)	2.750	Average:	conc 10%_ (F)	5.633
S.D.	conc 3.33%_ (F)	0.008	S.D.	conc 6.67%_ (F)	0.047	S.D.	conc 10%_ (F)	0.109
Coef. of Variation	conc 3.33%_ (F)	1.226	Coef. of Variation	conc 6.67%_ (F)	1.698	Coef. of Variation	conc 10%_ (F)	1.937
N/mm	conc 3.33%_ (F)	0.169	N/mm	conc 3.33%_ (F)	0.688	N/mm	conc 3.33%_ (F)	1.408

Table 3.7: Indentation test results along with a calculated E value.

wt%	P	R	h	v	Calculated E (Pa)
3.33	0.693	6	4	0.5	3446.70
6.67	2.826	6	4	0.5	14055.37
10	5.808	6	4	0.5	28886.62

The calculated Young's modulus is particularly varied from these calculations when compared to the mechanical compression tests performed in the previous section. This is due to other forces playing a role in the indentation testing procedure which is not accounted for in the calculations of E. As a result, the adhesion forces between the surface of the flat indentation probe may in fact vary the contact radius and thus

skew the applied load over the surface area. There is a precedent for this behaviour in literature [43, 64, 115].

Table 3.8: A comparison table of the Young's modulus determined through uniaxial compression, oscillatory rheometry, and indentation

wt%	Compression — E (Pa)	Rheometry — E (Pa)	Indentation — E (Pa)
3.33	4536.98	4260.17	3446.70
6.67	13676.54	15270.77	14055.37
10	37668.62	37502.81	28886.62

3.8.7 Discussion & Conclusion

In conclusion, this section has explored the physical properties of gelatine using quasistatic uniaxial compression, rheometry, and indentation testing. The comparison table presented above shows the Young's modulus obtained through compression and rheometry are particularly closely aligned, and therefore more precise representations of the mechanical characteristics of the gelatine samples. However, the indentation test results were affected by the adhesion between the probe and the specimen, which is a well-known issue in the literature. Further development of a mathematical approach to address this problem is needed.

Uniaxial compression of the gelatine specimens provided the clearest stress information as to the mechanical properties while the rheometry investigation provided insights into the viscoelastic properties of gelatine over time and temperature. This is significant due to the fact that it demonstrates the changes that gelatine undergoes over temperature and time. At high temperatures the gelatine weakens and becomes more liquid while over prolonged periods of time the gelatine becomes stiffer. This growing increase in stiffness is due to a settling nature of the gel as well as an aging process. If the gelatine were to age for longer periods of time (+48 hours), it can be expected to become stiffer and harder due to the aging of the gelatine molecules. This is worthy of a future study whereby these changes may be explained as to the reasons why and how. For the purposes of this thesis, however, the compression test is suitable enough to provide the stiffness information required to begin drawing a relationship between flexible steerable needle and body interaction characteristics through hyperspectral prediction.

3.9 Chapter Discussion & Conclusion

Steerable needle 3D printing is a technique which holds many possibilities in terms of polymer research and real-world applications. This chapter proposed an adapted steerable needle robot utilised as a 3D printing system which defines and advances an approach to utilise advanced motion planning algorithms and control in the pursuit of 3D printing polymers at a specific end-goal for a certain length. The fabrication of a system of interconnected fibres within a body that possesses internal obstacles is the goal of this research. Future work involves the development and testing of more advanced polymers and polymerisation techniques (e.g., shape changing, electro-activity, etc.), advancing the accuracy and reliability in reaching end-goal positions using refined control schemes and robotic mechanisms, and providing case studies and use-cases where this technique may have the most impact.

Hydrogels are characterised by various techniques to determine their mechanical or rheological properties such as their yield modulus, stiffness, cohesiveness, viscosity index, consistency, etc. From the presented models, it appears that HSI could effectively simplify the measurement procedure, allowing for a more straightforward characterisation of hydrogel samples, especially when considering a database of gel properties may be built for comparison and prediction. In recent years, machine vision-based algorithms have been successful in solving data classification and pattern recognition problems.

Typically, nonparametric regression approaches split the data into training and validation datasets. Being sampled from the same population the validation dataset is not truly independent. This statistical linkage causes high accuracy at the validation stage of the model development, which however is less likely to extend on an independent data. To date, there are a limited number of studies, which have investigated model transferability with the aim of developing a model in one location and applying it on different samples or times. Independent validation is considered as a most robust method for assessing model's ability to achieve the transferability thus used in this section on an independent dataset. The independent dataset was not included in the training or test data. A satisfactory range of the model accuracy is observed which might be attributed to richness of the training dataset achieved by samples combined with the capabilities of GPR modelling.

Furthermore, a novel approach of combining the principles of HSI with machine learning by utilising the physical spectral characteristics of hydrogel samples of varying mechanical properties such as stiffness. It can be, hence, concluded that the developed method is fast and reproducible to serve as part of the aforementioned steerable needle control system in relation to an estimation system based on a mechanical property database of hydrogels, polymers, or even tissue.

Chapter 4

Characterising a steerable needle robot to "3D print" biomaterials in a phantom body

A man can travel further in a single thought than he could in an entire lifetime. The distance travelled towards such palaces is infinite, but to reach even a fraction of such distances under the gaze of Sol is to toil one moment to the next ever onwards. There is a cost that must be paid to build these roads called the schools of knowledge which make up the infinite palace.

4.1 Introduction

This chapter describes the development and characterization of an open-loop, flexible, steerable needle robot for 3D printing, as introduced in Chapter 3. In addition to examining the properties of a potential phantom body in which the robot will operate and proposing a new method for estimating these properties using HSI and machine learning models, the chapter focuses on the behavior of the long, flexible needle as it is inserted into the phantom body, as well as the robot's ability to accurately place the needle at any desired point. The chapter's main objective is to address Objective 2 outlined in the Introduction.

There are two accuracy quantities that are necessary to consider in a steerable robot: 1. the accuracy of the target location generated by the motion planner with

respect to the coordinate location in the body under operation; 2. the accuracy of the electro-mechanical system to reach this target considering obstacles, body stiffness and other characteristics, and the machine "smoothness" or stability [114, 217]. Literature states that the medically constrained accuracy of any minimally invasive technique is defined at approximately 3mm. Therefore, it is the further purpose of this chapter to define the proposed steerable needle robot with respect to this constraint, see Figure 4.1 for an overview on the order of operations for the robot.

This chapter aims to evaluate the performance of the proposed flexible steerable needle robot for 3D printing in a phantom body. Two experiments are presented to achieve this goal. The first experiment aims to determine the maximum radius of curvature or deflection of the steerable needle within the phantom body. This is crucial since the exact needle properties related to the phantom body are unknown. Previous work involving HSI and a machine learning model attempted to estimate the deflection, but this process is still in development. Thus, manual experimentation is required to determine the deflection. The experiment is conducted using the Intel RealSense^{TM} cameras as presented in Chapter 3. The machine vision system triangulates the end coordinates of the needle tip by assessing its distance from the known outer edges of the stage frame.

The second experiment in this chapter involves selecting an entry point and a target point within the phantom body, and using the motion planner to generate the optimal trajectory between these two points. The proposed path "slicing" method is then implemented to generate the machine code for the steerable needle robot. The purpose of this experiment is to assess the accuracy of the steerable needle robot in executing its control operations. The focus of this experiment is not on the accuracy of the motion planning algorithms, as those have already been suggested in the literature [63]. The outcome of this experiment is to estimate the accuracy of the robot in reaching a relatively complex target with no obstacles. This experiment is a preliminary step towards conducting further experiments with the robot in the future.

From these experiments it is possible to identify the limitations of the proposed steerable needle robot in terms of its current design from the motion planning stage to the operation stage. Several opportunities, therefore, are discussed which would improve the design and implementation of this robot for the application of "3D printing" *in vivo*. For example, several improvements can be made to the electro-mechanical systems of the robot as well in terms of its "fineness" of actuation since machine "jitter" may impact the needle insertion. This assertion, among others, is explored in this chapter.

4.2 Materials and Method

The materials used in the following investigative experiments are as follows:

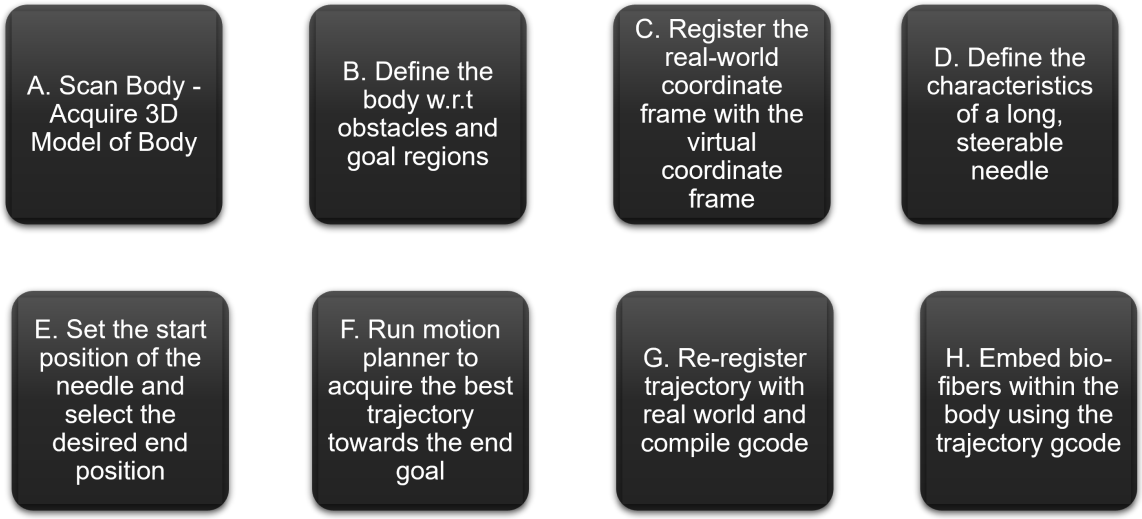

Figure 4.1: The flow of operations in order to run the steerable needle robot

- The steerable needle robot loaded with a 19G, 10 inch or 254mm needle
- The phantom body prepared within a special experimentally designed holding container (as presented in Chapter 3) as 250 bloom, 20 mesh gelatine powder mixed with water at 10%wt and left to set for 24 hours at 2°C.

Experiment 1 — the determination of the deflection of a 19G needle as controlled by the developed robotic system:

1. Set the maximum insertion depth @ 135mm in motion planner.
2. Set the insertion speed in the controller @ 5mm/s.
3. Remove the phantom body from cold storage and position on the testbed aligning the needle entry sheath.
4. Initiate insertion without rotation with the needle tip in the calibration position.
5. Record the end position of the needle tip using the machine vision setup.
   (a) Use Intel RealSense^{TM} camera depth measurement system to triangulate the end-point coordinates, see Figure 4.5.
   (b) To determine the effective deflection, δ, using coordinate triangulation, first, locate the entry point of the deviated needle curve. Next, draw a straight line from the entry point to intersect the deviated needle curve at a tangent point. The hypotenuse of the resulting right triangle, formed by the straight line and the two legs representing the distance between the entry point and the tangent point, and the distance between the tangent point and the tip of

the deviated needle curve, indicates the length of curvature. Measure the length of the hypotenuse, which is the length of curvature, δ, in accordance with equation 4.1.

6. Repeat x20

$$\delta = \sqrt{(x_{opp})^2 + (x_{base})^2} \tag{4.1}$$

$$radius(r) = \frac{H}{2} + \frac{W^2}{8H} \tag{4.2}$$

$$\theta = 2arcsin(\frac{c}{2r}) \tag{4.3}$$

$$L = r * \theta \tag{4.4}$$

Once the coordinate positions are recorded, and the coordinate triangulation is performed using trigonometry, statistical analysis on the output data is performed. The mean deflection is determined, the error, as well as the standard deviation. The coordinate triangulation is performed by measurements of the distance between the needle tip to the: top of the gelatine body; entry point of the gelatine body. The output coordinates are thus compared with the theoretical coordinates as input into the motion planner.

Table 4.1: Controllable vs. Unknown

Known and Controllable	Unknowns
Insertion Depth (100mm – 200mm)	Maximum Needle Curvature
Needle Gauge (19G)	Needle accuracy — point to point
Insertion Speed	Homogeneity of “printed” materials in place – What is volume for dispensing? Over or under injection
Rotation Speed – Rotation (Yes / No?)	Effectiveness at producing in-vivo fibres using chemistry – described by the polymerisability of the materials using the injection process
Gel Concentrations (3.33% – 15%)	Relationship between yield strength and needle curvature

Experiment 2 — the determination of the accuracy of the steerable needle robot as a whole:

1. Set the maximum insertion depth @ 135mm in motion planner.
2. Set the maximum insertion speed in the controller @ 5mm/s.
3. Define the entry point coordinates — set at x = 0mm, y = 125mm, z = 60mm.
4. Define the target goal coordinates within the gelatine phantom body — set at x = 133mm, y = 116.50mm, z = 60mm.
5. Run the motion planner to generate the trajectory output in a series of coordinate points.
6. "Slice" or run machine code generator script, disregarding any "injection" or "3D printing procedure", to convert coordinate points into machine translations and rotations.
7. Upload the machine code to the steerable needle robot.
8. Start the steerable needle robot, see Figure 4.4.
9. After completing the operation, record the end distances from the reference points of the needle tip, see Figure 4.5, using the machine vision setup and calculate the coordinate position using the equations 4.2, 4.3 and 4.4.
10. Repeat x20

The maximum radius of curvature can be calculated using equation 4.1 based on measurements of the needle tip in the phantom body. To obtain these measurements, the length from an imaginary straight line starting from the entry point to a horizontally drawn line intersecting the needle tip is measured. Additionally, the distance between the tip and this length is measured to obtain the variables x_{opp} and x_{base}, respectively.

In terms of determining the coordinate position of the needle tip, the length from the entry point in terms of the y axis is equivalent to the coordinate position. However, the x axis coordinate must be calculated using equations 4.2, 4.3 and 4.4, where the radii (r) of the arc may be calculated using the height (H) between a chord (c) (which describes the length of an imaginary line drawn between the entry point and the current needle tip point) and the arc. The variables H and c is measured using the vision system. The equation 4.2 derives from the intersecting chord theorem. Once the radii are calculated, the initial angle (in radians) between them is calculated by dividing the chord length by double the radius from which an inverse sine on the result is performed. This angle

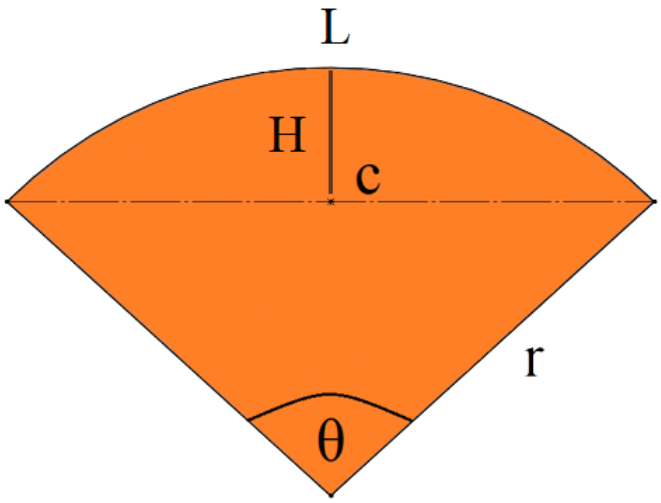

Figure 4.2: A diagram depicting the arc of a circle and its constituent lengths and angles.

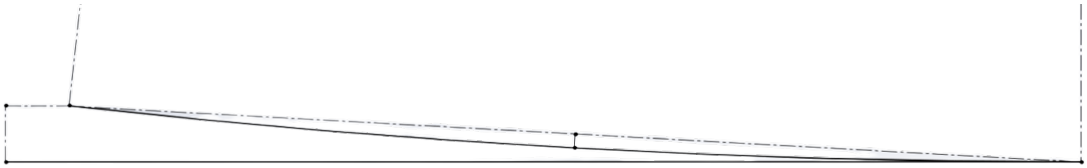

Figure 4.3: Another diagram depicting the arc of a circle and its constituent lengths and angles with a theoretical needle trajectory.

values is then converted to degrees and the arc length (which denotes the x coordinate) is calculated using the equation 4.4, see Figure 4.3.

Furthermore, utilising the steerability metric as proposed by [185] which is defined as the ratio of deflection divided by insertion length. Steerability defined by a ratio which is less than 1 (ratio < 1) dictates that the needle deflection is smaller than the insertion length, and similarly when the ratio is greater than 1 (ratio > 1) the deflection is larger than the insertion length. Thus, it serves as a metric to determine how much a needle can deflect for a certain length and therefore explains the limits of reach that a needle possesses inherently.

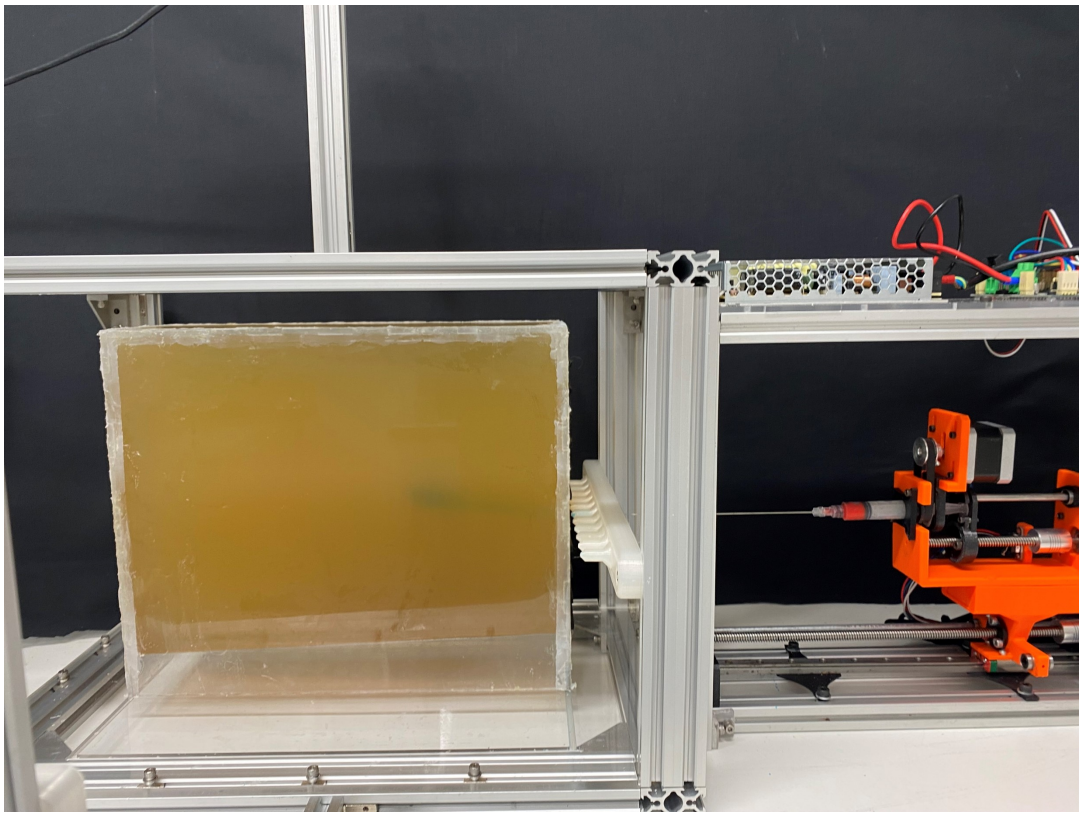

Figure 4.4: The steerable needle robot during operation.

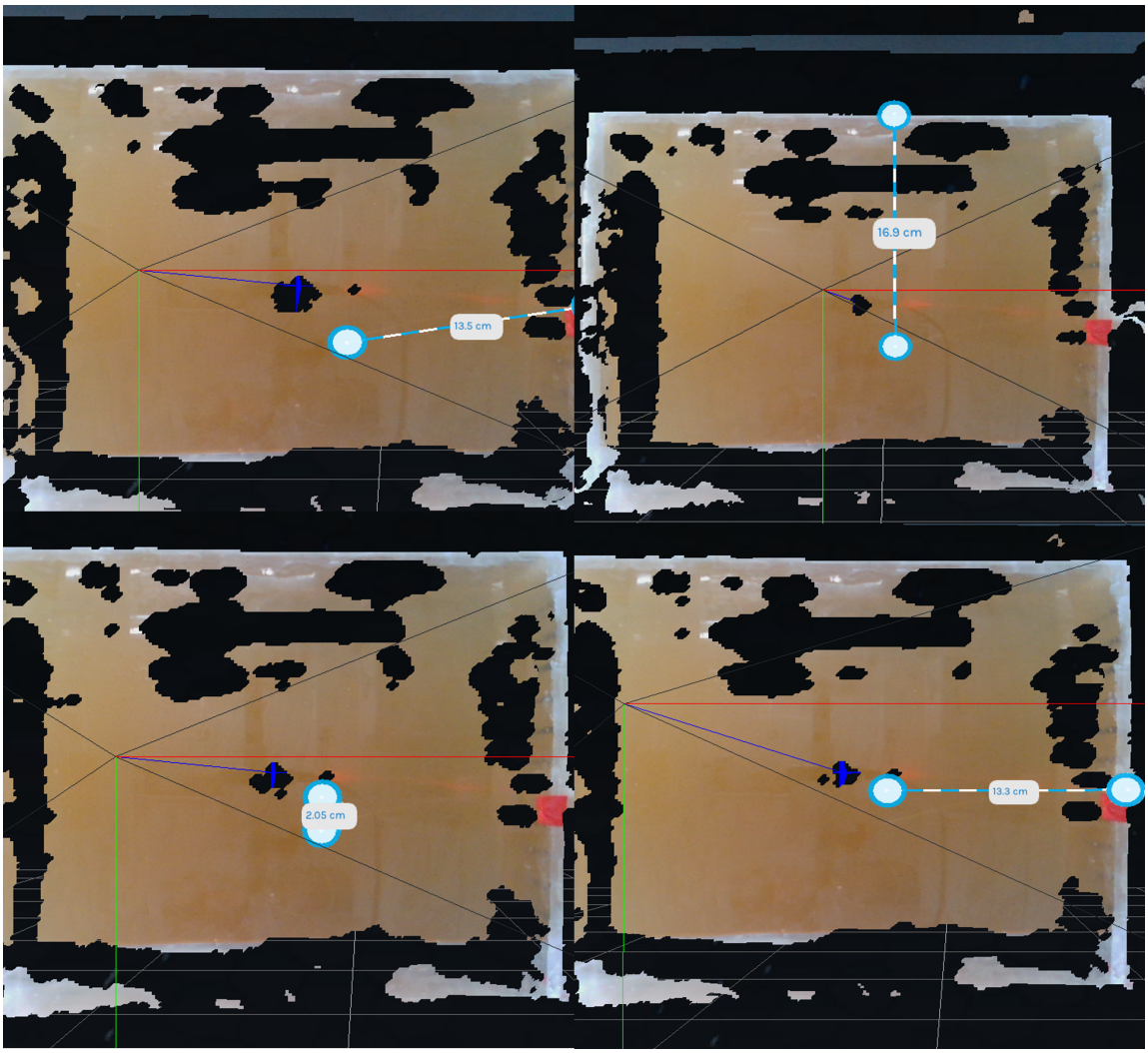

Figure 4.5: A graphic representation of the indentation test, specifically for the 10%wt specimen

4.3 Results

The aim of the designed experiments was to evaluate the performance of the proposed steerable needle robot within a phantom body. The following results attempt to define several factors associated with this performance, namely: the deflection associated with a needle as it interacts with the axial forces the body subjects its tip to; and the average reported accuracy of a trajectory generated by a motion plan utilising the previously acquired deflection value. Since this robot prototype is constrained by the needle size which it uses to attempt a 3D printing paradigm, the needle was tracked "offline" using the machine vision system as previously presented.

In Table 4.2, the results from experiment one is recorded and calculated to find the average deflection of the needle. In these results, it is clear that the needle has a maximum deflection of 20.96mm over an effective length of 135mm. When this deflection is subjected to the steerability metric, the result is particularly small which indicates relatively weak steerability. This is due to multiple factors: the 19G needle has an outer diameter of 1.067mm which is comparatively large to the needles using in literature [14, 81]; the mechanical properties of the stainless steel (304) needle results in greater rigidity and less flexibility which subsequently lowers the effective steerability.

This leads to the argument that a balance between steerability and what is now defined in this thesis injectability of a steerable needle is required in order to maximise the capabilities of a steerable needle robot. This, again, must also consider the tracking systems which play a significant role in the final accuracy of the system. These are complex problems that require development in order to achieve the ultimate aims which this thesis works towards.

Table 4.2: The effective deflection of the 19G needle using the steerable needle robot.

#	Insertion Length – IL (mm)	Deflection For Length – DF (mm)	Effective Deflection – Ratio: DF / IL (mm)
1	135.0	20.10	0.149
2	135.0	21.50	0.159
3	135.0	20.60	0.153
4	135.0	19.90	0.147
6	135.0	21.30	0.158
7	135.0	20.10	0.149
8	135.0	21.50	0.159
9	135.0	20.30	0.150
10	135.0	21.62	0.160
11	135.0	20.09	0.149
12	135.0	20.41	0.151
13	135.0	22.16	0.164
14	135.0	21.52	0.159
15	135.0	21.51	0.159
16	135.0	21.13	0.157
17	135.0	21.99	0.163
18	135.0	21.13	0.157
19	135.0	20.48	0.152
20	135.0	19.96	0.148
	Mean Deflection	20.96	0.155
	Standard Deviation	0.734	0.005

In Table 4.3, the results from experiment two are recorded and the x-y coordinates were calculated in attempt to determine the accuracy of the needle, excluding the z-axis at this time. The reported accuracy in the x-plane is approximately 2.13mm and in the y-plane it is 5.55mm. In Figure 4.6, there is little consistency in the output coordinates. Combining these reported accuracies, a general accuracy is calculated at 5.94mm. This is weakly comparable to other steerable needle robots reported in literature [2, 181, 52, 124]. It is worth noting, however, that the robot used in these experiments used an open-loop control scheme as opposed to other work. This accuracy, however, sets a good basis and platform for future research to refine the proposed systems and enable mechanism tailoring for a 3D printing application.

Table 4.3: The accuracy using a generated motion path towards a certain coordinate point within the body.

#	Theoretical Coord. x	Theoretical Coord. y	Real x	Real y	Coord. Diff. x	Coord. Diff. y
1	133.00	116.50	134.13	126.58	1.13	10.08
2	133.00	116.50	130.19	123.71	2.81	7.21
3	133.00	116.50	133.01	123.04	0.01	5.87
4	133.00	116.50	130.31	123.18	2.69	6.68
5	133.00	116.50	138.44	121.22	5.44	4.72
6	133.00	116.50	130.98	123.79	2.02	7.29
7	133.00	116.50	130.91	122.03	2.09	5.53
8	133.00	116.50	132.27	122.87	0.73	6.37
9	133.00	116.50	139.50	123.97	6.50	7.47
10	133.00	116.50	137.34	117.37	4.34	8.31
11	133.00	116.50	131.88	117.33	1.12	0.83
12	133.00	116.50	133.24	125.80	0.24	7.65
13	133.00	116.50	135.08	125.25	2.08	8.75
14	133.00	116.50	132.81	118.39	0.19	1.89
15	133.00	116.50	137.64	119.07	4.64	2.57
16	133.00	116.50	135.45	117.77	2.45	1.27
17	133.00	116.50	133.55	121.62	0.55	7.46
18	133.00	116.50	132.56	120.06	0.44	3.56
19	133.00	116.50	130.63	118.79	2.37	2.29
20	133.00	116.50	133.69	121.75	0.69	5.21
				Accuracy	2.13	5.55
				Standard Deviation	1.85	2.68

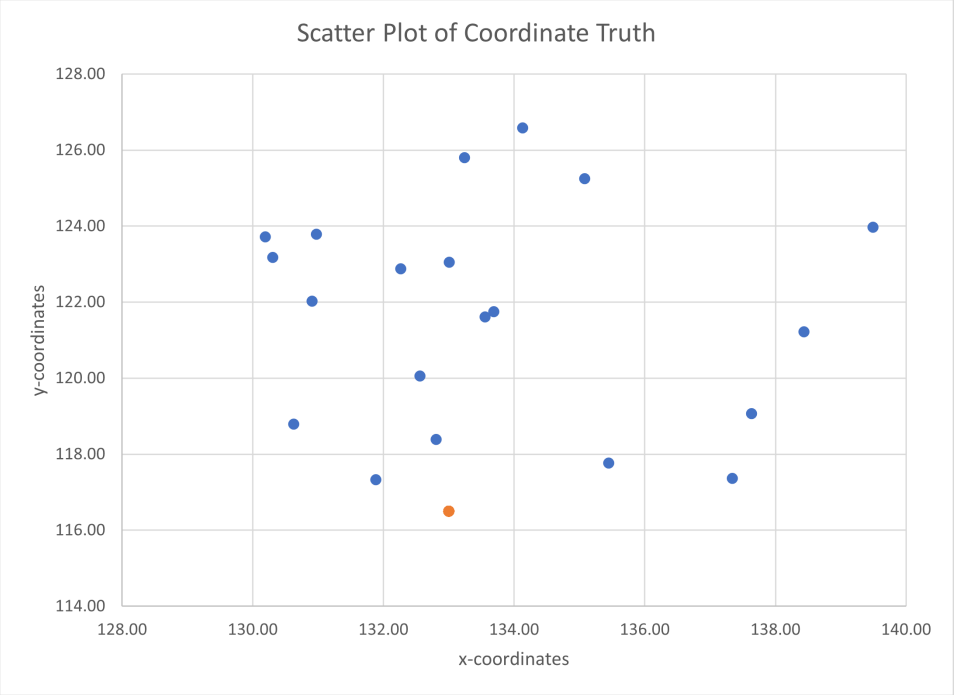

Figure 4.6: A scatter plot depicting the real x-y coordinates compared to the single point depicting the intended coordinate target.

4.4 Discussion

It is clear from these results that there are several limitations associated with the experiments as well as the proposed steerable needle robot design. The accuracy experiment was constrained to the x-y plane in order to simplify the assessment planned needle trajectory. The open-loop feedback associated with the camera visualisation system is another limitation due to the "offline" procedure currently instituted in the proposed robot. This significantly impacted the final accuracy of the system.

The final accuracy of a steerable needle robot could be influenced by various factors, including the roughness of the motor actuation. In particular, the rotation axis of the robot could be subject to irregularities that affect the smoothness of movement. Additionally, the forces exerted on the needle by the body during rotation can exacerbate this issue, leading to slight kinking and friction that further negatively impact accuracy. Therefore, it is crucial to ensure that the motor actuation is as smooth as possible and that the needle's interaction with the body is minimized to optimize accuracy.

Several improvements can be made to the steerable needle robot as a result of these experiments: 1. a closed feedback loop can be developed in conjunction with a more accurate and effective visualisation system utilising scanning technology like

electromagnetic tracking or Fibre Bragg Sensors; 2. more precise and finer control motors could be installed to minimise actuation jitter and improve the actuation precision.

4.5 Conclusions

This chapter presented two experiments for the assessment of the proposed steerable needle robot for the application of 3D printing (bio)polymers. The first experiment was a functional step towards the preparation for the trajectory generation of an entry point to an end goal. In the proposed system, the deflection of the needle over a set insertion length is required in the generation of possible trajectories. Once the deflection is manually acquired — in future it may be acquired using "online" tracking systems as well as the HSI approach previously described — the motion planner can generate a trajectory for the steerable needle robot.

This leads into the second experiment presented by this chapter. This experiment utilised trigonometry in conjunction with measurements taken by a machine vision system. The results from these calculations allowed for the determination of the coordinate points of the steerable needle tip in the real-world frame. These real coordinates were then compared with the theoretically defined and input coordinate points of the motion planner. Subsequently, the outcome accuracy as defined by this experiment is an acceptable starting point considering the limitations and constraints currently associated with a steerable needle robot for 3D printing. However, this accuracy may be refined utilising more advanced technology and techniques as well as the further advancement of certain aspects of this technology from a research point of view.

In future, several steps may be taken in order to refine the robot: first, more intelligent tracking and visualisation systems may be employed consisting of fibre optic sensors, electromagnetic tracking, ultrasounds, or CT scanning; secondly, the tracking system will be integrated in a closed feedback loop with the motion planner in order to enable "live" and "online" updating of the needle trajectory as it travels through a body; thirdly, a needle may be designed with greater tracking and steerability capabilities while simultaneously allowing for the 3D printing of relatively large quantities of polymers.

Thus far, several key aspects of a steerable needle robot have been explored — the electro-mechanical systems in conjunction with a control scheme and a motion plan, a methodology through which to assess and begin to estimate the properties of a phantom body, and the assessment of a steerable needle robot specification as presented by this chapter. This definition of the steerable needle robot is floating in the sense that upon refinement of its aspects these experiments may be repeated in order to improve the output accuracy. It is now possible to relatively accurately reach a target within a body, and thus the next stage of this research would be to investigate the "3D printing" process as applied to a steerable needle robot as well as the characterisation of the "3D printed" output as a result.

Chapter 5

An evaluation of steerable needle 3D printed bio-fibres

What we plant in the soil of contemplation, we shall reap in the harvest of action. — Meister Eckhart

This chapter presents the extraction, washing, and mechanical analysis of "3D printed" calcium alginate fibres embedded using the steerable needle robot proposed by this thesis. It also contributed towards a publication and presentation in The 16th Global Congress on Manufacturing and Management (GCMM 2022), see Appendix C.

5.1 Introduction

In this thesis, we previously defined the use of steerable needles for various surgical tasks that require flexible bevel-tipped needles, as is well-known in the medical field. These tasks may include drug delivery [41], catheter insertions [81], biopsies [46], or any other procedure that requires the navigation and reaching of specific targets within the body.

This study focuses on the novel concept of 3D printing a biopolymer effectively *in situ* for future *in vivo* use in the field of medical technology. To achieve this, we must address several challenges, such as establishing a three-dimensional (3D) coordinate space [42] to correctly identify internal structures and critical areas for the procedure, as well as steering a needle of specific geometries along a curvilinear path towards the end-goal. Additionally, an unexplored concept involves depositing fibres, wires, or other polymerisable materials to create new structures or facilitate regeneration.

Exploring this concept has the potential to revolutionize regenerative medicine by

enabling the development of new treatment modalities. However, achieving this goal requires addressing several challenges, including the biocompatibility of the materials used, optimizing the deposition process, and accurately navigating the needle towards the target site.

By overcoming these challenges, we can unleash the potential of 3D printing *in situ* as a powerful tool for regenerative medicine. The innovative approach of depositing new structures or materials within the body can open up new possibilities for treating a range of medical conditions. Through this study, we aim to contribute to the growing body of research in this exciting area of medical technology.

Medical application of this concept is still blue-sky research, however, a step towards this ultimate idea is presented here using the latest concepts in steerable needles [159] and attempting an integration with polymer chemistry and mechanisms often associated with 3D printing. This work explores a methodology through which simple fibres can be 3D printed in a phantom body (e.g., gelatine) avoiding all internal obstacles and following a specific curved trajectory. This involves using passive steerable needles (e.g., bevel-tipped) with well-defined kinematics to manipulate the needle tip to a point in a specific orientation.

This study explores the concept of utilizing steerable needles to 3D print biopolymers such as sodium alginate in a specific orientation inside a soft body. The system is reversed while concurrently depositing the biopolymer using a syringe pump system integrated with the steerable needle mechanisms. However, there are several challenges associated with this process. One of the main issues is the difficulty in initiating the polymerization process concurrently with the deposition of the material, similar to conventional Fused Deposition Modelling (FDM) techniques where a change in temperature can fuse polymer to polymer. In this case, temperature-based polymerization is challenging since the temperature at which polymers are injected into the body must be lower than the human body temperature (37^{o}C) [131]

To validate the hypothesis that steerable needles can function as a mechanism for 3D printing polymers in a pre-defined soft body, the polymerization process is simplified by utilizing a well-known polymer interaction called ionic polymerization [202]. Sodium alginate and calcium chloride are combined, where an ionic interaction occurs to form a solid fibre as a gel. Despite this, there are still several material science challenges that must be addressed to achieve the research's goal. This chapter fulfills Objective 3 as described in the Introduction.

Since sodium alginate and calcium chloride cross-link to form calcium alginate gels relatively well known in the biomedical field, etc. [7], this polymer chemistry was selected as the basis for this investigation into the effectiveness of steerable needles as a 3D printing (or additive manufacturing) mechanical approach which holds the advantage

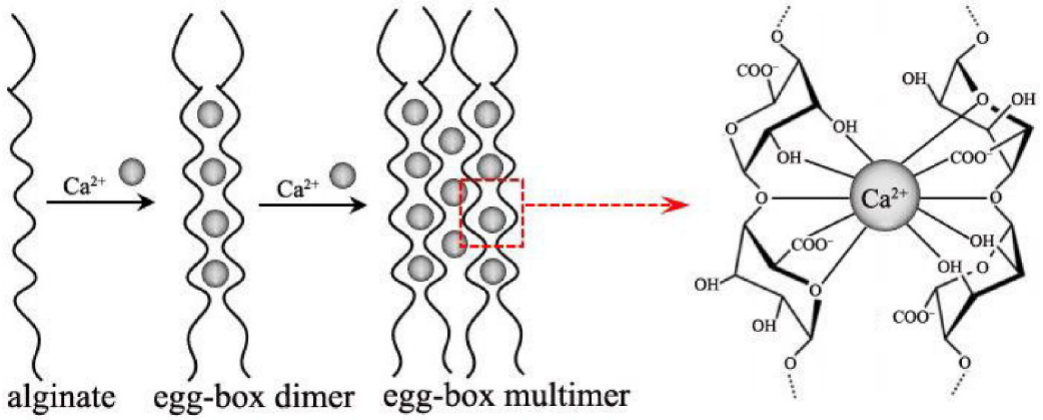

Figure 5.1: The chain conformation of the alginate molecular chain — G block — in response to a calcium ion. "Reproduced from [178] with permission from the Royal Society of Chemistry under the Creative Commons Attribution License"

of enabling the potential printing inside a pre-existing system or body as opposed to the traditional approach. This "injection" system deposits sodium alginate in the specific length and orientation that is desired inside of the phantom body. Subsequently, calcium chloride is added to the mixture and polymerisation is initiated, hence the "gelling" of the two polymers resulting in an embedded calcium alginate fibre. This work explores only a simple and unresponsive embedded calcium chloride fibre, however, a 4D printing aspect can be associated with this process where using certain polymers can be polymerised and embedded while simultaneously performing a certain function or providing reactivity to stimulus (such as heat, light, or electrical current, etc.) [102].

A technique through which a fibre or networks of fibres can be embedded in a soft body using certain polymerisation processes is presented in this chapter. Furthermore, the fibres were investigated for their physical characteristics in terms of diameter and mass as well as their mechanical properties in terms of linear density, tenacity, and elongation break.

5.2 Background

Alginate is a linear polysaccharide polymer which is, generally, extracted from brown algae. Due to its ability to gel or crosslink with polymers that possess metal ions, it offers a variety of different preparation strategies, such as electro-spinning, wet-spinning, freeze drying, and morphology of outputs like hydrogel fibres, fabrics, membranes, etc., [230]. Alginate polymerises through a process where the carboxyl groups of alinate and metal ions (calcium ions Ca^{2+}) form a coordination bond with the molecular chain of the alginate, see Figure 5.1. Alginate fibres are used in biomedical applications such as

tissue engineering scaffolds for skin, heart, microvessels, as well as for the reconnecting of severed muscle tissue [93]. It is effective as a tissue engineering scaffold due to its capabilities as an extracellular medium matrix which supports the encapsulation and growth of cells towards normal and stable cell function. Furthermore, it is considered to be an ideal biomaterial due its ability to imitate the physiochemical environment of the biological tissue and its biocompatibility, it serves as an effective material for tissue repair and regeneration.

Alginate fibres are known for their excellent hydrophilic properties and high moisture absorption capacity. These fibres can store water up to ten times their own weight, making them ideal for various biomedical applications [167, 214]. Recently, Roopavath et al. [178] reported the development of a 3D printable nanoparticle ink for bone regeneration, which utilizes a sodium alginate and gelatine composite to form a bone-graft. However, their proposed hydrogel ink falls under the traditional paradigm of 3D printing, where the bone graft must be surgically implanted after fabrication.

One of the main challenges associated with alginate fibre fabrication is the uncontrollable rate at which the fibres form. This can result in uneven structure and weaken the overall structural integrity of the fibre, leading to poor distribution of stress and concentration of stress in certain focal areas of the fibres, resulting in fibre failure at those areas. Although several studies have attempted to prolong the fibre formation rate, they have reported a decrease in the mechanical performance of the fibres [104, 135]. To address this issue, further research is required to optimize the fabrication process and improve the mechanical properties of alginate fibres.

A key reported challenge in the fabrication alginate fibres is the uncontrollable rate at which the fibres forms. This can cause uneven structure in fibres and create weaknesses in the total structural integrity of the fibre in question. This results in poor distribution of stress and a resulting concentration of stress in certain focal areas of the fibres and thence fibre failure at these areas. Several works attempt to prolong this formation rate but, have reported a decrease in the mechanical performance of the fibres [104, 135].

Theoretically, the steerable needle technique proposed in this thesis could offer methodology through which inks such as this may be directly 3D printed *in situ* and *in vivo*. Such combination of advanced materials science and robotics presents a promising opportunity for significant impact within the medical industry. For the purposes of this thesis, the mechanical properties of alginate fibres "3D printed" by this technique are explored to gain further insights into the capabilities and limitations of the flexible steerable needle 3D printing approach.

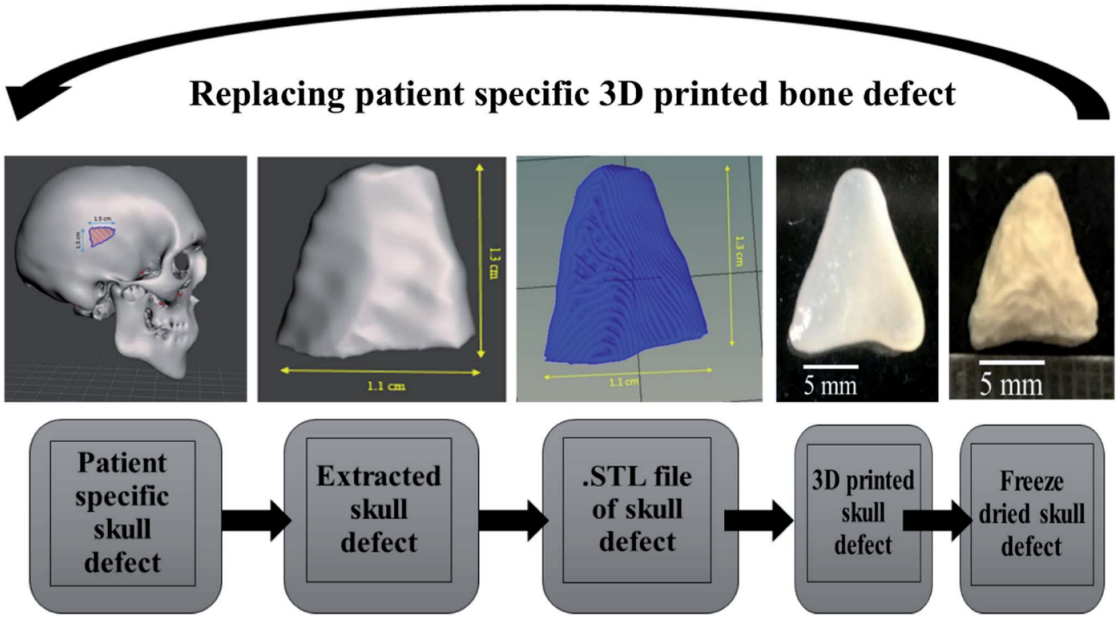

Figure 5.2: A bone-graft 3D printing process using alginate based bioink. "Reproduced from [178] with permission from the Royal Society of Chemistry under the Creative Commons Attribution License"

5.3 Materials and Method

5.3.1 Gelatine Phantom Preparation

The gelatine phantom is prepared using 250 bloom 20 mesh gelatine (GELITA Australia Pty Ltd). The gelatine powder is mixed into 10 litres of cold water at a concentration of 10%. This mixture is left to 'bloom' for 15 minutes after which it is heated to 60^{o} C and kept at this temperature while stirring for 10 minutes. The liquid gelatine is then poured into a custom-built acrylic tank (330mm x 110mm x 270mm), specifically to enable the testing of the steerable needles within the experimental platform. Once poured by running the gelatine liquid down the side of the tank to minimise the formation of bubbles, the tank is stored at 2^{o} C for 24 hours after which it is used to test the 3D printing of fibres within 72 hours.

5.3.2 Sodium Alginate Preparation

Alginic acid sodium salt from brown algae (W201502 Sodium Alginate, Sigma-Aldrich) was used in this study as the injectable polymer. Anhydrous, granular calcium chloride (C1016 Sigma-Aldrich) served as the material through which the sodium alginate was cross-linked. The needle used is a 10-inch, 19G, stainless steel (304) needle courtesy of Sigma-Aldrich (Z219355). A concentration of 2% sodium alginate solution in distilled water is prepared in a 100mL screw-cap tube and placed on a rocker platform at 21^{o} C overnight until fully dissolved.

5.3.3 Calcium Chloride Preparation

A calcium chloride bath is prepared of approximately 15 litres water at 5% calcium chloride concentration. The solution is stirred until all granules have dissolved.

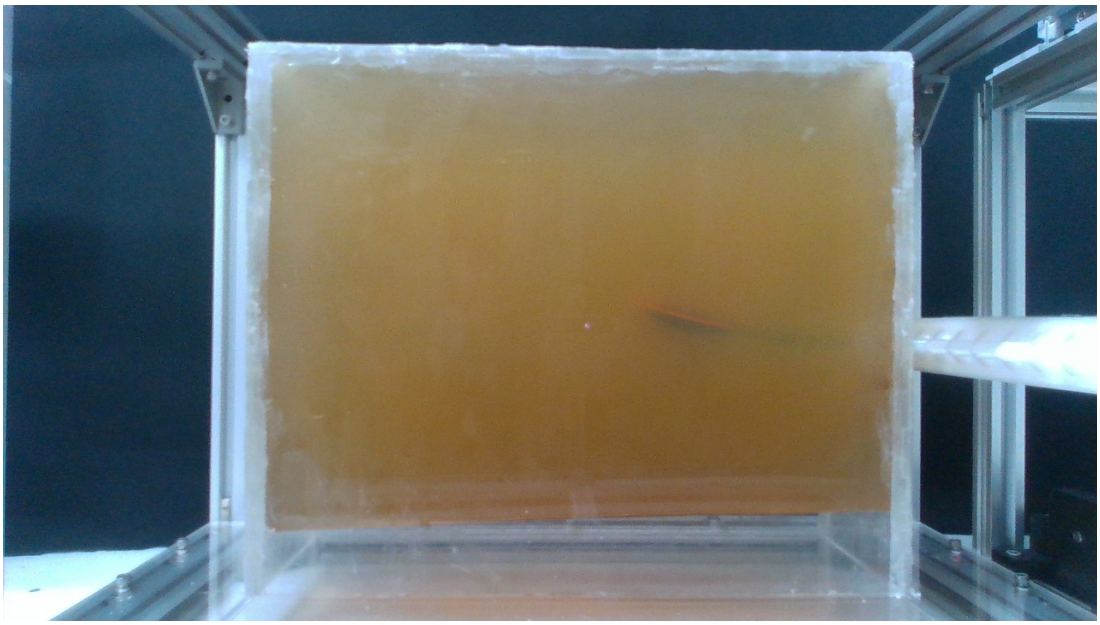

Figure 5.3: The side view of the steerable needle testbed with a view of the gelatine phantom body.

5.3.4 Steerable Needle Experimental Setup

To achieve the deposition of the sodium alginate solution, a custom steerable needle test bed was designed as previously shown in chapter 3 which consists of motors, a syringe pump, a needle sheath for stability, stereo-cameras to observe the needle associated with a computer vision system, and a platform (including a tank which consists of 6 entry points spaced 20mm apart) for the gelatine solution which can be used for other solutions or bodies, see Figure 5.3 and 5.4. This testbed makes use of several control kinematics based on previous research and achieves the generation of a simulation trajectory using steerability algorithms. This is integrated using a custom kinematics "slicer" which converts the coordinate-based trajectory into achievable motor positions. The kinematics, accuracy and position verifiability of start point to end goal using this system was explored in chapter 4. In the case of this experiment, no specific trajectory was entered and the needle was simply inserted with no rotation.

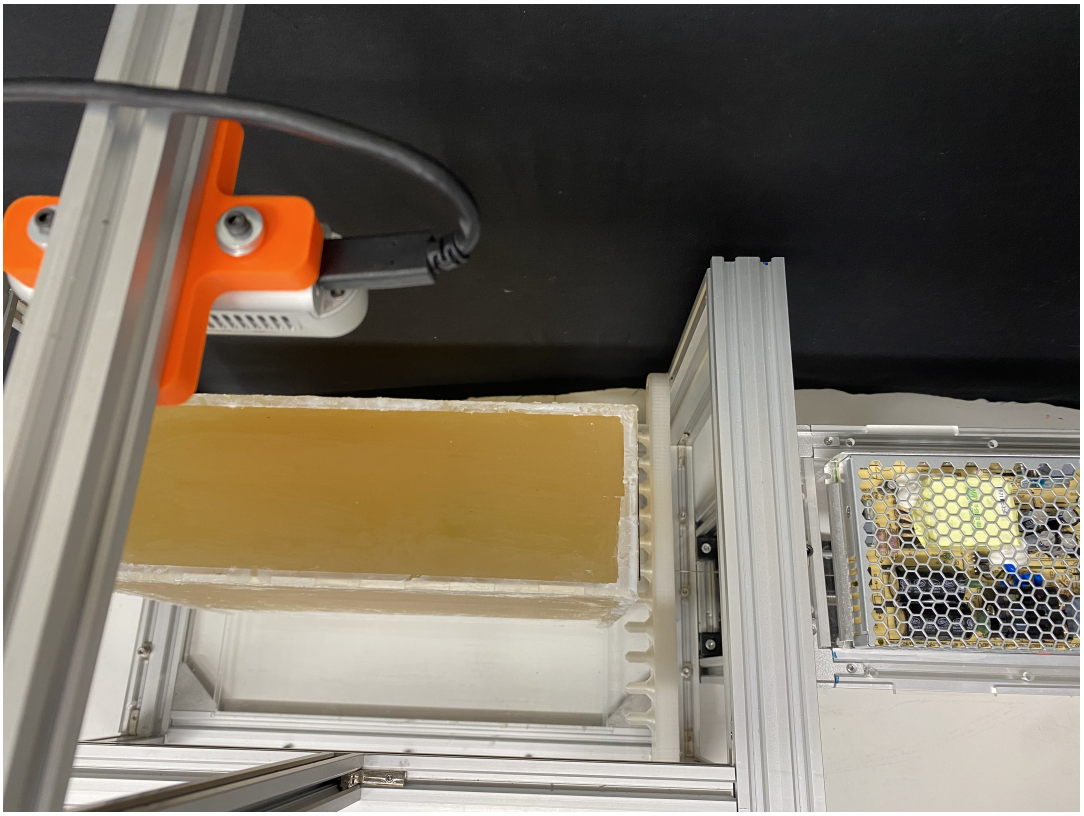

Figure 5.4: The top view of the steerable needle testbed with a view of the gelatine phantom body.

Figure 5.5: A view of alginate fibres formed *in situ* of the gelatine phantom body.

5.3.5 Calcium Alginate Fibre Formation Process

Using the steerable needle testbed controlled with a neutral path trajectory, i.e., simple insertion (150mm total) and full needle deflection without any steerability motions performed, the prepared sodium alginate solution which is loaded in a 10mL syringe is attached to the pumping mechanism of the testbed. Once the needle tip has achieved the end point of the trajectory, the controller begins the deposition process as the needle retracts from this position at a rate of 2mm/s. Sodium alginate solution is deposited at a rate of 0.01mL/mm over the entire insertion length. This equates to a total deposition of 1.5mL in the trajectory the needle has taken. This process may be repeated across the width and height of the gelatine tank, depending on the available entry point, and since the path of the needle could be controlled, a network of fibres could be prepared, but this is relegated to a future work where a network of simple fibres is 3D printed. Once all desired trajectories are deposited with the sodium alginate solution, the gelatine body or tank is lowered into the 15L 5% calcium chloride solution bath. The polymerisation effect is instantaneous, since the solution fills the still open cavities formed by the needle, see Figure 5.5. With more situationally effective polymer chemistry this process could be achieved even while the needle is still depositing. As a result, while the fibres are embedded in the gelatine, they have an equivalent length of 150mm and an effective diameter roughly equal to the diameter of the 19G needle. This may vary slightly due to mechanical jittering while the needle is traveling through

Figure 5.6: Separated blocks (250mm x 200mm x 150mm) of the gelatine phantom body enclosing the formed alginate fibres which is ready for extraction by subjecting the blocks to a temperature $> 35°$C.

the gelatine and due to possible uneven cross-linking, which may have a double effect of affecting the morphological structure and subsequent mechanical properties of the sodium alginate due to the speed at which it occurs [104].

5.3.6 Fibre Extraction Process

It is necessary that fibres are extracted from the gelatine for the purposes of mechanically testing the fibres which are embedded in the gelatine phantom. This is to determine the effectiveness of the polymerisation process by testing the homogeneity of the resulting fibres and the suitability of steerable needles in depositing a polymer and hence acting as a 3D printing technique. Since the gelatine body melts at approximately 35^{o} C, and from literature the resulting calcium alginate fibres have a melting point far beyond that of gelatine, the gelatine was heated, and the fibres removed. When these fibres are extracted using precision tweezers from the molten gelatine, they must be washed in cold water otherwise the gelatine acts as an effective coating. This process is incredibly delicate since calcium alginate fibres are particularly weak and tend to break apart

Figure 5.7: Partially-extracted calcium alginate fibres formed *inside of* gelatine using sodium alginate as the deposition and calcium chloride as the "binder" or reactant. The gelatine melts at $> 35°$C.

when wet. Unfortunately, the true length of fibres could not be preserved during this process. Once the varying length fibres are dipped in cold water and gently stirred to remove any attached gelatine, they are stored in a screw cap tube. For the purposes of these experiments, ten fibres were left to dry at $21^{\underline{o}}$ C and another ten were stored in distilled water, see Figures 5.6 and 5.7.

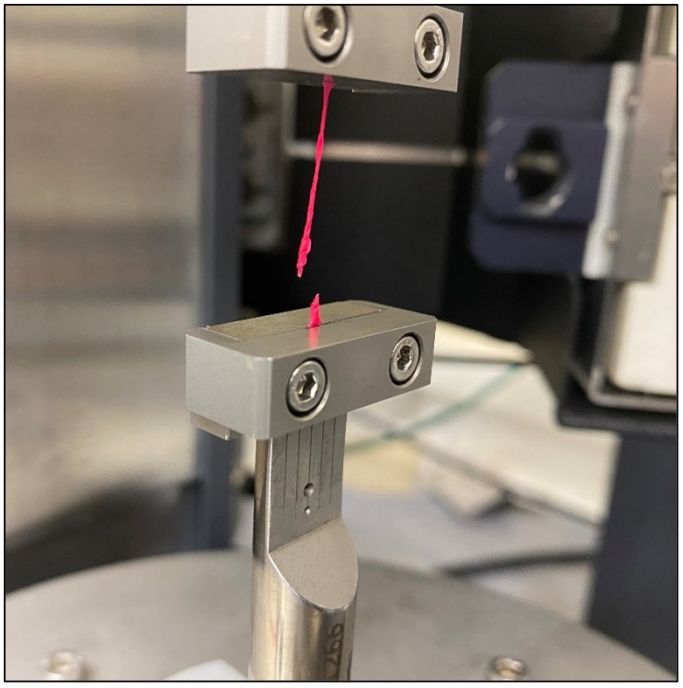

Figure 5.8: Cylinder tension fixture resulting a break of a calcium alginate fibre under load.

5.3.7 Calcium Alginate Fibre Mechanical Measurements

The mechanical analysis of the fibres was performed using an RSA-G2 solids analyser (TA Instruments, USA) using a quasi-static tensile testing geometry, see Figure 5.8. The linear rate of the geometry is 0.025mm/s acting in tension sampling 2.0 pts/s. Since the fibres were not formed perfectly evenly across their respective lengths and rarely conformed to a true cylindrical shape, the fibre diameters were approximated before undergoing any testing by recording the smallest diameter where they were most likely to break first. Secondly, the lengths and weights of the dry and wet fibres are recorded in data before being loaded into the geometry. Furthermore, this testing procedure complies with the ISO 5079:1999 standard to determine the breaking force and elongation at break of individual fibres. As such, the approximate linear density (dtex) of the fibres is determined to be equivalent to their overall mechanical strength through tenacity (cN/dtex) as a more accurate indicator than stress-strain since there is measurement error associated with the fibre diameters. Elongation at break, also known as ultimate elongation, is a measure of a material's ability to stretch before breaking. It is expressed as a percentage of the original length of the material and represents the maximum deformation the material can undergo before failure. When a material reaches its elongation at break point, it is no longer able to maintain its structural integrity and will fracture. The fibre masses, lengths, and minimum diameters with respect to their

moisture content is also explored in the results. As the fibres are extracted and washed, measure respective lengths and weights were measured immediately. After measuring their respective diameters, the fibres are then left to dry for an hour in a temperature and humidity-controlled environment. The fibres were then stored in multiple screw-cap tubes differentiating wet and dry.

5.4 Results and Discussion

The dry fibres exhibit a tenacity of approximately 7.5 ± 3.6 cN/dtex, with an elongation break of 0.624 ± 0.403, while the wet fibres show a tenacity of approximately 0.190 ± 0.096 cN/dtex, with an elongation break of 1.4 ± 0.5. These results clearly indicate that the dry fibres possess greater strength, as evidenced by their higher tenacity, and require more force to break as compared to wet fibres. However, the elongation break of dry fibres is lower than that of wet fibres, suggesting a lower level of plasticity.

Since the 19G needle has a nominal outer diameter of 1.067mm and it would be expected that the diameters of the fibres to equate to this value, however an approximately 26% reduction in diameter on average is seen in the results. This is most likely due to the sodium alginate not filling the entire cavity of the needle left by the needle when deposited. Furthermore, a shrinkage of the fibres is observed which is due to their total moisture content. The dry fibres possessing little to no moisture content, while the wet fibre possessing a variable quantity. One reducing factor for the accuracy of these results is the immediate drying effect caused by the surrounding environment as the fibres were loaded into the testing geometry. This effect may skew the results slightly. Interestingly, it can be noted that the dry fibres have an average mass of 0.0030 ± 0.00136g, while the wet fibres have an average mass of 0.0324 ± 0.0231g. This indicates a large variability in the total masses of the fibres specific to their moisture content. This difference is related to the total lengths associated with the fibre, but their total moisture content is the deciding factor in their masses.

As such, some dry fibres may not have perfectly dried out before testing and may have contained more moisture content than the rest, while some wet fibres dried out more than others before being tested. This is a limitation of this study. In any case, these differences are slight when comparing characteristically dry fibres with wet fibres – a mass difference of approximately 9.2%.

Interestingly, when this study's tenacity is compared to literature which reports a tenacity of approximately 10.21 cN/dtex for dry fibres and 2.51 cN/dtex for wet fibres [55] of 100% sodium alginate. These reported values are significantly different compared to the values found here (namely 7.26 cN/dtex dry to 0.19 cN/dtex wet). This is particularly evident in the comparison of the wet fibres' tenacity. However, when a gelatine / alginate blend fibre (namely a 3:7 ratio of alginate to gelatine) is considered,

Table 5.1: fibre Properties by Dry / Wet

Type	Diameter (mm)	Mass (mm)	Length (mm)	Tenacity (cN/d-tex)	Elongation Break
Dry	0.2390 ± 0.0729	0.0030 ± 0.0014	45.7590 ± 12.5725	7.2592 ± 3.5538	0.2390 ± 0.4029
Wet	0.3130 ± 0.0738	0.0324 ± 0.0232	55.9240 ± 16.1040	0.1899 ± 0.0958	0.3130 ± 0.5213

the values begin to align more closely – as reported 9.15 cN/dtex to 0.95 cN/dtex, see Figure 4. The conclusion is made in this paper that as gelatine content increases, so does the alginate fibre proportionally weaken. Therefore, the possibility that there is an interaction between the polymerisation of sodium alginate using calcium chloride and the gelatine phantom is considered.

Further investigation is required to exactly pinpoint whether the extraction process which heats both the gelatine, and the fibre causes an effective footprint on the alginate fibre weakening the fibre after its gelation. Another hypothesis is the effect that the heated gelatine has potentially caused the gelatine to bind to the alginate fibre which is also heated to the same degree thus altering its mechanical properties and essentially producing a hybrid fibre, particularly in the wet state which is the greatest indicator that there is an interaction when compared to literature. Alternatively, the calcium chloride and sodium alginate contents have a direct effect on the properties of the fibre with literature reporting a direct relationship between concentrations of calcium chloride and sodium alginate interactions to create fibres with greater linear densities. Another consideration to make is the process through which the fibres are formed which may directly impact the properties of these fibres. There is, however, relatively good parity with the tenacity properties reported by other works [25, 167, 216].

In terms of fibre homogeneity as it is polymerised, the relative weights by length of the fibre must be considered with respect to their estimated diameters. Since length is not a significant factor due the loading geometry fixing the fibres and only 20 mm being effective per fibre. However, when the approximate minimum diameters are considered as recorded before loading into the tensile testing geometry, it can be concluded that there is some shrinkage associated with the evaporation of the moisture content. This corresponds with the recorded weights in Table 5.1 where the dry fibres are demonstrably lighter than the wet fibres. Furthermore, the fact that certain structural discrepancies may exist between the fibres is observed because of the fabrication, extraction, and drying processes. Namely, the specific morphology and structural integrity non-visible unless magnified using a microscope (e.g., SEM). These factors primarily contribute to

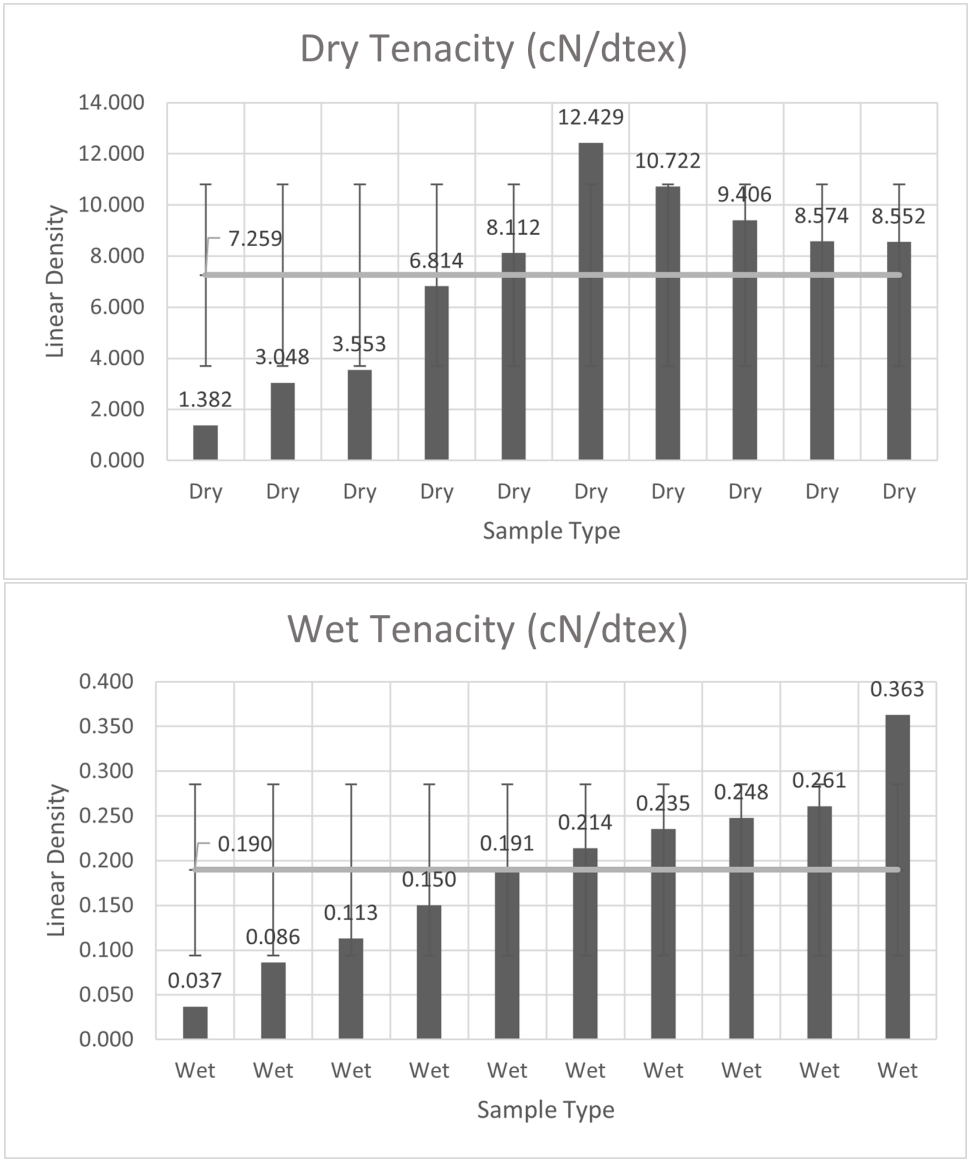

Figure 5.9: Dry / Wet tenacity graphs which depicts the mean value across the population of samples and allows their visual comparison.

the variations observed in the measurements and explains the differences between fibres as observed in the tensile test.

5.5 Chapter Conclusions

This chapter presented a novel approach to fabricating calcium alginate fibres essentially in vivo. It further explored the experimental setup required to achieve the task of depositing and subsequently polymerising a fibre. The cross-linking of two biopolymers (sodium alginate and calcium chloride) results in a relatively homogeneous fibre of a specific length and in a specific orientation embedded in a phantom tissue (gelatine) to simulate the human body. Relatively homogeneously formed calcium alginate fibres were observed using the tensile testing apparatus through the tenacity model of interpretation using steerable needles. The variations between fibre samples are because of the relative moisture content of the fibres, as well minor difference in their formation during the cross-linking process.

As such, steerable needles arranged in a 3D printing setup holds much potential especially when the challenges associated with the interface of biopolymers and the human body can be overcome. This research contributes to a body of work which seeks to define steerable needles as principal method in the 3D printing of structures internal to pre-existing bodies (human or otherwise) and seeks to play a part in the future fabrication of structures such as muscle, nerves, bone, etc.

Future work involves: the formation of complex calcium alginate networks in vivo using a phantom like gelatine; an investigation into the characteristics of these fibres while still embedded in the body; the application of fibres in vivo with 4D capability (i.e., reactivity to outside stimulus); the further advancement of a 3D printing capable steerable needle system to enable different polymerisation strategies in any suitable body; the improvement of the control systems of a steerable needle 3D printer; the investigation, utilisation, and development of suitable (bio)polymers which can be used in this system effectively. The preceding topics are concerned mainly with enabling the polymer chemistry to effectively fabricate fibres of certain characteristics using steerable needles as the primary deposition modality.

Chapter 6

Discussion

The price of inaction is far greater than the cost of making a mistake. — Meister Eckhart

The experiments and chapters presented in this thesis aimed to establish a fundamental basis for the development of steerable needles in 3D printing applications, particularly in medical surgery for animals and humans. The study established a process to embed fibres using steerable needles in any desired shape or trajectory. In the future, additional experimentation can be conducted to achieve fibre networks, utilize various polymer chemistry to achieve responsiveness to stimuli, or employ different polymerization strategies using steerable needles. These advancements will contribute to the development of more sophisticated and effective medical techniques, benefiting both animals and humans. This chapter explores these aims with respect to the research questions and aims as presented in Chapter 1. See Table 6.1 for a concise presentation of these questions, aims, and the objectives. With regard to the original hypothesis that was presented as a result of certain proof-concept-experiments and logical deduction based on literature, it is clear that its validation consisted of the product of the research questions, objectives, and outcomes which were developed through this research endeavour. In its validation, the ultimate question presented itself as, "How can 3D printing be achieved *in vivo* assuming that certain polymers desire to be embedded which offer certain functionality (e.g., shape changing behaviour)?". This question summarises the final goal of this thesis and seeks to answer it in technological and experimental terms.

The generation or embedding of simple bio-fibres is possible using steerable needle technology and bio-based polymers.

Figure 6.1: A table summarising the research questions, aims, and outputs.

Research Questions	Research Aims	Objectives	Related Chapters and Publications
i. What is a bio-fiber? **ii. Where and how should a bio-fiber be printed – describe the ideal processes and realistic expectations?** **iii. What stimuli exist to cause a reaction in a fiber – bio or otherwise?** **iv. What function could such a reaction serve?**	i. To gain an understanding of the underlying principles involved in constructs similar to natural muscle in terms of concepts such as electroactive actuators, artificial muscles, shape memory polymers, etc.	i. To identify the gaps in current technological capabilities in 3D printing bio-fibers using strategies such as bioprinting, etc.	Chapter 2 - Literature Review and Proof-of-concept experimentation
v. How could a bio-fiber be 3D printed internally and already in a desired location within a body (natural or synthetic)?	ii. To develop / advance robotic manufacturing systems in order to effectively 3D print or embed fibers in real world space or inside of a body.	ii. The development of a steerable needle robot with 3D printing strategies considered.	Chapter 3 – sections 3.1 - 3.4: - Publication in M2VIP2022 Chapter 3 – sections 3.5 – 3.9: - Publication in M2VIP2022 Chapter 4: - Two papers (in progress) written for publication in journals
vi. What drives this thesis investigation in terms of new knowledge or discovery for the fabrication of bio fibers? **vii. Why 3D printing and what types are currently available?** **viii. How is 3D printing used to develop this bio-fiber assuming a relevant implementation such as artificial muscles?**	iii. An exploration of the 3D printing technology currently available and the most suitable techniques and materials to effectively print bio-fibers. iv. An investigation into polymers (synthetic or bio-based) and the current state-of-the-art in their implementation within 3D printing or other processes. Answer the questions: "What polymers can effectively be used as bio-fibers?" and "How can these polymers be used?".	iii. To determine the technological and theoretical principles associated with 3D printing biopolymers from the engineering and materials science perspectives.	Chapter 5 - Publication in GCMM, see the Appendix

Chapter 2 performed a relatively large and indistinct survey (at the beginning) of the fields of bioprinting, 4D printing, polymer chemistry, artificial muscles and their associated fabrication techniques. It sought to identify and define research opportunities within or as a conglomerate of these specialties. From a broad perspective of the development of artificial muscles in terms of chemistry, manufacturing approaches, and performance, a further view was developed to attempt a relation between this and the field of 4D printing and / or bioprinting techniques.

Having thus established a solid literature basis for artificial muscles, their associated polymer chemistry, and potential techniques through which to 3D print them, certain proof-of-concept experiments were conducted in a simple manner to determine the fundamental theories which dictate the mechanisms associated with bioprinting or 4D printing. It is from these experiments that the opportunity of steerable needles as a 3D / 4D or bioprinting technique was identified. It is within the technological advancement, this thesis proposes, that the goal to achieve the embedding of artificial or natural muscles (as regeneration) *in vivo*. This seems, from a bird's eye perspective, akin to the realms of science fiction, however, the research opportunity remains and is worthy further development and investigation.

In order to gain a comprehensive understanding of the principles, kinematics, algorithms, and mechanisms of steerable needle robotics as a minimally invasive approach to surgical operations targeting specific diseases and organs in humans, an in-depth investigation was conducted. This chapter involved a thorough literature search, which was narrowed down to specific technologies that formed the basis for further development and alignment with the topical ideas proposed in this thesis. The following list summarizes the outcomes of this chapter:

1. Defined artificial muscles in terms of polymer chemistry and manufacturing approaches.
2. Reviewed additive manufacturing technology towards the fabrication of artificial muscles.
3. Identified opportunities using the aforementioned technology for the fabrication of artificial muscles.
4. Performed a proof-of-concept experiment to identify and summarise the current challenges and properties associated with these techniques.
5. Identified an opportunity using steerable needle technology to answer these challenges.
6. Undertook research to present a definition and exploration of steerable needle technology.

Chapter 3 utilised the outcomes of chapter two to undertake the development of a steerable needle robot in terms of its constituent components (see Objective 1). This included the implementation and development of the principles explored in chapter two. Namely, a motion planning algorithm was implemented to generate a path from several input variables — the needle properties, the entry point and goal point, the target body (assumed to be a gelatine block in experimentation, any obstacles within the body (set to none for experimentation purposes). A steerable needle robot with an injection or deposition system was then designed and built according to the specifications outlined in literature. This consisted of the development of an insertion and rotation mechanism; a visualisation and / or tracking system (stereoscopic cameras in the case of this thesis); an injection and needle positioning mechanism with respect to the actuation elements. This development forms part of the first sections (3.1–3.4) of this chapter. However, during this development a key problem was presented that needed immediate addressing: the needle-body interaction and a need to evaluate, estimate, and integrate this interaction in some form with the control mechanisms of the proposed robot.

As such, the latter sections of this chapter (3.5–3.9) explored the needle-body interactions associated with controlling a steerable needle using an electro-mechanical system. The behaviour of a needle as it travels through a body is related to the properties of the needle and the properties of the body in which it is inserted. The properties of the body were then explored in literature and an opportunity using hyperspectral imaging was identified for the evaluation and estimation of body properties before, during, or after a needle travels through this body. It then undertakes the building and comparison of approaches which estimate the mechanical properties of a body (e.g., gelatine). It is theorised from this work that these mechanical properties can be used in conjunction with hyperspectral imaging to estimate the needle-body interaction so as to take part in a closed feedback loop with steerable needle robot.

As a result of this chapter, a steerable needle robot is proposed with a hyperspectral imaging and camera system for the tracking and updating of a needle as it is inserted into a body during operation. The camera system, however, as proposed is only done for experimentation purposes as presented in chapter 4 and future work may be done where another methodology for tracking a needle is used such as: Fibre Bragg Sensors, CT scanning, ultrasound, etc. It is also clear as an outcome of this chapter that while a simple bevel-tipped needle can sufficiently be used for the application of 3D printing, new and more effective steerable needles may be designed to allow for optimal needle steerability with respect to a 3D printing application.

Chapter 4 presents an experimentation methodology for two key factors related to steerable needle robots. The first factor involves the maximum radius of curvature or deflection of a steerable needle as its tip interacts with the body. This is heavily related to the work presented in the latter sections of chapter 3. This characterisation of the deflection of the steerable needle robot contributes towards further development of the implemented control strategy to optimise the "reach" of a needle with respect to the possible / feasible trajectories towards a goal point. It is the relationship between the deflection of the needle as it is inserted into a body and the mechanical properties of that body which is a highly interesting and promising area in steerable needle and future research. Regardless, this chapter presented a methodology to estimate the mean deflection of the needle and thereafter attempted to utilise this deflection in a coordinate truth experiment where a custom trajectory is loaded, and the robot performs the operations to reach an arbitrarily selected end goal. Objective 2, as defined in the Introduction of this thesis, was achieved in chapter 4 effectively defining and exploring a potential methodology and associated parameters necessary to steer a needle tip of a certain geometry towards an end-goal accurately.

This second experiment involved a series of mathematical operations utilising several measurements made (within a certain level of accuracy) using the computer vision system as presented in chapter 3. These operations calculated the x and y coordinates of the needle tip after the insertion operation was completed and offered a direct comparison with the theoretical and expected "perfect" coordinates which thus offered a conclusive estimation of the accuracy to which the steerable needle robot is capable at this stage in development. For the applications of 3D printing as well as considering the other research in the pipelines as presented in the latter sections of chapter 3, the reported accuracy of approximately 6mm within a target goal is acceptable for the next step which is to perform 3D printing operations *in situ* towards eventual *in vivo* implementation.

Chapter 5 explored the specifications and procedures required in using a steerable needle robot to perform "3D printing" operations. This chapter, therefore, performed this exploration inn relation to the hypothesis and Objective 3 which dictated that a process to produce fibres *in situ* be demonstrated and that these fibres be investigated in terms of their structures and properties. Specifically, it presented the scope and metrics required in terms of a retraction rate — deposition rate ratio in order to not cause an "overload" in the deposition of material as well as a procedure through a biopolymer such as sodium alginate may be polymerised using its ionic gelling reaction with calcium chloride. As a result of this successfully proposed procedure, calcium alginate fibres could be effectively embedded in the phantom body. There are several limitations involved with this, however, being that the calcium chloride solution had to be added to the already deposited sodium alginate solution after its embedding. Future work could involve streamlining this procedure through the design of more advanced polymers which could theoretically be 3D printed in a continuous manner as opposed to the start-stop strategy as presented in this chapter.

These fibres once printed were then duly extracted out of the gelatine phantom body. Since calcium alginate fibres have different mechanical properties to the gelatine in which it was 3D printed, the fibres could safely be extracted after the melting of the gelatine body at a specific temperature. There were several challenges associated with this which is similarly reported in literature. When bioprinting is performed, the resulting printed material is usually particularly weak and can be destroyed easily without the support of an extra suspension matrix with which to support its structural integrity. This was the experience in the extraction of the calcium alginate fibres since they are in their printing supported by the gelatine in which they were placed to exist.

In any case, the fibres were preserved as best as possible through this extraction process, but since the fibres were approximately 135mm long embedded, they broke apart usually in half or in quarters. This resulted in slight difficulty in accurately reporting the average lengths and weights of the resulting samples. As such, the resulting fibres then underwent tensile testing in order to determine two potential facts: 1. the properties of the fibres compared with each other (i.e., is there consistency between the fibres utilising the steerable needle robot procedure?); 2. the properties of the fibres as compared to the fibres found in literature utilising other fabrication methodologies. It was found that the calcium alginate fibres differ greatly between the wet and dry states as well as slight differences in their properties.

As reported in literature, this is the tendency of calcium alginate fibres due to the speed of their gelation which causes inconsistency in their respective structures. There were, however, differences observed with the fibres as reported in literature with the fibres produced by this technique being slightly stronger in tenacity than their

equivalents in literature. This could be due to several factors which merit further investigation: 1. the extraction process heats the alginate and the gelatine at the same time and since the molten gelatine covers the alginate and despite attempts at washing these fibres there may be a thermal reaction between these two gels which could explain their greater strength; 2. the fibre source as well as the concentration of the alginate in solution with water may also contribute to their properties; 3. the water used in solution may contain certain minerals and other elements which contribute to slight variation in the preparation of the sodium alginate solution and as a result impact its mechanical properties after polymerisation.

Chapter 7

Thesis Conclusion and Recommendations

This thesis identified several opportunities within research fields not necessarily and obviously associated with each other. From artificial muscle fabrication to 3D printing with biopolymers and, finally, steerable needle robotics, it is clear that the potential research topics can be vast. Aspects of steerable needle robotics alone merit substantial amounts of research and development to effectively contribute towards the field and its effective understanding of the steerable needles. Therefore, with respect to the hypothesis as proposed with this thesis a final question is asked: "Can steerable needle robotics be used to 3D print biopolymers *in situ* or, otherwise, inside of a body?" In order to answer this question, the problems of this thesis are firstly summarised below:

- Artificial muscles and potential 3D printing techniques to effectively fabricate them.
- Polymer chemistry with respect to effective polymerisation strategies considering the constraints effected by steerable needle robotics.
- The motion planning, electro-mechanical systems, visualisation systems, and control systems present an extreme challenge in realising the ultimate aim of 3D printing *in vivo*.
- The associated polymer deposition strategy and polymerisation mechanisms involved in this process.

From these stated problems, which this thesis has attempted to account for and in some cases solve, certain contributions towards the combined field of steerable needle 3D printing may be suggested, as below:

- A developed steerable needle robot with 3D printing capabilities.

- A visualisation and control feedback system design using hyperspectral imaging and machine learning as an alternative method to machine vision as previously proposed in literature for steerable needle robotics.
  - This involves the estimation of the mechanical properties of the operable body in question using hyperspectral imaging, etc.
  - Thereafter utilising a mathematical relationship between these properties with respect to the needle properties in order to accurately steer the needle through the body.
- A methodology through which polymers may be deposited using a steerable needle robot.
- A suggested polymerisation strategy using said polymer chemistry in order to effectively polymerise the aforementioned materials *in situ*

There remains, however, exciting potential in future research regarding the topics of this thesis.

- The development of a more advanced integration between the hyperspectral imaging and machine learning model and the control and visualization systems of the steerable needle robot.
- The improvement in mechanism of the steerable needle robot in terms of its actuation capabilities as well as its polymer deposition capabilities
  - For example, a system could be developed where multiple polymers could be printed using the steerable needle robot at the same time or at least subsequent to each other using advanced mechanical design approaches and technology.
- The development of polymer chemistry specifically for this application of 3D printing *in vivo* using flexible steerable needle robotics.
- The design and engineering of a flexible steerable needle specifically for 3D printing while considering sensor integration, etc.

Another example of a more practical experiment which can be done in future is to effectively redo the experiment done by Luigi Galvani in 1780 where for the first time it was discovered that electricity can cause a physical response from muscle fibres. This experiment involved the replacement of the sciatic nerve in the leg of a frog with copper wire. It may be suggested that using the steerable needle 3D printing robot as proposed by this thesis that this sciatic may be replaced with conductive (bio)polymers without resorting to the need for open surgery. This is one potential proof-of-concept experiment which holds much value in the future of steerable needle 3D printing.

As a result, the conclusion can be made, when considering the proposed hypothesis presented through the conducted research as well as the thesis as argument in presenting a case for, that steerable needle robotics can, in fact, be used for 3D printing. Furthermore, steerable needle robotics holds great potential as a 3D printing or bioprinting technique since it steps away from the convention of petri dish 3D printing and offers a direct solution to potential problems within multiple industries, most notably, the field of tissue regeneration. A future, such as those imagined in science fiction, may be achieved through the continuation of research as presented by this thesis.

Bibliography

[1] p. d. m. 2015 and pratama dan marlinda 2015. XAAR 501 GS8, 1967. URL https://www.xaar.com/media/2387/xaar-501-gs8-datasheet-eng11.pdf.

[2] M. Abayazid, M. Kemp, and S. Misra. 3D flexible needle steering in soft-tissue phantoms using Fiber Bragg Grating sensors. *Proceedings - IEEE International Conference on Robotics and Automation*, pages 5843–5849, 2013. ISSN 10504729. doi: 10.1109/ICRA.2013.6631418.

[3] N. Abolhassani, R. Patel, and M. Moallem. Needle insertion into soft tissue: A survey. *Medical Engineering and Physics*, 29(4):413–431, 2007. ISSN 13504533. doi: 10.1016/j.medengphy.2006.07.003. URL https://www.sciencedirect.com/science/article/pii/S1350453306001457.

[4] M. Aboofazeli, P. Abolmaesumi, P. Mousavi, and G. Fichtinger. A new scheme for curved needle segmentation in threedimensional ultrasound images. *Proceedings - 2009 IEEE International Symposium on Biomedical Imaging: From Nano to Macro, ISBI 2009*, pages 1067–1070, 2009. doi: 10.1109/ISBI.2009.5193240.

[5] E. Acome, S. K. Mitchell, T. G. Morrissey, M. B. Emmett, C. Benjamin, M. King, M. Radakovitz, and C. Keplinger. Hydraulically amplified self-healing electrostatic actuators with muscle-like performance. *Science*, 359(6371):61–65, 1 2018. ISSN 0036-8075. doi: 10.1126/science.aao6139. URL https://www.sciencemag.org/lookup/doi/10.1126/science.aao6139.

[6] B. A. Aguado, W. Mulyasasmita, J. Su, K. J. Lampe, and S. C. Heilshorn. Improving viability of stem cells during syringe needle flow through the design of hydrogel cell carriers. *Tissue Engineering - Part A*, 18(7-8):806–815, 2012. ISSN 1937335X. doi: 10.1089/ten.tea.2011.0391. URL https://www.ncbi.nlm.nih.gov/pubmed/22011213.

[7] R. Ahmad Raus, W. M. F. Wan Nawawi, and R. R. Nasaruddin. Alginate and alginate composites for biomedical applications. *Asian Journal of Pharmaceutical Sciences*, 16(3):280–306, 2021. ISSN 1818-0876. doi: https://doi.org/10.1016/

j.ajps.2020.10.001. URL https://www.sciencedirect.com/science/article/pii/S1818087620306437.

[8] R. Alterovitz, K. Goldberg, and A. Okamura. Planning for steerable bevel-tip needle insertion through 2D soft tissue with obstacles. *Proceedings - IEEE International Conference on Robotics and Automation*, 2005(April):1640–1645, 2005. ISSN 10504729. doi: 10.1109/ROBOT.2005.1570348.

[9] R. Alterovitz, S. Patil, and A. Derbakova. Rapidly-exploring roadmaps: Weighing exploration vs. refinement in optimal motion planning. *Proceedings - IEEE International Conference on Robotics and Automation*, pages 3706–3712, 2011. ISSN 10504729. doi: 10.1109/ICRA.2011.5980286.

[10] A. Anthony, K. Hyun-Wook, L. S. Jin, and Y. James J. Integrated organ and tissue printing methods, system and apparatus, 2015. URL https://worldwide.espacenet.com/patent/search/family/045925755/publication/US2015119994A1?q=US2015%2F0119994.

[11] A. Arefi, B. Sturm, G. von Gersdorff, A. Nasirahmadi, and O. Hensel. Vis-NIR hyperspectral imaging along with Gaussian process regression to monitor quality attributes of apple slices during drying. *Lwt*, 152:112297, 2021. ISSN 00236438. doi: 10.1016/j.lwt.2021.112297. URL https://www.sciencedirect.com/science/article/pii/S002364382101450X.

[12] N. Arumugasaamy, H. B. Baker, D. S. Kaplan, P. C. W. Kim, and J. P. Fisher. Fabrication and Printing of Multi-material Hydrogels. In *3D Printing and Biofabrication*, chapter Chapter 13, pages 397–430. Springer International Publishing, Cham, 2018. ISBN 978-3-319-45443-6 978-3-319-45444-3. doi: 10.1007/978-3-319-45444-3{_}13. URL http://link.springer.com/10.1007/978-3-319-45444-3_13http://link.springer.com/10.1007/978-3-319-45444-3%7B%5C_%7D13.

[13] A. Atala. Tissue engineering of human bladder. *British Medical Bulletin*, 97(1):81–104, 2011. ISSN 00071420. doi: 10.1093/bmb/ldr003. URL https://www.ncbi.nlm.nih.gov/pubmed/21324973.

[14] M. A. Audette, S. P. Bordas, and J. E. Blatt. ¡p¿Robotically Steered Needles: A Survey of Neurosurgical Applications and Technical Innovations¡/p¿. *Robotic Surgery: Research and Reviews*, Volume 7:1–23, 2020. doi: 10.2147/rsrr.s224446.

[15] R. Balint, N. J. Cassidy, and S. H. Cartmell. Conductive polymers: Towards a smart biomaterial for tissue engineering. *Acta Biomaterialia*, 10(6):2341–2353,

2014. ISSN 18787568. doi: 10.1016/j.actbio.2014.02.015. URL https://www.ncbi.nlm.nih.gov/pubmed/24556448.

[16] Y. Bar-Cohen. Current and future developments in artificial muscles using electroactive polymers. *Expert Review of Medical Devices*, 2(6):731–740, 2005. ISSN 17452422. doi: 10.1586/17434440.2.6.731. URL https://www.ncbi.nlm.nih.gov/pubmed/16293100.

[17] Y. Bar-Cohen and I. A. Anderson. Electroactive polymer (EAP) actuators—background review. *Mechanics of Soft Materials*, 1(1):5, 12 2019. ISSN 2524-5600. doi: 10.1007/s42558-019-0005-1. URL http://link.springer.com/10.1007/s42558-019-0005-1.

[18] J. A. Barron, B. R. Ringeisen, H. Kim, B. J. Spargo, and D. B. Chrisey. Application of laser printing to mammalian cells. *Thin Solid Films*, 453-454:383–387, 2004. ISSN 00406090. doi: 10.1016/j.tsf.2003.11.161. URL https://www.sciencedirect.com/science/article/abs/pii/S004060900301681X?via%3Dihub.

[19] R. H. Baughman, L. W. Shacklette, R. L. Elsenbaumer, E. Plichta, and C. Becht. Conducting Polymer Electromechanical Actuators. In *Conjugated Polymeric Materials: Opportunities in Electronics, Optoelectronics, and Molecular Electronics*, pages 559–582. Springer, 1990. doi: 10.1007/978-94-009-2041-5{_}44.

[20] E. Belbachir, E. Golkar, B. Bayle, and C. Essert. Automatic planning of needle placement for robot-assisted percutaneous procedures. *International Journal of Computer Assisted Radiology and Surgery*, 13(9):1429–1438, 2018. ISSN 18616429. doi: 10.1007/s11548-018-1754-2. URL https://doi.org/10.1007/s11548-018-1754-2.

[21] K. H. Benam, S. Dauth, B. Hassell, A. Herland, A. Jain, K. J. Jang, K. Karalis, H. J. Kim, L. MacQueen, R. Mahmoodian, S. Musah, Y. S. Torisawa, A. D. Van Der Meer, R. Villenave, M. Yadid, K. K. Parker, and D. E. Ingber. Engineered in vitro disease models. *Annual Review of Pathology: Mechanisms of Disease*, 10:195–262, 2015. ISSN 15534014. doi: 10.1146/annurev-pathol-012414-040418. URL https://www.ncbi.nlm.nih.gov/pubmed/25621660https://www.annualreviews.org/doi/10.1146/annurev-pathol-012414-040418?url_ver=Z39.88-2003&rfr_id=ori%3Arid%3Acrossref.org&rfr_dat=cr_pub%3Dpubmed.

[22] T. Bhattacharjee, S. M. Zehnder, K. G. Rowe, S. Jain, R. M. Nixon, W. G. Sawyer, and T. E. Angelini. Writing in the granular gel

medium. *Science Advances*, 1(8):e1500655, 9 2015. ISSN 2375-2548. doi: 10.1126/sciadv.1500655. URL http://10.0.4.102/sciadv.1500655https://dx.doi.org/10.1126/sciadv.1500655https://advances.sciencemag.org/lookup/doi/10.1126/sciadv.1500655.

[23] E. S. Bishop, S. Mostafa, M. Pakvasa, H. H. Luu, M. J. Lee, J. M. Wolf, G. A. Ameer, T.-C. He, and R. R. Reid. 3-D bioprinting technologies in tissue engineering and regenerative medicine: Current and future trends. *Genes {\&} Diseases*, 4(4):185–195, 12 2017. ISSN 23523042. doi: 10.1016/j.gendis.2017.10.002. URL https://www.ncbi.nlm.nih.gov/pubmed/29911158https://linkinghub.elsevier.com/retrieve/pii/S2352304217300673.

[24] O. A. Bobrenkov, J. Lee, and W. Park. A new geometry-based plan for inserting flexible needles to reach multiple targets. *Robotica*, 32(6):985–1004, 2014. ISSN 14698668. doi: 10.1017/S0263574713001161.

[25] M. Boguń, T. Mikołajczyk, and S. Rabiej. Effect of formation conditions on the structure and properties of nanocomposite alginate fibers. *Journal of Applied Polymer Science*, 114(1):70–82, 2009. ISSN 00218995. doi: 10.1002/app.30465.

[26] T. Boland, V. Mironov, A. Gutowska, E. A. Roth, and R. R. Markwald. Cell and organ printing 2: Fusion of cell aggregates in three-dimensional gels. *Anatomical Record - Part A Discoveries in Molecular, Cellular, and Evolutionary Biology*, 272(2):497–502, 2003. ISSN 0003276X. doi: 10.1002/ar.a.10059. URL https://www.ncbi.nlm.nih.gov/pubmed/12740943.

[27] E. Breckenfeld, H. Kim, R. C. Y. Auyeung, and A. Piqué. Laser-induced Forward Transfer of Ag Nanopaste. *Journal of Visualized Experiments*, 2016 (109):e53728, 3 2016. ISSN 1940-087X. doi: 10.3791/53728. URL https://www.ncbi.nlm.nih.gov/pubmed/27077645https://www.ncbi.nlm.nih.gov/pmc/articles/PMC4841327/pdf/jove-109-53728.pdfhttp://www.jove.com/video/53728/laser-induced-forward-transfer-of-ag-nanopaste.

[28] P. Brochu and Q. Pei. Advances in Dielectric Elastomers for Actuators and Artificial Muscles. *Macromolecular Rapid Communications*, 31(1):10–36, 1 2010. ISSN 10221336. doi: 10.1002/marc.200900425. URL https://www.ncbi.nlm.nih.gov/pubmed/21590834https://onlinelibrary.wiley.com/doi/10.1002/marc.200900425.

[29] C. Caborni, S. Y. Ko, E. De Momi, G. Ferrigno, and F. R. Y Baena. Risk-based path planning for a steerable flexible probe for neurosurgical intervention. *Proceedings of the IEEE RAS and EMBS International Conference on Biomedical*

Robotics and Biomechatronics, -(0):866–871, 2012. ISSN 21551774. doi: 10.1109/BioRob.2012.6290859.

[30] E. Caló and V. V. Khutoryanskiy. Biomedical applications of hydrogels: A review of patents and commercial products. *European Polymer Journal*, 65:252–267, 2015. ISSN 00143057. doi: 10.1016/j.eurpolymj.2014.11.024.

[31] A. Cangialosi, C. K. Yoon, J. Liu, Q. Huang, J. Guo, T. D. Nguyen, D. H. Gracias, and R. Schulman. DNA sequence–directed shape change of photopatterned hydrogels via high-degree swelling. *Science*, 357(6356):1126–1130, 2017. ISSN 10959203. doi: 10.1126/science.aan3925.

[32] V. Caponigro, F. Marini, and A. Gowen. Hydration of hydrogels studied by near-infrared hyperspectral imaging. *Journal of Chemometrics*, 32(1):e2972, 2018. ISSN 1099128X. doi: 10.1002/cem.2972.

[33] F. Carpi, R. Kornbluh, P. Sommer-Larsen, and G. Alici. Electroactive polymer actuators as artificial muscles: Are they ready for bioinspired applications? *Bioinspiration and Biomimetics*, 6(4):45006, 2011. ISSN 17483182. doi: 10.1088/1748-3182/6/4/045006. URL `https://www.ncbi.nlm.nih.gov/pubmed/22126909`.

[34] N. J. Castro, W. Zhu, H. Cui, S.-J. Lee, and L. G. Zhang. 3D Bioprinting for Regenerative Engineering. In A. Khademhosseini and G. Camci-Unal, editors, *Regenerative Engineering*, pages 119–137. CRC Press, 4 2018. doi: 10.1201/9781315121079-7. URL `https://www.taylorfrancis.com/books/9781498738255/chapters/10.1201/9781315121079-7`.

[35] Q. Chai, Y. Jiao, and X. Yu. Hydrogels for biomedical applications: Their characteristics and the mechanisms behind them. *Gels*, 3(1), 2017. ISSN 23102861. doi: 10.3390/gels3010006.

[36] P. Chandrasekhar. *Conducting Polymers, Fundamentals and Applications*. Springer, 2018. ISBN 978-3-319-69376-7 978-3-319-69378-1. doi: 10.1007/978-3-319-69378-1.

[37] R. Chang, J. Nam, and W. Sun. Effects of dispensing pressure and nozzle diameter on cell survival from solid freeform fabrication-based direct cell writing. *Tissue Engineering - Part A.*, 14(1):41–48, 2008. ISSN 1937335X. doi: 10.1089/ten.a.2007.0004. URL `https://www.ncbi.nlm.nih.gov/pubmed/18333803`.

[38] S. Chiba, S. Stanford, R. Pelrine, R. Kornbluh, and H. Prahlad. Electroactive Polymer Artificial Muscle. *Journal of the Robotics Society of Japan*, 24 (4):466–470, 2006. ISSN 0289-1824. doi: 10.7210/jrsj.24.466. URL `http:`

//www.jstage.jst.go.jp/article/jrsj1983/24/4/24_4_466/_articlehttp://www.jstage.jst.go.jp/article/jrsj1983/24/4/24%7B%5C_%7D4%7B%5C_%7D466/%7B%5C_%7Darticle.

[39] G. S. Chirikjian. Conformational Modeling of Continuum Structures in Robotics and Structural Biology: A Review. *Advanced Robotics*, 29(13):817–829, 2015. ISSN 15685535. doi: 10.1080/01691864.2015.1052848. URL http://dx.doi.org/10.1080/01691864.2015.1052848.

[40] C. K. Chua and W. Y. Yeong. *Bioprinting: Principles and applications*. World Scientific Publishing Company, 2015. ISBN 9789814612128. doi: 10.1142/9193.

[41] M. J. Cotler, E. B. Rousseau, K. B. Ramadi, J. Fang, A. M. Graybiel, R. Langer, and M. J. Cima. Steerable Microinvasive Probes for Localized Drug Delivery to Deep Tissue. *Small*, 15(37):37–39, 2019. ISSN 16136829. doi: 10.1002/smll.201901459.

[42] N. J. Cowan, K. Goldberg, G. S. Chirikjian, G. Fichtinger, R. Alterovitz, K. B. Reed, V. Kallem, W. Park, S. Misra, and A. M. Okamura. Robotic needle steering: Design, modeling, planning, and image guidance. *Surgical Robotics: Systems Applications and Visions*, pages 557–582, 2011. doi: 10.1007/978-1-4419-1126-1{_}23.

[43] M. Czerner, L. S. Fellay, M. P. Suárez, P. M. Frontini, and L. A. Fasce. Determination of Elastic Modulus of Gelatin Gels by Indentation Experiments, 2015. ISSN 22118128.

[44] L. M. Dale, A. Thewis, C. Boudry, I. Rotar, P. Dardenne, V. Baeten, and J. A. Pierna. Hyperspectral imaging applications in agriculture and agro-food product quality and safety control: A review. *Applied Spectroscopy Reviews*, 48(2):142–159, 2013. ISSN 05704928. doi: 10.1080/05704928.2012.705800.

[45] N. V. Datla, B. Konh, and P. Hutapea. A flexible active needle for steering in soft tissues. *Proceedings of the IEEE Annual Northeast Bioengineering Conference, NEBEC*, 2014-Decem:1–2, 2014. ISSN 21607001. doi: 10.1109/NEBEC.2014.6972769.

[46] T. L. De Jong, N. J. van de Berg, L. Tas, A. Moelker, J. Dankelman, and J. J. van den Dobbelsteen. Needle placement errors: Do we need steerable needles in interventional radiology? *Medical Devices: Evidence and Research*, 11:259–265, 2018. ISSN 11791470. doi: 10.2147/MDER.S160444.

[47] S. Derakhshanfar, R. Mbeleck, K. Xu, X. Zhang, W. Zhong, and M. Xing. 3D bioprinting for biomedical devices and tissue engineering: A review of recent trends and advances. *Bioactive Materials*, 3 (2):144–156, 2018. ISSN 2452199X. doi: 10.1016/j.bioactmat.2017.11.008. URL `https://dx.doi.org/10.1016/j.bioactmat.2017.11.008https://www.ncbi.nlm.nih.gov/pmc/articles/PMC5935777/pdf/main.pdf`.

[48] T. Distler and A. R. Boccaccini. 3D printing of electrically conductive hydrogels for tissue engineering and biosensors – A review. *Acta Biomaterialia*, 101:1–13, 2020. ISSN 18787568. doi: 10.1016/j.actbio.2019.08.044. URL `https://doi.org/10.1016/j.actbio.2019.08.044`.

[49] A. Donder and F. R. Y. Baena. Kalman-Filter-Based, Dynamic 3-D Shape Reconstruction for Steerable Needles With Fiber Bragg Gratings in Multicore Fibers. *IEEE Transactions on Robotics*, 38(4):2262–2275, 2022. ISSN 19410468. doi: 10.1109/TRO.2021.3125853.

[50] R. Dong, P. X. Ma, and B. Guo. Conductive biomaterials for muscle tissue engineering. *Biomaterials*, 229:119584, 2020. ISSN 18785905. doi: 10.1016/j.biomaterials.2019.119584. URL `https://www.ncbi.nlm.nih.gov/pubmed/31704468`.

[51] B. Duan, L. A. Hockaday, K. H. Kang, and J. T. Butcher. 3D Bioprinting of heterogeneous aortic valve conduits with alginate/gelatin hydrogels. *Journal of Biomedical Materials Research - Part A*, 101 A(5):1255–1264, 2013. ISSN 15493296. doi: 10.1002/jbm.a.34420. URL `https://www.ncbi.nlm.nih.gov/pubmed/23015540`.

[52] G. Duchemin, P. Maillet, P. Poignet, E. Dombre, and F. Pierrot. A hybrid position/force control approach for identification of deformation models of skin and underlying tissues. *IEEE Transactions on Biomedical Engineering*, 52(2):160–170, 2005. ISSN 00189294. doi: 10.1109/TBME.2004.840505.

[53] V. Duindam, J. Xu, R. Alterovitz, S. Sastry, and K. Goldberg. 3D motion planning algorithms for steerable needles using inverse kinematics. *Springer Tracts in Advanced Robotics*, 57:535–549, 2010. ISSN 16107438. doi: 10.1007/978-3-642-00312-7{_}33.

[54] B. Fallahi, C. Rossa, R. Sloboda, N. Usmani, and M. Tavakoli. Partial estimation of needle tip orientation in generalized coordinates in ultrasound image-guided needle insertion. *IEEE/ASME International Conference on Advanced Intelligent Mechatronics, AIM*, 2016-Septe:1604–1609, 2016. doi: 10.1109/AIM.2016.7576999.

[55] L. Fan, Y. Du, R. Huang, Q. Wang, X. Wang, and L. Zhang. Preparation and characterization of alginate/gelatin blend fibers. *Journal of Applied Polymer Science*, 96(5):1625–1629, 2005. ISSN 00218995. doi: 10.1002/app.21610.

[56] J. Fauser, G. Sakas, and A. Mukhopadhyay. Planning nonlinear access paths for temporal bone surgery. *International Journal of Computer Assisted Radiology and Surgery*, 13(5):637–646, 2018. ISSN 18616429. doi: 10.1007/s11548-018-1712-z. URL `https://doi.org/10.1007/s11548-018-1712-z`.

[57] A. Favaro, L. Cerri, S. Galvan, F. R. Y. Baena, and E. De Momi. Automatic Optimized 3D Path Planner for Steerable Catheters with Heuristic Search and Uncertainty Tolerance. *Proceedings - IEEE International Conference on Robotics and Automation*, pages 9–16, 2018. ISSN 10504729. doi: 10.1109/ICRA.2018.8461262.

[58] A. Favaro, A. Segato, F. Muretti, and E. D. Momi. An Evolutionary-Optimized Surgical Path Planner for a Programmable Bevel-Tip Needle. *IEEE Transactions on Robotics*, 37(4):1039–1050, 2021. ISSN 19410468. doi: 10.1109/TRO.2020.3043692.

[59] G. Fichtinger, A. Deguet, K. Masamune, E. Balogh, G. S. Fischer, H. Mathieu, R. H. Taylor, S. J. Zinreich, and L. M. Fayad. Image overlay guidance for needle insertion in CT scanner. *IEEE Transactions on Biomedical Engineering*, 52(8):1415–1424, 2005. ISSN 00189294. doi: 10.1109/TBME.2005.851493.

[60] A. E. Forte, F. D'Amico, M. N. Charalambides, D. Dini, and J. G. Williams. Modelling and experimental characterisation of the rate dependent fracture properties of gelatine gels. *Food Hydrocolloids*, 46:180–190, 2015. ISSN 0268005X. doi: 10.1016/j.foodhyd.2014.12.028. URL `http://dx.doi.org/10.1016/j.foodhyd.2014.12.028`.

[61] K. O. Fu and A. Rosenfeld. Pattern Recognition and Computer Vision. *Computer*, 17(10):274–282, 1984. ISSN 00189162. doi: 10.1109/MC.1984.1658977.

[62] M. Fu, A. Kuntz, R. J. Webster, and R. Alterovitz. Safe Motion Planning for Steerable Needles Using Cost Maps Automatically Extracted from Pulmonary Images. *IEEE International Conference on Intelligent Robots and Systems*, pages 4942–4949, 2018. ISSN 21530866. doi: 10.1109/IROS.2018.8593407.

[63] M. Fu, O. Salzman, and R. Alterovitz. Toward Certifiable Motion Planning for Medical Steerable Needles. *Robotics: Science and Systems*, 2021. ISSN 2330765X. doi: 10.15607/RSS.2021.XVII.081.

[64] C. Gamonpilas, M. N. Charalambides, J. G. Williams, P. J. Dooling, and S. R. Gibbon. Predicting the mechanical behaviour of starch gels through inverse analysis of indentation data. *Applied Rheology*, 20(3):1–9, 2010. ISSN 14306395. doi: 10.3933/ApplRheol-20-33283.

[65] X. Gao, E. LeProust, H. Zhang, O. Srivannavit, E. Gulari, P. Yu, C. Nishiguchi, Q. Xiang, and X. Zhou. A flexible light-directed DNA chip synthesis gated by deprotection using solution photogenerated acids. *Nucleic Acids Research*, 29(22):4744–4750, 2001. ISSN 03051048. doi: 10.1093/nar/29.22.4744. URL `https://www.ncbi.nlm.nih.gov/pubmed/11713325`.

[66] Q. Ge, H. J. Qi, and M. L. Dunn. Active materials by four-dimension printing. *Applied Physics Letters*, 103(13), 2013. ISSN 00036951. doi: 10.1063/1.4819837. URL `https://aip.scitation.org/doi/10.1063/1.4819837`.

[67] D. Glozman and M. Shoham. Image-guided robotic flexible needle steering. *IEEE Transactions on Robotics*, 23(3):459–467, 2007. ISSN 15523098. doi: 10.1109/TRO.2007.898972.

[68] M. Gonzalez, J. Silva, M. Videla, and M. Orchard. Data-Driven Representations for Testing Independence: Modeling, Analysis and Connection with Mutual Information Estimation. In *IEEE Transactions on Signal Processing*, volume 70, pages 158–173, 2022. doi: 10.1109/TSP.2021.3135689.

[69] R. A. Green, R. T. Hassarati, J. A. Goding, S. Baek, N. H. Lovell, P. J. Martens, and L. A. Poole-Warren. Conductive Hydrogels: Mechanically Robust Hybrids for Use as Biomaterials. *Macromolecular Bioscience*, 12(4):494–501, 2012. ISSN 16165187. doi: 10.1002/mabi.201100490. URL `https://www.ncbi.nlm.nih.gov/pubmed/22344960`.

[70] D. A. Gregory, P. Kumar, A. Jimenez-Franco, Y. Y. Zhang, Y. Y. Zhang, S. J. Ebbens, and X. Zhao. Reactive Inkjet Printing and Propulsion Analysis of Silk-based Self-propelled Micro-stirrers. *Journal of Visualized Experiments*, 2019(146), 4 2019. ISSN 1940-087X. doi: 10.3791/59030. URL `https://www.ncbi.nlm.nih.gov/pubmed/31081811https://www.jove.com/video/59030/reactive-inkjet-printing-propulsion-analysis-silk-based-self`.

[71] V. Guarino, S. Zuppolini, A. Borriello, and L. Ambrosio. Electro-active polymers (EAPs): A promising route to design bio-organic/bioinspired platforms with on demand functionalities. *Polymers*, 8(5), 2016. ISSN 20734360. doi: 10.3390/polym8050185. URL `https://www.ncbi.nlm.nih.gov/pubmed/30979278`.

[72] A. Guiseppi-Elie. Electroconductive hydrogels: Synthesis, characterization and biomedical applications. *Biomaterials*, 31(10):2701–2716, 2010. ISSN 01429612. doi: 10.1016/j.biomaterials.2009.12.052. URL `https://www.ncbi.nlm.nih.gov/pubmed/20060580`.

[73] N. Hamzé, I. Peterlík, S. Cotin, and C. Essert. Preoperative trajectory planning for percutaneous procedures in deformable environments. *Computerized Medical Imaging and Graphics*, 47:16–28, 2016. ISSN 18790771. doi: 10.1016/j.compmedimag.2015.10.002.

[74] J. G. Hardy, R. C. Cornelison, R. C. Sukhavasi, R. J. Saballos, P. Vu, D. L. Kaplan, and C. E. Schmidt. Electroactive tissue scaffolds with aligned pores as instructive platforms for biomimetic tissue engineering. *Bioengineering*, 2(1): 15–34, 2015. ISSN 23065354. doi: 10.3390/bioengineering2010015.

[75] K. Hauser, R. Alterovitz, N. Chentanez, A. Okamura, and K. Goldberg. Feedback control for steering needles through 3D deformable tissue using helical paths. *Robotics: Science and Systems*, 5:289–296, 2010. ISSN 2330765X. doi: 10.15607/rss.2009.v.037.

[76] L. L. Hench, R. J. Splinter, W. C. Allen, and T. K. Greenlee. Bonding mechanisms at the interface of ceramic prosthetic materials. *Journal of Biomedical Materials Research*, 5(6):117–141, 1971. ISSN 10974636. doi: 10.1002/jbm.820050611.

[77] T. J. Hinton, Q. Jallerat, R. N. Palchesko, J. H. Park, M. S. Grodzicki, H. J. Shue, M. H. Ramadan, A. R. Hudson, and A. W. Feinberg. Three-dimensional printing of complex biological structures by freeform reversible embedding of suspended hydrogels. *Science Advances*, 1(9):e1500758, 2015. ISSN 23752548. doi: 10.1126/sciadv.1500758. URL `http://10.0.4.102/sciadv.1500758https://dx.doi.org/10.1126/sciadv.1500758`.

[78] T. J. Hinton, A. Hudson, K. Pusch, A. Lee, and A. W. Feinberg. 3D Printing PDMS Elastomer in a Hydrophilic Support Bath via Freeform Reversible Embedding. *ACS Biomaterials Science and Engineering*, 2(10):1781–1786, 2016. ISSN 23739878. doi: 10.1021/acsbiomaterials.6b00170. URL `http://10.0.3.253/acsbiomaterials.6b00170https://dx.doi.org/10.1021/acsbiomaterials.6b00170`.

[79] S. D. Hoath, editor. *Fundamentals of Inkjet Printing*. Wiley-VCH Verlag GmbH & Co. KGaA, Weinheim, Germany, 1 2016. ISBN 9783527684724. doi: 10.1002/9783527684724. URL `https://onlinelibrary.wiley.com/doi/book/10.1002/9783527684724http://doi.wiley.com/10.1002/9783527684724`.

[80] E. Hoch, T. Hirth, G. E. Tovar, and K. Borchers. Chemical tailoring of gelatin to adjust its chemical and physical properties for functional bioprinting. *Journal of Materials Chemistry B*, 1(41):5675–5685, 2013. ISSN 20507518. doi: 10.1039/c3tb20745e. URL http://dx.doi.org/10.1039/C3TB20745Ehttps://pubs.rsc.org/en/content/articlelanding/2013/TB/c3tb20745e.

[81] X. Hu, A. Chen, Y. Luo, C. Zhang, and E. Zhang. Steerable catheters for minimally invasive surgery: a review and future directions. *Computer Assisted Surgery*, 23 (1):21–41, 2018. ISSN 24699322. doi: 10.1080/24699322.2018.1526972. URL https://doi.org/10.1080/24699322.2018.1526972.

[82] C. Huang and Y. Lei. A novel model-based path planning method for robot-assisted flexible needle insertion. *IEEE International Conference on Automation Science and Engineering*, 2017-Augus:1414–1419, 2017. ISSN 21618089. doi: 10.1109/COASE.2017.8256301.

[83] S. Hunt, T. G. McKay, and I. A. Anderson. A self-healing dielectric elastomer actuator. *Applied Physics Letters*, 104(11), 2014. ISSN 00036951. doi: 10.1063/1.4869294.

[84] B. Huo, X. Zhao, J. Han, and W. Xu. Path-tracking control of bevel-tip needles using Model Predictive Control. *2016 IEEE 14th International Workshop on Advanced Motion Control, AMC 2016*, -(61273356):197–202, 2016. doi: 10.1109/AMC.2016.7496350.

[85] I. M. Hutchings and G. D. Martin. *Inkjet Technology for Digital Fabrication*. John Wiley & Sons, Ltd, Chichester, UK, 11 2012. ISBN 9781118452943. doi: 10.1002/9781118452943. URL http://doi.wiley.com/10.1002/9781118452943.

[86] C. B. Hutson, J. W. Nichol, H. Aubin, H. Bae, S. Yamanlar, S. Al-Haque, S. T. Koshy, and A. Khademhosseini. Synthesis and characterization of tunable poly(ethylene glycol): Gelatin methacrylate composite hydrogels. *Tissue Engineering - Part A*, 17(13-14):1713–1723, 2011. ISSN 1937335X. doi: 10.1089/ten.tea.2010.0666. URL https://www.ncbi.nlm.nih.gov/pubmed/21306293https://www.ncbi.nlm.nih.gov/pmc/articles/PMC3118706/.

[87] S. Iwanaga, K. Arai, and M. Nakamura. Inkjet Bioprinting. In *Essentials of 3D Biofabrication and Translation*, pages 61–79. Elsevier, 2015. ISBN 9780128010150. doi: 10.1016/B978-0-12-800972-7.00004-9. URL https://linkinghub.elsevier.com/retrieve/pii/B9780128009727000049.

[88] K. Jakab, A. Neagu, V. Mironov, and G. Forgacs. Organ printing: Fiction or science. *Biorheology*, 41(3-4):371–375, 2004. ISSN 0006355X. URL `https://www.ncbi.nlm.nih.gov/pubmed/15299269`.

[89] F. A. Johnston-Banks. Gelatine. *Food Gels*, pages 233–289, 1990. doi: 10.1007/978-94-009-0755-3{_}7.

[90] R. R. Jose, M. J. Rodriguez, T. A. Dixon, F. Omenetto, and D. L. Kaplan. Evolution of Bioinks and Additive Manufacturing Technologies for 3D Bioprinting. *ACS Biomaterials Science and Engineering*, 2(10):1662–1678, 2016. ISSN 23739878. doi: 10.1021/acsbiomaterials.6b00088.

[91] B. Kaczmarek, K. Nadolna, and A. Owczarek. The physical and chemical properties of hydrogels based on natural polymers. *Hydrogels Based on Natural Polymers*, pages 151–172, 2019. doi: 10.1016/B978-0-12-816421-1.00006-9.

[92] V. Kallem and N. J. Cowan. Image guidance of flexible tip-steerable needles. *IEEE Transactions on Robotics*, 25(1):191–196, 2009. ISSN 15523098. doi: 10.1109/TRO.2008.2010357.

[93] E. Kang, Y. Y. Choi, Y. J. Choi, and S. H. Lee. Microfludics spinning of flat fiber with micro grooves for cell-aligning scaffolds. In *Proceedings of the 16th International Conference on Miniaturized Systems for Chemistry and Life Sciences, MicroTAS 2012*, pages 1726–1728. Chemical and Biological Microsystems Society, 2012. ISBN 9780979806452.

[94] E. Käpylä, T. Sedlačík, D. B. Aydogan, J. Viitanen, F. Rypáček, and M. Kellomäki. Direct laser writing of synthetic poly(amino acid) hydrogels and poly(ethylene glycol) diacrylates by two-photon polymerization. *Materials Science and Engineering C*, 43:280–289, 2014. ISSN 09284931. doi: 10.1016/j.msec.2014.07.027. URL `https://www.ncbi.nlm.nih.gov/pubmed/25175215`.

[95] A. Katchalsky and M. Zwick. Mechanochemistry and ion exchange. *Journal of Polymer Science*, 16(82):221–234, 1955. ISSN 00223832. doi: 10.1002/pol.1955.120168212.

[96] A. Khademhosseini and R. Langer. A decade of progress in tissue engineering. *Nature Protocols*, 11(10):1775–1781, 2016. ISSN 17502799. doi: 10.1038/nprot.2016.123. URL `https://dx.doi.org/10.1038/nprot.2016.123https://www.nature.com/articles/nprot.2016.123`.

[97] F. Khosrosereshki, F. Rasouli, H. A. Talebi, F. Koochaki, and I. Sharifi. Path planning for insertion of a bevel tip steerable needle into a soft tissue in the

presence of obstacles. *22nd Iranian Conference on Electrical Engineering, ICEE 2014*, -(Icee):1348–1353, 2014. doi: 10.1109/IranianCEE.2014.6999743.

[98] K. Kim, S. I. Ahn, and K. C. Choi. Simultaneous synthesis and patterning of graphene electrodes by reactive inkjet printing. *Carbon*, 66:172–177, 2014. ISSN 00086223. doi: 10.1016/j.carbon.2013.08.055.

[99] D. Kongahage and J. Foroughi. Actuator Materials: Review on Recent Advances and{\&}{\#}13; Future Outlook for Smart Textiles. *Fibers*, 7(3):21, 3 2019. ISSN 2079-6439. doi: 10.3390/fib7030021. URL `https://www.mdpi.com/2079-6439/7/3/21`.

[100] A. Krieger, S. E. Song, N. Bongjoon Cho, I. I. Iordachita, P. Guion, G. Fichtinger, and L. L. Whitcomb. Development and evaluation of an actuated MRI-compatible robotic system for MRI-guided prostate intervention. *IEEE/ASME Transactions on Mechatronics*, 18(1):273–284, 2013. ISSN 10834435. doi: 10.1109/TMECH.2011.2163523.

[101] C. Kryou, V. Leva, M. Chatzipetrou, and I. Zergioti. Bioprinting for liver transplantation. *Bioengineering*, 6(4), 2019. ISSN 23065354. doi: 10.3390/bioengineering6040095. URL `https://www.ncbi.nlm.nih.gov/pubmed/31658719`.

[102] X. Kuang, D. J. Roach, J. Wu, C. M. Hamel, Z. Ding, T. Wang, M. L. Dunn, and H. J. Qi. Advances in 4D Printing: Materials and Applications. *Advanced Functional Materials*, 29(2):1–23, 2019. ISSN 16163028. doi: 10.1002/adfm.201805290.

[103] W. Kuhn, B. Hargitay, A. Katchalsky, and H. Eisenberg. Reversible dilation and contraction by changing the state of ionization of high-polymer acid networks. *Nature*, 165(4196):514–516, 1950. ISSN 00280836. doi: 10.1038/165514a0. URL `https://doi.org/10.1038/165514a0https://www.nature.com/articles/165514a0`.

[104] C. K. Kuo and P. X. Ma. Ionically crosslinked alginate hydrogels as scaffolds for tissue engineering: Part 1. Structure, gelation rate and mechanical properties. *Biomaterials*, 22(6):511–521, 2001. ISSN 01429612. doi: 10.1016/S0142-9612(00)00201-5. URL `https://doi.org/10.1016/S0142-9612(00)00201-5`.

[105] W. A. Laftah, S. Hashim, and A. N. Ibrahim. Polymer hydrogels: A review. *Polymer - Plastics Technology and Engineering*, 50(14):1475–1486, 2011. ISSN 03602559. doi: 10.1080/03602559.2011.593082.

[106] R. Lanza, R. Langer, and J. P. Vacanti. *Principles of Tissue Engineering: Fourth Edition*. CRC Press, 2013. ISBN 9780123983589. doi: 10.1016/C2011-0-07193-4.

[107] H. P. Le. Progress and trends in ink-jet printing technology. *Journal of Imaging Science and Technology*, 42(1):49–62, 1998. ISSN 10623701.

[108] J. Lee and W. Park. Insertion planning for steerable flexible needles reaching multiple planar targets. *IEEE International Conference on Intelligent Robots and Systems*, pages 2377–2383, 2013. ISSN 21530858. doi: 10.1109/IROS.2013.6696690.

[109] J. A. Lee, N. Li, C. S. Haines, K. J. Kim, X. Lepró, R. Ovalle-Robles, S. J. Kim, and R. H. Baughman. Electrochemically Powered, Energy-Conserving Carbon Nanotube Artificial Muscles. *Advanced Materials*, 29(31), 2017. ISSN 15214095. doi: 10.1002/adma.201700870. URL `https://www.ncbi.nlm.nih.gov/pubmed/28627770`.

[110] J. Y. Lee, J. An, and C. K. Chua. Fundamentals and applications of 3D printing for novel materials. *Applied Materials Today*, 7:120–133, 2017. ISSN 23529407. doi: 10.1016/j.apmt.2017.02.004.

[111] S. W. Lewis and K. F. Lim. Spectroscopy: Basic Principles. In J. A. Siegel, P. J. Saukko, and M. M. Houck, editors, *Encyclopedia of Forensic Sciences: Second Edition*, pages 635–640. Academic Press, Waltham, 2 edition, 2013. ISBN 9780123821652. doi: 10.1016/B978-0-12-382165-2.00256-7.

[112] N. L'heureux, S. Pâquet, R. Labbé, L. Germain, and F. A. Auger. A completely biological tissue-engineered human blood vessel. *The FASEB Journal*, 12(1):47–56, 1998. ISSN 0892-6638. doi: 10.1096/fasebj.12.1.47. URL `https://www.ncbi.nlm.nih.gov/pubmed/9438410`.

[113] J. Li, M. Chen, X. Fan, and H. Zhou. Recent advances in bioprinting techniques: Approaches, applications and future prospects. *Journal of Translational Medicine*, 14(1):271, 2016. ISSN 14795876. doi: 10.1186/s12967-016-1028-0. URL `https://www.ncbi.nlm.nih.gov/pubmed/27645770`.

[114] X. Li, C. A. Lehocky, and C. N. Riviere. Efficient 3D control for needle steering using duty-cycled rotation. *ICINCO 2013 - Proceedings of the 10th International Conference on Informatics in Control, Automation and Robotics*, 2:192–199, 2013. doi: 10.5220/0004456501920199.

[115] D. C. Lin, D. I. Shreiber, E. K. Dimitriadis, and F. Horkay. Spherical indentation of soft matter beyond the Hertzian regime: Numerical and experimental validation

of hyperelastic models. *Biomechanics and Modeling in Mechanobiology*, 8(5): 345–358, 2009. ISSN 16177959. doi: 10.1007/s10237-008-0139-9.

[116] G. Lu and B. Fei. Medical hyperspectral imaging: a review. *Journal of Biomedical Optics*, 19(1):010901, 2014. ISSN 1083-3668. doi: 10.1117/1.jbo.19.1.010901.

[117] J. D. W. Madden, N. A. Vandesteeg, P. A. Anquetil, P. G. A. Madden, A. Takshi, R. Z. Pytel, S. R. Lafontaine, P. A. Wieringa, and I. W. Hunter. Artificial muscle technology: Physical principles and naval prospects. *IEEE Journal of Oceanic Engineering*, 29(3):706–728, 2004. ISSN 03649059. doi: 10.1109/JOE.2004.833135.

[118] A. Majewicz, J. J. Siegel, A. A. Stanley, and A. M. Okamura. Design and evaluation of duty-cycling steering algorithms for robotically-driven steerable needles. *Proceedings - IEEE International Conference on Robotics and Automation*, pages 5883–5888, 2014. ISSN 10504729. doi: 10.1109/ICRA.2014.6907725.

[119] M. S. Mannoor, Z. Jiang, T. James, Y. L. Kong, K. A. Malatesta, W. O. Soboyejo, N. Verma, D. H. Gracias, and M. C. McAlpine. 3D printed bionic ears. *Nano Letters*, 13(6):2634–2639, 2013. ISSN 15306984. doi: 10.1021/nl4007744. URL `https://www.ncbi.nlm.nih.gov/pubmed/23635097`.

[120] D. G. Manolakis, R. B. Lockwood, and T. W. Cooley. *Hyperspectral Imaging Remote Sensing*. Cambridge University Press, 2016. doi: 10.1017/cbo9781316017876.

[121] M. R. Matanović, J. Kristl, and P. A. Grabnar. Thermoresponsive polymers: Insights into decisive hydrogel characteristics, mechanisms of gelation, and promising biomedical applications. *International Journal of Pharmaceutics*, 472(1-2):262–275, 2014. ISSN 18733476. doi: 10.1016/j.ijpharm.2014.06.029. URL `https://doi.org/10.1016/j.ijpharm.2014.06.029`.

[122] A. McCormack, C. B. Highley, N. R. Leslie, and F. P. W. Melchels. 3D Printing in Suspension Baths: Keeping the Promises of Bioprinting Afloat. *Trends in Biotechnology*, 38(6):584–593, 2020. ISSN 18793096. doi: 10.1016/j.tibtech.2019.12.020. URL `http://10.0.3.248/j.tibtech.2019.12.020https://dx.doi.org/10.1016/j.tibtech.2019.12.020`.

[123] S. Midha and S. Ghosh. Silk-based bioinks for 3D bioprinting. In *Regenerative Medicine: Laboratory to Clinic*, chapter Chapter 15, pages 259–276. 2017. ISBN 9789811037016. doi: 10.1007/978-981-10-3701-6{_}15.

[124] P. Mignon, P. Poignet, and J. Troccaz. Automatic Robotic Steering of Flexible Needles from 3D Ultrasound Images in Phantoms and Ex Vivo Biological Tissue.

Annals of Biomedical Engineering, 46(9):1385–1396, 2018. ISSN 15739686. doi: 10.1007/s10439-018-2061-3.

[125] D. S. Minhas, J. A. Engh, M. M. Fenske, and C. N. Riviere. Modeling of needle steering via duty-cycled spinning. *Annual International Conference of the IEEE Engineering in Medicine and Biology - Proceedings*, pages 2756–2759, 2007. ISSN 05891019. doi: 10.1109/IEMBS.2007.4352899.

[126] T. Mirfakhrai, J. D. W. Madden, and R. H. Baughman. Polymer artificial muscles. *Materials Today*, 10(4):30–38, 2007. ISSN 13697021. doi: 10.1016/S1369-7021(07)70048-2.

[127] V. Mironov, N. Reis, and B. Derby. Bioprinting: A beginning. *Tissue Engineering*, 12(4):631–634, 2006. ISSN 10763279. doi: 10.1089/ten.2006.12.631. URL `https://www.ncbi.nlm.nih.gov/pubmed/16674278`.

[128] V. Mironov, R. P. Visconti, V. Kasyanov, G. Forgacs, C. J. Drake, and R. R. Markwald. Organ printing: Tissue spheroids as building blocks. *Biomaterials*, 30(12):2164–2174, 2009. ISSN 01429612. doi: 10.1016/j.biomaterials.2008.12.084. URL `https://www.ncbi.nlm.nih.gov/pubmed/19176247`.

[129] V. Mironov, V. Kasyanov, and R. R. Markwald. Organ printing: From bioprinter to organ biofabrication line. *Current Opinion in Biotechnology*, 22(5):667–673, 2011. ISSN 09581669. doi: 10.1016/j.copbio.2011.02.006. URL `https://www.ncbi.nlm.nih.gov/pubmed/21419621`.

[130] S. M. Mirvakili and I. W. Hunter. Artificial Muscles: Mechanisms, Applications, and Challenges. *Advanced Materials*, 30(6), 2018. ISSN 15214095. doi: 10.1002/adma.201704407. URL `https://www.ncbi.nlm.nih.gov/pubmed/29250838`.

[131] O. A. Mohamed, S. H. Masood, and J. L. Bhowmik. Optimization of fused deposition modeling process parameters: a review of current research and future prospects. *Advances in Manufacturing*, 3(1):42–53, 2015. ISSN 21953597. doi: 10.1007/s40436-014-0097-7.

[132] N. I. Moldovan, N. Hibino, and K. Nakayama. Principles of the kenzan method for robotic cell spheroid-based three-dimensional bioprinting. *Tissue Engineering - Part B: Reviews*, 23(3):237–244, 2017. ISSN 19373376. doi: 10.1089/ten.teb.2016.0322. URL `https://www.ncbi.nlm.nih.gov/pubmed/27917703`.

[133] F. Momeni, S. M.Mehdi Hassani.N, X. Liu, and J. Ni. A review of 4D printing. *Materials and Design*, 122:42–79, 2017. ISSN 18734197. doi: 10.1016/j.matdes.2017.02.068.

[134] S. Mondal, S. Das, and A. K. Nandi. A review on recent advances in polymer and peptide hydrogels. *Soft Matter*, 16(6):1404–1454, 2020. ISSN 17446848. doi: 10.1039/c9sm02127b.

[135] Y. A. Mørch, I. Donati, B. L. Strand, and G. Skjåk-Bræk. Effect of Ca2+, Ba2+, and Sr2+ on alginate microbeads. *Biomacromolecules*, 7(5):1471–1480, 2006. ISSN 15257797. doi: 10.1021/bm060010d. URL `https://pubs.acs.org/sharingguidelines`.

[136] P. Moreira, S. Patil, R. Alterovitz, and S. Misra. Needle steering in biological tissue using ultrasound-based online curvature estimation. *Proceedings - IEEE International Conference on Robotics and Automation*, pages 4368–4373, 2014. ISSN 10504729. doi: 10.1109/ICRA.2014.6907495.

[137] G. Moretti, S. Rosset, R. Vertechy, I. Anderson, and M. Fontana. A Review of Dielectric Elastomer Generator Systems. *Advanced Intelligent Systems*, 2(10): 2000125, 2020. ISSN 2640-4567. doi: 10.1002/aisy.202000125.

[138] L. Moroni, T. Boland, J. A. Burdick, C. De Maria, B. Derby, G. Forgacs, J. Groll, Q. Li, J. Malda, V. A. Mironov, C. Mota, M. Nakamura, W. Shu, S. Takeuchi, T. B. Woodfield, T. Xu, J. J. Yoo, and G. Vozzi. Biofabrication: A Guide to Technology and Terminology. *Trends in Biotechnology*, 36(4):384–402, 2018. ISSN 18793096. doi: 10.1016/j.tibtech.2017.10.015. URL `https://www.ncbi.nlm.nih.gov/pubmed/29137814`.

[139] M. Motaharifar, H. A. Talebi, F. Abdollahi, and A. Afshar. Nonlinear Adaptive Output-Feedback Controller Design for Guidance of Flexible Needles. *IEEE/ASME Transactions on Mechatronics*, 20(4):1912–1919, 2015. ISSN 10834435. doi: 10.1109/TMECH.2014.2359181.

[140] A. Munaz, R. K. Vadivelu, J. St. John, M. Barton, H. Kamble, and N. T. Nguyen. Three-dimensional printing of biological matters. *Journal of Science: Advanced Materials and Devices*, 1(1):1–17, 2016. ISSN 24682179. doi: 10.1016/j.jsamd.2016.04.001.

[141] K. Murphy. Devices, Systems, and Methods for the Fabrication of Tissue (US20120116568), 2012. URL `http://goo.gl/0o8YXu`.

[142] S. V. Murphy and A. Atala. 3D bioprinting of tissues and organs. *Nature Biotechnology*, 32(8):773–785, 2014. ISSN 15461696. doi: 10.1038/nbt.2958. URL `http://10.0.4.14/nbt.2958https://dx.doi.org/10.1038/nbt.2958https://www.ncbi.nlm.nih.gov/pubmed/25093879`.

[143] H. R. S. Neshat and R. V. Patel. Real-time parametric curved needle segmentation in 3D ultrasound images. *Proceedings of the 2nd Biennial IEEE/RAS-EMBS International Conference on Biomedical Robotics and Biomechatronics, BioRob 2008*, pages 670–675, 2008. doi: 10.1109/BIOROB.2008.4762877.

[144] Z. Neubach and M. Shoham. Ultrasound-guided robot for flexible needle steering. *IEEE Transactions on Biomedical Engineering*, 57(4):799–805, 2010. ISSN 00189294. doi: 10.1109/TBME.2009.2030169.

[145] W. L. Ng, S. Wang, W. Y. Yeong, and M. W. Naing. Skin Bioprinting: Impending Reality or Fantasy? *Trends in Biotechnology*, 34(9):689–699, 2016. ISSN 18793096. doi: 10.1016/j.tibtech.2016.04.006. URL `https://www.ncbi.nlm.nih.gov/pubmed/27167724`.

[146] N. Noor, A. Shapira, R. Edri, I. Gal, L. Wertheim, and T. Dvir. 3D Printing of Personalized Thick and Perfusable Cardiac Patches and Hearts. *Advanced Science*, 6(11):1900344, 2019. ISSN 21983844. doi: 10.1002/advs.201900344. URL `http://10.0.3.234/advs.201900344https://dx.doi.org/10.1002/advs.201900344`.

[147] J. Odent, T. J. Wallin, W. Pan, K. Kruemplestaedter, R. F. Shepherd, and E. P. Giannelis. Highly Elastic, Transparent, and Conductive 3D-Printed Ionic Composite Hydrogels. *Advanced Functional Materials*, 27(33):1–10, 2017. ISSN 16163028. doi: 10.1002/adfm.201701807.

[148] S. Okazawa, R. Ebrahimi, J. Chuang, S. E. Salcudean, and R. Rohling. Hand-held steerable needle device. *IEEE/ASME Transactions on Mechatronics*, 10(3): 285–296, 2005. ISSN 10834435. doi: 10.1109/TMECH.2005.848300.

[149] K. Oliver, A. Seddon, and R. S. Trask. Morphing in nature and beyond: a review of natural and synthetic shape-changing materials and mechanisms. *Journal of Materials Science*, 51(24):10663–10689, 2016. ISSN 15734803. doi: 10.1007/s10853-016-0295-8.

[150] Y. Osada and J. P. Gong. Soft and wet materials: Polymer gels. *Advanced Materials*, 10(11):827–837, 1998. ISSN 09359648. doi: 10.1002/(SICI)1521-4095(199808)10:11⟨827::AID-ADMA827⟩3.0.CO;2-L.

[151] T. F. Otero and J. G. Martinez. Electro-chemo-biomimetics from conducting polymers: fundamentals, materials, properties and devices. *Journal of Materials Chemistry B*, 4(12):2069–2085, 2016. ISSN 2050750X. doi: 10.1039/C6TB00060F. URL `http://dx.doi.org/10.1039/C6TB00060Fhttps://pubs.rsc.org/en/content/articlelanding/2016/TB/C6TB00060F`.

[152] M. L. Oyen. Mechanical characterisation of hydrogel materials. *International Materials Reviews*, 59(1):44–59, 2014. ISSN 09506608. doi: 10.1179/1743280413Y.0000000022.

[153] I. T. Ozbolat and Y. Yu. Bioprinting toward organ fabrication: Challenges and future trends. *IEEE Transactions on Biomedical Engineering*, 60(3):691–699, 2013. ISSN 00189294. doi: 10.1109/TBME.2013.2243912. URL `https://www.ncbi.nlm.nih.gov/pubmed/23372076`.

[154] O. Pabst, J. Perelaer, E. Beckert, U. S. Schubert, R. Eberhardt, and A. Tünnermann. Inkjet printing of electroactive polymer actuators on polymer substrates, 2011. ISSN 0277786X.

[155] L. Pan, G. Yu, D. Zhai, H. R. Lee, W. Zhao, N. Liu, H. Wang, B. C. K. Tee, Y. Shi, Y. Cui, and Z. Bao. Hierarchical nanostructured conducting polymer hydrogel with high electrochemical activity. *Proceedings of the National Academy of Sciences of the United States of America*, 109(24):9287–9292, 2012. ISSN 00278424. doi: 10.1073/pnas.1202636109.

[156] M. E. Paoletti, J. M. Haut, J. Plaza, and A. Plaza. Deep learning classifiers for hyperspectral imaging: A review. *ISPRS Journal of Photogrammetry and Remote Sensing*, 158(November):279–317, 2019. ISSN 09242716. doi: 10.1016/j.isprsjprs.2019.09.006. URL `https://doi.org/10.1016/j.isprsjprs.2019.09.006`.

[157] I. S. Park, K. Jung, D. Kim, S. M. Kim, and K. J. Kim. Physical principles of ionic polymer-metal composites as electroactive actuators and sensors. *MRS Bulletin*, 33(3):190–195, 2008. ISSN 08837694. doi: 10.1557/mrs2008.44.

[158] S. Patil and R. Alterovitz. Interactive motion planning for steerable needles in 3D environments with obstacles. *2010 3rd IEEE RAS and EMBS International Conference on Biomedical Robotics and Biomechatronics, BioRob 2010*, pages 893–899, 2010. doi: 10.1109/BIOROB.2010.5625965.

[159] S. Patil, J. Burgner, R. J. Webster, and R. Alterovitz. Needle steering in 3-D Via rapid replanning. *IEEE Transactions on Robotics*, 30(4):853–864, 2014. ISSN 15523098. doi: 10.1109/TRO.2014.2307633.

[160] N. Paxton, W. Smolan, T. Böck, F. Melchels, J. Groll, and T. Jungst. Proposal to assess printability of bioinks for extrusion-based bioprinting and evaluation of rheological properties governing bioprintability. *Biofabrication*, 9(4):44107, 2017. ISSN 17585090. doi: 10.1088/1758-5090/aa8dd8. URL `https://www.ncbi.nlm.nih.gov/pubmed/28930091`.

[161] S. M. Peltola, F. P. Melchels, D. W. Grijpma, and M. Kellomäki. A review of rapid prototyping techniques for tissue engineering purposes. *Annals of Medicine*, 40(4):268–280, 2008. ISSN 07853890. doi: 10.1080/07853890701881788. URL https://www.ncbi.nlm.nih.gov/pubmed/18428020.

[162] R. F. Pereira and P. J. Bártolo. 3D bioprinting of photocrosslinkable hydrogel constructs. *Journal of Applied Polymer Science*, 132(48):n/a–n/a, 2015. ISSN 10974628. doi: 10.1002/app.42458. URL https://onlinelibrary.wiley.com/doi/pdfdirect/10.1002/app.42458?download=true.

[163] M. Pinzi, T. Watts, R. Secoli, S. Galvan, and F. R. Y. Baena. Path Replanning for Orientation-Constrained Needle Steering. *IEEE Transactions on Biomedical Engineering*, 68(5):1459–1466, 2021. ISSN 15582531. doi: 10.1109/TBME.2021.3060470.

[164] G. H. Pollack. Polymer-gel phase-transition as the mechanism of muscle contraction. *Materials Research Society Symposium - Proceedings*, 600:237–247, 2000. ISSN 02729172. doi: 10.1557/proc-600-237. URL https://www.cambridge.org/core/journals/mrs-online-proceedings-library-archive/article/polymergel-phasetransition-as-the-mechanism-of-muscle-contraction/B8EB93A79F243294E300FA29933F8FCD.

[165] R. R. Pullanagari and M. Li. Uncertainty assessment for firmness and total soluble solids of sweet cherries using hyperspectral imaging and multivariate statistics. *Journal of Food Engineering*, 289:110177, 2020. ISSN 02608774. doi: 10.1016/j.jfoodeng.2020.110177.

[166] R. R. Pullanagari, M. Dehghan-Shoar, I. J. Yule, and N. Bhatia. Field spectroscopy of canopy nitrogen concentration in temperate grasslands using a convolutional neural network. *Remote Sensing of Environment*, 257:112353, 2021. ISSN 00344257. doi: 10.1016/j.rse.2021.112353.

[167] Y. Qin. Alginate fibres: An overview of the production processes and applications in wound management. *Polymer International*, 57(2):171–180, 2008. ISSN 09598103. doi: 10.1002/pi.2296.

[168] S. Ramakrishnan. From a laboratory curiosity to the market place. *Resonance*, 16 (12):1254–1265, 12 2011. ISSN 0971-8044. doi: 10.1007/s12045-011-0141-x. URL http://link.springer.com/10.1007/s12045-011-0141-x.

[169] C. E. Rasmussen and C. K. I. Williams. *Gaussian Processes for Machine Learning*. The MIT Press, 2018. ISBN 026218253X. doi: 10.7551/mitpress/3206.001.0001.

[170] L. Ravikanth, D. S. Jayas, N. D. White, P. G. Fields, and D. W. Sun. Extraction of Spectral Information from Hyperspectral Data and Application of Hyperspectral Imaging for Food and Agricultural Products. *Food and Bioprocess Technology*, 10(1):1–33, 2017. ISSN 19355149. doi: 10.1007/s11947-016-1817-8. URL `http://dx.doi.org/10.1007/s11947-016-1817-8`.

[171] D. Raviv, W. Zhao, C. McKnelly, A. Papadopoulou, A. Kadambi, B. Shi, S. Hirsch, D. Dikovsky, M. Zyracki, C. Olguin, R. Raskar, and S. Tibbits. Active printed materials for complex self-evolving deformations. *Scientific Reports*, 4:7422, 2014. ISSN 20452322. doi: 10.1038/srep07422. URL `https://www.ncbi.nlm.nih.gov/pmc/articles/PMC4270353/pdf/srep07422.pdf`.

[172] K. B. Reed, V. Kallem, R. Alterovitzt, K. Goldberg, A. M. Okamura, and N. J. Cowan. Integrated planning and image-guided control for planar needle steering. *Proceedings of the 2nd Biennial IEEE/RAS-EMBS International Conference on Biomedical Robotics and Biomechatronics, BioRob 2008*, pages 819–824, 2008. doi: 10.1109/BIOROB.2008.4762833.

[173] S. M. Richardson-Burns, J. L. Hendricks, and D. C. Martin. Electrochemical polymerization of conducting polymers in living neural tissue. *Journal of Neural Engineering*, 4(2), 2007. ISSN 17412560. doi: 10.1088/1741-2560/4/2/L02.

[174] C. Robert. *Machine Learning, a Probabilistic Perspective*, volume 27. MIT Press, Cambridge, Mass. [u.a.], 2014. ISBN 9780262018029 0262018020. doi: 10.1080/09332480.2014.914768.

[175] M. Rocca, A. Fragasso, W. Liu, M. A. Heinrich, and Y. S. Zhang. Embedded Multimaterial Extrusion Bioprinting. *SLAS Technology*, 23(2):154–163, 2018. ISSN 24726311. doi: 10.1177/2472630317742071. URL `http://10.0.4.153/2472630317742071https://dx.doi.org/10.1177/2472630317742071`.

[176] E. Rodr, A. P. Kypson, S. C. Moten, L. W. Nifong, and W. R. C. Jr. Robotic mitral surgery at East Carolina University :. *International Journal*, -(April): 211–215, 2006. doi: 10.1002/rcs.

[177] J. M. Romano, R. J. Webster, and A. M. Okamura. Teleoperation of steerable needles. *Proceedings - IEEE International Conference on Robotics and Automation*, -(April):934–939, 2007. ISSN 10504729. doi: 10.1109/ROBOT.2007.363105.

[178] U. K. Roopavath, R. Soni, U. Mahanta, A. S. Deshpande, and S. N. Rath. 3D printable SiO2 nanoparticle ink for patient specific bone regeneration. *RSC Advances*, 9(41):23832–23842, 2019. ISSN 20462069. doi: 10.1039/c9ra03641e.

[179] S. B. Ross-Murphy. Structure and rheology of gelatin gels: recent progress. *Polymer*, 33(12):2622–2627, 1992. ISSN 00323861. doi: 10.1016/0032-3861(92)91146-S.

[180] P. Rothemund, N. Kellaris, S. K. Mitchell, E. Acome, and C. Keplinger. HASEL Artificial Muscles for a New Generation of Lifelike Robots—Recent Progress and Future Opportunities. *Advanced Materials*, 33(19):1–28, 2021. ISSN 15214095. doi: 10.1002/adma.202003375. URL `https://onlinelibrary.wiley.com/doi/full/10.1002/adma.202003375`.

[181] D. C. Rucker, J. Das, H. B. Gilbert, P. J. Swaney, M. I. Miga, N. Sarkar, and R. J. Webster. Sliding mode control of steerable needles. *IEEE Transactions on Robotics*, 29(5):1289–1299, 2013. ISSN 15523098. doi: 10.1109/TRO.2013.2271098.

[182] S. C. Ryu, Z. F. Quek, J. S. Koh, P. Renaud, R. J. Black, B. Moslehi, B. L. Daniel, K. J. Cho, and M. R. Cutkosky. Design of an optically controlled MR-compatible active needle. *IEEE Transactions on Robotics*, 31(1):1–11, 2015. ISSN 15523098. doi: 10.1109/TRO.2014.2367351.

[183] N. Sadati and M. Torabi. Adaptive 2D-path optimization of steerable bevel-tip needles in uncertain model of brain tissue. *2009 WRI World Congress on Computer Science and Information Engineering, CSIE 2009*, 5:254–260, 2009. doi: 10.1109/CSIE.2009.855.

[184] M. Sasaki, B. C. Karikkineth, K. Nagamine, H. Kaji, K. Torimitsu, and M. Nishizawa. Highly Conductive Stretchable and Biocompatible Electrode-Hydrogel Hybrids for Advanced Tissue Engineering. *Advanced Healthcare Materials*, 3(11):1919–1927, 2014. ISSN 21922659. doi: 10.1002/adhm.201400209. URL `https://www.ncbi.nlm.nih.gov/pubmed/24912988`.

[185] M. Scali, P. A. Veldhoven, P. W. Henselmans, D. Dodou, and P. Breedveld. Design of an ultra-thin steerable probe for percutaneous interventions and preliminary evaluation in a gelatine phantom. *PLoS ONE*, 14(9):1–24, 2019. ISSN 19326203. doi: 10.1371/journal.pone.0221165. URL `http://dx.doi.org/10.1371/journal.pone.0221165`.

[186] R. Secoli and F. R. Y. Baena. Adaptive path-following control for bio-inspired steerable needles. *Proceedings of the IEEE RAS and EMBS International Conference on Biomedical Robotics and Biomechatronics*, 2016-July(Llc):87–93, 2016. ISSN 21551774. doi: 10.1109/BIOROB.2016.7523603.

[187] K. M. Seiler, S. P. N. Singh, S. Sukkarieh, and H. Durrant-Whyte. Using Lie group symmetries for fast corrective motion planning. *International Journal of Robotics Research*, 31(2):151–166, 2012. ISSN 02783649. doi: 10.1177/0278364911429977.

[188] Y. J. Seol, H. W. Kang, S. J. Lee, A. Atala, and J. J. Yoo. Bioprinting technology and its applications. *European Journal of Cardio-thoracic Surgery*, 46(3):342–348, 2014. ISSN 1873734X. doi: 10.1093/ejcts/ezu148. URL `https://www.ncbi.nlm.nih.gov/pubmed/25061217`.

[189] D. Shalon, S. J. Smith, and P. O. Brown. A DNA microarray system for analyzing complex DNA samples using two-color fluorescent probe hybridization. *Genome Research*, 6(7):639–645, 1996. ISSN 10549803. doi: 10.1101/gr.6.7.639. URL `https://www.ncbi.nlm.nih.gov/pubmed/8796352`.

[190] X. Shen and H. E. Naguib. A robust ink deposition system for binder jetting and material jetting. *Additive Manufacturing*, 29, 2019. ISSN 22148604. doi: 10.1016/j.addma.2019.100820.

[191] T. Shimizu, M. Yamato, T. Akutsu, T. Shibata, Y. Isoi, A. Kikuchi, M. Umezu, and T. Okano. Electrically communicating three-dimensional cardiac tissue mimic fabricated by layered cultured cardiomyocyte sheets. *Journal of Biomedical Materials Research*, 60(1):110–117, 2002. ISSN 00219304. doi: 10.1002/jbm.1284. URL `https://www.ncbi.nlm.nih.gov/pubmed/11835166`.

[192] S. R. Shin, R. Farzad, A. Tamayol, V. Manoharan, P. Mostafalu, Y. S. Zhang, M. Akbari, S. M. Jung, D. Kim, M. Comotto, N. Annabi, F. E. Al-Hazmi, M. R. Dokmeci, and A. Khademhosseini. A Bioactive Carbon Nanotube-Based Ink for Printing 2D and 3D Flexible Electronics. *Advanced Materials*, 28(17): 3280–3289, 2016. ISSN 15214095. doi: 10.1002/adma.201506420. URL `https://www.ncbi.nlm.nih.gov/pubmed/26915715`.

[193] A. Simaite, F. Mesnilgrente, B. Tondu, P. Souères, and C. Bergaud. Towards inkjet printable conducting polymer artificial muscles. *Sensors and Actuators, B: Chemical*, 229:425–433, 2016. ISSN 09254005. doi: 10.1016/j.snb.2016.01.142.

[194] A. Skardal. Principles and applications of bioprinting. In G. C.-U. Ali Khademhosseini, editor, *3D Bioprinting in Regenerative Engineering*, chapter 1, pages 1–24. CRC Press, 2018. doi: 10.1201/b21916-1.

[195] A. Skardal, M. Devarasetty, H. W. Kang, I. Mead, C. Bishop, T. Shupe, S. J. Lee, J. Jackson, J. Yoo, S. Soker, and A. Atala. A hydrogel bioink toolkit for mimicking native tissue biochemical and mechanical

properties in bioprinted tissue constructs. *Acta Biomaterialia*, 25:24–34, 2015. ISSN 18787568. doi: 10.1016/j.actbio.2015.07.030. URL https://www.ncbi.nlm.nih.gov/pubmed/26210285https://www.sciencedirect.com/science/article/abs/pii/S1742706115300283?via%3Dihub.

[196] M. A. Skylar-Scott, S. G. M. Uzel, L. L. Nam, J. H. Ahrens, R. L. Truby, S. Damaraju, and J. A. Lewis. Biomanufacturing of organ-specific tissues with high cellular density and embedded vascular channels. *Science Advances*, 5(9): eaaw2459, 2019. ISSN 23752548. doi: 10.1126/sciadv.aaw2459. URL http://10.0.4.102/sciadv.aaw2459https://dx.doi.org/10.1126/sciadv.aaw2459.

[197] E. M. Southern. DNA chips: Analysing sequence by hybridization to oligonucleotides on a large scale. *Trends in Genetics*, 12(3):110–115, 1996. ISSN 01689525. doi: 10.1016/0168-9525(96)81422-3. URL https://www.ncbi.nlm.nih.gov/pubmed/8868349.

[198] A. R. Spencer, E. Shirzaei Sani, J. R. Soucy, C. C. Corbet, A. Primbetova, R. A. Koppes, and N. Annabi. Bioprinting of a Cell-Laden Conductive Hydrogel Composite. *ACS Applied Materials and Interfaces*, 11(34):30518–30533, 2019. ISSN 19448252. doi: 10.1021/acsami.9b07353. URL https://www.ncbi.nlm.nih.gov/pubmed/31373791.

[199] P. J. Swaney, J. Burgner, H. B. Gilbert, and R. J. Webster. A flexure-based steerable needle: High curvature with reduced tissue damage. *IEEE Transactions on Biomedical Engineering*, 60(4):906–909, 2013. ISSN 15582531. doi: 10.1109/TBME.2012.2230001.

[200] P. J. Swaney, A. W. Mahoney, B. I. Hartley, A. A. Remirez, E. Lamers, R. H. Feins, R. Alterovitz, and R. J. Webster. Toward Transoral Peripheral Lung Access: Combining Continuum Robots and Steerable Needles. *Journal of Medical Robotics Research*, 2(1):139–148, 2017. ISSN 24249068. doi: 10.1142/S2424905X17500015.

[201] A. G. Szent-Györgyi. Milestone in physiology: The early history of the biochemistry of muscle contraction. *Journal of General Physiology*, 123(6):631–641, 2004. ISSN 00221295. doi: 10.1085/jgp.200409091. URL https://dx.doi.org/10.1085/jgp.200409091https://www.ncbi.nlm.nih.gov/pmc/articles/PMC2234565/pdf/200409091.pdf.

[202] M. Szwarc and M. Van Beylen. *Ionic polymerization and living polymers*. Springer Science & Business Media, 2012. ISBN 9401114781.

[203] H. Tadayyon, A. Lasso, A. Kaushal, P. Guion, and G. Fichtinger. Target motion tracking in MRI-guided transrectal robotic prostate biopsy. *IEEE Transactions*

on Biomedical Engineering, 58(11):3135–3142, 2011. ISSN 00189294. doi: 10.1109/TBME.2011.2163633.

[204] X. Tan, P. Yu, K. B. Lim, and C. K. Chui. Robust path planning for flexible needle insertion using Markov decision processes. *International Journal of Computer Assisted Radiology and Surgery*, 13(9):1439–1451, 2018. ISSN 18616429. doi: 10.1007/s11548-018-1783-x. URL `https://doi.org/10.1007/s11548-018-1783-x`.

[205] D. L. Taylor and M. in het Panhuis. Self-healing hydrogels. *Advanced Materials*, 28(41):9060–9093, 2016.

[206] K. Tian, J. Bae, S. E. Bakarich, C. Yang, R. D. Gately, G. M. Spinks, M. in het Panhuis, Z. Suo, and J. J. Vlassak. 3D Printing of Transparent and Conductive Heterogeneous Hydrogel–Elastomer Systems. *Advanced Materials*, 29(10), 2017. ISSN 15214095. doi: 10.1002/adma.201604827.

[207] S. Tibbits. The emergence of "4D printing", 2013. URL `https://www.ted.com/talks/skylar_tibbits_the_emergence_of_4d_printing,`.

[208] F. Tsai and W. Philpot. Derivative analysis of hyperspectral data. *Remote Sensing of Environment*, 66(1):41–51, 1998. ISSN 00344257. doi: 10.1016/S0034-4257(98)00032-7. URL `https://www.sciencedirect.com/science/article/pii/S0034425798000327`.

[209] N. J. Van De Berg, D. J. Van Gerwen, J. Dankelman, and J. J. Van Den Dobbelsteen. Design Choices in Needle Steering - A Review. *IEEE/ASME Transactions on Mechatronics*, 20(5):2172–2183, 2015. ISSN 10834435. doi: 10.1109/TMECH.2014.2365999.

[210] J. Van Den Berg, S. Patil, R. Alterovitz, P. Abbeel, and K. Goldberg. LQG-based planning, sensing, and control of steerable needles. *Springer Tracts in Advanced Robotics*, 68(STAR):373–389, 2010. ISSN 16107438. doi: 10.1007/978-3-642-17452-0{_}22.

[211] J. van Otterloo and A. R. Cruden. Rheology of pig skin gelatine: Defining the elastic domain and its thermal and mechanical properties for geological analogue experiment applications. *Tectonophysics*, 683:86–97, 2016. ISSN 00401951. doi: 10.1016/j.tecto.2016.06.019. URL `https://www.sciencedirect.com/science/article/pii/S0040195116302256`.

[212] G. J. Vrooijink, M. Abayazid, S. Patil, R. Alterovitz, and S. Misra. Needle path planning and steering in a three-dimensional non-static environment using

two-dimensional ultrasound images. *International Journal of Robotics Research*, 33(10):1361–1374, 2014. ISSN 17413176. doi: 10.1177/0278364914526627.

[213] C. Wang, B. Liu, L. Liu, Y. Zhu, J. Hou, P. Liu, and X. Li. *A review of deep learning used in the hyperspectral image analysis for agriculture*, volume 54. Springer Netherlands, 2021. ISBN 0123456789. doi: 10.1007/s10462-021-10018-y. URL `https://doi.org/10.1007/s10462-021-10018-y`.

[214] Q. Wang, L. Zhang, Y. Liu, G. Zhang, and P. Zhu. Characterization and functional assessment of alginate fibers prepared by metal-calcium ion complex coagulation bath. *Carbohydrate Polymers*, 232, 2020. ISSN 01448617. doi: 10.1016/j.carbpol.2019.115693.

[215] M. Wartenberg, J. Schornak, K. Gandomi, P. Carvalho, C. Nycz, N. Patel, I. Iordachita, C. Tempany, N. Hata, J. Tokuda, and G. S. Fischer. Closed-Loop Active Compensation for Needle Deflection and Target Shift During Cooperatively Controlled Robotic Needle Insertion. *Annals of Biomedical Engineering*, 46(10):1582–1594, 2018. ISSN 15739686. doi: 10.1007/s10439-018-2070-2.

[216] A. Watthanaphanit, P. Supaphol, H. Tamura, S. Tokura, and R. Rujiravanit. Fabrication, structure, and properties of chitin whisker-reinforced alginate nanocomposite fibers. *Journal of Applied Polymer Science*, 110(2):890–899, 2008. ISSN 00218995. doi: 10.1002/app.28634.

[217] T. Watts, R. Secoli, and F. R. Y. Baena. A Mechanics-Based Model for 3-D Steering of Programmable Bevel-Tip Needles. *IEEE Transactions on Robotics*, 35(2):371–386, 2019. ISSN 15523098. doi: 10.1109/TRO.2018.2879584.

[218] R. J. Webster, J. S. Kim, N. J. Cowan, G. S. Chirikjian, and A. M. Okamura. Nonholonomic modeling of needle steering. *International Journal of Robotics Research*, 25(5-6):509–525, 2006. ISSN 02783649. doi: 10.1177/0278364906065388.

[219] T. R. Wedlick and A. M. Okamura. Characterization of pre-curved needles for steering in tissue. *Proceedings of the 31st Annual International Conference of the IEEE Engineering in Medicine and Biology Society: Engineering the Future of Biomedicine, EMBC 2009*, -(Needle 2):1200–1203, 2009. doi: 10.1109/IEMBS.2009.5333407.

[220] S. Wen and R. Alterovitz. Motion planning under uncertainty for medical needle steering using optimization in belief space. *IEEE International Conference on Intelligent Robots and Systems*, -(Iros):1775–1781, 2014. ISSN 21530866. doi: 10.1109/IROS.2014.6942795.

[221] W. C. Wilson and T. Boland. Cell and organ printing 1: Protein and cell printers. *Anatomical Record - Part A Discoveries in Molecular, Cellular, and Evolutionary Biology*, 272(2):491–496, 2003. ISSN 0003276X. doi: 10.1002/ar.a.10057. URL `https://www.ncbi.nlm.nih.gov/pubmed/12740942`.

[222] J. Wu, C. Yuan, Z. Ding, M. Isakov, Y. Mao, T. Wang, M. L. Dunn, and H. J. Qi. Multi-shape active composites by 3D printing of digital shape memory polymers. *Scientific Reports*, 6:24224, 2016. ISSN 20452322. doi: 10.1038/srep24224. URL `https://www.ncbi.nlm.nih.gov/pmc/articles/PMC4829848/`.

[223] J. Xiong, X. Li, Y. Gan, and Z. Xia. Path planning for flexible needle insertion system based on Improved Rapidly-Exploring Random Tree algorithm. *2015 IEEE International Conference on Information and Automation, ICIA 2015 - In conjunction with 2015 IEEE International Conference on Automation and Logistics*, -(61403368):1545–1550, 2015. doi: 10.1109/ICInfA.2015.7279532.

[224] X. Xiong, C. Wu, C. Zhou, G. Zhu, Z. Chen, and W. Tan. Responsive DNA-based hydrogels and their applications. *Macromolecular Rapid Communications*, 34(16): 1271–1283, 2013. ISSN 10221336. doi: 10.1002/marc.201300411.

[225] J. L. Xu, S. Hugelier, H. Zhu, and A. A. Gowen. Deep learning for classification of time series spectral images using combined multi-temporal and spectral features. *Analytica Chimica Acta*, 1143:9–20, 2021. ISSN 18734324. doi: 10.1016/j.aca.2020.11.018.

[226] T. Xu, C. Baicu, M. Aho, M. Zile, and T. Boland. Fabrication and characterization of bio-engineered cardiac pseudo tissues. *Biofabrication*, 1(3):35001, 2009. ISSN 17585082. doi: 10.1088/1758-5082/1/3/035001. URL `https://www.ncbi.nlm.nih.gov/pubmed/20811105`.

[227] J. Yang, X. Yang, X. Ye, and J. Lin. Optimal parameters for laccase-mediated destaining of Coomassie Brilliant Blue R-250-stained polyacrylamide gels. *Data in Brief*, 7:1–7, 2016. ISSN 23523409. doi: 10.1016/j.dib.2016.01.029. URL `http://dx.doi.org/10.1016/j.dib.2016.01.029`.

[228] S.-Z. Yow, T. H. Lim, E. K. F. Yim, C. T. Lim, and K. W. Leong. A 3D Electroactive Polypyrrole-Collagen Fibrous Scaffold for Tissue Engineering. *Polymers*, 3(1):527–544, 2011. ISSN 2073-4360. doi: 10.3390/polym3010527.

[229] L. Zhang, W. Du, A. Nautiyal, Z. Liu, and X. Zhang. Recent progress on nanostructured conducting polymers and composites: synthesis, application and future aspects. *Science China Materials*, 61(3):303–352, 2018. ISSN 21994501. doi: 10.1007/s40843-017-9206-4.

[230] X. Zhang, X. Wang, W. Fan, Y. Liu, Q. Wang, and L. Weng. Fabrication, Property and Application of Calcium Alginate Fiber: A Review. *Polymers*, 14(15):1–18, 2022. ISSN 20734360. doi: 10.3390/polym14153227.

[231] Y. Zhang, C. Tse, D. Rouholamin, and P. J. Smith. Scaffolds for tissue engineering produced by inkjet printing. *Central European Journal of Engineering*, 2(3):325–335, 2012. ISSN 20819927. doi: 10.2478/s13531-012-0016-2.

[232] D. Zhou, J. Chen, B. Liu, X. Zhang, X. Li, and T. Xu. Bioinks for jet-based bioprinting. *Bioprinting*, 16, 2019. ISSN 24058866. doi: 10.1016/j.bprint.2019.e00060.

[233] Y. Zhou, W. M. Huang, S. F. Kang, X. L. Wu, H. B. Lu, J. Fu, and H. Cui. From 3D to 4D printing: approaches and typical applications. *Journal of Mechanical Science and Technology*, 29(10):4281–4288, 2015. ISSN 1738494X. doi: 10.1007/s12206-015-0925-0. URL `https://link.springer.com/article/10.1007/s12206-015-0925-0`.

[234] H. Zhu, B. Chu, Y. Fan, X. Tao, W. Yin, and Y. He. Hyperspectral Imaging for Predicting the Internal Quality of Kiwifruits Based on Variable Selection Algorithms and Chemometric Models. *Scientific Reports*, 7(1):1–13, 2017. ISSN 20452322. doi: 10.1038/s41598-017-08509-6. URL `http://dx.doi.org/10.1038/s41598-017-08509-6`.

[235] M. Zhu and S. E. Salcudean. Real-time image-based B-mode ultrasound image simulation of needles using tensor-product interpolation. *IEEE Transactions on Medical Imaging*, 30(7):1391–1400, 2011. ISSN 02780062. doi: 10.1109/TMI.2011.2121091.

Appendix A

Raw Alginate Tensile Test Results

BL1	Young's Modulus	Fracture Point	Approx. Diam.	Mass	Length	Wet / Dry	dtex	Fracture Force (N)	cN/dtex	Initial L	Final L	Elongation %	Elongation delta
1	2.66E+07	1.56E+07	1.50E-01	5.30E-03	5.86E+01	Dry	9.04E+02	2.76E-01	3.05E+00	1.99E+01	2.00E+01	1.01	0.15
2	1.02E+07	1.63E+07	2.70E-01	4.60E-03	4.23E+01	Dry	1.09E+03	9.32E-01	8.57E+00	2.00E+01	2.06E+01	1.03	0.52
3	1.95E+07	2.47E+07	1.40E-01	1.20E-03	3.92E+01	Dry	3.06E+02	3.80E-01	1.24E+01	1.99E+01	2.03E+01	1.02	0.31
4	1.51E+07	1.80E+07	1.60E-01	1.90E-03	3.57E+01	Dry	5.32E+02	3.63E-01	6.81E+00	2.00E+01	2.03E+01	1.01	0.27
5	7.78E+06	1.59E+07	2.70E-01	4.40E-03	6.54E+01	Dry	6.72E+02	7.21E-01	1.07E+01	2.00E+01	2.05E+01	1.02	0.45
6	1.69E+06	8.76E+06	3.50E-01	2.90E-03	3.24E+01	Dry	8.96E+02	8.42E-01	9.41E+00	2.00E+01	2.10E+01	1.05	1.03
7	1.40E+06	1.47E+06	3.10E-01	2.80E-03	3.49E+01	Dry	8.03E+02	1.11E-01	1.38E+00	2.00E+01	2.03E+01	1.01	0.25

8	2.02E+05	3.88E+06	2.90E-01	1.41E-02	4.10E+01	Wet	3.44E+03	3.73E-01	1.08E+00	2.00E+01	2.38E+01	1.19	3.84
9	2.36E+05	1.10E+06	3.80E-01	1.46E-02	4.13E+01	Wet	3.54E+03	8.33E-02	2.35E-01	2.00E+01	2.28E+01	1.14	2.75
10	3.45E+06	9.24E+06	3.00E-01	9.00E-03	6.18E+01	Wet	1.46E+03	5.29E-02	3.63E-01	2.00E+01	2.08E+01	1.04	0.84

BL2	Young's Modulus	Fracture Point	Approx. Diam.	Mass	Length	Wet / Dry	dtex	Fracture Force (N)	cN/dtex	Initial L	Final L	Elongation %	Elongation delta
1	3.71E+07	1.34E+07	2.10E-01	2.20E-03	4.05E+01	Dry	5.43E+02	4.64E-01	8.55E+00	2.00E+01	2.02E+01	1.01	0.21
2	2.97E+05	5.78E+06	2.30E-01	2.90E-03	4.32E+01	Dry	6.71E+02	2.38E-01	3.55E+00	2.00E+01	2.46E+01	1.23	4.55
3	3.65E+05	2.11E+06	2.10E-01	7.92E-02	5.17E+01	Wet	1.53E+04	1.73E-01	1.13E-01	2.08E+01	2.33E+01	1.12	2.56
4	3.24E+06	2.99E+06	3.00E-01	1.70E-03	6.53E+01	Dry	2.60E+02	2.11E-01	8.11E+00	2.00E+01	2.02E+01	1.01	0.20
5	9.87E+04	1.99E+06	3.20E-01	3.33E-02	4.64E+01	Wet	7.18E+03	1.54E-01	2.14E-01	2.00E+01	2.80E+01	1.40	8.00
6	1.78E+05	1.05E+06	3.50E-01	1.54E-02	3.97E+01	Wet	3.88E+03	1.01E-01	2.61E-01	2.00E+01	2.33E+01	1.17	3.33
7	5.89E+04	3.31E+05	2.80E-01	1.66E-02	7.01E+01	Wet	2.37E+03	2.04E-02	8.60E-02	2.00E+01	2.14E+01	1.07	1.42
8	5.72E+04	1.07E+06	3.50E-01	3.50E-02	8.47E+01	Wet	4.13E+03	1.02E-01	2.48E-01	2.01E+01	2.81E+01	1.40	8.00
9	5.57E+04	3.92E+05	3.40E-01	6.46E-02	6.75E+01	Wet	9.57E+03	3.56E-02	3.72E-02	2.00E+01	2.23E+01	1.11	2.30
10	2.09E+04	6.42E+05	4.20E-01	3.71E-02	6.27E+01	Wet	5.92E+03	8.90E-02	1.50E-01	2.00E+01	2.65E+01	1.32	6.50
11	6.63E+04	1.06E+06	4.80E-01	9.80E-03	3.91E+01	Wet	2.51E+03	1.92E-01	7.68E-01	2.00E+01	2.81E+01	1.41	8.13
12	2.50E+05	4.33E+06	1.80E-01	1.94E-02	3.35E+01	Wet	5.78E+03	1.10E-01	1.91E-01	2.00E+01	2.68E+01	1.34	6.80

BL3	Young's Modulus	Fracture Point	Approx. Diam.	Mass	Length	Wet / Dry
1	4.69E+06	2.12E+06	0.25	N/A	N/A	Wet
2	6.98E+05	6.09E+05	0.57	N/A	N/A	Wet
3	8.56E+04	9.23E+05	0.41	N/A	N/A	Wet
4	1.10E+06	9.10E+05	0.41	N/A	N/A	Wet
5	6.73E+04	1.04E+06	0.36	N/A	N/A	Wet
6	4.63E+05	1.03E+06	0.47	N/A	N/A	Wet
7	9.28E+04	6.06E+05	0.56	N/A	N/A	Wet
8	7.63E+04	1.67E+06	1.01	N/A	N/A	Wet
9	1.40E+05	1.07E+06	0.41	N/A	N/A	Wet
10	9.92E+04	1.01E+06	0.53	N/A	N/A	Wet
11	4.33E+07	4.14E+07	0.25	N/A	N/A	Dry
12	1.89E+06	7.25E+06	0.41	N/A	N/A	Wet
13	7.02E+06	1.80E+07	0.38	N/A	N/A	Dry

Appendix B

Raw Gelatine Compression Test Results

wt%	Young's Modulus	Approximate Yield Modulus @ 20% strain	Approximate Yield Modulus @ 30% strain	Fracture Point	Fracture Strain
3.33	4.34E+03	9.01E+02	1.61E+03	5.78E+03	53.87%
3.33	4.39E+03	9.55E+02	1.59E+03	3.54E+03	46.12%
3.33	6.43E+03	1.29E+03	2.23E+03	5.15E+03	46.83%
3.33	4.82E+03	1.02E+03	1.89E+03	6.00E+03	51.98%
3.33	3.06E+03	6.57E+02	1.23E+03	4.32E+03	53.17%
3.33	5.04E+03	1.07E+03	1.92E+03	1.03E+04	58.34%
3.33	3.75E+03	8.17E+02	1.38E+03	1.66E+03	34.24%
3.33	3.94E+03	8.50E+02	1.55E+03	7.38E+03	57.23%
3.33	4.81E+03	1.02E+03	1.76E+03	3.77E+03	46.60%

3.33	4.25E+03	8.96E+02	1.63E+03	5.62E+03	46.60%
3.33	3.76E+03	8.17E+02	1.46E+03	1.17E+04	65.38%
3.33	6.94E+03	1.48E+03	2.70E+03	6.83E+03	48.63%
3.33	3.73E+03	8.18E+02	1.45E+03	6.81E+03	57.62%
3.33	4.55E+03	9.71E+02	1.68E+03	3.03E+03	42.46%
3.33	5.09E+03	1.09E+03	2.01E+03	5.42E+03	47.82%
3.33	5.36E+03	1.14E+03	2.07E+03	3.24E+03	39.09%
3.33	3.45E+03	7.48E+02	1.37E+03	4.35E+03	53.58%
3.33	5.27E+03	1.10E+03	2.02E+03	5.86E+03	48.16%
3.33	4.49E+03	9.82E+02	1.75E+03	3.89E+03	45.54%
3.33	4.25E+03	9.04E+02	1.58E+03	6.94E+03	59.45%
3.33	3.56E+03	7.89E+02	1.43E+03	5.69E+03	55.45%
6.67	1.33E+04	2.71E+03	5.03E+03	1.47E+04	51.10%
6.67	7.71E+03	1.59E+03	2.99E+03	2.07E+04	61.94%
6.67	1.09E+04	2.28E+03	4.48E+03	1.84E+04	53.95%
6.67	1.41E+04	2.86E+03	5.52E+03	2.10E+04	53.34%
6.67	8.93E+03	1.89E+03	3.57E+03	6.17E+04	72.35%
6.67	1.11E+04	2.27E+03	3.98E+03	2.90E+04	66.18%
6.67	1.66E+04	3.44E+03	6.06E+03	3.20E+04	61.32%
6.67	1.39E+04	2.83E+03	5.55E+03	4.01E+04	62.30%
6.67	1.49E+04	3.03E+03	5.29E+03	1.98E+04	54.93%
6.67	1.25E+04	2.56E+03	4.76E+03	3.89E+04	65.89%
6.67	1.23E+04	2.56E+03	4.46E+03	1.06E+04	48.23%

6.67	1.46E+04	2.96E+03	5.54E+03	2.20E+04	54.13%
6.67	1.62E+04	3.34E+03	5.85E+03	1.33E+04	48.09%
6.67	1.75E+04	3.58E+03	6.40E+03	2.18E+04	53.61%
6.67	1.41E+04	2.91E+03	5.61E+03	1.47E+04	50.31%
6.67	1.66E+04	3.47E+03	6.02E+03	2.34E+04	55.82%
6.67	1.47E+04	3.01E+03	5.71E+03	1.57E+04	48.30%
6.67	1.43E+04	2.94E+03	5.56E+03	2.17E+04	53.60%
6.67	1.49E+04	3.04E+03	5.70E+03	1.39E+04	46.43%
6.67	1.46E+04	3.04E+03	5.78E+03	1.43E+04	46.74%
10	3.32E+04	8.20E+03	1.45E+04	4.46E+04	50.88%
10	2.38E+04	4.62E+03	8.61E+03	1.18E+04	36.63%
10	4.72E+04	9.26E+03	1.56E+04	1.72E+05	71.53%
10	4.06E+04	8.17E+03	1.36E+04	1.77E+05	70.51%
10	3.92E+04	8.02E+03	1.41E+04	3.16E+04	46.85%
10	3.99E+04	8.08E+03	1.46E+04	3.29E+04	46.22%
10	3.39E+04	6.94E+03	1.20E+04	1.67E+04	40.83%
10	5.17E+04	1.03E+04	1.73E+04	7.98E+04	59.12%
10	2.82E+04	5.65E+03	1.01E+04	2.61E+04	48.46%
10	2.63E+04	5.38E+03	9.94E+03	1.29E+04	38.41%
10	3.32E+04	6.80E+03	1.20E+04	3.51E+04	59.54%
10	3.30E+04	6.82E+03	1.23E+04	2.74E+04	45.35%
10	2.90E+04	5.91E+03	1.10E+04	3.90E+04	52.12%
10	3.52E+04	8.00E+03	1.36E+04	4.01E+04	50.65%

10	4.35E+04	8.90E+03	1.62E+04	4.27E+04	50.07%
10	5.94E+04	1.19E+04	1.89E+04	1.76E+05	70.69%
10	3.74E+04	7.58E+03	1.32E+04	7.11E+04	60.53%
10	4.15E+04	8.36E+03	1.47E+04	2.52E+04	41.85%
10	3.60E+04	7.42E+03	1.28E+04	3.21E+04	52.27%
10	4.18E+04	8.17E+03	1.29E+04	7.61E+04	62.38%
10	3.72E+04	7.50E+03	1.35E+04	6.93E+04	59.22%
15	5.95E+04	1.19E+04	1.90E+04	1.76E+05	70.69%
15	5.08E+04	1.02E+04	1.82E+04	1.48E+05	64.55%
15	5.53E+04	1.13E+04	1.94E+04	1.46E+05	66.41%
15	6.77E+04	1.36E+04	2.32E+04	1.34E+05	62.92%
15	5.12E+04	1.03E+04	1.87E+04	1.21E+05	63.59%
15	4.71E+04	9.63E+03	1.71E+04	1.53E+05	68.49%
15	5.19E+04	1.03E+04	1.78E+04	1.37E+05	63.85%
15	5.01E+04	1.02E+04	1.78E+04	1.02E+05	62.39%
15	3.88E+04	7.97E+03	1.69E+04	1.38E+05	65.72%
15	7.57E+04	1.50E+04	2.61E+04	1.34E+05	60.11%
15	7.26E+04	1.09E+04	1.93E+04	1.55E+05	66.18%
15	6.22E+04	1.24E+04	2.15E+04	1.51E+05	64.91%
15	5.28E+04	1.06E+04	1.92E+04	1.91E+05	69.22%
15	4.23E+04	8.50E+03	1.50E+04	1.71E+05	68.84%
15	6.37E+04	1.29E+04	2.25E+04	7.90E+04	53.04%
15	5.61E+04	1.11E+04	1.92E+04	6.64E+04	55.14%

15	5.14E+04	9.65E+03	1.75E+04	1.54E+05	68.86%
15	3.97E+04	7.95E+03	1.46E+04	5.85E+04	56.50%
15	5.42E+04	1.09E+04	1.92E+04	7.75E+04	55.20%
15	5.31E+04	1.07E+04	1.89E+04	1.64E+05	66.20%

Appendix C

List of Publications

Jean-Henri Odendaal, Nitin Bhatia, Russell Wilson, and Johan Potgieter. Exploring non-destructive mechanical characterisation of hydrogels using hyperspectral imaging and machine vision. In *28th International Conference on Mechatronics and Machine Vision in Practice*, 2022.

Jean-Henri Odendaal, Marie Joo Le Guen, Olaf Diegel, Nitin Bhatia, Russell Wilson, and Johan Potgieter. 3D Printing using steerable needles. In *28th International Conference on Mechatronics and Machine Vision in Practice*, 2022.

Jean-Henri Odendaal, Marie Joo Le Guen, Olaf Diegel, Nitin Bhatia, Russell Wilson, and Johan Potgieter. On Using Steerable Needles for the 3D Printing of Biomaterials. In *Global Congress of Manufacturing and Management*, 2022.

DRC 16

MASSEY UNIVERSITY
GRADUATE RESEARCH SCHOOL

STATEMENT OF CONTRIBUTION
DOCTORATE WITH PUBLICATIONS/MANUSCRIPTS

We, the candidate and the candidate's Primary Supervisor, certify that all co-authors have consented to their work being included in the thesis and they have accepted the candidate's contribution as indicated below in the *Statement of Originality*.

Name of candidate:	Jean Henri Odendaal
Name/title of Primary Supervisor:	Prof. Johan Potgieter
Name of Research Output and full reference:	
Exploring non-destructive mechanical characterisation of hydrogels using hyperspectral imaging and machine vision	
In which Chapter is the Manuscript /Published work:	Chapter 3
Please indicate:	
• The percentage of the manuscript/Published Work that was contributed by the candidate:	80%
and	
• Describe the contribution that the candidate has made to the Manuscript/Published Work:	
The candidate conducted / authored the research reported in the published work.	
For manuscripts intended for publication please indicate target journal:	
IEEEXplore	
Candidate's Signature:	Jean Henri Odendaal Digitally signed by Jean Henri Odendaal Date: 2022.11.21 13:24:19 +13'00'
Date:	21/11/2022
Primary Supervisor's Signature:	Prof. Johan Potgieter Digitally signed by Prof. Johan Potgieter DN: cn=Prof. Johan Potgieter, c=NZ, o=Massey University, ou=Massey Agrifood Digital Lab, email=j.potgieter@massey.ac.nz Date: 2022.11.21 13:31:28 +13'00'
Date:	21/11/2022

(This form should appear at the end of each thesis chapter/section/appendix submitted as a manuscript/ publication or collected as an appendix at the end of the thesis)

DRC 16

MASSEY UNIVERSITY
GRADUATE RESEARCH SCHOOL

STATEMENT OF CONTRIBUTION
DOCTORATE WITH PUBLICATIONS/MANUSCRIPTS

We, the candidate and the candidate's Primary Supervisor, certify that all co-authors have consented to their work being included in the thesis and they have accepted the candidate's contribution as indicated below in the *Statement of Originality*.

Name of candidate:	Jean Henri Odendaal
Name/title of Primary Supervisor:	Prof. Johan Potgieter
Name of Research Output and full reference:	
3D Printing using Steerable Needles	
In which Chapter is the Manuscript /Published work:	Chapter 3
Please indicate:	
• The percentage of the manuscript/Published Work that was contributed by the candidate:	80%
and	
• Describe the contribution that the candidate has made to the Manuscript/Published Work:	
The candidate conducted / authored the research reported in the published work.	
For manuscripts intended for publication please indicate target journal:	
IEEEXplore	
Candidate's Signature:	Jean Henri Odendaal Digitally signed by Jean Henri Odendaal Date: 2022.11.21 13:24:19 +13'00'
Date:	21/11/2022
Primary Supervisor's Signature:	Prof. Johan Potgieter Digitally signed by Prof. Johan Potgieter DN: cn=Prof. Johan Potgieter, c=NZ, o=Massey University, ou=Massey Agrifood Digital Lab, email=j.potgieter@massey.ac.nz Date: 2022.11.21 13:30:53 +13'00'
Date:	21/11/2022

(This form should appear at the end of each thesis chapter/section/appendix submitted as a manuscript/ publication or collected as an appendix at the end of the thesis)

DRC 16

MASSEY UNIVERSITY
GRADUATE RESEARCH SCHOOL

STATEMENT OF CONTRIBUTION
DOCTORATE WITH PUBLICATIONS/MANUSCRIPTS

We, the candidate and the candidate's Primary Supervisor, certify that all co-authors have consented to their work being included in the thesis and they have accepted the candidate's contribution as indicated below in the *Statement of Originality*.

Name of candidate:	Jean Henri Odendaal
Name/title of Primary Supervisor:	Prof. Johan Potgieter
Name of Research Output and full reference:	
On Using Steerable Needles for the 3D Printing of Biomaterials	
In which Chapter is the Manuscript /Published work:	Chapter 5
Please indicate:	
• The percentage of the manuscript/Published Work that was contributed by the candidate:	80%
and	
• Describe the contribution that the candidate has made to the Manuscript/Published Work:	
The candidate conducted / authored the research reported in the published work.	
For manuscripts intended for publication please indicate target journal:	
Materials Today Proceedings	
Candidate's Signature:	Jean Henri Odendaal Digitally signed by Jean Henri Odendaal Date: 2022.11.21 13:24:19 +13'00'
Date:	21/11/2022
Primary Supervisor's Signature:	Prof. Johan Potgieter Digitally signed by Prof. Johan Potgieter DN: cn=Prof. Johan Potgieter, c=NZ, o=Massey University, ou=Massey Agrifood Digital Lab, email=j.potgieter@massey.ac.nz Date: 2022.11.21 13:32:00 +13'00'
Date:	21/11/2022

(This form should appear at the end of each thesis chapter/section/appendix submitted as a manuscript/ publication or collected as an appendix at the end of the thesis)